REPORT DOCUMENTATION PAGE

Form Approved
OMB NO. 0704-0188

1. AGENCY USE ONLY (Leave Blank)	2. REPORT DATE 13 October 2004	3. REPORT TYPE AND DATES COVERED Final Report, 28 Sep 00 - 30 Jun 04

4. TITLE AND SUBTITLE
Elastic Properties of Advanced Superhard Thin Films by Surface Brillouin Scattering: Effects of Composition, Structure and P-T Environments

5. FUNDING NUMBERS
DAAD19-00-1-0569

6. AUTHOR(S)
Murli H. Manghnani and Pavel V. Zinin

7. PERFORMING ORGANIZATION NAME(S) AND ADDRESS(ES)
University of Hawaii, Hawaii Institute of Geophysics and Planetology (HIGP/SOEST), Honolulu, Hawaii 96822

8. PERFORMING ORGANIZATION REPORT NUMBER   UH-HIGP/SOEST Final Report (2000-2004)

9. SPONSORING / MONITORING AGENCY NAME(S) AND ADDRESS(ES)

U. S. Army Research Office
P.O. Box 12211
Research Triangle Park, NC 27709-2211

10. SPONSORING / MONITORING AGENCY REPORT NUMBER

41032-MS-H

1 12

11. SUPPLEMENTARY NOTES
   The views, opinions and/or findings contained in this report are those of the author(s) and should not be construed as an official Department of the Army position, policy or decision, unless so designated by other documentation.

12 a. DISTRIBUTION / AVAILABILITY STATEMENT Approved for public release; distribution unlimited.	12 b. DISTRIBUTION CODE

13. ABSTRACT (Maximum 200 words)

14. SUBJECT TERMS
Thin films
Elastic properties
Structure
Brillouin scattering
cBN, BC_2N nc-TiN/a-Si_3N_4, DLC, BC_2N, ZrO_2, HfO_2

15. NUMBER OF PAGES
7 + appendices (8)

16. PRICE CODE

17. SECURITY CLASSIFICATION OR REPORT **UNCLASSIFIED**	18. SECURITY CLASSIFICATION ON THIS PAGE **UNCLASSIFIED**	19. SECURITY CLASSIFICATION OF ABSTRACT **UNCLASSIFIED**	20. LIMITATION OF ABSTRACT UL

20041102 074

BEST AVAILABLE COPY

Final Report: Elastic Properties of Advanced Superhard Thin Films by Surface Brillouin Scattering: Effects of Structure, and T, P Environments.

(1). Statement of the problem studied

Recent theoretical predictions of the new superhard materials and production of the new superhard films such as cubic boron nitride (cBN), carbon nitride β-C_3N_4, B_4C and chemical vapor deposited (CVD) diamond films have surged considerable interest in mechanical properties of thin hard and superhard films. Their hardness and abrasive qualities, highly valued in applied technology and defense industry, are controlled by their large elastic moduli. Elastic properties of the superhard films need to be determined experimentally because they strongly depend on the synthesis conditions, and they cannot be derived from theoretical considerations and modeling alone.
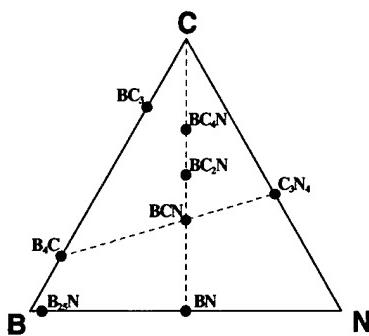

Figure 1. The C-N-B system, as a basis for the conducted work on hard and superhard multicomponent coatings.

The goals of this project were to determine the elastic properties and microstructure of the new superhard thin (30-500 nm) coatings, such as those based on the B-C-N triangle (Fig 1), by surface Brillouin spectroscopy (SBS), in conjunction with atomic force microscopy, as a function of composition, structure and P-T environments. We focused our research work on thin films that had best mechanical properties. Results of the research conducted have so far resulted in 17 publications [1-17]. A graduate student is participating in this research project. The main accomplishments are:

(2). Summary of the most important results

(a) Diamond-Like Carbon Films and Materials

1. We studied various types of diamond-like carbon (DLC) films [9,10,16]: Cr doped DLC films on steel, and DLC films deposited on Si (001) and containing only carbon. The results have demonstrated that the elastic moduli of the films decreased when foreign atoms, especially metals, were incorporated into the DLC-structure.

2. To measure the elastic properties of the DLC films thicker than 1 μm, we proposed techniques which combined two methods, i.e., surface Brillouin scattering (SBS) and laser-surface acoustic wave (SAW) technique [9,10,16]. It was found that reasonable estimates could be obtained for the longitudinal wave velocity, shear wave velocity, and Young's modulus of the film (see Fig. 2 and Table 1).

3. Combination of the SBS and laser-SAW technique allowed us to characterize set of DLC films with thickness from 25 to 500 nm. We did not find conformation of the "softening effect", i.e. decreasing elasticity of the film with thickness decrease, for DLC films.
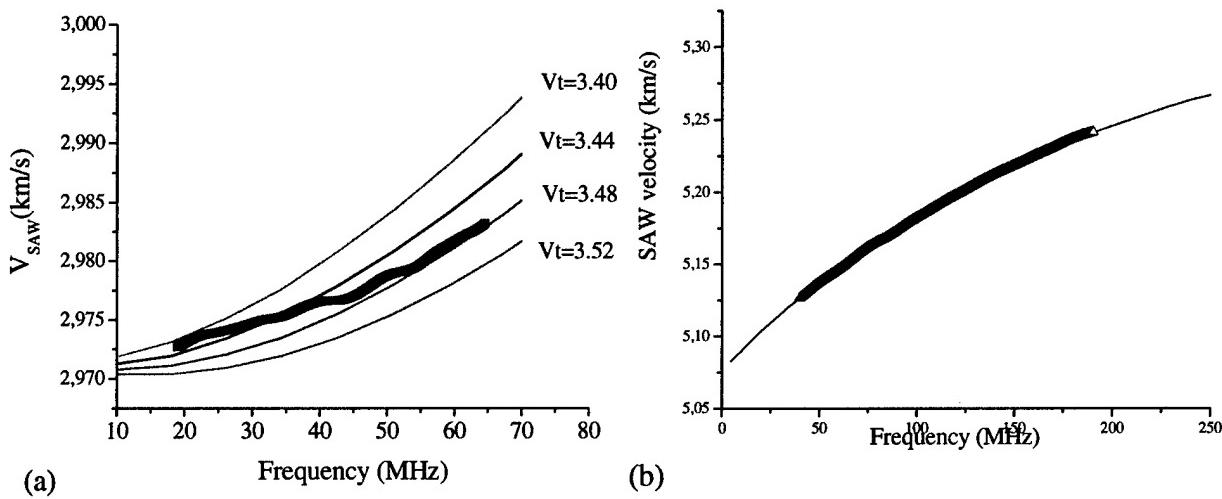

Figure 2. SAW dispersion curves of the and DLC/Si samples. (a) Cr-DLC. Solid red line is from the Laser-SAW measurement, solid thin lines are theoretical curves [10]; (b) DLC/Si. Solid red line is from the Laser-SAW measurement, solid thin line is the best fit [16].

4. Some of the new and prospective diamond films are synthesized from C_{60} under high pressure and temperature. It was predicted that such new phases obtained form C_{60} under high pressure and temperature could be harder than diamond. To prove this prediction we measured the elastic properties of superhard amorphous carbon, synthesized from C_{60} under high pressure (13 - 13.5 GPa) and temperature (900±100°C) by SBS [1,5,6]. Detection of the lateral and Rayleigh SAW in the samples enabled us to determine the bulk and shear moduli of the specimens, which showed that the elastic moduli of the new phase were not higher than those of diamond. To our knowledge it was the first reliable determination of bulk and shear elastic moduli for this type of amorphous carbon material.

(b) Cubic Boron Nitride films

1. We conducted measurements of the elastic properties of thin hard submicron cubic boron nitride (cBN) films grown on silicon [2,4,7]. The cBN films (Fig. 3) were prepared via mass selected ion beam deposition (MSIBD) at the University of Guettengen (Germany). Our results demonstrate that the elastic properties of the cBN films are not softer than those of bulk cBN.
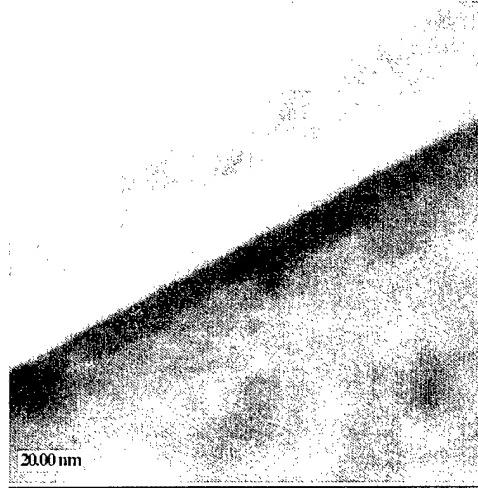
Figure 3. . TEM-picture of sample with 16 nm cBN layer.

2. The other task of this study was to investigate the cause of the "softening effect" of the c-BN film at room temperature. Green's function method was used to predict Brillouin scattering spectra of the acoustic excitation at the free surface (Fig. 4). Our results demonstrated that the effect of the thin hexagonal boron nitride (hBN) interlayer located between cBN film and Si substrate on the velocity of the surface acoustic wave (SAW) does not exceed 2% for a thin (16 nm) film and is negligible for cBN films thicker than 100 nm.

Figure 4. Theoretical SAW dispersion curve for cBN film (60 nm cBN /10 nm hBN) on Si (001) calculated for [100] direction, and compared with experimental data (stars).

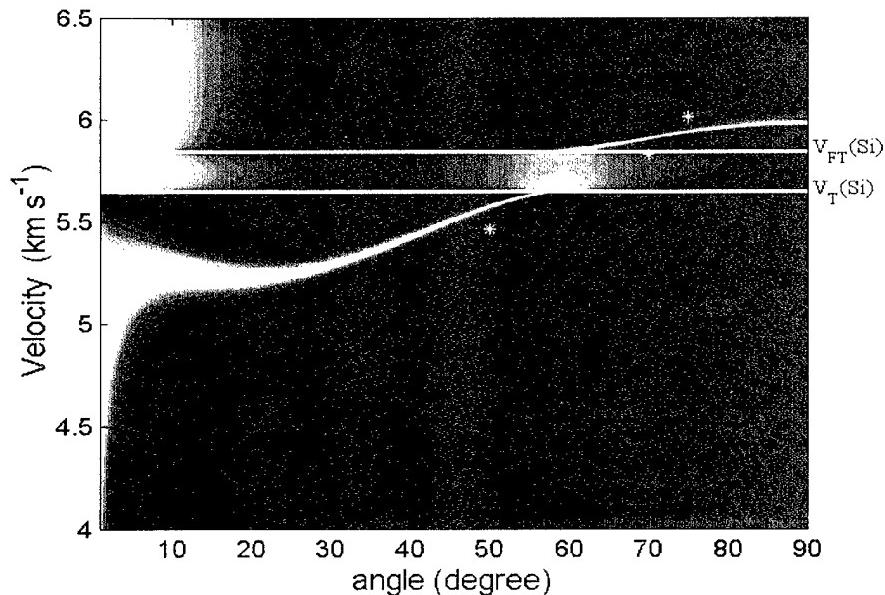*(c) ZrO₂ and HfO₂ Thin Films*

1. We also studied the variation of structure in atomic-layer-deposited (ALD) ZrO_2 and HfO_2 thin films as function of thickness (depth) and synthesis temperature environments by X-ray diffraction and Raman spectroscopy [12,15]. Both techniques detected a preferential formation of metastable phases in ZrO_2 and HfO_2, at 500° and 600° C, respectively.

(d) New Nano-crystalline Materials

2. The hardness of nanocomposite (*nc*) films developed recently appears to reach the hardness of diamond. In order to understand the origin of the extreme hardness of the novel nanocomposites, the elastic properties of two types of novel nanocomposite (*nc*) films were investigated: *nc*-TiN/*a*-Si₃N₄ and *nc*-TiN/*a*-BN. Further more, the first Brillouin scattering measurements on such nanocomposite films have been successfully performed using the backscattering geometry [14, 8]. It was also found that high hardness could be attributed to the nanostructure structure of nanocomposites (Hall-Petch effect).

3. New nano-crystalline BC_2N (*c*-BC_2N) phase recently synthesized under high pressure and temperature, exhibit extremely high hardness. Nano-crystalline BC_2N (*c*-BC_2N) phase was found to be the second hardest material. The first Brillouin scattering measurements on nanocrystalline cubic phase of BC_2N, second hardest solid, have been successfully performed using the "emulated" platelet scattering geometry [3,10]. We measured both longitudinal (V_p) and shear (V_s) and calculated the bulk and the shear moduli as 259 ± 22 GPa and 238 ± 8 GPa, respectively.

4. In view of continuing effort to investigate the structure-property relationship for hard thin films, we have installed atomic force acoustic microscope and have studied superhard BC_2N phase, and selected DLC films [13]. For BC_2N phase it was found that the small crystallites of 20-30 nm (Fig. 5), are combined into bigger aggregates (~ 200 nm). Such a nanostructure fetchers may have contributed to the unique mechanical properties observed in the BC_2N phase.
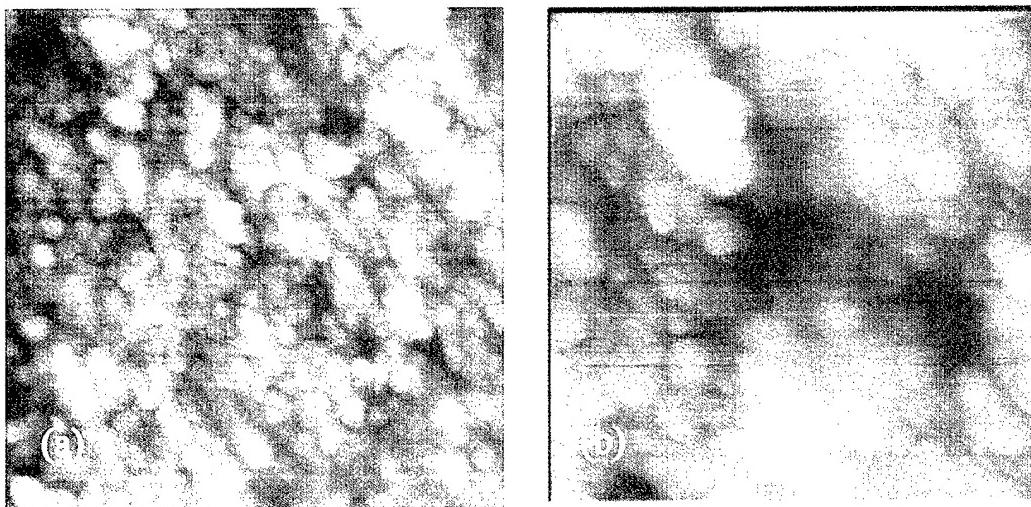

Figure 5. Contact mode AFM images of the *c*-BC_2N sample. The scan areas and data scales (heights) for images are : (a) 5.2 x 5.2 μm, and 195 nm; (b) 2.0 x 2.0 μm, and 106 nm, respectively.

(e) Developing the Theoretical Approach

1. We have developed a theory, based on Green's function approach, of surface acoustic waves (SAWs) propagation in for a two-layered anisotropic system (cBN/hBN/Si) [2,4]. Fortran code, used previously for a single anisotropic layer on an anisotropic substrate, was modified and has now been successfully applied.

(f) Vacuum Optical Furnace for High-Temperature Measurements

We have constructed (Fig. 6) and tested high-temperature furnace to investigate temperature dependence of the elastic properties of the DLC films to 600° C.
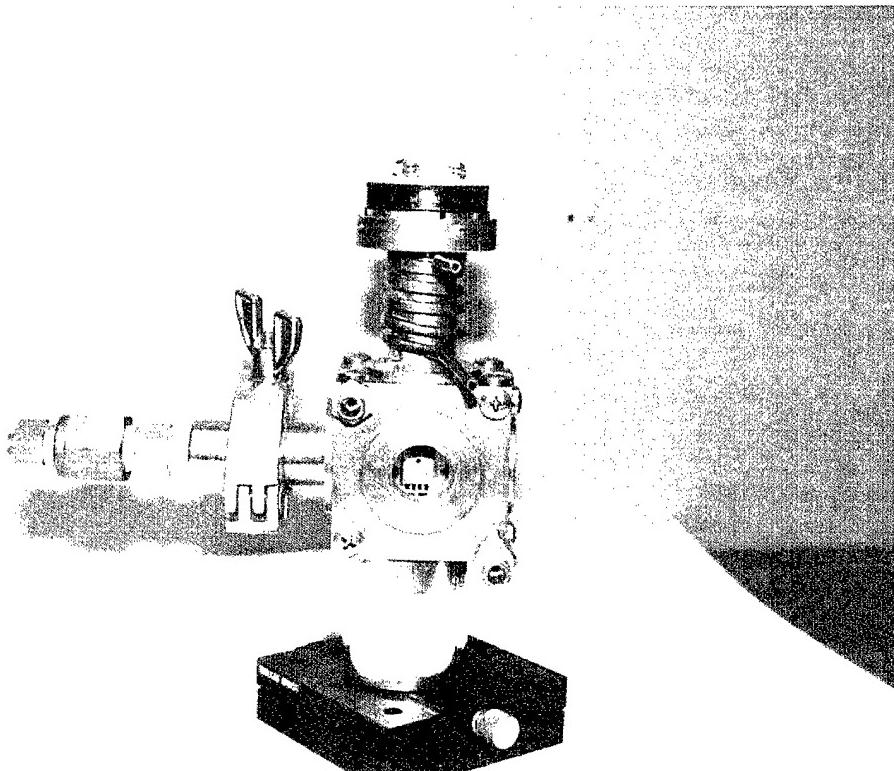

Figure 6. Photo of Vacuum Optical Furnace for High Temperature Measurements.

(g) Atomic Force Acoustic Microscope

We are now completing the installation of atomic force acoustic microscope.

In regards to items (*f*) and (*g*), we contemplate making excellent use of these two facilities in the renewal proposal.

Table I: Elastic properties of isotropic superhard films and materials studied.

Materials	ρ (kg/m^3)	V_L (km/s)	V_S (km/s)	K_V (GPa)	μ (GPa)	Poisson's ratio
BC$_2$N	3358	13.09	8.410	259	238	0.149
Amorphous carbon from C$_{60}$	3150	16.6	10.92	367	376	0.121
nc-TiN/a-Si$_3$N$_4$ (7.8 µm)	5400	8.98	5.02	254	136	0.273
nc-TiN/a-BN (7.8 µm)	5400	9.40	5.319	273	153	0.265
DLC film (495 nm)	2780	13.21	8.5	487	200	0.148
Cr-DLC film (2.9 µm)	2600	5.21	3.47	28.8	31.3	0.100
cBN film (60 nm)	3500	15.80	9.91	416	434	0.176

(6) LIST OF PUBLICATIONS

(a) Papers published in peer-reviewed journals

1. M. H. Manghnani, S. Tkachev, P. V. Zinin, X. Zhang, V. V. Brazhkin, A. G. Lyapin, and I. A. Trojan, "Elastic properties of superhard amorphous carbon pressure- synthesized from C$_{60}$ by surface Brillouin scattering," *Physical Review B*, vol. 6412, pp. 121403, 2001.
2. P. Zinin, M. H. Manghnani, X. Zhang, H. Feldermann, C. Ronning, and H. Hofsass, "Surface Brillouin scattering of cubic boron nitride films," *Journal of Applied Physics*, vol. 91, pp. 4196-4204, 2002.
3. S. N. Tkachev, V. L. Solozhenko, P. V. Zinin, M. H. Manghnani, and L. C. Ming, "The elastic moduli of the superhard cubic BC$_2$N phase by Brillouin scattering," *Physical Review B*, vol. 68, pp. 052104(3), 2003.
4. M. G. Beghi, A. G. Every, and P. V. Zinin, "Brillouin Scattering Measurement of SAW Velocities for Determining Near-Surface Elastic Properties," in *Ultrasonic Nondestructive Evaluation: Engineering and Biological Material Characterization*, T. Kundu, Ed. Boca Raton: CRC Press, 2004, pp. 581-651.
5. P. V. Zinin and W. Weise, "Theory and Applications of Acoustic Microscopy," in *Ultrasonic Nondestructive Evaluation: Engineering and Biological Material Characterization*, T. Kundu, Ed. Boca Raton: CRC Press, 2004, pp. 654-724.

(b) Papers published in non-peer-reviewed journals or in conference proceedings

6. P. V. Zinin, M. H. Manghnani, X. Zhang, A. G. Lyapin, V. V. Brazhkin, and I. A. Trojan, "Acoustic microscopy and surface Brillouin scattering of amorphous carbon pressure-synthesized from C$_{60}$," in *Nanotubes, Fullerenes, Nanostructured and Disordered Carbon*, vol. 675, J. Robertson, T. A. Friedmann, D. B. Geohegan, D. E. Luzzi, and R. S. Ruoff, Eds. NY: MRS, 2002, pp. W9.1-6.
7. P. Zinin, M. H. Manghnani, X. Zhang, H. Feldermann, C. Ronning, and H. Hofsäss, "Surface Brillouin Scattering of cBN Films," in *Smart Nondestructive Evaluation for Health Monitoring of Structural and Biological Systems*, vol. 4702, T. Kundu, Ed. Bellingham: SPIE, 2002, pp. 389-396.
8. S. Veprek, S. Mukherjeea, P. Karvankova, H.-D. Männling, J. L. He, J. Xu, J. Prochazka, A. S. Argon, A. S. Li, Q. F. Fang, S. Z. Li, S. Tkachev, M. H. Manghnani, and P. Zinin, "Possible artifacts in measurement of hardness and elastic modulus on superhard coatings and the verification of the correctness of the data," in *Surface Engineering--Synthesis, Characterization and Applications*, vol. MRS 750, A. Kumar, W. Meng, Y.-T. Cheng, J. Zabinski, G. Doll, and S. Veprek, Eds. N.Y.: MRS, 2003, pp. Y13.1-6.

9. P. Zinin, D. Fei, D. Rebinsky, M. Manghnani, S. Berezina, R. Lemor, C. Blasé, A. Caron, D. Schneider, K. Kraemer, "Acoustic microscopy, Brillouin scattering and Laser-SAW technique for defect characterization in DLC films", in W. Arnold and S. Hirsekorn eds. *Acoustical Imaging*, Kluwer Publ., New York, Vol. 27. (2004) pp. 221-228

(c) Papers presented at meetings, but not published in conference proceedings

10. S. N. Tkachev, V. L. Solozhenko, P. V. Zinin, M. H. Manghnani, and L. C. Ming, "Elastic properties of the superhard cubic BC_2N phase by Brillouin scattering," in *Bulletin of the American Society*, vol. 48(1). Melville: The American Physical Society, 2003, pp. 1120.

(d) Manuscripts submitted, but not published

11. S. Berezina, P. V. Zinin, D. Schneider, D. Fei, and D. A. Rebinsky, "Combining Brillouin spectroscopy and laser-SAW technique for elastic property characterization of thick DLC films," *Ultrasonics*, in press, 2004.
12. S. N. Tkachev, M. H. Manghnani, A. Niilisk, J. Aarik, and H. Mändar, "Raman and Brillouin scattering spectroscopy studies of atomic-layer-deposited ZrO_2 and HfO_2 thin films," *Spectrochimica Acta A*, in press, 2005.
13. P. V. Zinin, V. L. Solozhenko, A. Malkin, and L. C. Ming, "Atomic force microscopy studies of cubic BC_2N, a new superhard phase," *Journal of Materials Science Letters*, in press, 2004.
14. M. H. Manghnani, S. N. Tkachev, P. V. Zinin, S. Veprek, P. Karvankova, and C. Glorieoux, "Elastic properties of nc-TiN/a-Si_3N_4 nanocomposite films by surface Brillouin scattering," *J. Appl. Phys.*, under review, 2004.
15. S. N. Tkachev, M. H. Manghnani, A. Niilisk, J. Aarik, and H. Mandar, "Micro-Raman spectroscopy and X-ray diffraction studies of atomic-layer-deposited ZrO_2 and HfO_2 thin films," *J. Mater. Res.*, submitted 2004.
16. P. Zinin, S. Berezina, D. Schneider, D. Fei, D. A. Rebinsky, M. H. Mangnani, and S. Tkachev, "Brillouin scattering and laser-SAW technique for elastic property characterization of diamond-like carbon (DLC) films," in *Review of Progress in Quantitative Nondestructive Evaluation*, vol. 25, D. O. Thompson and D. E. Chimenti, Eds. Melville: AIP, 2004, pp. in press.
17. P. V. Zinin and M. H. Manghnani, "Elasticity Characterization of Covalent (B-C-N-Si) Hard Materials and Films by Brillouin scattering," in *Recent Advances in Materials Characterization*, G. Amarendra and M. H. Manghnani, Eds. India: University Press., 2004, pp. in preparation.
18. A. Niilisk, J. Aarik, S. N. Tkachev, M. H. Manghnani, "Structural study of ZrO_2 and HfO_2 thin films grown by atomic-layer-deposition," submitted to SPIE Proc., 2004.

(5) Technology transfer: N/A

<u>MEMORANDUM OF TRANSMITTAL</u>

U.S. Army Research Office
ATTN: AMSRL-RO-BI (TR)
P.O. Box 12211
Research Triangle Park, NC 27709-2211

☐ Reprint (Orig + 2 copies)   ☐ Technical Report (Orig + 2 copies)

☐ Manuscript (1 copy)   ☐ Final Progress Report (Orig + 2 copies)

     ☐ Related Materials, Abstracts, Theses (1 copy)
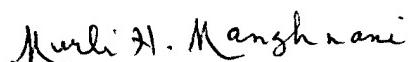
CONTRACT/GRANT NUMBER:

REPORT TITLE:

is forwarded for your information.

SUBMITTED FOR PUBLICATION TO (applicable only if report is manuscript):

Sincerely,

Murli H. Manghnani
Professor

Surface Brillouin scattering of cubic boron nitride films

P. Zinin,[a)] M. H. Manghnani, and X. Zhang
School of Ocean and Earth Science and Technology, University of Hawaii, Honolulu, Hawaii 96822

H. Feldermann, C. Ronning, and H. Hofsäss
II. Institute of Physics, University of Göttingen, D-37073 Göttingen, Germany

Surface Brillouin scattering has been used to determine the elastic properties of thin hard submicron cubic boron nitride (cBN) films grown on silicon by mass selected ion beam deposition. The elastic properties of the films have been determined by fitting experimental data to theoretical dispersion curves. A Green's function method was used to predict Brillouin scattering spectra of the acoustic excitation at the free surface. Our results demonstrate that the effect of the thin hexagonal boron nitride interlayer located between cBN film and the Si substrate on the velocity of the surface acoustic wave does not exceed 2% for a thin (16 nm) film and is negligible for cBN films thicker than 100 nm. The elastic properties of the cBN films are not softer than those of bulk cBN. © 2002 American Institute of Physics. [DOI: 10.1063/1.1456242]

I. INTRODUCTION

Cubic boron nitride (cBN) is the second hardest material next to diamond. It has attracted much research interest by its extreme physical and chemical properties, such as super high hardness, and elastic moduli, high atomic density, and chemical inertness.[1] The cBN films have several advantages over diamond films and many technological potential properties characteristic for hard coating,[2] however despite recent progress, significant barriers still exist to commercial production of cBN films. The thickness of these films commonly ranges from a few tens of nanometers up to the order of 1 μm, and therefore it is challenging to characterize the elastic properties of such thin films. Elastic properties of the cBN films need to be determined experimentally because they depend strongly on the synthesis conditions, and these properties cannot be derived from theoretical considerations alone. The nanoindentation technique widely used for mechanical characterization of thin submicron films does not allow measurements of the hardness and elastic moduli of the submicron coating and substrate separately. Obtaining good estimates of the hardness of cBN has been challenging[2] mainly because of the small thickness of available cBN films. Conventional methods usually employ surface acoustic waves (SAWs). The surface wave displacements are concentrated within a wavelength from the surface and can thus probe the samples within a depth inversely proportional to the frequency used. For submicron films, frequencies in the range 1–50 GHz are needed. The surface Brillouin scattering (SBS) technique offers the unique opportunity to cover this range of frequencies.[3]

While SBS has been used in the past for measuring the properties of thin films, its application specifically to hard films has been very limited.[4] This has resulted from the fact that for the hard films, SAW dispersion is determined mainly

by highly attenuated pseudosurface acoustic waves (PSAWs), and the theory of PSAW propagation in hard layers had not been developed until recently. Recent theoretical and experimental studies conducted have demonstrated that the thin hard films can be characterized by SBS.[5–8] First SBS studies of cBN films have revealed that experimental SAW values for cBN films are ubiquitously lower than theoretical values.[9] This large reduction in the elastic constants was surprising. SBS studies conducted by Pastorelli *et al.*[10] on thick (700 nm) cBN films also revealed 25% reduction in SAW velocity. Recently, the SAW dispersion curve for cBN films was measured by SBS;[11] however, no quantitative data on the elastic properties of the cBN films have been provided, as the SAW dispersion curve was not modeled. It is necessary to point out that the elastic constants determined in these studies[10,11] were derived from experiments made on thick films, in which the wavelength of the Rayleigh wave (RW) in cBN was shorter than the thickness of the film.

The purpose of this article is to characterize the elastic properties of thin cBN films (thinner than RW wavelength), and to evaluate the effect of the soft hexagonal BW (hBN) interlayer, which is common in these films, on SAW dispersion behavior. We will demonstrate that the "softening effect" characteristic of many thin films cannot be explained even if the thin hBN interlayer is taken into account. The influence of the hBN layer on the SAW velocity does not exceed 2% for very thin cBN films. Two thin cBN films were chosen for this study and their thicknesses were carefully measured (16 and 60 nm) (see Fig. 1).

II. EXPERIMENTAL TECHNIQUE

A detailed description of the Brillouin scattering experimental setup has been published elsewhere.[12,13] In brief, light from an argon ion laser ($\lambda = 514.5$ nm and beam power of 60 mW) was focused onto the film with a $f/5.6$ lens ($f = 50$ mm). The scattered light was collected with the same lens in the backscattering geometry and analyzed using a
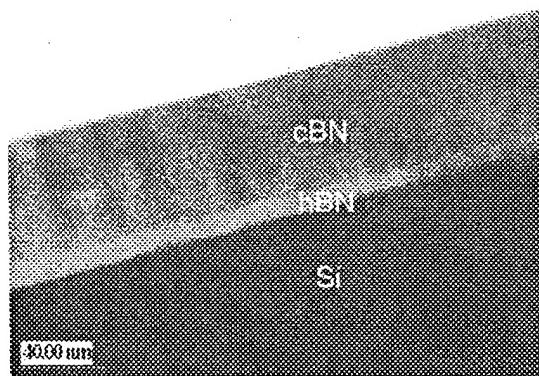
FIG. 1. TEM picture of sample B and geometry of the SBS measurements.

FIG. 2. Geometry of the SBS measurements.

high contrast and high resolution Brillouin spectrometer, which incorporated a tandem six-pass Fabry–Perot interferometer.[3] The light was detected by a single photon counting module and its output was stored in a multichannel scaler card for further analysis. Each spectrum was accumulated for 1–2 h. The frequencies corresponding to each of the peaks were determined by a curve-fitting routine. For the 180° backscattering geometry, the surface acoustic modes, which cause the diffraction of the incident light, have a wave vector (Fig. 2) given by

$$k_{\parallel} = \frac{4\pi \sin\theta}{\lambda}, \tag{1}$$

where λ is the wavelength of the incident laser light, $k_{\parallel}$ is the projection on the surface of the scattering wave vector, and θ is the scattering angle. The Doppler frequency shift f in the light scattering is related to the surface wave velocity ν_{SAW} by

$$\nu_{saw} = \frac{\lambda}{2\sin\theta} f. \tag{2}$$

III. cBN FILMS

Two cBN thin films were prepared via mass selected ion beam deposition. Details of the deposition process can be found elsewhere.[14] Briefly, B^+ and N^+ ions are produced in a plasma ion source. After acceleration to 30 keV and magnetic mass separation, the isotopically pure $^{14}N^+$ or $^{11}B^+$ ion beam is guided into the deposition chamber, where the ions are decelerated down to an energy of 600 eV and deposited onto Si (100) substrates at a temperature of 350 °C. These
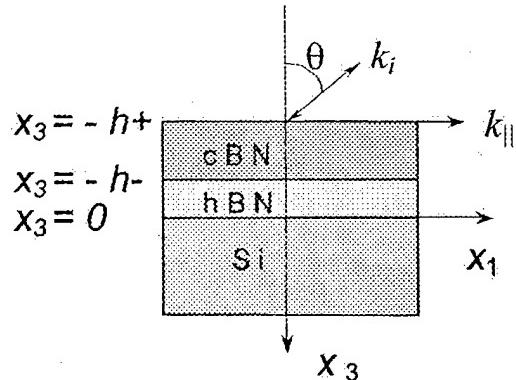
deposition parameters are well within the cBN nucleation regime.[14] The pressure during deposition was below 3×10^{-7} Pa, and prior to deposition the substrates were sputter cleaned by 1 keV Ar^+ ions. The amount of deposited ions is accurately measured by the ion charge, which is used to switch the separation magnet periodically to select $^{11}B^+$ or $^{14}N^+$. During each cycle, 10^{15} ions with an ion ratio of $B^+/N^+ = 1$ were deposited to ensure the growth of homogeneous and stoichiometric films.

In situ Auger electron spectroscopy measurements indicate contamination-free and stoichiometric BN films. The formation of the cubic phase was verified with *in situ* electron energy loss spectroscopy as well as with *ex situ* Fourier transform infrared spectroscopy. The thickness as well as the typical nucleation sequence of the two films was investigated by transmission electron microscopy (TEM). As shown in the TEM image of sample B displayed in Fig. 1, the deposited films exhibit a layered structure consisting of a very thin disordered Si–B–N interface, followed by a layer of textured hBN, then by cBN. The obtained data are summarized in Table I. The mass density of the films was derived from Rutherford backscattering (RBS) measurements using the film thickness as the input parameter. The RBS spectra were analyzed by means of the computer code NDF,[15] which takes not only the shift of the Si edge into account but also the B and N signals for the calculation of the area density and composition of the films.

TABLE I. Parameters of the cBN films.

	Deposition conditions			TEM results				
Sample	E (eV)	T (°C)	charge (C)	hBN (nm)	cBN (nm)	Total (nm)	RBS 10^{15} (atoms/cm³)	Density Film average (g/cm³)
A	600	350	0.176	15(1)	16(1)	31(2)	333(20)	2.2(3)
B	600	345	0.487	10(1)	60(6)	70(7)	1204(50)	3.5 (+0,−0.4)

FIG. 3. Two-dimensional image of the Brillouin spectra of cBN film (400 nm) on Si(001) calculated for direction [100], using experimentally obtained elastic moduli for cBN (Ref. 20). V_T is the transverse-wave threshold; and V_{FT} is the fast transverse threshold.
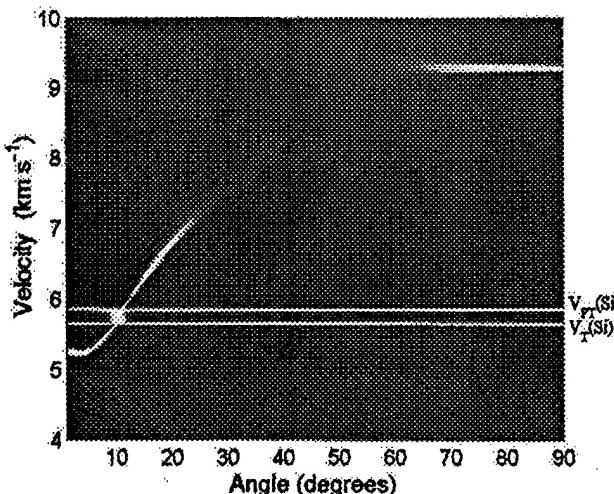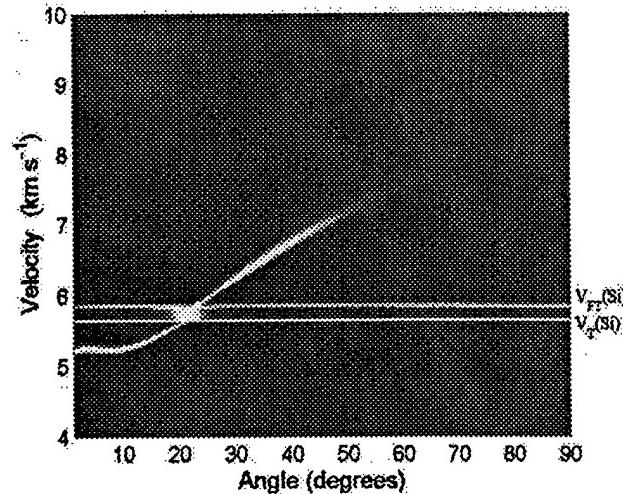

FIG. 4. Two-dimensional image of the Brillouin spectra of cBN film (200 nm) on Si(001) calculated for direction [100], using experimentally obtained elastic moduli for cBN (Ref. 20). Notations are the same as in Fig. 3.

IV. THEORY

At room temperature and above, the Brillouin scattering efficiency or intensity for scattering from the surface of opaque materials by dynamic rippling of the surface can be represented as[16–18]

$$I(\omega) \propto \frac{A}{\omega} \text{Im}[g_{33}(\mathbf{k}_\parallel, x_3 = -h_+, \omega)], \tag{3}$$

where A is a constant and depends on the density and dielectric constants of the medium, scattering geometry, and incident photon frequency and polarization, and ω is the angular frequency. The g_{33} is the Fourier coefficient of the elastodynamic Green's function[17]

$$g_{33}(\mathbf{k}_\parallel, x_3 = -h_2, \omega) = \int_{-\infty}^{\infty} \int_{-\infty}^{\infty} d^2 \mathbf{x}_\parallel G_{33}(\mathbf{x}_\parallel, \omega)$$

$$\times \exp(-i\mathbf{k}_\parallel \mathbf{x}_\parallel) \mathbf{x}_\parallel \tag{4}$$

pertaining to a force and response normal to the surface. Derivation of the elastodynamic Green's function g_{33} for a two layered system is presented in the Appendix. Briefly, the cBN/hBN layered system on Si is considered to be an anisotropic elastic continuum (Si) of density ρ and elastic modulus tensor C_{ij} occupying the halfspace $x_3 > 0$ and two layers: hBN and cBN (see Fig. 2). The hBN interlayer occupies the region $-h^- < x_3 < 0$ (Fig. 2), and the cBN layer occupies the region $-h^+ < x_3 < -h^-$. For the upper layer, we denote the elastic tensor as C_{ij}^+, and density as ρ^+ and for the interlayer as C_{ij}^- and density as ρ^-. A detailed description of how g_{33} is calculated for a one-layer anisotropic medium is given in Refs. 18 and 19.

V. RESULTS AND DISCUSSION

The two images in Figs. 3 and 4 show the variation of the Brillouin spectra with θ for two cBN films of different thicknesses (200 and 400 nm). They were calculated by the Green's function method mentioned above. The brightness in

the gray scale is a measure of the scattering intensity which is related to the displacement amplitude of these modes at the surface or at the interface. Thus, the intensity is indicative of the mode displacement patterns in the layer. The elastic constants of the cBN film were taken from ultrasonic study of bulk polycrystalline cBN.[20] Brillouin spectra calculated for 400 nm cBN film on Si (001) with scattering taking place at the surface is shown in Fig. 3. For $\theta = 0$ [$k_\parallel h_1 = k_\parallel h_2 = 0$, see Eq. (1)], the velocity corresponds to the SAW velocity on the Si substrate. Basic features of the SBS spectra of Si have been described elsewhere.[18] The calculated Brillouin spectrum for Si (Fig. 5) displays a sharp peak, which is associated with the Rayleigh SAW, and a continuum extending from the transverse-wave threshold V_T (5.648 km/s) to higher frequencies, which is known as the Lamb shoulder.[18] There are also two minima at the Lamb shoulder.[18] One is at the fast transverse (FT) threshold V_{FT} (5.844 km/s), and another is near the longitudinal threshold (8.344 km/s).
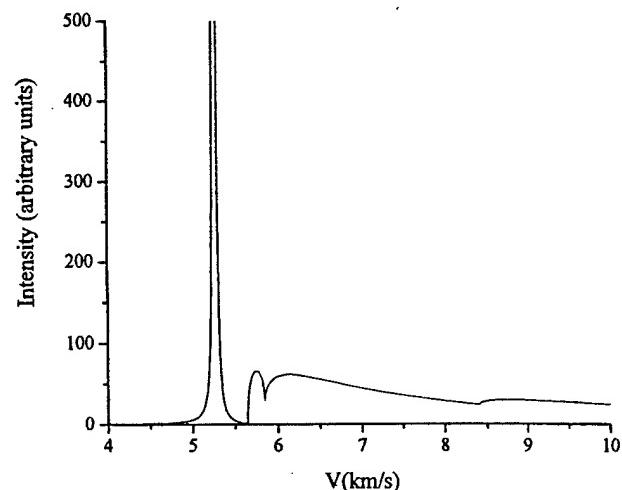

FIG. 5. Brillouin spectrum of Si(001) calculated for [100] direction at angle $\theta = 0°$.
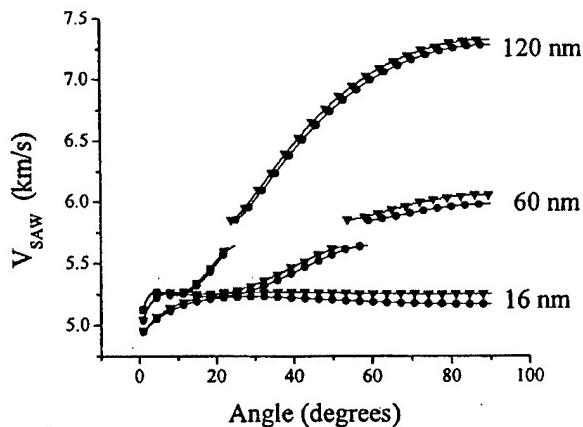
FIG. 6. Theoretical SAW dispersion curves for cBN film on Si(001) calculated for [100] direction for three different thicknesses, with 10 nm hBN interlayer (lower curves, circles) and without hBN interlayer (upper curves, triangles).

FIG. 8. Theoretical SAW dispersion curve for cBN film (60 nm$c$BN/10 nm$h$BN) on Si(001) calculated for the [100] direction, and compared with experimental data (triangles).

Referring to Fig. 3, with increasing θ, the SAW velocity approaches the bulk wave threshold V_T (transverse-wave threshold), which is reached at $\theta \approx 10°$. Below V_T the Brillouin spectrum displays a sharp peak, which is associated with the true surface waves. At V_T, the SAW degenerates with the bulk continuum; beyond cutoff there is no true SAW. Somewhat above V_{FT}, the Brillouin spectrum displays a broad peak that gradually disappears. This peak is associated with leaky or PSAW.[5] As θ or kh increases, the PSAW is transferred into the leaky interface wave.[5,13] In the same spectral region, another broad peak appears, which with increasing θ becomes narrower as the associated mode tends toward the Rayleigh mode of cBN. For very large θ this becomes the true nondispersive Rayleigh wave. It is obvious from Fig. 3 that for the 400 nm cBN films it is difficult to measure the SAW, since in the range of $20 < \theta$ 70°, the spectrum contains only highly attenuated PSAW. Dispersion curves for the films thicker than 400 nm, measured by SBS, should contain only Rayleigh SAW in cBN films. Brillouin spectra calculated for 200 nm cBN film on Si (001) are shown in Fig. 4. For 200 nm cBN film the part of the dispersion curve containing only PSAW can be detected by SBS (20°–70°). The Rayleigh surface wave propagating only in-

side the cBN layer (upper brunch in Fig. 3) is not visible by SBS. A brunch of true SAW (nonattenuating SAW) running below shear cutoff can be measured by SBS only in films thinner than 200 nm.

The SAW velocities reported in Ref. 11 for 123 and 277 nm cBN films appeared to be lower than expected in cBN films having elastic moduli of bulk cBN. The softening of the SAW was attributed by these authors to the presence of a soft hBN interlayer. Since SAW propagation in the system cBN/hBN/Si has not yet been modeled theoretically, it is of interest to consider the effect of the hBN interlayer on the behavior of the SAW dispersion curve. Results of the simulations are presented in Fig. 6. It can be seen that the influence on the dispersion curve of the hBN interlayer is not significant. For 16 and 60 nm cBN layers, the hBN interlayer decreases the SAW velocity by only 2%, which is just above the accuracy of the SBS measurements. As the thickness of the cBN layer increases, the influence of the 10 nm hBN interlayer becomes negligible. For 120 nm cBN film, it is smaller than the SBS accuracy measurements (1%).[4]

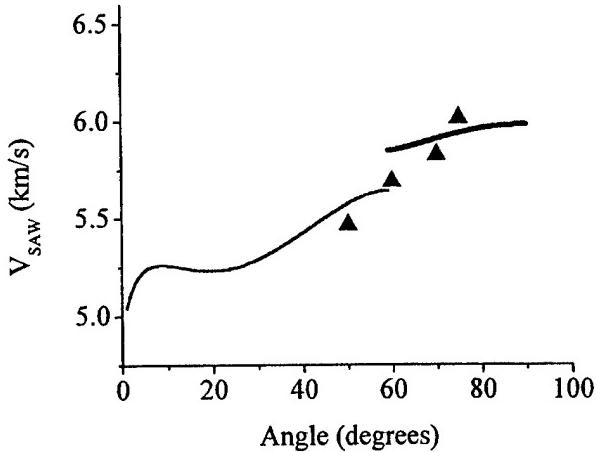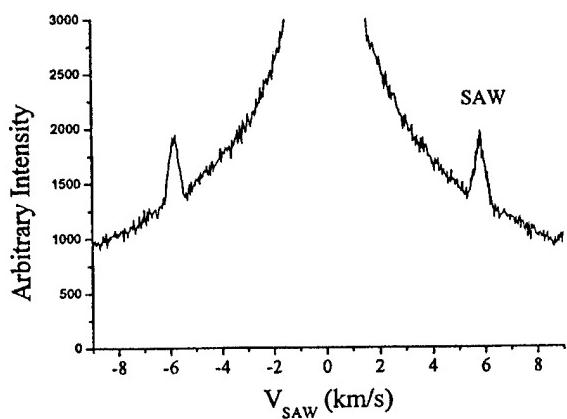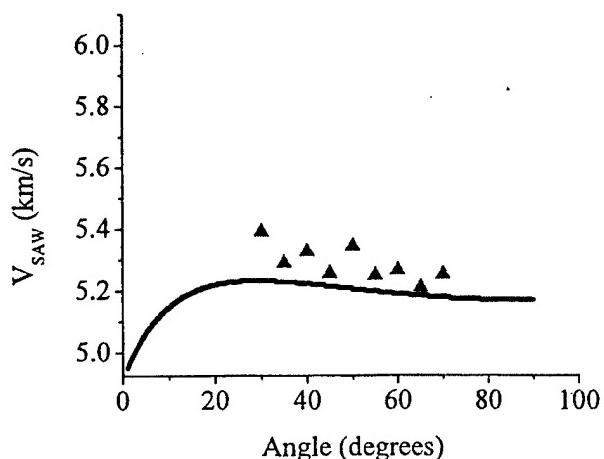FIG. 7. Experimental Brillouin spectrum of cBN/Si film for the angle of 70°.

FIG. 9. Theoretical SAW dispersion curve for cBN film (16 nm cBN/15 nm hBN) on Si(001) calculated for [100] direction, and compared with experimental data (triangles).

TABLE II. Velocities and moduli of cBN, hBN, and Si.

Materials	Density (kg/m³)	C_{11} (GPa)	C_{12}	C_{44}	C_{13}	C_{33}
hBN hexagonal[a]	2230[b]	750	150	1.54	12.5	17.7
hBN hexagonal[c]	2140	65	⋯	53	7	92
hBN hexagonal[d]	2270	44±2	⋯	35±4	50	293±29
hBN hexagonal[e]	2270	38±2	⋯	55±6	8	392±39
cBN polycrystalline[f]	3500	875.73	⋯	377.69	⋯	⋯
cBN polycrystalline[g]	3300	941	⋯	401	⋯	⋯
cBN isotropic[h]	3300	(525)	⋯	226	⋯	⋯
cBN isotropic[i]	⋯	594	⋯	266	⋯	⋯
cBN cubic[j]	3480	820	190	480	⋯	⋯
60 nm cBN/10 nm hBN	3500	875	⋯	344	⋯	⋯
16 nm cBN/15 nm hBN	3500	875	⋯	434	⋯	⋯
Si cubic[k]	2339	165.7	63.9	79.6	⋯	⋯

[a]Reference 25.
[b]Reference 26.
[c]Film 21.
[d]rf sputtered film 11.
[e]dc sputtered film 11.
[f]Reference 20.
[g]Voigt-Reuss-Hill Average (Reference 11).
[h]Film (Reference 11).
[i]Film (Reference 10).
[j]Reference 27.
[k]Reference 28.

An experimental SBS spectrum taken for the 60 nm thick film is shown in Fig. 7. Peaks associated with the SAW are quite strong. Results of measurements for the 60 nm thick film are depicted by normal triangles and for the 16 nm film by inverted triangles in Figs. 8 and 9 as a function of the angle. Theoretical Brillouin spectra have been calculated on the basis of the ripple mechanism for scattering at the surface [Eq. (3)]. The dispersion curves in Figs. 8 and 9 represent the traces of the maxima of the calculated Brillouin intensity for the surface of the measured Brillouin intensity. The assumed elastic properties of the hBN layer were based on the reported SBS determined values[21] (see Table II). As can be seen from Table II, experimentally obtained elastic moduli of the hBN films vary considerably even if they have been obtained by the same method (SBS) and in the same research group.[11,12] However, for our simulation it is of importance that the set of the elastic constants chosen does describe the behavior of the SAW dispersion curve of hBN film. Moreover, for transversely isotropic films the shape of the SAW dispersion curve is determined mostly by C_{44},[22] which does not vary for the measured hBN film in Table II.

The theoretical dispersion curve and experimental data obtained for 60 nm cBN layer sample are shown in Fig. 8. For this case only the lower part of the experimental points can be attributed to true SAW. The upper points belong to PSAW. The theoretical dispersion curve, based on the elastic constants reported in Ref. 20, is in good agreement with experimental data. To find the best fit of the experimental data, both C_{11} and C_{44} are varied, assuming that the density of cBN film is 3.5 g/cm³. The error sum of squares (ESS) over all number of experiments n_{exp}[23,24]

$$ESS = \sum_{i=1}^{n_{exp}} (\nu_{calc}^i - \nu_{meas}^i)^2 \qquad (5)$$

is minimized with respect to the variation of the elastic constants of the layered solid. In Eq. (4) ν_{meas}^i are measured values of the SAW velocity and ν_{calc}^i are the corresponding theoretical values. Behavior of the minimum of ESS as a function of C_{11} is presented in Fig. 10(a) for 60 nm cBN film. The minimum of ESS decays rapidly as C_{11} increases to 730 GPa; for $C_{11} > 730$ GPa, ESS is practically independent of C_{11}. The sharp rise of the ESS below 730 GPa indicates the lower boundary of the C_{11} of the cBN film. The position of the ESS minima as a function of moduli C_{11} and C_{44} is presented in Fig. 10(b). Figure 10(b) provides us with the possible range of C_{44}. As C_{11} varies from 700 to 1100 GPa, C_{44} varies from 300 to 420 GPa. Since ESS is practically independent of C_{11}, we assume the value C_{11} equal to those measured experimentally for polycrystalline cBN:[20] $C_{11} = 875$ GPa. With fixed $C_{11} = 875$ GPa, ESS reaches its minimum at $C_{44} = 344$ GPa, which is only 9% lower than $C_{44} = 378$ GPa measured by an ultrasonic experiment.[20] With confidence of 0.9, the range of C_{44} variation is from 310 to 372 GPa. Therefore, the upper boundary of the interval is in agreement with the value obtained in ultrasonic experiments, and the lower limit of the interval is only 18% lower than the experimental value. Obviously, the values of the C_{44} of films deposited by the ion deposition technique are higher that those measured in the films deposited by rf sputtering at low temperature (around 350 K), $C_{44} = 266$ GPa, and in the cBN film deposited in a hollow cathode arc evaporation device,[11] $C_{44} = 226$ GPa.

Deriving elastic constants from experimental data for 16 nm cBN film is more difficult because velocity of the SAW is practically independent of the angle (see Fig. 9). In the case of 16 nm cBN film, the SAW branch can be attributed to the true surface waves for all angles of incidence, and their
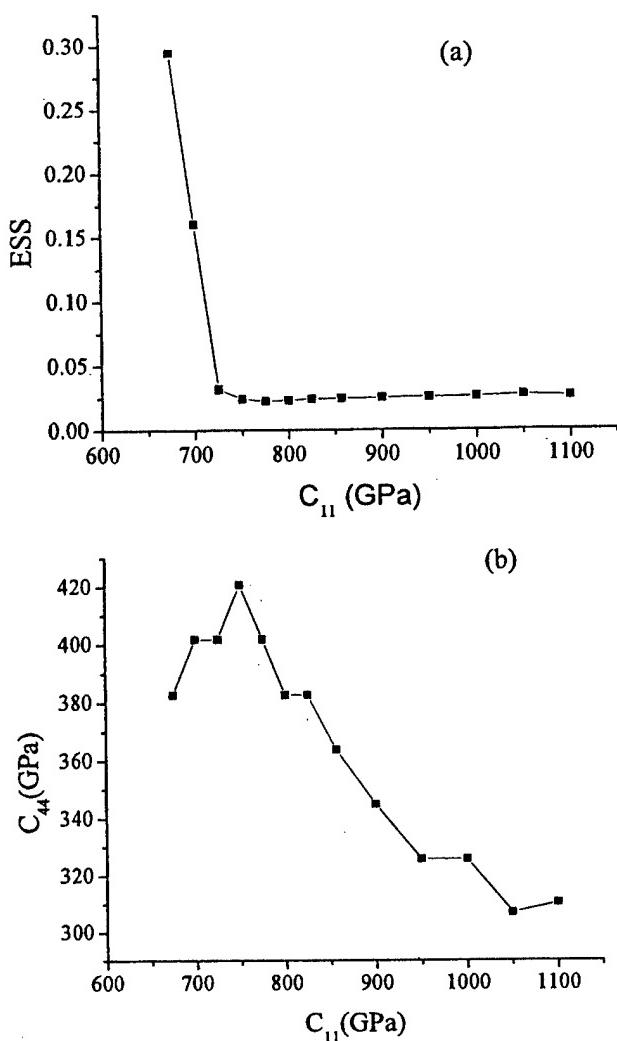
FIG. 10. Fitting of the experimental data for (60 nm cBN/10 nm hBN) film: (a) ESS as a function of C_{44}; (b) behavior of the ESS minima as a function of C_{11} and C_{44}.

FIG. 11. Fitting of the experimental data for (16 nm cBN/15 nm hBN) film: (a) ESS as a function of C_{44}; (b) behavior of the ESS minima as a function of C_{11} and C_{44}.

velocities are below shear cutoff (see also Fig. 3). Behavior of the minima of ESS as a function of C_{11} and behavior of the ESS minima as a function of moduli C_{11} and C_{44} are presented in Fig. 11 for 16 nm cBN film. It is interesting to note that when C_{44} varies from 400 to 620 GPa, C_{11} increases from 700 to 1300 GPa [Fig. 11(b)]. As in the case of 60 nm cBN film, we assume that C_{11} of 16 nm cBN film equals 875 GPa. For a chosen value of C_{11}, the best fit of the experimental data gives 443 GPa for C_{44}, which is higher than the C_{44} of polycrystalline cBN, 378 or 401 GPa (see Table II). However, because of the weak dependence of the SAW dispersion curve on the angle of the light incidence, we could not regard the 16 nm film as stronger than polycrystalline bulk cBN. With confidence of 0.9, the variation of the C_{44} is rather large: from 272 to 591 GPa, which is still higher than that obtained in Refs. 10 and 11. Even though the difference in elastic constants obtained from ion deposition and other deposition techniques[10,11] is not high, the difference between experimental results and theoretical prediction is really evident. Experimental points in Fig. 12 are taken from Ref. 11, and the dispersion curve was calculated with elastic
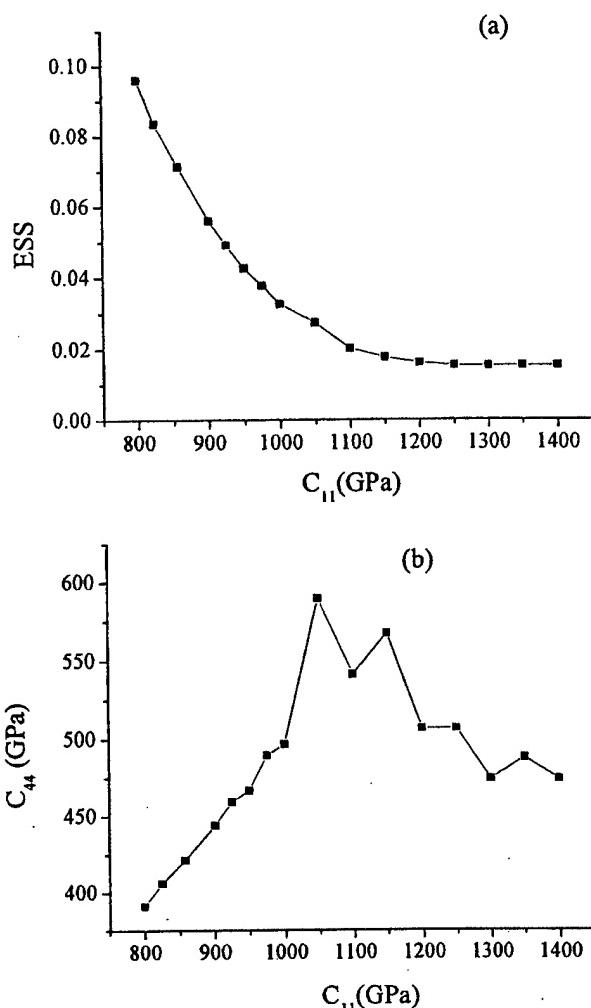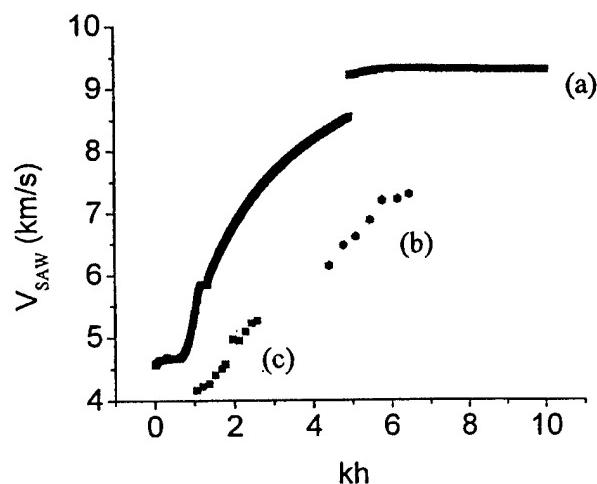

FIG. 12. Theoretical SAW dispersion of 500 nm cBN film on Si(111) calculated for direction [1$\bar{1}$1] (a); and experimental data (Ref. 11) for 277 nm cBN film (b); and 123 nm cBN film (c).

constants taken from Ref. 20. Since for cBN films the effect of the hBN interlayer is small, the hBN layer was not taken into account in the simulation presented in Fig. 12. As it can be seen, experimental data and theoretical curve do not show good agreement, and are a contrast with the present results (see Figs. 8 and 9).

One can conclude that the cBN films deposited by the ion deposition method are not softer than the polycrystalline bulk cBN. This conclusion contradicts the results obtained in Refs. 10 and 11 and can be attributed to the different deposition methods.

VI. CONCLUSIONS

A dispersion curve of SAWs on cBN film on Si (100) has been obtained by SBS.

Incorporating the hBN interlayer into the model of the SBS response and precise thickness measurement of the cBN layer and hBN interlayer fully describes the behavior of the SAW dispersion in deposited cBN layered systems.

The elastic properties of the cBN films are not softer than those of bulk cBN.

The SBS technique is of potential value in interpreting the elasticity of hBN/cBN layered films.

ACKNOWLEDGMENTS

APPENDIX

To derive the elastodynamic Green's function g_{33} Eq. (A6) for two-layers system we will follow approach described for the one layer system.[29,30] For a concentrated point force acting at the top surface $(F_j(x') = F_j \delta(x_1') \delta(x_2') \delta(x_3' = -h^+)$, $\delta(x)$ is the delta function) we have[19,31,32]

$$u_i(x_\parallel, x_3 = -h^+, \omega) = G_{ij}(x_\parallel, x_3 = -h^+, \omega) F_j, \quad (A1)$$

where G_{ij} is the is called the surface Green's function. The Fourier coefficient of the surface Green's function g_{33} is defined as a double Fourier integral[29,30] of the surface Green's function G_{33} in the variables x_1 and x_2

$$g_{33}(k_\parallel, x_3 = -h^+, \omega) = \int_\infty^{-\infty} d^3 x_\parallel G_{ij}(x_\parallel, x_3 = -h_3^+, \omega)$$

$$\times \exp(-i k_\parallel x_\parallel),$$

$$G_{ij}(x_\parallel, x_3 = -h^+, \omega)$$

$$= \frac{1}{(2\pi)^2} \int_\infty^{-\infty} d^3 k_\parallel, x_{33}(k_\parallel, x_3 = -h^+, \omega) \exp(i k_\parallel x_\parallel),$$

$$(A2)$$

here $x_\parallel = (x_1, x_2)$ and $k_\parallel = (k_1, k_2)$. For calculation of the Brillouin spectrum we need only the normal to the surface component of the external force $F = (0, 0, F)$. Following

Every,[29] let us consider the response of the system to external harmonic force applied at the layer's upper surface

$$\sigma_{33}(x_\parallel, x_3 = -h^+, \omega) = -F\delta(x_\parallel), \quad (A3)$$

where $\delta(x_\parallel)$ is the two dimensional delta function. Taking into account the definition of the delta function, we can rewrite Eq. (A3) as an inverse Fourier transform

$$\sigma_{33}^+(x_\parallel, x_3 = -h^+, \omega) = -\frac{F}{(2\pi)^2} \int_\infty^{-\infty} d^2 k_\parallel$$

$$\times \exp(i k_\parallel x_\parallel). \quad (A4)$$

Equation (A4) provides one of boundary conditions. For the force acting tangent on the surface, two other boundary conditions have the form

$$\sigma_{13}^+(x_\parallel, x_3 = -h^+, \omega) = 0, l = 1, 2. \quad (A5)$$

To find the response of the system to the force F we seek the solution of the equations of motion in the form of a superposition of outgoing plane waves whose amplitudes are proportional to F. In the top layer $(+)$ the solution is given by

$$u_i^+(x, \omega) = \frac{F}{(2\pi)^2} \int_\infty^{-\infty} d^2 k_\parallel \sum_{n=1}^{6} A^{(n)} U_i^n$$

$$\times \exp(i k_\parallel x_\parallel + k_3^{(n)} x_3), \quad (A6)$$

in the interlayer solution has the form

$$u_i^-(x, \omega) = \frac{F}{(2\pi)^2} \int_\infty^{-\infty} d^2 k_\parallel \sum_{n=7}^{12} A^{(n)} U_i^n$$

$$\times \exp(i k_\parallel x_\parallel + k_3^{(n)} x_3), \quad (A7)$$

and, finally, in the substrate

$$u_i(x, \omega) = \frac{F}{(2\pi)^2} \int_\infty^{-\infty} d^2 k_\parallel \sum_{n=13}^{15} A^{(n)} U_i^n$$

$$\times \exp(i k_\parallel x_\parallel + k_3^{(n)} x_3). \quad (A8)$$

For each value of $k_\parallel$ and ω, coefficients $A^{(n)}$ in Eqs. (A6)–(A8) are the 15 unknown constants for plane wave decomposition. The third component k_3 of k and the polarization vector U_i are related by the Christoffel equations

$$(C_{ijkl} k_j k_l - \rho\omega^2 \delta_{ik}) u_k = 0, \quad (A9)$$

where $k_3^{(n)}$ are roots of the characteristic sextic equation, and δ_{ik} is the Kronecker delta symbol

$$\Omega(k, \omega) = |C_{ijkl} k_j k_l - \rho\omega^2 \delta_{ik}| = 0. \quad (A10)$$

Generally Eq. (A10) yields six solutions. In the layer all six partial waves must be taken into account. For a substrate only these solutions that correspond to outgoing waves are chosen. Those waves should be chosen that are either homogeneous (bulk) waves ($k_3^{(n)}$ real) with ray or group velocity vectors $V = \nabla_k \omega(k)$, directed into the interior ($x_3 > 0$), or inhomogeneous (evanescent) waves ($k_3^{(n)}$ complex or pure imaginary) which decay into the interior ($\text{Im}(k_3^{(n)}) > 0$). The calculation of the roots of Eq. (A10) can be simplified by first rotating the crystal to the coordinate frame, where the surface of the sample defines the $x_1 x_2$ plane, and the propa-

gation direction is always along x_1. Then, the determinant Eq. (A10) describes a sixth order polynomial in k_3, with ω and k_3 as parameters. For monoclinic symmetry, the implicit form of the coefficients in Eq. (A10) is given by Nayfeh.[33] For triclinic symmetry, the implicit form of the polynomial equation (A10) can be found elsewhere.[34]

From the stress–strain relationship, $\sigma_{ij} = C_{ijpq} \partial u_p / \partial x_q$, and Eq. (A6) it follows that the surface tensions are given by

$$\sigma_{13}^+(\mathbf{x}_\parallel, x_3 = -h^+, \omega)$$

$$= \frac{i\omega F}{(2\pi)^2} \int_\infty^{-\infty} d^2\mathbf{k}_\parallel \sum_{n=1}^6 A^{(n)} B_i^{(n)} \exp(i\mathbf{k}_\parallel \mathbf{x}_\parallel), \qquad (A11)$$

where matrix $B_l^{(n)}$ has been introduced as in[29]

$$B_l^{(n)} = C_{13pq}^+ U_p^{(n)} k_q^{(n)} \exp(-ik_3^{(n)} h^+)/\omega,$$

$$n = 1,2,3,4,5,6, \quad l = 1,2,3. \qquad (A12)$$

Now boundary conditions (A3) and (A5) can be written as a set of three linear equations for the partial wave amplitudes $A^{(n)}$

$$\sum_{n=1}^6 B_l^{(n)} A^{(n)} = i\frac{\delta_{3l}}{\omega}, \quad l = 1,2,3. \qquad (A13)$$

Index l in Eq. (A13) denotes the number of the equation in the linear system of 15 equations. Another three equations for the amplitude arise from the continuity of stress at the interface between upper layer and interlayer

$$\sigma_{j3}^+(\mathbf{x}_\parallel, x_3 = -h^-, \omega) - \sigma_{j3}^-(\mathbf{x}_\parallel, x_3 = -h^-, \omega) = 0, \quad (A14)$$

where σ_{j3}^+ and σ_{j3}^- denote tensions calculated in the upper layer and the interlayer, respectively. Stress must be continuous at the interface between interlayer and substrate

$$\sigma_{j3}^-(\mathbf{x}_\parallel, x_3 = 0, \omega) - \sigma_{j3}(\mathbf{x}_\parallel, x_3 = 0, \omega) = 0. \qquad (A15)$$

Finally there are three equations for the partial wave amplitudes arising from continuity of the displacement field at the interfaces. At the upper layer/interlayer interface

$$u_j^+(\mathbf{x}_\parallel, x_3 = -h^-, \omega) - u_j^-(\mathbf{x}_\parallel, x_3 = -h^-, \omega) = 0. \quad (A16)$$

The continuity of the displacement field at the interlayer/substrate interfaces gives the last three equations

$$u_j^-(\mathbf{x}_\parallel, x_3 = 0, \omega) - u_j(\mathbf{x}_\parallel, x_3 = 0, \omega) = 0. \qquad (A17)$$

Combining Eqs. (A13)–(A17) we come to the system of 15 linear equation with 15 unknown $A^{(n)}$ and a left side vector Y

$$B*A = \frac{i}{\omega} Y, \qquad (A18)$$

where $Y_1 = 0$, if $l \neq 3$, and $Y_l = 1$, $l = 3$. The solution of Eq. (A18) takes the form

$$A^{(n)} = \frac{i}{\omega}(B^{-1})^{(n)} = \frac{i}{\omega} \frac{\mathrm{adj}(B)^{(n)}}{\det|B|}, \qquad (A19)$$

adj denoting matrix adjoint. From Eqs. (A1), (A2), and (A19) it follows

$$G_{33}(\mathbf{x}_\parallel, x_3 = -h^+, \omega)$$

$$= \frac{F}{(2\pi)^2} \int_\infty^{-\infty} d^2\mathbf{k}_\parallel \left\{ \sum_{n=1}^6 \frac{i}{\omega}(B^{-1})^{(n)} U_3^{(n)} \right.$$

$$\left. \times \exp(-ik_3^{(n)} h^+) \right\} \exp(i\mathbf{k}_\parallel \mathbf{x}_\parallel). \qquad (A20)$$

Comparing Eq. (A20) with Eq. (A2) we finally, obtain the surface Green's function

$$g_{33}(\mathbf{k}_\parallel, x_3 = -h^+, \omega) = \frac{i}{\omega} \sum_{n=1}^6 (B^{-1})^{(n)} U_3^{(n)}$$

$$\times \exp(-ik_3^{(n)} h^+). \qquad (A21)$$

[1] W. Kulisch, *Deposition of Diamond-Like Superhard Materials* (Springer, Berlin, 1999).

[2] P. B. Mirkarimi, K. F. McCarty, and D. L. Medlin, Mater. Sci. Eng., R. **21**, 47 (1997).

[3] J. R. Sandercock, in *Light Scattering in Solids III. Recent Results*. edited by G. Guntherodt (Springer, Berlin, 1982), Vol. 51, pp. 173–206.

[4] P. Mutti, C. E. Bottani, G. Ghislotti, M. Beghi, G. A. D. Briggs, and J. R. Sandercock, in *Advanced in Acoustic Microscopy*, edited by A. Briggs (Plenum, New York, 1995), Vol. I, pp. 249–300.

[5] O. Lefeuvre, P. Zinin, G. A. D. Briggs, and A. Every, Appl. Phys. Lett. **72**, 856 (1998).

[6] O. Lefeuvre, P. Zinin, and G. A. D. Briggs, Ultrasonics **36**, 229 (1998).

[7] O. Lefeuvre, W. Pang, P. Zinin, J. D. Comins, A. G. Every, G. A. D. Briggs, B. D. Zeller, and G. E. Thompson, Thin Solid Films **342**, 1 (1999).

[8] W. Pang, A. G. Every, J. D. Comins, P. R. Stoddart, and X. Zhang, J. Appl. Phys. **86**, 311 (1999).

[9] M. H. Manghnani, X. Zhang, S. Tkachev, P. Zinin, H. Feldermann, C. Ronning, H. Hofsass, and A. G. Every, in *Nondestructive Characterization of Materials IX*, edited by R. E. Green (American Institute of Physics, New York, 1999), pp. 315–320.

[10] R. Pastorelli, P. M. Ossi, C. E. Bottani, R. Checchetto, and A. Miotello, Appl. Phys. Lett. **77**, 2168 (2000).

[11] T. Wittkowski, P. Cortina, J. Jorzick, K. Jung, and B. Hillebrands, Diamond Relat. Mater. **9**, 1957 (2000).

[12] V. Askarpour, M. H. Manghnani, S. Fassbender, and A. Yoneda, Phys. Chem. Miner. **19**, 511 (1993).

[13] P. Zinin, M. H. Manghnani, S. Tkachev, V. Askarpour, O. Lefeuvre, and A. Every, Phys. Rev. B **60**, 2844 (1999).

[14] H. Hofsass, H. Feldermann, M. Sebastian, and C. Ronning, Phys. Rev. B **55**, 13230 (1997).

[15] N. P. Barradas, C. Jeynes, and R. P. Webb, Appl. Phys. Lett. **71**, 291 (1997).

[16] R. Loudon, Phys. Rev. Lett. **40**, 581 (1978).

[17] A. G. Every, W. Pang, J. D. Comins, and P. R. Stoddart, Ultrasonics **36**, 223 (1998).

[18] X. Zhang, J. D. Comins, A. G. Every, P. R. Stoddart, W. Pang, and T. E. Derry, Phys. Rev. B **58**, 13677 (1998).

[19] J. D. Comins, in *Handbook of Elastic Properties of Solids, Liquids, and Gases*, edited by M. Levy, H. Bass, R. Stern, and V. Keppens (Academic, New York, 2000), Vol. I, pp. 349–378.

[20] M. H. Manghnani, in *The 5th NIRIM International Symposium on Advances Materials (ISAM' 98)* (National Institute For Research in Inorganic Materials, Chicherster, 1998), pp. 73–78.

[21] T. Wittkowski, J. Joizick, K. Jung, and B. Hillebrands, Thin Solid Films **353**, 137 (1999).

[22] P. Zinin, O. Lefeuvre, A. Briggs, B. D. Zeller, P. Cawley, A. Kinloch, X. Zhou, and G. Thompson, J. Acoust. Soc. Am. **106**, 2560 (1999).

[23] P. V. Zinin, in *Handbook of Elastic Properties of Solids, Liquids, and Gases*, edited by M. Levy, H. Bass, R. Stern, and V. Keppens (Academic, New York, 2001), Vol. I, pp. 187–226.

[24] N. R. Draper and H. Smith, *Applied Regression Analysis* (Wiley, New York, 1966).

[25] G. F. Cardinale, D. L. Medlin, P. B. Mirkarimi, K. F. McCarty, and D. G. Howitt, J. Vac. Sci. Technol. A **15**, 196 (1997).

[26] L. Duclaux, B. Nysten, J.-P. Issi, and A. W. Moore, Phys. Rev. B **46**, 3362 (1992).

[27] M. Grimsditch, E. S. Zouboulis, and A. Polian, J. Appl. Phys. **76**, 832 (1994).

[28] G. W. Farnell, in *Physical Acoustics*, edited by R. N. Thurston (Academic, New York, 1970), pp. 109–166.

[29] A. G. Every (unpublished, 1996).

[30] A. G. Every, in *Handbook of Elastic Properties of Solids, Liquids, and Gases*, edited by M. Levy, H. Bass, R. Stern, and V. Keppens (Academic, New York, 2000), Vol. I, pp. 3–36.

[31] E. H. E. Boudouti, B. Djafari-Rouhani, and A. Akjouj, Phys. Rev. B **55**, 4442 (1997).

[32] M. G. Cottam and A. A. Maradudin, in *Surface Excitations*, edited by R. Loudon (Elsevier Science, London, 1984), pp. 5–193.

[33] A. H. Nayfeh, J. Acoust. Soc. Am. **89**, 1521 (1991).

[34] Z. Sklar, *Quantitative Acoustic Microscopy of Coated Materials* (University of Oxford Press, Oxford, 1993).

Elastic moduli of the superhard cubic BC$_2$N phase by Brillouin scattering

S. N. Tkachev

School of Ocean and Earth Science and Technology, University of Hawaii, Honolulu, Hawaii 96822, USA

V. L. Solozhenko

Institute for Superhard Materials of the National Academy of Sciences of Ukraine, Kiev 04074, Ukraine

P. V. Zinin, M. H. Manghnani, and L. C. Ming*

School of Ocean and Earth Science and Technology, University of Hawaii, Honolulu, Hawaii 96822, USA

Brillouin scattering measurements on the nanocrystalline cubic phase of BC$_2$N, the hardest known solid after diamond, have been successfully performed using the "emulated" platelet scattering geometry. We were able to measure both longitudinal (V_p) and shear (V_s) velocities independent of refractive index, and thus obtained values of 13.09±0.22 and 8.41±0.14 km/s, respectively. Using these values, we calculated the bulk and the shear moduli as 259±22 and 238±8 GPa, respectively.

Following the successful synthesis of the superhard phase of cubic nanocrystalline BC$_2$N (c-BC$_2$N) both in a diamond-anvil cell and in a large-volume press,[1] it became possible to characterize its mechanical properties by microindentation and nanoindentation.[2–4] The Vickers hardness of 76 GPa measured for nanocrystalline c-BC$_2$N has been found to lie between 115 GPa (Refs. 5, 6) for the (111) face of a single-crystal diamond and 62 GPa for the (111) face of a single-crystal cubic boron nitride (c-BN).[2–4] Based on the nanohardness measurements, the value of the shear modulus of the c-BC$_2$N was predicted to be 447±18,[2] which is even higher than that of diamond. The bulk modulus derived earlier from the x-ray diffraction data was as low as 280 GPa.[1] These results appear to differ from recent theoretical simulations,[7,8] which show that the phases of the cubic BC$_2$N with high shear moduli, without exception, have very high bulk moduli. Despite several reports on the synthesis of diamondlike phases in the B-C-N system, no experimental data on the elastic properties of these new phases are available.[9–13] In this paper, we report on experimental data on the elastic moduli of nanocrystalline bulk c-BC$_2$N obtained by Brillouin spectroscopy.

The sample used in this study is the same one used for hardness and refractive index measurements, a nanocrystalline sample of c-BC$_2$N.[1,2,14] It was synthesized[1] by direct conversion of graphitelike (BN)$_{0.48}$C$_{0.52}$ solid solution at 25 GPa and 2100 K using a large-volume multianvil system and Sumitomo 1200-ton press at the Bayerisches Geolnstitut. One side of the recovered c-BC$_2$N sample (1.1 mm in diameter and 0.9 mm thick disk) was polished by a cast iron scaife and 15- to 2-μm diamond grit, and finished with 0.5-μm diamond paste. The polishing of the specimen reduced sample size to approximately 0.3 mm depth from the exposed surface to the bottom of encapsulated surface. The transmission electron microscopy (TEM) of the sample[4,15] shows that the grain size ranges from 10 to 30 nm with a narrow size distribution.

The presence of microcracks (inclined at 10°−15° to the polished plane), visible both at the surface and within the encapsulated sample, yielded some artifacts in the Brillouin spectra. To overcome such a problem, the formerly open side of the sample was attached to a reflective mirror by epoxy and the sample was thinned from ~300 down to ~90 μm by polishing the encapsulated side. At the end of this process, several areas, ranging from 50 to 100 μm in size, appeared to be especially well cleared of microcracks and, thus, were chosen to emulate the platelet scattering configuration. In this specific assemblage the laser beam reflected from the mirror serves as incident light for giving rise to a signal scattered in platelet geometry.[16–18] The frequency shift Δf thus obtained is related to the bulk sound velocity V as

$$V = \frac{\lambda \Delta f}{2 \sin \theta}, \quad (1)$$

where θ is the angle between the incident wave vector and normal to the sample surface, and λ is the wavelength of the incident light. The advantage of the "emulated" geometry enables measurements of the longitudinal (V_L) and transverse (V_T) velocities independent of refractive index n. Moreover, mounting the sample with only one side exposed has significantly reduced the risk of disintegrating the brittle specimen. Measurements done with "emulated" platelet geometry also confirmed that the elastic anisotropy, revealed in preliminary surface Brillouin scattering measurements prior to polishing, was an artifact attributed to the light scattering from inclined microcracks.

The Brillouin scattering (BS) experimental setup is an improved version of the system utilized in a recent study[19] on bulk amorphous carbon samples. It is a fully automated, self-aligning spectrometer with increased stability and flexibility,[20] and it operates on the basis of a Sandercock-type tandem six-pass Fabry-Perot interferometer.[21] The beam from an argon ion laser ($\lambda = 514.5$ nm and beam power of 70 mW) was focused on the sample with 1:1.4 ($f = 50$ mm) lens. The high-resolution spectra were typically accumulated for 1–2 h.
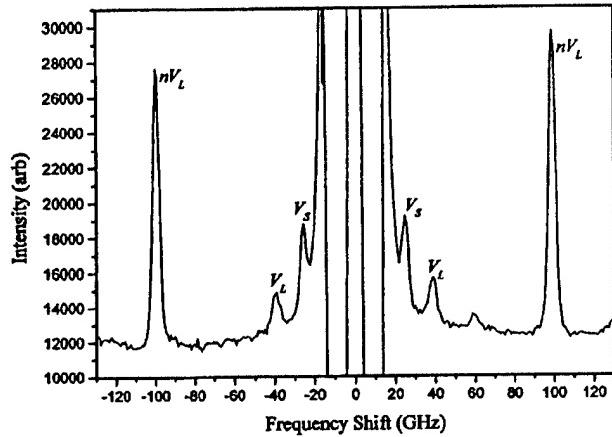
FIG. 1. Experimental BS spectrum ($\theta = 50°$) of nanocrystalline c-BC$_2$N. An asymmetric peak at ≈ 60 GHz resulted from the saturation of the system by the strong elastic scattering (Ref. 19).

FIG. 2. Experimental azimuth dependence of longitudinal (solid circles) and shear velocities (solid squares) in c-BC$_2$N. Thick lines are linear fits to present data.

A typical Brillouin spectrum of the nanocrystalline c-BC$_2$N sample (Fig. 1) shows well-defined peaks associated with both longitudinal and transverse acoustic modes. The azimuth dependencies of V_L and V_S (Fig. 2) do not indicate velocity anisotropy and therefore provide evidence that the nanocrystalline cubic BC$_2$N phase is elastically isotropic. Using average V_L and V_S values of 13.09 ± 0.22 and 8.41 ± 0.14 km/s, respectively, we calculated bulk and shear moduli, Poisson's ratio, and the Young's modulus. The results and relevant data from the literature are compiled in Table I with the standard deviations indicated as uncertainties. We find good agreement among the presently obtained bulk modulus and the corresponding value obtained from independent x-ray compressibility measurements.[1]

Experimental spectra show also a strong peak around 100 GHz (Fig. 1). This peak is attributed to interaction between laser light and longitudinal phonons in backscattering geometry.[22] In such a geometry, the longitudinal velocity is related to the frequency shift Δf, by the expression

$$V_L = \frac{\lambda \Delta f}{2n}. \qquad (2)$$

From the measured value of the frequency shift, we obtained $nV_L = 25.65 \pm 0.4$ km/s. The refractive index of c-BC$_2$N has been determined to be 2.06, using the multi-angle-of-incidence ellipsometry measurements.[14] Thus, from these measurements, the longitudinal velocity can be determined independently. The value is 12.45 ± 0.31 km/s, and it agrees reasonably well with $V_L = 13.09 \pm 0.33$ km/s obtained by "emulated" platelet geometry. We can also calculate n from measured values of nV_L. Results presented in Fig. 3 clearly show that the nanocrystalline c-BC$_2$N is optically isotropic as well, with an average value of $n = 1.96 \pm 0.03$. This is in agreement with multi-angle-of-incidence ellipsometry measurements.[14]

The cubic BC$_2$N phase has an unusual combination of mechanical properties: its elastic moduli measured by Brillouin scattering and x-ray diffraction are lower than those of c-BN, whereas its hardness measured independently by microindentation technique[2] is higher than that of the single-crystal c-BN and only slightly lower than that of diamond. The fact that the values of bulk and shear moduli of c-BC$_2$N are lower than those for c-BN and diamond may be attrib-

TABLE I. Summary of experimental data on V_L, V_S, density (ρ), K, G, and ν of c-BC$_2$N, c-BN, and diamond. Elastic moduli and Poisson's ratio of c-BC$_2$N were calculated using Brillouin scattering data and value of density measured in Ref. 1. Acoustic velocities and elastic moduli of c-BN and diamond were calculated using experimentally measured parameters for single crystals.

Phase	ρ (g/cm^3)	V_L (km/s)	V_S (km/s)	ν	K (GPa)	G (GPa)
c-BC$_2$N	3.358[a]	13.09 $\pm$ 0.22[b]	8.41 $\pm$ 0.14[b]	0.149[c]	259 $\pm$ 22[c]	238 $\pm$ 8[c]
c-BN[d]	3.500	15.82	10.39	0.121	372.3	377.8
Diamond[e]	3.512	18.17	12.238	0.071	442	538

[a]Reference 1.

[b]Present study.

[c]Calculated using V_L and V_S from current measurements and density from Ref. 1.

[d]Reference 24.

[e]Isotropic (Voigt-Reuss-Hill) average using elastic moduli reported in Ref. 25.
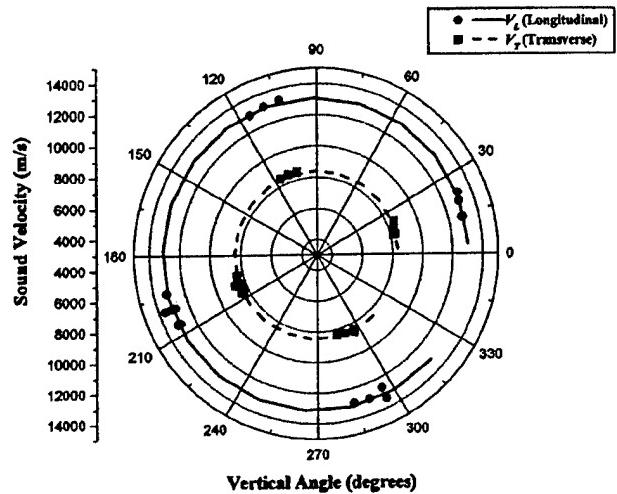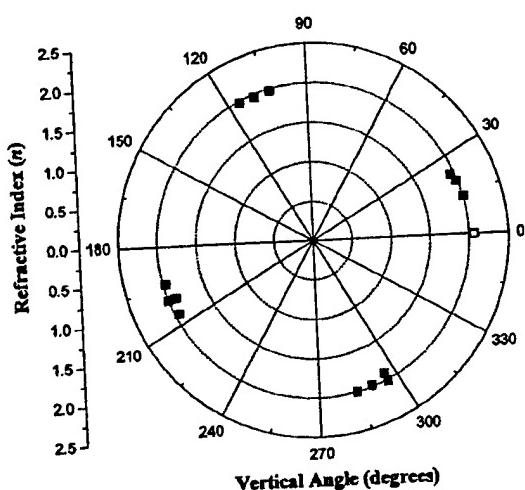
FIG. 3. Experimental azimuth dependence of refractive index (n) in c-BC_2N. Solid squares are present data; open square is the value of n determined from multi-angle-of-incidence ellipsometry measurements (Ref. 14).

uted to the lattice parameter of c-BC_2N being larger than those in diamond and c-BN.[1] The shear modulus value of (447 GPa) for the c-BC_2N evaluated from the nanohardness

measurement[4] is most likely an overestimate due to distinct deformation of the diamond indenter. Clearly the Oliver-Pharr relation between the experimentally measured stiffness and projected area of the elastic contact[23] cannot be used to estimate Young's modulus for superhard phases (H_V > 40 GPa). Nonetheless, it is to be noted that for the diamondlike B-N-C phases synthesized by shock compression at pressure higher than 30 GPa and temperature above 3000 K, very high bulk modulus values were reported for c-$BC_{2.5}N$ (K_0 = 401 GPa) (Ref. 13) and for $BC_{0.9\pm0.2}N$ (K_0 = 412 GPa).[4] These results indicate that the elastic properties of diamondlike B-C-N phases are dependent upon the structure of the phases and, hence, upon the synthesis p-T routes. Further studies are needed to establish any relationship between properties and structure and, hence, the synthesis conditions.

*Author to whom correspondence should be addressed: Electronic address: ming@soest.hawaii.edu

[1] V. L. Solozhenko, D. Andrault, G. Fiquet, M. Mezouar, and D. C. Ruby, Appl. Phys. Lett. **78**, 1385 (2001).

[2] V. L. Solozhenko, S. N. Dub, and N. V. Novikov, Diamond Relat. Mater. **10**, 2228 (2001).

[3] V. L. Solozhenko, S. N. Dub, and N. V. Novikov, J. Superhard. Mater. **23**, 72 (2001).

[4] V. L. Solozhenko, Int. J. High Pressure Res. **22**, 519 (2002).

[5] N. V. Novikov and S. N. Dub, J. Hard Mater. **2**, 3 (1991).

[6] C. A. Brooks, in *Properties and Growth of Diamond*, edited by G. Davies (INSPEC, London, 1994), p. 36.

[7] M. Mattesini and S. F. Matar, Int. J. Inorg. Mater. **3**, 943 (2001).

[8] H. Sun, S.-H. Jhi, D. Roundy, M. L. Cohen, and S. G. Louie, Phys. Rev. B **64**, 094108 (2001).

[9] S. Nakano, T. Sasaki, M. Akaishi, and S. Yamaoka, Mater. Sci. Eng., A **209**, 26 (1996).

[10] E. Knittle, R. B. Kaner, R. Jeanloz, and M. L. Cohen, Phys. Rev. B **51**, 12 149 (1995).

[11] T. Komatsu, J. Chem. Soc., Faraday Trans. **94**, 101 (1998).

[12] T. Komatsu, M. Nomura, Y. Kakadate, and S. Fujiwara, J. Chem. Soc., Faraday Trans. **94**, 1649 (1998).

[13] T. Komatsu, M. Samedima, T. Awano, Y. Kakadate, and S. Fujiwara, J. Mater. Process. Technol. **85**, 69 (1999).

[14] V. L. Solozhenko, O. S. Kondratenko, V. G. Litovchenko, and N. L. Dmitruk, Superhard Mater. **2**, 77 (2002).

[15] F. Langenhorst and V. L. Solozhenko, Phys. Chem. Chem. Phys. **4**, 5183 (2002).

[16] C. H. Whitfield, E. M. Brody, and W. A. Bassett, Rev. Sci. Instrum. **47**, 942 (1976).

[17] J. Bak and R. Sooryakumar, High Press. Res. **11**, 329 (1994).

[18] C. S. Zha, T. S. Duffy, H. K. Mao, and R. J. Hemley, Phys. Rev. B **48**, 9246 (1993).

[19] M. H. Manghnani, S. Tkachev, P. V. Zinin, X. Zhang, V. V. Brazhkin, A. G. Lyapin, and I. A. Trojan, Phys. Rev. B **64**, 121403(R) (2001).

[20] B. Hillebrands, Rev. Sci. Instrum. **70**, 1589 (1999).

[21] J. R. Sandercock, in *Light Scattering in Solids III. Recent Results*, edited by M. C. a. G. Guntherodt (Springer-Verlag, Berlin, 1982), Vol. 51, p. 173.

[22] M. Grimsditch, in *Handbook of Elastic Properties of Solids, Liquids, and Gases. Volume I: Dynamic Methods for Measuring the Elastic Properties of Solids*, edited by M. Levy, H. Bass, R. Stern, and V. Keppens (Academic Press, New York, 2001), Vol. I, p. 331.

[23] W. C. Oliver and G. M. Pharr, J. Mater. Res. **7**, 1564 (1992).

[24] M. H. Manghnani, in *The 5th NIRIM International Symposium on Advances Materials (ISAM' 98)* (National Institute For Research in Inorganic Materials, Chicherster, 1998), p. 73.

[25] H. J. McSkimin, P. Andreatch, and P. Glynn, J. Appl. Phys. **43**, 985 (1972).

10

Brillouin Scattering Measurement of Saw Velocities for Determining Near-Surface Elastic Properties

Marco G. Beghi, Arthur G. Every, and Pavel V. Zinin

CONTENTS

10.1 Introduction

Surface Brillouin scattering (SBS) is a noncontact measurement technique that exploits light scattering to probe the properties of surface acoustic waves (SAWs), either at the surface of homogeneous solids or in thin supported layers. The objective is to obtain information on the elastic properties of the near-surface region, extending down to a depth of the order of a micron. The near-surface elastic properties of solids often differ markedly from those of the underlying bulk material. They are a sensitive indicator of residual stress, annealing, and other near-surface physical conditions. SBS is widely used in the characterization of thin (submicron) supported layers, whose elastic properties can differ from those of the corresponding bulk material. It can alternatively be exploited to measure other properties, such as the layer thicknesses or mass density or the presence of interfacial layers. The systems that have been studied to date are many and diverse. They include inorganic materials such as silicon and silicides; a variety of carbonaceous materials such as diamond, chemical vapor deposited (CVD) diamond, and diamond-like films; various types of hard coatings like carbides and nitrides; Langmuir-Blodgett (LB) films; and various types of multilayers.

The SBS technique does not involve the excitation of SAWs, but relies on spontaneous thermal fluctuations in these modes. It does not observe SAW propagation over macroscopic distances, but is based on local inelastic scattering of light, and is therefore applicable to small samples. Most other SAW techniques are based on the excitation of surface waves, at frequencies determined by the particular technique and experimental conditions; quantitative acoustic microscopy, for example, measures SAW at frequencies ranging from 30 MHz to 2 GHz,[1] while typical frequencies of the broadband SAW

pulses obtained by laser excitation lie within the range 5 to 500 MHz.[2] In SBS the wave vector is determined by the experimental conditions, and with visible light the explored SAW wavelengths are of the order of half a micron or less; typical SAW speeds of such wavelengths correspond to frequencies ranging from a few GHz up to 30 GHz. Surface Brillouin scattering is the only technique able to detect SAWs in this frequency range.[3,4] In order to cover broader frequency ranges, and thus obtain fuller information on the near surface properties, SBS has also been used in conjunction with other techniques such as acoustic microscopy,[5] laser-ultrasonic techniques, or microindentation.[6,7] Wavelengths of a fraction of a micron are still orders of magnitude larger than interatomic distances, and their analysis by a continuum model is therefore fully appropriate.

Thermal fluctuations are governed by the equipartition principle of thermodynamics, which says that at a temperature T each vibrational degree of freedom of a mechanical system is endowed with on average an amount of energy k_BT, where $k_B = 1.38 \times 10^{-23}$ J/K is Boltzmann's constant. In an elastic continuum the vibrational degrees of freedom correspond to acoustic modes of any wave vector. The thermal noise can thus be seen as a superposition of all the acoustic modes. In SBS the scattering geometry selects a specific wave vector and probes the thermal noise at that wave vector, performing a sampling of the surface wave dispersion. This is done by illuminating the surface with a laser beam and examining the spectrum of the scattered light. The laser is of fairly modest power (usually less that a watt) and supposedly causes minimal heating of the surface; it is not the driving force producing the fluctuations, but it is the tool used to detect them. For a highly polished surface, most of the incident light is specularly reflected, refracted, or absorbed. However, because of the thermal fluctuations, a small amount is diffusely scattered, undergoing a change in frequency in the process. This is akin to Raman scattering, but entailing long wavelength acoustic modes rather than molecular vibrations (in microscopic terms, acoustic phonons rather than optical phonons). From the spectrum of the inelastically scattered light and the scattering geometry, one can derive the SAW dispersion relation for the surface and infer the elastic properties of the near-surface region. How this is done is the subject matter of this chapter.

SBS is commonly but not invariably observed in opaque or semiopaque materials, in which the scattering volume is the surface and the small region near the surface that the light is able to penetrate. Some materials studied in SBS are transparent or semitransparent, and in these cases one observes a substantial amount of light scattering from within the bulk. While the main focus of this chapter is on SBS, for completeness we will address some remarks at the issue of bulk Brillouin scattering. Bulk Brillouin scattering is, among other things, used to study the elastic properties of transparent materials as a function of temperature and pressure, particularly with regard to their behavior near phase transitions. When bulk scattering can also be observed, it can be advantageously exploited, since it provides additional information on which to base elastic properties determination.

Brillouin spectrometry is particularly suited to measurements under controlled temperature and/or pressure, because the measurements are contactless, and require only one (for the backscattering configuration) or two (for other configurations) optical windows to access the specimen. This has allowed measurements in furnaces equipped with optical windows,[8-10] and in diamond anvil cells, exploiting the transparency of diamond.[11]

The outline of this chapter is as follows. In Section 10.2 we discuss the underlying physics of SBS, the mechanisms for the scattering of light by thermally excited acoustic vibrations, and the nature of the various bulk and guided waves that play a role in the scattering. An analysis of the various acoustic modes was already presented in Chapter 1 for the case of isotropic media and layers. However, much of the recent experimental work in the area of SBS has been concerned with crystals, epitaxial layers, superlattices, and other types of solids that are elastically anisotropic. The analysis of Chapter 1 is therefore extended to anisotropic media and follows a somewhat different approach, giving results in a form that is more directly linked to the scattering cross section.

In Section 10.3, the SBS technique is described in more detail, and some classical applications are discussed. The observation of SBS has greatly benefited in recent years from developments in multi-pass tandem Fabry-Perot interferometry and low noise high sensitivity detectors.[12] These developments have brought about improvements in resolution and have significantly reduced the data collection time required to achieve adequate signal to noise ratio. Finally, Section 10.4 contains a review of recent SBS applications to the study of single- and multilayers, particularly hard and superhard materials.

This chapter presupposes familiarity with the elementary principles of elasticity, as expounded in Chapter 1 of this book and in the reviews.[13-15] It is a fairly self-contained overview of the SBS technique and its application in the nondestructive characterization of materials. We draw attention to a number of other recent reviews on the subject of SBS.[3,4,12,16] Theoretical treatments of SBS have been published by a number of authors [17-26]. Bulk Brillouin scattering has been reviewed by Dil.[27]

10.2 Theory

10.2.1 Brillouin Scattering: The Principle

The principle of Brillouin scattering is shown in Figure 10.1. A laser beam of angular frequency Ω_i and wave vector q_i is incident on the highly polished surface of a sample at angle θ to the normal. Most of this light is specularly reflected, refracted at angle θ', or absorbed. However, as a result of thermally excited dynamic fluctuations in the strain field within the solid and dynamic rippling of the surface, a small amount of light is diffusely scattered, undergoing in the process a fractional change in frequency of the

(a)

(b)

(c)
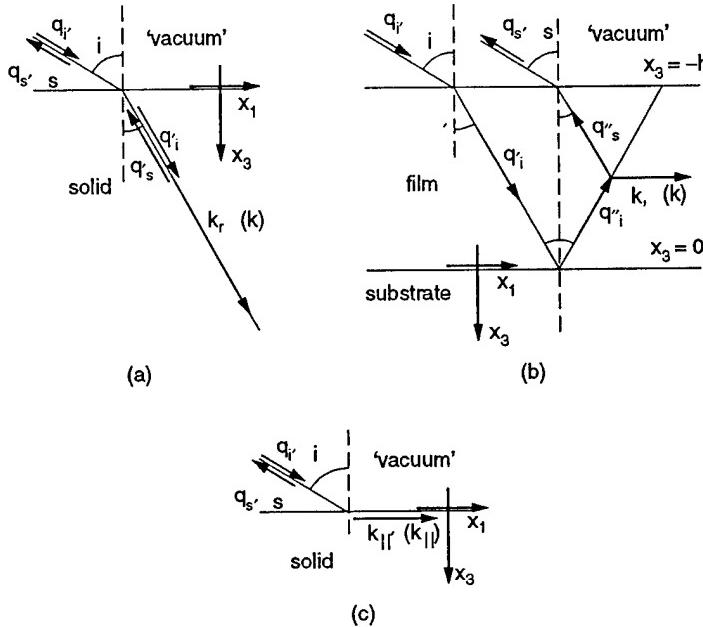
FIGURE 10.1

Brillouin scattering geometry. Ω_i, Ω_s incident and scattered optical circular frequencies; ω: acoustical circular frequency; q_i, q_s: incident and scattered optical wave vectors, in vacuum; q'_i, q''_i, q'_s, q''_s: incident and scattered optical wave vectors, in the solid; k: acoustical wave vector. (a) transparent solid, of refractive index n: $q_i \sin\theta \cong q'_i \sin\theta'$, by Snell's law, $k = q'_i - q'_s$, $q'_s \cong q'_i = nq_i$, $k = 2nq_i$. (b) supported transparent film, of refractive index n : $q_i \sin\theta \cong q'_i \sin\theta'$, by Snell's law, $k = q''_i - q''_s$, $q''_s \cong q''_i = q'_i = nq_i$, $k = 2q''_i \sin\theta' = k = 2q_i \sin\theta$. (c) opaque solid: $k_{||} = (q_i - q_s)_{||}$, $q_s \cong q_i$, $k_{||} = 2q_i \sin\theta$.

order of $c_{acoust}/c_{light} \sim 10^{-5}$, where c_{acoust} is the acoustic wave speed and c_{light} is the speed of light (see Section 10.2). Present in the spectrum of scattered radiation is a relatively intense central peak, unshifted in frequency, which is due to static inhomogeneities and surface roughness in the sample. Because of the fluctuations, in the spectrum there are two more or less mirror image sidebands straddling the central peak. The frequency-downshifted one is called the Stokes band, and the frequency-upshifted one the anti-Stokes band. The inelastic (frequency shifted) spectrum, which is our concern here, depends on the optical and elastic properties of the sample, the scattering geometry, and the vibrational modes of the solid that the light is able to couple to. Since, as already mentioned, the average amount of energy per vibrational degree of freedom is $k_B T$, the intensity of the inelastic spectrum turns out to be proportional to the absolute temperature.

From a quantum mechanical point of view, the scattering is interpreted as a phonon creation (Stokes) or annihilation (anti-Stokes) process in which the photon loses or gains the energy of the phonon. It must also be noted that

AU: (see Section 10.2): Sections have been renumbered: Are you referring to Sect. 10.2.1.2? Please confirm.

the quantum of energy $\hbar\omega$ ($\hbar$ is Planck's constant) associated with an oscillator of 30 GHz frequency corresponds to an equivalent temperature $\hbar\omega/k_B$ of about 1.5 K. This means that even at rather low temperatures the classical approach adopted in this chapter is adequate for calculating the spectrum. It is only at extremely low temperatures where $k_B T$ becomes comparable to $\hbar\omega$, and quantum mechanical effects become pronounced so that a more sophisticated approach is required.

In the usual implementation of SBS, the backscattered light of frequency Ω_s, and wave vector q_s in a small cone around $-q_i$, is collected and analyzed. Three common scattering processes are depicted in Figure 10.1 pertaining to a (a) transparent solid, (b) transparent supported layer, and (c) an opaque or semiopaque solid or supported layer. Because of the small frequency shift $|\omega| = |\Omega_s - \Omega_i| \ll \Omega_i$, it follows that the incident and scattered light wavelengths differ only very slightly, so that to a good approximation $q_s \approx q_i$. Taking into account the change in the wavelength due to the refractive index n for the light when it is in the solid, it follows that $q_s' \approx q_s'' \approx q_s' \approx q_s'' \approx nq_i$ (see Section 10.2.1.1). Further, Snell's law of refraction requires that $q_i' \approx q_s'' \approx q_s' \approx q_s'' \approx nq_i$ and $q_i \sin\theta \approx q_i' \sin\theta'$.

10.2.1.1 Acoustic Modes in Anisotropic Media

Interpretation of SBS spectra can become a complex task when the spectra contain several peaks and when an estimate of the specimen's elastic properties is not available *a priori*. A proper assignment for each peak requires an understanding the basics of SAW propagation in layered solids, especially when the layers are anisotropic. Extensive discussions of bulk and surface waves can be found in a number of books.[15,28-35] We discuss only some salient features here.

The theoretical approach we present here is formulated for anisotropic media and includes as a special case isotropic solids. It was shown in Chapter 1 that in isotropic solids 2 types of bulk acoustic modes exist: primary waves, longitudinally polarized, and secondary waves, transversely polarized. Two independent (orthogonal) transverse polarization directions exist. In isotropic solids the secondary waves are perfectly equivalent, while in anisotropic solids they are not. These modes, called fast transverse (FT) and slow transverse (ST) from their generally different velocities, have phase velocities and polarization vectors that depend on the propagation direction. Also the phase velocity and polarization vector of the longitudinal (P) mode depend on the propagation direction. Although in the anisotropic case the polarization vectors are generally neither exactly parallel nor exactly perpendicular to the wave vector (and therefore, in strict terms, the modes are quasi longitudinal and quasi-transverse) the above names and the corresponding labels P, ST, and FT are customarily used in this context, and are also adopted in this chapter.

At surfaces other acoustic modes are encountered. The Rayleigh wave (RW) at the free surface of a semi-infinite isotropic elastic half space and at

the surface of an isotropic substrate covered by an isotropic layer were discussed in detail in Chapter 1. The RW propagating along the stress-free boundary of a homogeneous solid is a nondispersive acoustic wave which has its energy and displacement field confined near the surface.[36,37] Similar waves existing on anisotropic surfaces are called generalized RW (GRW).[38] The solutions of the wave equation for such waves differ from the true RW on isotropic media only in the form of the variation of the displacement with depth.[36] Antiplane and inplane modes in free standing plates (Lamb waves) were also discussed in Chapter 1, as well as transverse modes in a layered half space (Love waves). Unattenuated waves traveling along interfaces between two solids (Stoneley waves)[39] exist in certain cases; the conditions for their existence have been established.[40] The existence of attenuated interfacial waves was also shown.[41]

Along a stress-free boundary, surface skimming longitudinal (LA) and transverse (T) acoustic waves can exist. The former, from being encountered in different contexts, has acquired various names, including the high frequency pseudo-surface wave (HFPSW),[42] leaky longitudinal surface wave (LLSW), and longitudinal guided wave (LGW) or mode (LGM). Furthermore, waves exist that are surface-like but slowly radiate energy away from the surface and for which the displacement field does not vanish at infinite depth. They are not surface waves in the strict sense, but since their energy is mainly confined near the surface they are called pseudo-surface acoustic waves (PSAWs).[36] PSAWs have a phase velocity higher than that of the lowest of the bulk waves in the substrate. The presence of a layer over a substrate leads to the appearance of a number of waves confined within the layer.[43] For a single layer on solid substrate, these waves are called generalized Lamb[32] or Sezawa waves,[26] because of their similarity to Lamb waves in free-standing isotropic plates. Degenerate Lamb modes have been identified by Sezawa. The behavior of generalized Lamb waves depends on the thickness of the layer in relation to the wavelength, on whether the layer is stiffer or less stiff than the substrate, and the relative densities of the layer and substrate.

In addition to Chapter 1, reviews of the SAW propagation on plates and layered materials can be found in references at the end of this chpater.[33,36,37,43,44]

10.2.1.2 Transparent Solids: The Elasto-Optic Scattering Mechanism

In the case of a transparent solid (Figure 10.1[a]), most of the scattered light emanates from the refracted beam in a region well away from the surface, and the kinematic conditions relating wave vector and frequency shift of the light pertain to bulk acoustic wave scattering. The scattering in this case is mediated by the *elasto-optic scattering mechanism*, in which dynamic fluctuations in the strain field ε_{ij} bring about fluctuations in the dielectric constant, and these in turn translate into fluctuations in the refractive index. These fluctuating optical inhomogeneities result in inelastic scattering of the light as it passes through the solid. In the general anisotropic case the dielectric

constant is a tensor χ_{ij} of rank two, and its fluctuations are given by $\delta\chi_{ij} = p_{ijkl}\varepsilon_{kl}$, where p_{ijkl} is the tensor of the elasto-optic constants.

The strain field in the bulk, well away from the surface, can be expressed as the superposition of the displacement fields of all the bulk P, FT, and ST acoustic waves of the solid. For a particular scattering geometry, (i.e., specific incident light wave vector $\mathbf{q}_i'$ and scattered light wave vector $\mathbf{q}_s'$ [both within the solid], the scattering wave vector is $\mathbf{k} = \mathbf{q}_i' - \mathbf{q}_s'$, and only acoustic waves having precisely this wave vector $\mathbf{k}$ contribute to the detected signal. Bearing in mind that $\mathbf{q}_i'$ and $\mathbf{q}_s'$ differ only very slightly in magnitude, it follows that for back scattering $k = 2q_i'$. The spectrum of the scattered radiation thus contains in principle three pairs of peaks, at frequency shifts

$$\omega = \pm 2q_i' c_{acoust} = \pm 2nq_i c_{acoust} \qquad (10.1)$$

where c_{acoust} stands for phase velocity of the P, FT, or ST wave in the direction of $\mathbf{k}$. The intensities of these peaks vary considerably, depending on the elasto-optic constants p_{ijkl} of the solid, wave polarization, and direction and other factors; it is quite common for one or more of the peaks to be too faint to be detected or even to be zero. These peaks yield up to three bulk wave velocities as a function of direction θ', from which individual elastic constants or combinations of constants can be inferred.[45] In bulk wave scattering the frequency shifts of Equation 10.1 are much larger (up to 150 GHz or so) than for surface wave scattering (typically below 30 GHz). The presence of bulk wave peaks, well separated from surface wave scattering, is of advantage in determining elastic constants using SBS.

10.2.1.3 Brillouin Scattering in Thin Supported Transparent Layers

In the case of a transparent layer on a substrate (Figure 10.1[b]), in addition to Brillouin scattering from the refracted beam, there have been several reported observations of scattering from the beam of wave vector $\mathbf{q}_i''$ that is reflected from the interface. From the geometry of Figure 10.1(b), one readily infers that the scattering wave vector $\mathbf{k} = \mathbf{q}_i' - \mathbf{q}_s'$ of the acoustic modes that are coupled to, is parallel to the surface, and of magnitude $k = 2q_i'' \sin\theta'$. Invoking Snell's law, it follows that $k = 2q_i \sin\theta$, which is, somewhat surprisingly at first sight, independent of the refractive index. Bulk waves are thus detected, having direction parallel to the surface, and frequency

$$\omega = \pm 2q_i c_{acoust} \sin\theta \qquad (10.2)$$

yielding one or more bulk wave velocities parallel to the surface.

10.2.1.4 Opaque Solids: Surface Ripple Scattering Mechanism

In the case of an opaque or semiopaque solid or layer, the Brillouin scattering occurs at or near the surface. In this case the wave vector constraint on the acoustic modes that are coupled to is limited to the component $k_{||}$ parallel to the surface, which is of magnitude

$$k_{||} = 2q_i \sin\theta \qquad (10.3)$$

This allows coupling to a continuous spectrum of bulk modes, incident on the surface and having this value of $\mathbf{k}_{||} = (k_1, k_2)$ and any value of k_3, the component of k normal to the surface. This part of the spectrum is called the Lamb shoulder. Also coupled to are surface waves of various kinds that have this value of $k_{||}$. The modes detected in backscattering have frequencies

$$\omega = \pm 2q_i c_{acoust} \sin\theta \qquad (10.4)$$

yielding a continuum of values of c_{acoust} for the bulk modes and discrete values of wave velocity for the surface modes.

In the case of an opaque solid, SBS is mediated by the *surface rippling scattering mechanism*, (i.e., scattering by dynamic corrugations in the surface profile)[17,46] due to the wave displacements. The dynamic rippling of the surface can be resolved into a superposition of harmonic waves, which act as moving diffraction gratings at the surface, traveling in the reverse (+) or forward (-) directions at velocity c_{acoust}. These cause diffraction of the light together with a Doppler frequency shift. It can be shown that in the classical regime, the cross section for scattering of light with frequency change ω and surface scattering wave vector $k_{||}$, is proportional to the power spectrum $<|u_3(k_{||}, \omega)|^2>$ of the normal fluctuations in the surface profile.[16,20] According to the fluctuation dissipation theorem

$$<|u_3(\mathbf{k}_{||}, \omega)|^2> \propto \frac{T}{\omega}\, \mathrm{Im}\, G_{33}(\mathbf{k}_{||}, \omega) \qquad (10.5)$$

where $\mathrm{Im}\, G_{33}(\mathbf{k}_{||}, \omega)$ is the imaginary (dissipative) part of the Fourier $(\mathbf{k}_{||}, \omega)$ domain surface dynamic response function (Green's function) for force and displacement normal to the surface. Hence, the scattering cross section for dynamic ripple mediated scattering is given by

$$\frac{d^2\sigma}{d\Omega d\omega} = \frac{AT}{\omega}\, \mathrm{Im}\, G_{33}(\mathbf{k}_{||}, \omega) \qquad (10.6)$$

where A is a constant that depends on the scattering geometry, the frequency and polarization of the incident light, and the optical properties of the medium. How $\mathrm{Im}\, G_{33}(\mathbf{k}_{||}, \omega)$ is calculated will be explained shortly.

In the case of a semiopaque solid, there can also be a contribution to the scattering from the elasto-optic effect in the region close to the surface that the light is able to penetrate. This scattering can be expressed in terms of the Green's function tensor G_{ij}, in this case not limited to the normal component G_{33} or to the response exactly at the surface. Accurate calculations of the elasto-optic scattering in semi-opaque solids require a knowledge of the complex dielectric constant as well as the p_{ijkl}, which are not always readily available. We will not treat this aspect further here, but refer the reader to the investigations by various authors.[47-51]

Note that the angular dependences given by Equation 10.2 and Equation 10.4 are exactly the same, but the physical interpretation is quite different. Regarding bulk modes, Equation 10.2 refers to isolated peaks in the Brillouin spectrum associated with modes with k parallel to the surface, while Equation 10.4 pertains to a continuum of bulk modes. In SBS, it is tempting to take a $\sin\theta$ dependence of the frequency shift of a peak as the tell-tale sign of a surface mode. As we have seen here, this can also be an indication of a surface skimming bulk wave.

10.2.2 Computation of Brillouin Spectra

10.2.2.1 Green's Function for Anisotropic Layered Media

Here we briefly describe the derivation of the Fourier $(k_{||}, \omega)$ domain surface dynamic response function (Green's function) $G_{33}(k_{||}, \omega)$ for an anisotropic layer of thickness h perfectly bonded to an anisotropic half space, following Every.[52] In the following sections we also discuss the nature of the various surface and guided waves, and how some of their properties can be obtained from $G_{33}(k_{||}, \omega)$. We adopt the coordinate system shown in Figure 10.1, with the x_1- and x_2-axes in the interface between the layer and substrate and the x_3-axis normal to the surface and directed into the substrate. By letting h tend to zero, the properties of the substrate alone are obtained. We consider a general anisotropic elastic continuum of mass density ρ^+ and elastic modulus tensor C^+_{ijkl} in the half-space $x_3 > 0$ and a layer of density ρ^- and elastic modulus tensor C^-_{ijkl} in the region $-h < x_3 < 0$ (Figure 10.1). The superscripts $+$ and $-$ will also be used for other quantities such as stress or displacement to distinguish them when they pertain specifically to the substrate or respectively to the layer.

We first provide a brief introduction to the subject of bulk waves in anisotropic solids, extending the detailed analysis presented in Chapter 1 for the isotropic case. We then show how bulk waves are used as partial waves in the calculation of the surface dynamic response of a layered solid. The wave equation for an infinite anisotropic elastic solid is

$$\rho \frac{\partial^2 u_i}{\partial t^2} = C_{ijkl} \frac{\partial^2 u_k}{\partial^2 x_j x_l} \tag{10.7}$$

summation over repeated indices being implied. Equation 10.7 admits plane wave solutions of the form

$$u_i = U_i \exp[i(\mathbf{k} \cdot \mathbf{x} - \omega t)] \tag{10.8}$$

where the wave vector k, angular frequency ω and polarization vector U are related by the set of three linear equations

$$(C_{ijkl}k_j k_l - \rho\omega^2 \delta_{ik})U_k = 0 \tag{10.9}$$

δ_{ik} being the Kronecker symbol, and the corresponding secular equation being

$$D(\mathbf{k}, \omega) = |C_{ijkl}k_j k_l - \rho\omega^2 \delta_{ik}| = 0 \tag{10.10}$$

These linear equations (10), the Christoffel equations, represent the bulk wave dispersion relation for the anisotropic medium. It is more convenient to analyze wave propagation in anisotropic media using the slowness vector $s = k/\omega$ instead of the wave vector. In terms of the slowness vector, Equation 10.9 and 10.10 take the forms

AU: Three linear equations (10): Is this phrase refering to Eq. 10.10 or 10.8-10.10?

$$(C_{ijkl}s_j s_k - \rho\omega^2 \delta_{il})U_l = 0 \tag{10.11}$$

$$\Omega(\mathbf{s}) = |C_{ijkl}s_j s_k - \rho\delta_{il}| = 0 \tag{10.12}$$

A section of the slowness surface of GaAs in the (001) plane, defined by Equation 10.12, is shown by the solid lines in Figure 10.2. It is a centrosymmetric surface of three sheets corresponding to the P, FT, and ST modes. The slowness surface depicts the directional dependence of the slowness or inverse phase velocity $s = 1/c_{acoust}$. In the case of isotropic solids all three sheets of the slowness surface are spherical, the outer two sheets coincide and correspond to pure transverse (secondary) waves, and the inner sheet corresponds to pure longitudinal (primary) waves. For anisotropic solids, the outer two sheets (corresponding to FT and ST quasi-transverse waves) are separated. They are in contact only in isolated directions, known as acoustic axes, which can be found in both symmetry and nonsymmetry directions.

The energy flow velocity for a plane homogeneous wave is the ray or group velocity vector $c_g = \nabla_k \omega(k) = \nabla_s \Omega(s)$, which has the property of being normal to the constant frequency surface at any point. The direction of the
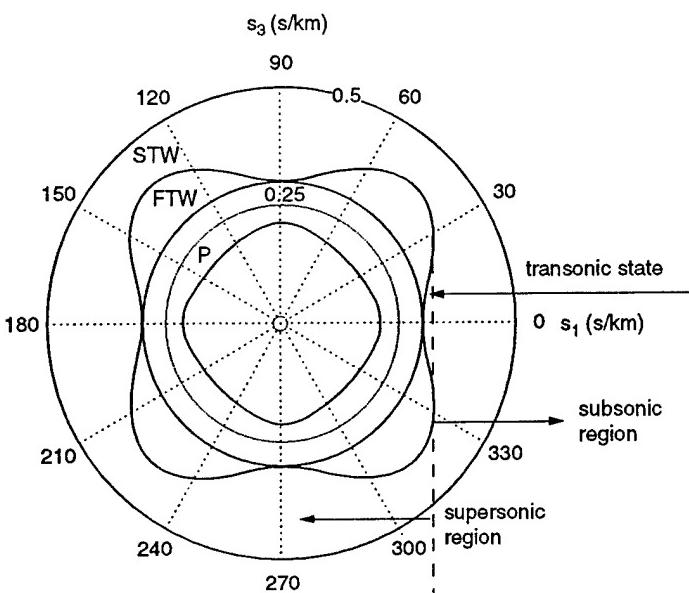
FIGURE 10.2

The slowness curve of silicon for the (001) plane. The dashed line corresponds to the transonic state. The solid curves correspond to the slowness curves for longitudinal P, FT, and ST bulk waves.

ray vector is an important consideration when selecting partial waves in the boundary problem we discuss in the next section.

The dotted line in the Figure 10.2 is the slow transverse threshold.[26] It corresponds to the limiting point on the ST slowness curve where $s_{||} = k_{||}/\omega$ is a maximum, and where the ray vector, which is perpendicular to the slowness surface, is parallel to the physical surface of the sample. At larger values of $s_{||}$, corresponding to smaller velocities, all solutions for the slowness component $s_3 = k_3/\omega$ are complex and correspond to inhomogeneous waves; the maximum value of $s_{||}$ is thus known as the limiting transonic state. For an isotropic solid, the slowness curves are circles, and the transonic state coincides with the transverse slowness along the surface, $s_S = (\rho/C_{44})^{1/2}$, but this is not generally true for anisotropic solids as Figure 10.2 demonstrates.

We now determine the Green's function, following the procedure of Cottam and Loudon.[53] It is assumed that the medium is subjected to a time- and position-dependent distribution of body force F(x, t), defined per unit mass and having a harmonic time dependence

$$F(x,t) = F(x)\exp(-i\omega t) \tag{10.13}$$

The equation of motion for the components of the elastic displacement field $u(x,\omega)\exp(-i\omega t)$ in the medium is then given by

$$C_{ijkl}\frac{\partial^2 u_l}{\partial^2 x_j x_k}+\rho\omega^2 u_i = -F_i(\mathbf{x}), \quad x_3 > 0 \tag{10.14}$$

summation over repeated indexes being again implied. The particular integral of Equation 10.14 can be written formally

$$u_i(\mathbf{x},\omega) = -\int_{-\infty}^{\infty} d^3x' g_{ij}(\mathbf{x},\mathbf{x}',\omega)F_j(\mathbf{x}') \tag{10.15}$$

where $g_{ij}(x,\omega)$ is the elastodynamic Green's tensor. When the point force is located at the surface of the film $[\mathbf{F}_j(\mathbf{x}') = \mathbf{F}_j\delta(x_1')\delta(x_2')\delta(x_3'+h)]$ where $\delta(x)$ is the delta function], g_{ij} is called the surface Green's function; if the point force is applied at the film/substrate interface $(x_3 = 0)$ we call $g_{33}(x_{||}, x_3 = 0, \omega)$ the interface Green's function. For a concentrated point force acting at the top surface we have

$$u_i(\mathbf{x},\omega) = g_{ij}(\mathbf{x},\omega)F_j \tag{10.16}$$

The Fourier $(k_{||}, \omega)$ domain surface dynamic response function (Green's function) G_{ij} is defined as a double Fourier integral of the elastodynamic Green's tensor $g_{ij}(\mathbf{x}, \omega)$ in the variables x_1 and x_2.

$$G_{ij}(\mathbf{k}_{||},x_3,\omega) = \int_{-\infty}^{\infty} d^2 x_{||} g_{ij}(\mathbf{x}_{||},x_3,\omega)\exp\{-i k_{||} x_{||}\}, \tag{10.17}$$

where $x_{||} = (x_1,x_2)$ and $k_{||} = (k_1, k_2)$; the inverse transform is

$$g_{ij}(\mathbf{x}_{||},x_3,\omega) = \frac{1}{(2\pi)^2}\int_{-\infty}^{\infty} d^2 k_{||} G_{ij}(\mathbf{k}_{||},x_3,\omega)\exp\{i k_{||} x_{||}\} \tag{10.18}$$

The purpose of the following simulations is to find a response of the system to an external harmonic force (Equation 10.13) applied at the layer's upper surface

$$\sigma_{l3}^-(\mathbf{x}_{||},x_3 = -h,\omega) = -F_l\delta(\mathbf{x}_{||}), l = 1, 2, 3 \tag{10.19}$$

where $\delta(x_{||}) = \delta(x_1)\delta(x_{2||})$ is the two dimensional δ-function. In the Equation 10.19, superscript in the stress component σ_{l3}^- indicates that it has been

calculated in the layer. The negative sign in Equation 10.19 has to do with the fact that the surface tractions $\sigma_{j3}(x_{||}, x_3 = -h, \omega)$ are in reaction to the applied force.

Equation 10.19 is written in the spatial or Cartesian coordinate system, but we can also write it in the Fourier domain (*k*-space) using properties of the delta function[54]

$$\delta(x) = \frac{1}{(2\pi)} \int_{-\infty}^{\infty} dk \exp\{ikx\} \qquad (10.20)$$

and it can then be rewritten then as an inverse Fourier transform

$$\sigma_{l3}^-(x_{||}, x_3 = -h, \omega) = -\frac{1}{(2\pi)^2} \int_{-\infty}^{\infty} d^2k_{||} F_l \exp\{ik_{||}x_{||}\}, \quad l = 1, 2, 3 \quad (10.21)$$

In order to calculate the Brillouin spectrum (Equation 10.6) we need only the component of the external force **F** normal to the surface [**F** = (0,0,*F*)]. Therefore, the conditions (Equation 10.21) can be rewritten as

$$\sigma_{33}^-(x_{||}, x_3 = -h, \omega) = -\frac{F}{(2\pi)^2} \int_{-\infty}^{\infty} d^2k_{||} \exp\{ik_{||}x_{||}\} \qquad (10.22)$$

$$\sigma_{l3}^-(x_{||}, x_3 = -h, \omega) = 0, \quad l = 1, 2 \qquad (10.23)$$

To find the response of the system to the force *F* we seek the solution of the equations of motion (Equation 10.14) in the form of a superposition of outgoing plane waves whose amplitudes are proportional to *F*. In the film the displacement field is given by

$$u_i^-(x, \omega) = \frac{F}{(2\pi)^2} \int_{-\infty}^{\infty} d^2k_{||} \sum_{n=1}^{6} A^{(n)} U_i^{(n)} \exp\left\{i\left(k_{||}x_{||} + k_3^{(n)}x_3\right)\right\} \qquad (10.24)$$

and in the substrate it is given by

$$u_i^+(x, \omega) = \frac{F}{(2\pi)^2} \int_{-\infty}^{\infty} d^2k_{||} \sum_{n=7}^{9} A^{(n)} U_i^{(n)} \exp\left\{i\left(k_{||}x_{||} + k_3^{(n)}x_3\right)\right\} \qquad (10.25)$$

For each value of $k_{||}$ and ω, the coefficients $A^{(n)}$ in (Equation 10.24) and (Equation 10.25) are the nine unknown constants for the decomposition into

plane waves. The third component k_3 of k and the polarization vector U are related by the Christoffel equations (9) where $k_3^{(n)}$ are roots of the characteristic sextic equation (Equation 10.10). Generally Equation (10) yields 6 solutions; in the substrate the 3 ($n = 7,8,9$) are chosen which correspond to outgoing waves, on the basis that they are either homogeneous (bulk) waves ($k_3^{(n)}$ real) with ray or group velocity vectors, c_g, directed into the interior ($c_{g3} > 0$), or they are inhomogeneous (evanescent) waves ($k_3^{(n)}$ complex or pure imaginary) which decay into the interior ($Im\ k_3^{(n)} > 0$). In the film all six partial waves ($n = 1, 2, 3, 4, 5, 6$) must be taken into account.

In computer codes the slowness equation is written in the form of a polynomial equation

$$\sum_{i,j,k=1}^{6} D_{ijk} s_1^i s_2^j s_3^k = 0 \qquad (10.26)$$

where the coefficients D_{ijk} depend on the C_{ijkl} and ρ. For a given $s_{||} = (s_1, s_2)$ this becomes a sextic equation

$$E_{3k} s_3^k = 0, \quad E_{3k} = \sum_{i,j=1}^{6} D_{ijk} s_1^i s_2^j$$

in s_3. For s_3 perpendicular to a mirror plane, all odd powers of s_3 are zero, and it reduces to a cubic in $(s_3)^2$. To obtain the component along x_3 of the group velocity when s_3 is real, we simply differentiate the above equation and do similarly for the other two components. The calculation of the roots of the Equation 10.26 can be simplified by first rotating the crystal to the coordinate frame, where the surface of the sample defines the $x_1 x_2$ plane, and the propagation direction is always along x_1. For monoclinic symmetry, the implicit form of the coefficients in Equation 10.26 is given by Nayfeh.[55] For triclinic symmetry, the implicit form of the polynomial Equation 10.26 can be found elsewhere.[56]

From the stress-strain relationship, $\sigma_{lm} = C_{lmpq} \partial u_p / \partial x_q$, and Equation 10.24 and Equation 10.25 it follows that the surface tractions are given by

$$\sigma_{l3}^-(\mathbf{x}_{||}, x_3 = -h, \omega) = \frac{i\omega F}{(2\pi)^2} \int_{-\infty}^{\infty} d^2\mathbf{k}_{||} \sum_{n=1}^{6} A^{(n)} B_l^{(n)} \exp\{i(\mathbf{k}_{||}\mathbf{x}_{||})\} \qquad (10.27)$$

where the matrix $B_l^{(n)}$ has been introduced

$$B_l^{(n)} = C_{3lpq}^- U_p^{(n)} k_q^{(n)} \exp\{-ik_3^{(n)}h\}/\omega \quad n = 1,2,3,4,5,6; \quad l = 1, 2, 3 \qquad (10.28)$$

AU: Christoffel equations (9): Should this be Equation 10.9 or equations 10.8-10.10 (see previous comment)?

Summation is implied over repeating indexes (p,q) in Equation 10.28. Comparing Equation 10.27 and Equation 10.28 and Equation 10.23, we arrive at a set of 3 linear equations for the partial wave amplitudes $A_j^{(n)}$

$$\sum_{n=1}^{6} B_l^{(n)} A^{(n)} = \frac{i\delta_{3l}}{\omega}, \quad l = 1,2,3 \tag{10.29}$$

Another three equations for the amplitudes arise from the continuity of stress at the interface

$$\sigma_{j3}^{+}(\mathbf{x}_{||}, x_3 = 0_+, \omega) - \sigma_{j3}^{-}(\mathbf{x}_{||}, x_3 = 0_-, \omega) = 0 \tag{10.30}$$

which yield

$$\sum_{n=1}^{9} B_l^{(n)} A^{(n)} = 0, \quad l = 4, 5, 6 \tag{10.31}$$

where

$$B_l^{(n)} = C_{3(l-3)pq}^{+} U_p^{(n)} k_q^{(n)} / \omega, \quad n = 7, 8, 9; \quad l = 4, 5, 6 \tag{10.32}$$

and

$$B_l^{(n)} = -C_{3(l-3)pq}^{-} U_p^{(n)} k_q^{(n)} / \omega, \quad n = 1, 2, 3, 4, 5, 6; \quad l = 4, 5, 6 \tag{10.33}$$

Finally there are three equations for the partial wave amplitudes arising from continuity of the displacement field at the boundary

$$u_i^{+}(\mathbf{x}_{||}, x_3 = 0_+, \omega) - u_i^{-}(\mathbf{x}_{||}, x_3 = 0_-, \omega) = 0 \tag{10.34}$$

which yield

$$\sum_{n=1}^{9} B_l^{(n)} A^{(n)} = 0, \quad l = 7, 8, 9 \tag{10.35}$$

where

$$B_l^{(n)} = U_{l-6}^{(n)}, \quad l = 7, 8, 9, \quad n = 7, 8, 9 \tag{10.36}$$

and

$$B_l^{(n)} = -U_{l-6}^{(n)}, \quad l = 7, 8, 9; \quad n = 1, 2, 3, 4, 5, 6 \tag{10.37}$$

Note the $-$ sign in the defining Equation (37) for $B_l^{(n)}$.

Combining Equation 10.29, Equation 10.31, and Equation 10.35 we arrive at a system of 9 linear equations in 9 unknown $A^{(n)}$ and a right-hand side vector Y.

$$\mathbf{B}^* A = \frac{i}{\omega} Y \tag{10.38}$$

where $Y_l = 0$ for $l \neq 3$ and $Y_l = 1$ for $l = 3$. The solution of Equation 10.38 takes the form

$$A^{(n)} = \frac{i}{\omega} (\mathbf{B}^{-1})^{(n)} = \frac{i}{\omega} \frac{adj(\mathbf{B})^{(n)}}{\det|\mathbf{B}|} \tag{10.39}$$

adj denoting matrix adjoint. From Equation 10.19, Equation 10.24, and Equation 10.39 it follows

$$g_{33}(\mathbf{x}_{||}, x_3 = -h, \omega) = \frac{1}{(2\pi)^2} \int_{\infty}^{-\infty} d^2\mathbf{k}_{||} \left\{ \sum_{n=1}^{6} \frac{i}{\omega} (\mathbf{B}^{-1})^{(n)} U_3^{(n)} \exp\left(-ik_3^{(n)}h\right) \right\} \exp(i\mathbf{k}_{||}|\mathbf{x}_{||}|) \tag{10.40}$$

Comparing Equation 10.40 with Equation 10.18 we finally obtain Surface Green's function

$$G_{33}(\mathbf{k}_{||}, x_3 = -h, \omega) = \frac{i}{\omega} \sum_{n=1}^{6} (\mathbf{B}^{-1})^{(n)} U_3^{(n)} \exp\left(-ik_3^{(n)}h\right) \tag{10.41}$$

Green's function for interface is obtained in a similar way. Instead of Equation 10.19 we have

$$\sigma_{33}(\mathbf{x}_{||}, x_3 = 0, \omega) = -F \delta(\mathbf{x}_{||}) \tag{10.42}$$

the stresses at the outer surface of the layer are null

$$\sigma_{l3}^-(\mathbf{x}_{||}, x_3 = -h, \omega) = 0, \quad l = 1, 2, 3 \tag{10.43}$$

while the stress at the interface is continuous only in the interface plane

$$\sigma_{l3}^{+}(\mathbf{x}_{||}, x_3 = 0_+, \omega) - \sigma_{l3}^{-}(\mathbf{x}_{||}, x_3 = 0_-, \omega) = 0, \quad l = 1, 2 \tag{10.44}$$

and is discontinuous in x_3-direction

$$\sigma_{33}^{-}(\mathbf{x}_{||}, x_3 = 0, \omega) - \sigma_{33}^{-}(\mathbf{x}_{||}, x_3 = 0, \omega) = -\frac{F}{(2\pi)^2} \int_{-\infty}^{\infty} d^2\mathbf{k}_{||} \exp\{i\mathbf{k}_{||} \cdot \mathbf{x}_{||}\} \tag{10.45}$$

A set of linear equations is accordingly obtained, which differs from Equation 10.38 only in the right-hand side: $Y_l = 0$ for $l \neq 6$ and $Y_l = 1$ for $l = 6$. For the interfacial Green's function we obtain

$$G_{33}(\mathbf{k}_{||}, x_3 = 0, \omega) = \frac{i}{\omega} \sum_{n=1}^{6} (\mathbf{B}^{-1})^{(n)} U_3^{(n)} \tag{10.46}$$

Equation 10.16 was said earlier to describe Brillouin scattering from the free surface of a semi-infinite solid. It has been shown[52] that it can also be applied also to more complicated situations such as (1) scattering from the interface between two perfectly bonded solids, one transparent and the other opaque; (2) scattering from the surface of an opaque film supported on a substrate; and (3) scattering from the interface between a thin supported film and substrate when either the film or substrate are transparent. In cases where the light passes through a transparent medium before or after meeting a scattering surface, there will also be elasto-optic scattering and interference between this and the ripple scattering. The emphasis in the present treatment is on the surface dynamics, and no account is taken of elasto-optic scattering.

By way of example, Figure 10.3 shows the anti-Stokes (frequency upshifted) component of the SBS spectrum of the (110) surface of the cubic crystal $VC_{0.75}$ for $k_{||}$ in the $[1\bar{1}0]$ direction obtained by Zhang et al.[57] Only that part of the spectrum well away from the central peak is shown. The dominant features in the spectrum are a sharp peak due to the RW, and the Lamb shoulder continuum, due to the continuum of bulk modes that participate in surface scattering. As can be seen, the measured spectrum is well accounted for by the theoretical spectrum calculated from $ImG_{33}(k_{||}, \omega)$.

10.2.2.2   *Computation of Dispersion Relations*

The maxima of the surface Green's function (Equation 10.41) or the interfacial one (Equation 10.46) identify the dispersion relations for surface and interface acoustic modes, respectively. These Green's functions are inversely proportional to the determinant $\det|\mathbf{B}|$ (see also Equation (10.39); divergencies are therefore expected when

$$\det|\mathbf{B}| = 0 \tag{10.47}$$

and maxima are possibly (but not exclusively) found when $\det|\mathbf{B}|$ is minimum.
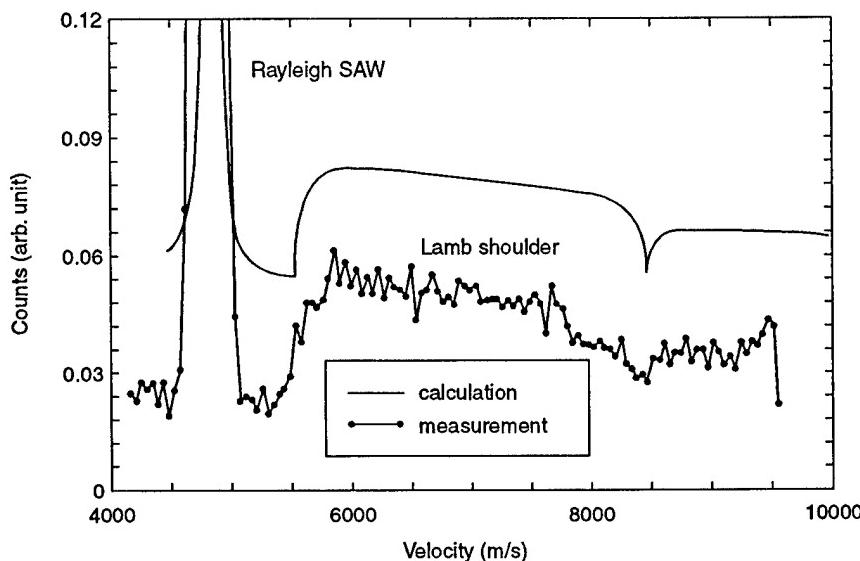
FIGURE 10.3

Theoretical and measured spectra of $VC_{0.75}$ for the $[1\bar{1}0]$ direction in the (110) surface. (From Zhang, X. et al., *Int. J. Refrac. Metals Hard Mater.*, 16, 303, 1998. With permission.)

Equation 10.47 is essentially the equation obtained by the approach presented in Chapter 1, which considers the free motion of the medium in the absence of the external forces and identifies the resonant frequencies. The meaning of the corresponding divergences of the Green's function is straightforward. Since the model considered here (Equation 10.14) is perfectly elastic and does not include dissipation mechanisms, the response to a resonant harmonic external force (Equation 10.13) is divergent. Equation (10.47) identifies the true surface waves. Their displacement field vanishes at infinite depth, and typically falls off to a negligible amplitude within a few wavelengths from the surface; their power flow is exclusively parallel to the surface. Nondivergent maxima of the Green's function instead identify damped resonances. Damping is not provided by dissipative mechanisms, but by a component of the power flow which is perpendicular to the surface and irradiates part of the wave energy towards the interior of the medium. Such resonances are the PSAWs, also called leaky surface waves (see Section 1), whose displacement field does not vanish at infinite depth, but still behaves similarly to SAWs because the displacement field is still mainly confined close to the surface. In numerical computations divergencies can be avoided by a simulation of a dissipative mechanism, obtained by attributing a non null imaginary part to the frequency ω. Delta function resonances are thus transformed into finite and broadened peaks.[58]

The dispersion equation (Equation 10.47) can be solved for $k_{||}$ for fixed ω. The roots of Equation 10.47 located on the real axis $k_{||}$ correspond to the

AU: (see Section 10.1): Sections have been renumbered: Are you referring to Sect. 10.2.2.1? Please confirm.

true RWs and generalized Lamb surface waves, while PSAWs are attenuated by energy leakage, and correspond to complex values of $k_{||}$ (pole).[36] The velocity of the PSAW is determined by the real part of the reciprocal of $k_{||}$ ($c_{PSAW} = Re[\omega/k_{||}]$) and the attenuation is given by the imaginary part.

In Green's function calculations for SBS the wave vector component $k_{||}$ is kept fixed and the imaginary part of the Green's function is calculated as a function of frequency $Im[G_{33}(\omega)]$. True surface waves, such as the RW, show up as δ-function singularities. The RW corresponds to a singularity at ω_R, its velocity being $\omega_R/k_{||}$. For the true surface waves the velocities obtained by solving Equation 10.47 or by locating the divergencies of the Green's function are identical. In Green's function calculations PSAWs show up as resonances of finite height and width centered at frequency ω_{MAX}, and the velocity of the PSAW is $c_{PSAW} = \omega_{MAX}/k_{||}$. The higher the attenuation or the farther the pole from the real axis, the broader is the PSAW peak in the Green's function, and the higher is the discrepancy between the modal (Equation 10.47) and Green's function solutions for PSAW velocity.

For the surface of an isotropic half-space the Equation (10.47) can be written in analytical form. It is the famous Rayleigh equation, already analyzed in Chapter 1

$$\chi^6 - 8\chi^4 + 8(3 - 2\varsigma^2)\chi^2 - 16(1 - \varsigma^2) = 0 \tag{10.48}$$

where $\chi = c/c_S$ and $\zeta = c_S/c_P$. It can be simplified by introducing another variable $y = \chi^2 - 8/3$

$$y^3 + 3py + 2q = 0 \tag{10.49}$$

where $p = 8/9(1 - 6\zeta_2)$ and $q = 8/3(17/9 - 5\zeta^2)$. Rayleigh's equation was derived more than a century ago, but still attracts the attention of researchers.[59-61] Nkemzi[62] applied the theory of Cauchy integrals to derive an explicit form for the RW velocity in an elastic solid. The solution of Equation 10.49 derived by Lord Rayleigh and discussed in Chapter 1 is the Rayleigh surface wave RW of velocity c_R. The RW at the stress-free surface of a solid is a superposition of three phase-matched evanescent waves that satisfies the free surface boundary conditions. The absence of any power flow normal to the surface comes from the absence of any incoming or outgoing bulk waves.

For isotropic solids $c_R < c_S$, and c_R lies in the range[44] $0.87\,c_S < c_R < 0.96\,c_S$. Measurements of the Rayleigh wave velocity give a lower bound for c_S, and hence a lower bound for C_{44}. The value of C_{44} can be obtained from the approximate relation[44]

$$c_R = c_S \frac{0.718 - (c_S/c_R)^2}{0.75 - (c_S/c_R)^2} \tag{10.50}$$

or using Poisson's ratio ν

$$c_R = c_S \frac{0.87 + 1.12\nu}{1 + \nu} \tag{10.51}$$

Turning back to Green's function calculations, for an isotropic half-space, the power spectrum $<|u_3(k_{||}, \omega)|^2>$ can be written in closed form[18,63]

$$<|u_3(k_{||}, \omega)|^2> = \frac{k_B T}{S \pi \rho k_{||} c_S^3} I_3(k_{||}, \omega) \tag{10.52}$$

$$I_3(k_{||}, \omega) = \text{Re} \left\{ \frac{k_{p3} k_s k_{||}^2}{4 k_{p3} k_{s3} k_{||}^2 + \left(k_{s3}^2 - 2k_{||}^2 \right)^2} \right\} \tag{10.53}$$

where $k_p = \omega/c_p$ and $k_s = \omega/c_S$ are wave numbers for the longitudinal and shear modes respectively, and $k_{p3} = \sqrt{k_p^2 - k_{||}}$ and $k_{s3} = \sqrt{k_s^2 - k_{||}}$ are the wave vector components normal to the surface.

A PSW can be found in the form of a surface skimming longitudinal wave. The computation is performed considering in Equation 10.21 a harmonic force (Equation 10.13) directed along x_1 instead of x_3, and computing the longitudinal power spectrum[19,46] $<|u_1(k_{||}, \omega)|^2>$. The latter can be written in closed form for isotropic half-space[63]

$$<|u_1(k_{||}, \omega)|^2> = \frac{k_B T}{S \pi \rho k_{||} c_S^3} I_1(k_{||}, \omega) \tag{10.54}$$

$$I_1(k_{||}, \omega) = \text{Re} \left\{ \frac{k_{s3} k_s k_{||}^2}{4 k_{p3} k_{s3} k_{||}^2 + \left(k_{s3}^2 - 2k_{||}^2 \right)^2} \right\} \tag{10.55}$$

its form being very similar to that of $<|u_3(k_{||}, \omega)|^2>$. This mode, called LLSW or longitudinal mode (LM) (see Figure 10.4), does not cause surface corrugations, but it does interact with light by the elasto-optic mechanism.[46] Sandercock[64] first observed the LLSW in the Brillouin spectrum of the (110) surface in GaAs. Detailed studies of the detection of LLSW by SBS solid were performed.[22,63,65] It was shown[65] that the peak in the longitudinal spectrum corresponds to a leaky surface wave; it was found[63] that when the Poisson's ratio ν is smaller than 1/3, the longitudinal power spectrum $<|u_1(k_{||}, \omega)|^2>$ exhibits a sharp and well-defined peak, very close to c_p (see Figure 4). For $\nu > 1/3$ the peak becomes broader and lies between $2c_S$ and c_p. Note, however, that in the power spectrum for $<|u_3(k_{||}, \omega)|^2>$, there is a sharp dip at the
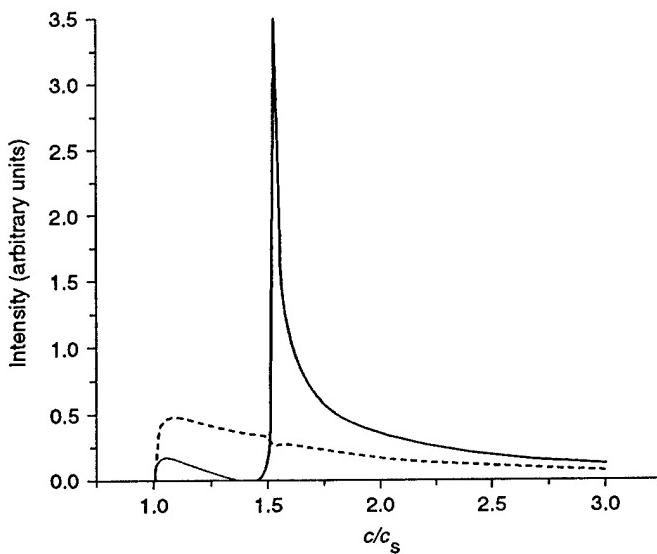
FIGURE 10.4

The factors I_p (broken line) and I_S (solid line) as function of c/c_S at fixed $k_{||}$ simulated for hard amorphous carbon synthesized from C_{60} (sample B) with elastic parameters given in Table 2. Region of c/c_S with RW is omitted.

LLSW, and so this mode can also be measured even if there is only ripple scattering.

It must be mentioned that for $v < 0.263$ the Rayleigh equation has 3 distinct real roots. One is the RW velocity, lying in the $(0, c_S)$ interval, and another one, out of this interval, coincides with the longitudinal velocity c_p.[66] Mozhaev et al.[66] described this high velocity solution as the Brewster angle reflections of homogeneous (along the plane front) bulk acoustic waves. Analytical expressions for the roots of the Rayleigh equation were derived in several articles.[60,62,67]

10.3 Experimental Method

10.3.1 Experimental Setup

The most common configuration for Brillouin scattering experiments is presented in Figure 10.1 (see Section A). The specimen is illuminated by a laser beam, the light scattered in a given direction is collected and its spectrum is analyzed. Figure 1 presents the usual configuration of backscattering which, as discussed below, is often advantageous; in volume Brillouin scattering other geometries are also adopted, in which the collection direction
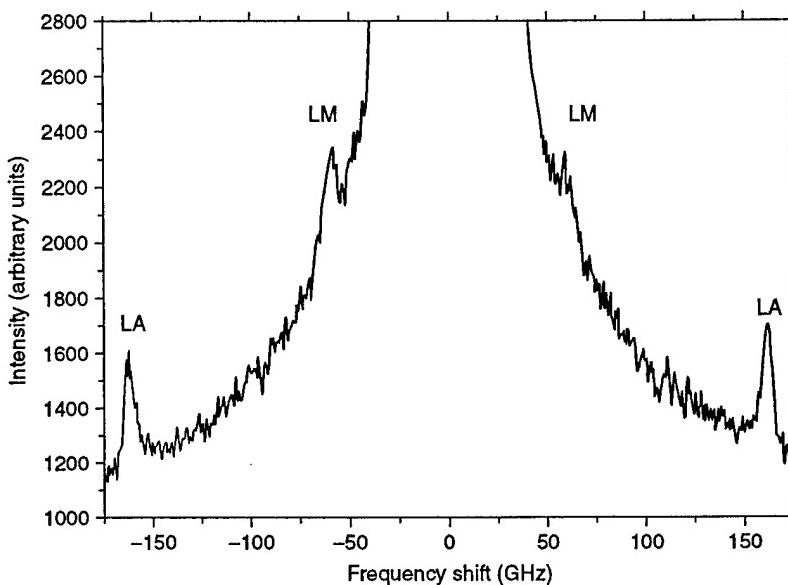
FIGURE 10.5

Experimental Brillouin spectrum, at $\theta = 70°$, of amorphous carbon synthesized from C_{60} sample B. (From Manghnani, M.H. et al., *Phys. Rev. B*, 6412, 121403, 2001. With permission.)

forms an angle other than 180° (typically 90°[45,68,69]) with the incidence direction. Other types of configuration have sometimes been used and will be mentioned below.

The common configuration will be discussed here in some detail, although not limited exclusively to the backscattering case. The incident laser light is monochromatic: it has wavelength (in vacuum) λ_0, wave vector q_i, and circular frequency Ω_i ($|q_i| = q_i = 2\pi/\lambda_0$ and $\Omega_i = c_{light} q_i$, c_{light} being the velocity of light). The spectrum of scattered light was already introduced in Section A. The most intense feature is the sharp peak at Ω_i, due to light elastically reflected by static inhomogeneities; a weaker and much broader feature, still centered at Ω_i, can be present. It is due to scattering by dynamic, but non-traveling, excitations, and is called quasi-elastic scattering (see Figure 10.5). Scattering by dynamic and traveling excitations, (i.e., acoustic waves) produces symmetric doublets. The scattered light collected along the direction of a wave vector q_s interacted with an acoustic wave, of any kind, of wave vector

$$k = \pm (q_s - q_i) \qquad (10.56)$$

the $\pm$ sign referring to anti-Stokes and Stokes events, respectively (see Section A), and contains a doublet at frequencies

$$\Omega_s = \Omega_i \pm \omega \qquad (10.57)$$

where the ± sign refers again to anti-Stokes and Stokes events, and $\omega = c_{acoust}$ $|k|$ is the frequency of the acoustic wave, of velocity c_{acoust}. In the analysis of Equation 10.57 and Equation 10.56 the wide difference between the velocity of light and any acoustic velocity allows some simplification.

10.3.1.1 Scattering Geometry

Volume Brillouin scattering is the scattering by bulk acoustic waves of velocity c_{acoust}, where c_{acoust} stands for the velocity of any of the three bulk waves P, FT, and ST (see Section 1). In this case the optical wave vectors appearing in Equation 10.56 are those (q_i' and q_s') present in the bulk; their directions are determined by the incidence and collection directions out of the sample, and by the refractive index n, with $q_i' = n\ q_i$ and $q_s' = n\ q_s$ (see Section A). The angular frequencies are $\omega = c_{acoust}\ k$, $\Omega_i = (c_{light}/n)q_i'$ and $\Omega_s = c_{light}/n)q_s'$, ($c_{light}/n$) being the light velocity in the medium. Equation 10.56 implies that $|k|$ can possibly be much smaller than $|q_s'|$ and $|q_i'|$, but not larger than their sum. Since $|k|$ is at most of the same order as $|q_s'|$ and $|q_i'|$, the ratio ω/Ω_i is at most of the order of the ratio $c_{acoust}/(c_{light}/n)$ (i.e., at most 10^{-4} to 10^{-5}) for any physical values of c_{acoust} and n). The relative difference $|\Omega_s - \Omega_i|/\Omega_i$ is therefore at most of the same order as $c_{acoust}/(c_{light}/n)$ (see Equation 10.57), as well as the relative difference $|q_s' - q_i'|/q_i'$. The scattering event can therefore be analyzed neglecting the difference between the magnitudes of the two moduli: $q_i' \cong q_s'$ (see Section A). This means that the directions of $\mathbf{q}_i'$ and $\mathbf{q}_s'$ (i.e., the directions of the incident and scattered beams, identify uniquely the scattering configuration and the acoustic wave vector k). In particular, the backscattering geometry ($\mathbf{q}_s' = -\mathbf{q}_i'$, and therefore $\mathbf{q}_s = -\mathbf{q}_i$) maximizes the modulus of k: in this geometry

$$k = 2\frac{2\pi}{\lambda_0}n \qquad (10.58)$$

Equation 10.1 accordingly holds, and $|q_s - q_i|/q_i$ reaches its maximum achievable value of $2(c_{acoust}/c_{light})n$, which is typically of the order of 10^{-5}.

In SBS (i.e., scattering by SAWs), Equation 10.56 holds only for the wave vector components parallel to the surface, due to the breaking of translational invariance in the direction normal to the surface:

$$k_{||} = \pm (q_s - q_i)_{||} \qquad (10.59)$$

Since Snell's law means that upon refraction both $q_{i||}$ and $\mathbf{q}_{s||}$ remain unchanged, Equation 10.59 is conveniently analyzed in terms of the optical wave vectors q_i and q_s outside of the sample. Also in this case their directions determine the acoustic wave vector $k_{||}$. The scattered direction q_s is conveniently taken in the incidence plane, defined by q_i and the normal to the surface. In this case $k_{||}$ also belongs to the incidence plane and

$$k_{||} = q_i(\sin\theta_i - \sin\theta_s) \qquad (10.60)$$

θ_i and θ_s being the incidence and scattering angles, referred to the surface normal. In Equation 10.60 the sign of θ_s indicates forward (positive θ_s) or backward (negative θ_s) scattering. As already noted in Sections 3 and 4 the wave vectors probed by surface scattering do not depend on the refractive index. The very small upper limit for the relative difference $|q_s - q_i|/q_i$ discussed above is even smaller in SBS; in backscattering ($\theta_s = -\theta_i$), again a typical choice since it maximizes $k_{||}$,

$$k_{||} = 2q_i \sin\theta_i = 2\frac{2\pi}{\lambda_0}\sin\theta_i \qquad (10.61)$$

Equation 10.4 accordingly holds, and $|q_s - q_i|/q_i = 2(c_{SAW}/c_{light})\sin\theta_i$, which is always (also for diamond) well below 10^{-4}, down to below 10^{-6}.

Equation 10.58 and Equation 10.61 imply that in transparent or semitransparent samples, in which surface and volume scattering can be simultaneously observed, in backscattering the bulk acoustic waves are probed at wavelength $\lambda_0/(2n)$, while the surface waves are probed at wavelength $\lambda_0/(2\sin\theta_i)$. Since the RW is slower than bulk waves, the spectral contributions from surface waves and from bulk waves are well separated. In any scattering geometry, and for both types of waves, the wave vector k or $k_{||}$ is determined by the scattering geometry; the frequency ω is obtained by the spectrum of the scattered light (see Section B), and the velocity of acoustic waves is immediately derived as ω/k for bulk waves and $\omega/k_{||}$ for SAWs. It can be mentioned that silicon, with a penetration depth for green light of $\approx 1\ \mu m$, is transparent enough to give a good scattering signal from bulk waves; from truly transparent materials, such as glass, the scattering volume for bulk waves is large and gives a signal from bulk waves much more intense than that from surface waves.

10.3.1.2 The Backscattering Configuration

A typical experimental set-up for a SBS measurement in backscattering is shown in Figure 10.6. The laser beam is directed onto the specimen by a small mirror, called here the incidence mirror, and focused onto the specimen surface by a lens, called here the front lens. The same lens also collects the scattered light, transforming the light coming from the focusing spot into a parallel beam that is sent to the spectrometer. Typically, spatial filtering is needed and is provided by a pinhole: the scattered beam is focused onto the pinhole by a lens and can then be reconverted to a parallel beam. On the optical path to the spectrometer a couple of steering mirrors can be inserted to give additional degrees of freedom, which is useful for alignment purposes. A similar configuration is obtained using, instead of the incidence mirror, a larger mirror that deflects all the scattered light with a hole drilled in it, the incident beam passing through the hole.
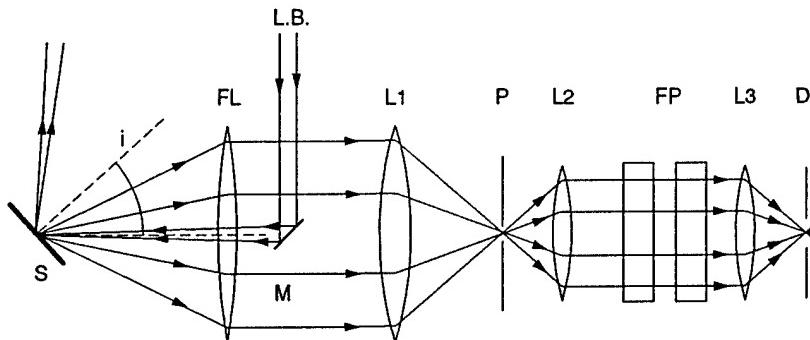
FIGURE 10.6

Experimental setup in backscattering. LB: laser beam; M: mirror; FL: front lens; S: sample, L1, P, and L2: spatial filtering by two lenses and a pinhole; FP: Fabry-Perot interferometer (for simplicity, a single interferometer is shown, instead of the tamdem multipass one); D: light detector.

Beside the maximization of the exchanged wave vector, another advantage of backscattering emerges clearly: a single lens focuses the incident beam and collects the scattered light. In any other scattering geometry two separate lenses must be adopted, and their focal points must coincide to high precision. For this reason other geometries have been adopted in volume scattering,[68] but very rarely in SBS. In volume scattering, due to the finite extension of the waist of the focused incident beam, the requirement of coincident foci is less stringent than in SBS, where the additional requirement of precise coincidence at the surface must be satisfied. Another advantage of backscattering is that, at least for incidence not too close to the normal, the collection direction is far from the specular reflection one, and in the collected beam the amount of light that was elastically scattered is therefore minimized.

Example 1

Determine the range of SAW wavelengths probed in backscattering, with incidence angle varying from 20 to 70°, and with: (a) the $\lambda_0 = 532$-nm light of a frequency-doubled Nd:YAG laser, and (b) the $\lambda_0 = 488$-nm light of the blue line of an Ar ion laser.

SOLUTION

Equation 10.61 states that

$$k_{||} = 2q_i \sin \theta_i = 2\frac{2\pi}{\lambda_0}\sin \theta_i$$

therefore $\lambda_{||} = \lambda_0/(2\backslash\sin\theta_i)$. With $20° \leq \theta_i \leq 70°$, we have $0.342 \leq \sin \theta_I \leq 0.940$. For the two cases, $778\,\text{nm} \geq \lambda_{||} \geq 283\,\text{nm}$ and $713\,\text{nm} \geq \lambda_{||} \geq 260\,\text{nm}$.

Example 2

Estimate the frequencies of bulk acoustic waves (if any) and of SAWs probed in backscattering, with incidence angles of 30° and of 70°, by the $\lambda_0 = 514.5$ nm light of the green line of an Ar ion laser, for a) silicon, b) diamond, c) aluminum.

SOLUTION

From Example 1, the parallel wavelengths probed in backscattering with $\lambda_0 = 514.5$ and $\theta_i = 20°$ and 70°, (i.e., $\sin \theta_i = 0.5$ and 0.94) are $\lambda_{||} = 514.5$ and 273.8 nm. From Equation 10.58 the bulk wavelength probed in backscattering with $\lambda_0 = 514.5$ is $\lambda = \lambda_0/(2n) = 257.2/n$, where n is the refractive index. An estimate of the frequency requires an estimate of the velocity.

In aluminum only the Rayleigh surface wave can be observed. Polycrystalline aluminum is isotropic. From the SBS point of view, if the focusing spot of the incident laser beam is smaller than a single grain, the properties of that grain, which is anisotropic, are mainly probed. However, beside the possibility of focusing close to the grain border, single grain properties can realistically be probed only with grains of several tens of microns. The isotropic properties of polycrystalline aluminum (i.e., $c_S \cong 3$ km/secec [see Chapter 1] and $v \cong 0.35$) are then considered here. It was discussed in Section 10.3.4 that in the isotropic case, $0.87c_S < c_R < 0.96c_S$, with the approximate expression (see Equation 10.50) $c_R = c_S(0.87 + 1.12\,v)/(1 + v)$. This gives respectively $2.61 < c_R < 2.88$ km/secec, and $c_R = 2.80$ km/secec (the uncertainty in c_S, see Chapter 1, limits the precision of this number), meaning $f_{SAW} = 5.44$ and 10.2 GHz.

Crystalline diamond and silicon have cubic anisotropy. Cubic symmetry guarantees the isotropy of quantities like the refractive index, represented by tensors of rank 2, but the elastic behavior is anisotropic. Available values or mass density, elastic constants and refractive index are, for silicon, $\rho = 2.33 \times 10^3$ kg/m^3, $C_{11} = 166$ GPa, $C_{44} = 79.6$ GPa, $C_{12} = 64$ GPa, and $n \sim 4$ (real part), and for diamond[70] $\rho = 3.51 \times 10^3$ kg/m^3, $C_{11} = 1080$ GPa, $C_{44} = 578$ GPa and $C_{12} = 125$ GPa, and $n = 2.43$. In crystalline media the velocities depend on the direction, and the usual formulas for bulk waves, $c_P = (C_{11}/\rho)^{1/2}$ and $c_S = (C_{44}/\rho)^{1/2}$, give the appropriate values only for propagation along the [100] crystalline direction. Similarly, the RW velocity is direction dependent, and the above expressions are no longer valid. A detailed solution of this example would require the analysis of the anisotropic wave velocity. An estimate of bulk velocities can be obtained by the isotropic expressions. It can be noted that, due to the high values of the refractive indexes, for incidence not too far from normal on a (100) face the propagation direction of the probed bulk waves is close to the [100]. It can also be noted that for propagation exactly along the [100] direction the scattering cross section for the shear waves is null. An even rougher estimate for the Rayleigh velocity can be taken as the velocity c_S of the shear wave given by the isotropic formula.

With the above values, $c_s = 5.84$ km/secec and $c_p = 8.44$ km/secec for silicon, and $c_s = 12.83$ km/secec and $c_p = 17.54$ km/secec for diamond. These values of velocity give the following estimates: for silicon, $f_{SAW} = 11.3$ and 21.3 GHz for the two incidence angles, $f_s = 91$ GHz and $f_p = 131$ GHz; for diamond, $f_{SAW} = 24.9$ and 46.9 GHz for the two incidence angles, $f_s = 121$ GHz and $f_p = 166$ GHz.

In reality, observed values of the RW velocity c_{SAW} vary with the propagation direction, and are closer to 5 km/secec for silicon [71] and to 11 km/secec for diamond,[72] with frequencies that are accordingly lower.

10.3.1.3 Other Scattering Configurations

Before proceeding in the present analysis, other types of experimental configurations are briefly mentioned. They have been used in Brillouin scattering measurements, but their applicability is less general than that of the scheme considered here.

Surface enhancement of Brillouin scattering by the excitation of surface plasmon polaritons was theoretically predicted[73,74] and observed.[75,76] This kind of experiment is interesting for the physics because it involves different types of excitations and it gives intense signals. However, it seems to be restricted to the special case of metal films of 40 to 80 nm thickness deposited on transparent substrates.

Brillouin scattering was observed in an optical waveguide, formed by a transparent film surrounded by two media of lower refractive index (including vacuum or air). The light propagates in the film by multiple total internal reflection, and repeatedly interacts with the acoustic wave. In various experiments,[24,77] prisms were exploited to insert the laser beam into the film and then to extract it. It can be mentioned that in the widely used signal transmission in optical fibers (specifically a transparent fiber surrounded by a medium of lower refractive index) Brillouin scattering occurs as an unwanted disturbance to be minimized, since it diverts power from the signal and thus introduces a transmission loss.

For transparent films a simple and effective geometry was developed, which allows simultaneous collection of the backscattered light and light scattered by bulk waves having wave vector parallel to the film surface.[78,79] The technique is applicable to transparent films with a reflecting substrate, or on which a metallic film has been evaporated.

AU: (see Section A): Sections have been renumbered: Are you referring to Sect. 10.3.1? Please confirm

10.3.2 Spectral Analysis

The analysis of Brillouin spectra, and especially of SBS spectra, is not a trivial task. The collected light contains (see Section A) an intense elastic peak at the incident frequency Ω_i and one (or more) weak doublet at frequencies $\Omega_i \pm \omega$. The difficulty arises from the low intensity of the doublet and from its small relative frequency shift. The intensity is several orders of magnitude lower than that of the elastic peak, and the relative spectral shift ω/Ω_i is, for

SBS, well below 10^{-4}, down to 10^{-6} (see Section 1). With green light the incident frequency is ~6×10^{14} Hz and the spectral shift is below 30 GHz. It can be noted that 30 GHz means exactly 1 cm^{-1}, and that typical frequency shifts observed in Raman scattering range from hundreds to thousands of cm^{-1}. The smallness of the frequency shift prevents the analysis by dispersive means such as diffraction gratings; also, the triple grating configurations do not achieve a sufficient resolution.

AU: (see Section 1): Sections have been renumbered: Are you referring to Sect. 10.3.1.1? Please confirm.

Two methods have been exploited to overcome this difficulty: narrow bandwidth tunable band-pass filters and beating or heterodyne methods. Due to the optical frequency range, both types of instruments have to be implemented by optical means. Scanning multipass Fabry-Perot interferometers achieve the required filtering performances, and have become the standard choice. Most of the experimental SBS work published in the last decade was performed by this type of spectrometer, which is described here in some detail. In heterodyne methods the beating is observed, resulting from mixing the collected light with a reference beam. These methods have advantages and limitations. However since the limitations are severe for SBS applications, these applications are seldom used and are briefly outlined at the end of this section.

10.3.2.1 Multipass Fabry-Perot interferometers

The Fabry-Perot interferometer[80] is an optical resonator that transmits only the light of its resonant wavelength, and thus acts as a band-pass filter. Since its resonant frequency is adjustable, it can exploited to scan the spectrum to be measured. Conventional Fabry-Perot interferometers do not achieve the contrast (the ratio of the maximum to the minimum transmissivity) needed to resolve the weak Brillouin doublets, and especially the SBS doublets. Sandercock first showed that the contrast could be significantly improved by multipassing (see below) the interferometer [81]. His demonstration, by a double pass, of the potential of multipassing prompted the development of multipass Fabry-Perot interferometers, with three or five passes[82] with a maximum of seven passes.[83] The usefulness of coupling two synchronized Fabry-Perot, avoiding the overlapping of different orders of interference (see below), was also recognized. Couples of multipass interferometers operated in series were accordingly developed: 3 + 3 passes with synchronous piezoelectric scanning[84] and 5 + 4 passes with synchronization obtained by a single scanning stage common to the 2 interferometers.[85] The latter configuration evolved into the 3 + 3 passes tandem interferometer,[3,12,64] which has become the type of spectrometer most commonly adopted in Brillouin spectrometry. A fully computer controlled version was described recently.[86] For specialized applications requiring extreme resolution, the combination of a plane multipassed Fabry-Perot and a spherical confocal one was also adopted.[87]

The basic principles of the operations of Fabry-Perot interferometers and multipass interferometers are summarized here, from the user's point of view, for readers not familiar with optical instrumentation. Reference is made to

the mentioned configuration, commonly exploited for Brillouin spectroscopy. More detailed discussions can be found in existing excellent reviews, both general[80] and more specific.[3,12]

A single plane Fabry-Perot interferometer is an optical resonator (an optical cavity) formed by two plane parallel partially reflecting mirrors, at distance d from each other. Light enters the cavity through one of the incompletely reflecting mirrors, and is reflected back and forth, part of it being leaked at each reflection; the light leaking from the second mirror is the transmitted light. In the multiple reflection process the intensity of the wavelengths that satisfy the constructive interference condition is enhanced, while all the other wavelenghts eventually interfere destructively and decay. The transmitted light contains only the wavelengths whose intensity in the cavity is high. For light of wavelength λ and frequency $v = c_{light}/\lambda$, entering the resonator with incidence normal to the mirrors, the constructive interference condition for a 'round trip' between the mirrors is $2d = m\lambda$, where m is any positive integer. The equally spaced frequencies $v_m = m(c_{light}/2d)$ are thus selected, the frequency spacing being called the free spectral range: $FSR = c_{light}/2d$. For light entering the resonator with non normal incidence, the resonance condition depends on the incidence angle, and the interferometer acts as a dispersive device, selecting a different frequency for any angle; this configuration is not useful in this context and will not be considered further.

More precisely, for normal incidence on mirrors of equal reflectivity R the phase delay φ between two consecutive round trips is $\varphi = 2d(2\pi/\lambda) = 2d(2\pi f/c_{light})$, and the superposition of the infinite reflections (having decreasing intensity due to incomplete reflection) gives a transmitted intensity

$$I = \frac{I_{max}}{1 + R'\sin^2(\varphi/2)}$$

where $R' = 4R/(1-R)^2$. The shape function $[1 + R'\sin_2(\varphi/2)]^{-1}$ is called the Airy function; it is a set of equally spaced maxima that become sharper for increasing R. Its maxima ($I = I_{max}$) occur for $\varphi/2 = m\pi$, which identify the frequencies f_m mentioned above, and the minima ($I = I_{max}/(1 + R')$ are at halfway between maxima. The ratio of maximum to minimum transmission is called contrast or extinction ratio; it is $(1 + R') = (1 + R^2)/(1 - R^2)$ and diverges when R approaches unity, exceeding 100 for $R > 0.82$ and 1000 for $R > 0.94$. The sharpness of the maxima is also an increasing function of R. The common characterization of sharpness by the full width at half maximum (FWHM) is usually presented in terms of the finesse F, defined as the ratio of the distance $\Delta\varphi = 2\pi$ between consecutive maxima to the FWHM. The Airy function gives a finesse $F = \pi\sqrt{R}/(1 - R)$, which exceeds 30 for $R > 0.9$ and 60 for $R > 0.95$; these values of F can be lowered by imperfections of the mirrors and by geometrical effects like the collection geometry discussed below.

Summarizing, the Fabry-Perot interferometer acts as a band-pass filter, transmitting all the frequencies f_m that are at equal spacing FSR from each other, with bandwidth FSR/F around each of them. High performance filtering requires high values of the finesse F, in order to have a narrow transmitted bandwidth, and of the contrast, in order to have a strong attenuation of the nontransmitted wavelengths. Both parameters are increasing functions of the reflectivity R, and, beside the imperfections, are limited because for values of R too close to unity the maximum transmission declines.

The FSR, and therefore the transmitted frequencies f_m, can be modulated by modulating the distance d between the mirrors. Accordingly, the interferometer can be operated as a spectrometer using one of the transmitted frequencies as a narrow bandwidth band-pass filter, whose frequency is scanned across the spectral interval to be measured.

Operation of the interferometer as a Brillouin spectrometer is accomplished by first adjusting d to a central value $\bar{d}$ such that the incident laser frequency $\Omega_i/2\pi$ is transmitted, and then varying d around $\bar{d}$: $d = \bar{d} + \delta d$. This means that the $\bar{m}$th transmission peak coincides with the laser frequency: $\bar{f}_{\bar{m}} = \bar{m}(c_{light}/2\bar{d}) = \Omega_i/2\pi$ (i.e., $\bar{d} = \bar{m}\lambda_0/2$); the selected FSR is ($c_{light}/2\bar{d}$). Then d is varied, typically by one order of interference (i.e., with $|\delta d| \leq \lambda_0/2 = \bar{d}/\bar{m}$); the extrema of this interval are easily identified by the laser frequency being transmitted again by the $f_{\bar{m}-1}$ and $f_{\bar{m}+1}$ transmission peaks, respectively. By this distance scan the $f_{\bar{m}}$ transmission frequency scans the frequency range $\delta\Omega/2\pi = \pm (\Omega_i/2\pi)/\bar{m} = \pm (c_{light}/2\bar{d}) =$ FSR around $\Omega_i/2\pi$. With frequency shifts to be measured ranging from a few gigahertz to some tens of giaghertz, FSR of tens of gigahertz are the typical choice, meaning distances $\bar{d}$ of a few millimeters. With $|\delta d| \leq \lambda_0/2 = \bar{d}/\bar{m}$ such distances mean that $\bar{d}/|\delta d| = \bar{m} \sim 10^4$. Although the frequency is inversely proportional to the distance, with such small scanning amplitudes the relationship can be linearized: the relative accuracy of the linearized relationship is $|\delta d|/\bar{d} = 1/\bar{m}$ and is acceptable in most cases.

The Fabry-Perot interferometer is thus operated as a narrow band-pass filter that scans the frequency interval of interest. Light is then detected by a photomultiplier; due to the low intensity of SBS doublets, the photomultiplier is typically operated in the single photon counting mode. The distance (i.e., frequency) scan is usually performed by discrete steps. The distance is kept fixed for a given time, with photons being counted and attributed to that channel. The distance is then changed to a new value, and photons are counted and attributed to the new channel. The overall scanning amplitude is typically twice the FSR; the number of channels into which the scan is subdivided should be correlated to the finesse. Since the filtered bandwidth is FSR/F, and since the filter transfer function is an Airy function (which is similar to a Gaussian), if the number of channels is significantly smaller than $2F$, the adjacent channels do not overlap and part of the spectral information is lost. On the other hand, if the number of channels is much higher than $2F$ the adjacent channels strongly overlap, and measurement time is consumed

to collect redundant data. The optimal number of channels is therefore larger, but not much larger, than twice the finesse.

Since the finesse is a parameter of each specific interferometer and is independent of mirror distance, once the number of channels is fixed the only parameter to be chosen for each measurement is the FSR, (i.e., the mirror distance). Since the spectrum is measured in the ± FSR interval, the optimal choice of the FSR requires an estimate of the frequency of the peaks to be measured. The FSR must obviously be larger than the frequency to be measured, but not too much larger. As in any measurement, if the adopted full scale range is too large, the resolution becomes poor. As a rule of thumb, the FSR should not exceed twice the expected value of the frequency that should be measured. When performing sets of measurements, typically when measuring the spectrum at a set of different incidence angles, the practical requirement of not too often changing the mirror distance can lead to a partial relaxation of the above criterion.

As mentioned above, the filtering efficiency is measured by the finesse and the contrast. Measurement of Brillouin doublets has to face the proximity of the elastic peak, with more intense orders of magnitude; the contrast typically achievable by a single Fabry-Perot is not sufficient to effectively filter it off. Multipassing is therefore adopted. Passing the scattered light more times by the same interferometer increases both the contrast and the finesse, although the practically achieved values do not fully reach the theoretical limits (the product of the single-pass contrasts and the sum of the single-pass finesses). Similarly, tandem interferometers are adopted because in a single interferometer transmission simultaneously occurs by the $f_{\bar{m}}$, $f_{\bar{m}-1}$, and $f_{\bar{m}+1}$ transmission peaks, resulting in overlapping shifted replicas of the same spectrum and making the interpretation of the spectra more difficult. Two interferometers having slightly different FSR can be synchronously scanned, keeping their $f_{\bar{m}}$ transmission peaks coincident, with a high overall transmissivity; due to the different values of the FSR, if the $f_{\bar{m}}$ transmission peaks coincide and the $f_{\bar{m}-1}$ and $f_{\bar{m}+1}$ peaks of the two interferometers do not coincide, each of the interferometers cancels these transmission peaks of the other, avoiding replication of spectra.

In practice, full consideration of the detailed operation of a tandem multipass interferometer is not required. Such an interferometer, when properly synchronized, behaves as a peculiar single interferometer in which transmission from adjacent orders is almost completely suppressed, and which achieves high values of contrast and finesse, not realistically achievable by a single pass. The not perfect suppression shows up by the partial transmission of the intense laser light. This occurs at the extremes of the FSR, when only one of the interferometers does not transmit the laser frequency, giving rise to the instrumental ghosts typical of Fabry-Perot spectrometers. These ghosts, at ± FSR, can be usefully exploited for calibration purposes once the distance among the mirrors is known. Operationally, for each measurement two parameters have to be set: the number of channels and the FSR. The number of channels being optimally set at or above twice the finesse, and

the finesse achievable by a multipass Fabry-Perot being of the order of 100, numbers of channels of 256 or 512 are typical choices. The FSR should instead be set, exactly as for a single-pass interferometer, above the expected frequency of the spectral feature to be measured, but not above twice or three times it.

It should finally be mentioned that operational modes slightly different from that outlined here can be useful for specific applications. For instance, frequency scanning by more than one FSR can be useful for high accuracy measurement of a peak frequency, when this frequency is already approximately known.[70]

Example 3

Evaluate the mirror distances to be adopted for the measurement of SAWs and respectively bulk acoustic waves (if any), for measurements performed in backscattering, with incidence angles of 30 and of 70°, by the $\lambda_0 = 514.5$-nm light of the green line of an Ar ion laser, for (a) silicon, (b) diamond, (c) aluminum.

SOLUTION

The evaluation is a straightforward consequence of the estimates of Example 2. Since FSR = $c_{light}/2d$ and, in the most common case, the FSR coincides with the full scale range of the measurements, d is immediately obtained keeping in mind that the numbers obtained in example 2 were only estimates. In order to observe the bulk waves in silicon and diamond, appropriate choices of the FSR could be at least 150 and 200 GHz, meaning a d of at most 1 mm and 0.75 mm, respectively. With these values of the FSR the RW can still be observed, but with a relatively poor resolution. In order to better measure the RW of the three materials, more appropriate choices of the FSR could be around 60, 30, and 15 GHz respectively, meaning a d of 2.5, 5, and 10 mm.

10.3.2.2   Optical Beating Methods

Optical beating methods are based on the heterodyne detection technique.[88] The scattered light is mixed, by beam splitters, with a reference beam derived from the incident beam, and the beating resulting from the interference of the two beams is observed. The measured signal is accordingly shifted to a frequency accessible by high-speed optical sensors, and frequency resolution becomes possible, which is much better than that achieved by optical filtering. After the method was first proposed, the first observation of a spectrum containing a Brillouin doublet from bulk waves was limited to frequencies below 100 MHz. A variant of the method achieved very high resolution, but remained limited to a few hundred megahertz. Scattering by surface waves was later observed in this frequency range. The upper frequency limit was extended to 800 MHz and to 1.7 GHz; more recently, by a more complex superheterodyne technique[89] a frequency range extending from 10 MHz

to 3 GHz, with very high frequency resolution, was achieved. The optical beating methods intrinsically have a very small collection solid angle; since the collected light must interfere with a reference beam, its wave vector q_s must have a well-defined direction. This gives a good q_s resolution and allows the good frequency resolution, but with the usually weak surface scattering signals the larger collection angle allowed by filtering methods is typically necessary to gather a sufficient signal. The optical beating methods remain essentially devoted to transparent media, either solid or liquid.[88]

10.3.3   Nonideality of the Scattering Configuration

A further step in the analysis of the experimental setup involves the consideration of its geometrical nonidealities, which are at the origin of experimental uncertainties and of the broadening of spectral peaks. The analysis is presented mainly with reference to the case of backscattering from SAWs. Indications concerning scattering by SAWs in other geometries and scattering by bulk waves are also given.

10.3.3.1   Geometrical Imperfections

First, for the scattering geometry, the values of the incidence and scattering angles (see Equation 10.60) are known with finite accuracy. For both volume and surface scattering the backscattering configuration exploiting a single lens is better suited to minimize this error.[45,69] Once the alignment of the incidence mirror and the front lens is carefully performed (see next section) the coincidence of the incident and scattered direction is automatically obtained, and the measurement uncertainties concern only the incidence angle θ_i. A given θ_i is obtained by specimen rotation from a reference position. Rotators are available by which rotations can be performed and measured with accuracy better than 0.1 mrad; the error in θ_i is essentially the error in the identification of the reference position. A practical reference position is normal incidence, identified by the perfect superposition of incident and reflected beams. By common procedures the exact superposition is typically found with an uncertainty in θ_i of at most $\delta\theta_i \cong 0.2° \cong 3.5$ mrad.[90] This means a relative uncertainty in $k_{||}$ of (see Equation 10.61) $\delta k_{||}/k_{||} = (\partial k_{||}/\partial\theta_i)\,\delta\theta_i/k_{||} = \delta\theta_i/\tan\theta_i$, which is nearly 1% at $\theta_i = 20°$, decreases to 0.6% at $\theta_i = 30°$, and falls to 0.13% at $\theta_i = 70°$. This uncertainty contributes to the uncertainty of the measured velocity. Its reduction requires some specific setup, (e.g., a sufficiently long optical path with pinholes). The uncertainty $\delta\theta_i$ can thus be lowered to around 0.5 mrad, meaning that the relative uncertainty $\delta q_{||}/q_{||0}$ is reduced to 0.14% at $\theta_i = 20°$ and 0.1% at $\theta_i = 30°$, down to 0.02% at $\theta_i = 70°$.

10.3.3.2   Finite Collection Angle

In the outline presented above the wave vectors q_i and q_s were implicitly treated as perfectly determined vectors, implying a perfectly defined wave vector $k_{||}$. In reality, as it is discussed below and as it can be seen from

Figure 6, both q_i and q_s lie within cones around their nominal values and correspond to a whole range of wave vectors $k_{||}$.

The incident beam is focused onto the sample, because otherwise the optical power density is not sufficient to give a detectable scattered signal. Due to the finite width of the laser beam, after focusing the incident beam contains all the wave vectors of given $|q_i|$ lying in a cone around the nominal incidence direction. More importantly, the front lens collects scattered light with all the directions of q_s falling within the solid angle Ω delimited by the lens aperture (i.e., with all the wave vectors within a cone around the nominal collection direction; see Figure 10.6). Due to the small width of the laser beam the spread of q_i is a minor effect, while the spread of q_s can be significant, since a wider collection angle means a higher signal intensity. A sufficiently accurate analysis can be performed considering only the spread of q_s.

A first consideration concerns the axis of the collection cone, (i.e., the nominal scattering direction). The normal incidence can be identified as mentioned above by the perfect superposition of incident and reflected beams, but can also be found with superposed beams not passing through the center of the front lens. In that case the axis of the collection cone, which passes through the center of the lens, does not coincide with the incidence direction: backscattering is not perfectly achieved, an error $\delta\theta_s$ being present in the scattered direction alone. This error gives a relative uncertainty in $k_{||}$, evaluated for a fixed θ_i, of (see Equation 10.60) $\delta k_{||}/k_{||} = (\partial k_{||}/\partial\theta_s)\, \delta\theta_s/k_{||} = \delta\theta_s/(2\tan\theta_i)$. The same type of error occurs when the alignment of the collected light beam with the optical axis of the interferometer is not perfect. If this is the case, the finite apertures on the optical path of the interferometer can clip the light beam asymmetrically with respect to the beam axis. The light that is eventually analyzed is collected not symmetrically around the incidence direction.

This type of error is not easily detected, although it can be significant. An iris diaphragm mounted on the front lens can be of great help in the procedure of centering the beams.

A second consideration concerns the aperture of the collection cone. The lens, of numerical aperture N.A., collects all the wave vectors q_s whose direction differs from the nominal one by an angle smaller than $\gamma_{lens} = \arctan[1/(2\ \text{N.A.})]$; with a lens of aperture f/2 the collection cone has a semiangle $\gamma_{lens} \sim (1/4)$ radian $\sim 14°$, which is reduced to $\gamma_{lens} \sim (1/11)$ radian $\sim 5°$ for a lens of aperture f/5.6. When a wide lens aperture is adopted the whole optical path, also within the interferometer, should be considered. Other finite apertures can be present, which can limit the collected light beam to a diameter smaller than that accepted by the front lens.

The wave vectors q_s belonging to the collection solid angle Ω are the outcome of interactions with SAWs whose wave vectors $k_{||}$, determined by Equation (59), belong to a whole region in the $\mathbf{k}_{||}$ plane [4,90]. This region is symmetrically located around the incidence plane; the average $<k_{||}>_\sigma$ of the wave vectors belonging to it can be computed integrating over the solid

angle Ω and weighting each value of $k_{||}$ by the corresponding cross section $d\sigma/d\Omega$, which is a function of both q_i and q_s.[90]

$$\left\langle k_{||} \right\rangle_\sigma = \frac{\int_\Omega (q_i - q_s)_{||} \dfrac{d\sigma(q_i,q_s)}{d\Omega}}{\int_\Omega \dfrac{d\sigma(q_i,q_s)}{d\Omega}} \tag{10.62}$$

The cross section for scattering by the ripple effect alone from an isotropic solid can be expressed in closed form.[20,90,91] If the elasto-optic mechanism is not negligible, the cross section is instead a function of the strain field within the material, and its evaluation is computationally much more expensive and requires the elasto-optic coefficients of the material, which are seldom known. An average value $<k_{||}>_g$, which only takes into account geometric effects,[90] can be computed in a simpler way by ignoring the dependence of $d\sigma/d\Omega$ on k_s: $<k_{||}>_g = \frac{1}{\Omega}\int_\Omega (q_i - q_s)_{||} \, d\Omega$. In this integration, as well as in that of Equation 10.62, the small solid angle intercepted by the incidence mirror (or by any other means exploited to direct the incident beam onto the sample) should be eliminated from the integration solid angle; the scattered light impinging on it is reflected back towards the laser and is not collected.[4]

It should be noted that the relationship between q_s and $k_{||}$ is nonlinear, since it involves a projection, (i.e., a trigonometric function). As a consequence, although the collection cone has perfect rotation symmetry around the nominal collection direction, meaning that the average collection direction coincides with the nominal one, the averages $<k_{||}>_\sigma$ and $<k_{||}>_g$ do not coincide with the nominal value of $k_{||}$, given by Equation 10.61. Due to the reflection symmetry with respect to the incidence plane the averages $<k_{||}>_\sigma$ and $<k_{||}>_g$ still belong to the incidence plane itself, but their modulus is not exactly given by Equation 10.61. The difference can be appreciated in simplified way evaluating $<k_{||}>_g$ by considering, instead of the whole solid angle Ω (Equation 10.62), only the collected wave vectors belonging to the incidence plane. This subset of collected wave vectors is significant, because it includes the minimum and the maximum of all the collected k_s, and is easily analyzed, because it is the set of wave vectors for which Equation 10.60 holds. It is the set of wave vectors for which θ_s lies in the interval $(-\theta_i - \gamma_{lens}, -\theta_i + \gamma_{lens})$; accordingly, the values of $k_{||}$ are spread over the interval

$$\frac{2\pi}{\lambda_0}(\sin\theta_i - \sin(-\theta_i \pm \gamma_{lens})) \cong 2\frac{2\pi}{\lambda_0}\sin\theta_i\left(1 \pm \frac{\gamma_{lens}}{\tan\theta_i}\right) \tag{10.63}$$

$$\left\langle k_{||} \right\rangle_g = \frac{2\pi}{\lambda_0}\frac{1}{2\gamma_{lens}}\int_{-\gamma_{lens}}^{\gamma_{lens}} (\sin\theta_i - \sin(-\theta_i \pm \gamma))d\gamma = 2\frac{2\pi}{\lambda_0}\sin\theta_i\left[1 \pm \frac{1}{2}\left(\frac{\sin\gamma_{lens}}{\gamma_{lens}} - 1\right)\right] \tag{10.64}$$

and the relative difference between this value and the nominal one given by Equation 10.61 is

$$\frac{1}{2}\left(\frac{\sin\gamma_{lens}}{\gamma_{lens}} - 1\right) = -\frac{1}{12}\gamma_{lens}^2 + \frac{1}{240}\gamma_{lens}^4 + \cdots \quad (\gamma_{lens} \text{ in radians})$$

which does not depend on θ_i and can be not negligible when the best accuracy is needed with wide lens apertures. Similar conclusions are reached by the full integration of Equation 10.62.[90]

10.3.3.3 Instrumental Peak Width

The finite collection aperture also gives the main contribution to the instrumental width of the spectral peaks. An estimate is straightforwardly obtained in the simple case of a SAW propagating with velocity c_{SAW} independent of wavelength (a nondispersive SAW). In this case each collected wave vector corresponds to a circular frequency $\omega = c_{SAW}|k_{||}|$, and the spread of the frequencies is simply proportional to the spread of wave vectors given by Equation 10.63. In a more detailed analysis, still in the case of a SAW propagating with velocity c_{SAW} independent of wavelength and of the propagation direction, the actual spectrum of the collected light can be predicted by a procedure analogous to the integration of Equation 10.62.[4,90] The collection angle Ω is subdivided in infinitesimal angles $d\Omega$, each one corresponding to a specific direction of q_s (i.e., to a specific value of $k_{||}$). Each infinitesimal angle contributes to the spectrum of the collected light an elemental peak centered at $\omega = c_{SAW}|k_{||}|$. The superposition of all the elemental peaks, possibly weighted by the corresponding scattering cross sections, supplies the spectrum of the collected light.

If the SAW velocity depends on wavelength or on the propagation direction, the spread in the value of the velocity further contributes to the spread of the frequencies of the elemental peaks. Other minor contributions to spectral broadening come from the finite width of the laser beam and from its finite spectral purity. In the above prediction procedure, if the intrinsic width of the spectral line corresponding to the acoustic mode is small, the width of each elemental peak is negligible, and the width of the measured peak is essentially the instrumental width. If instead the spectral line is broadened, by, for example, scattering or damping processes, each elemental peak has a finite width, and the width of the measured peak is the outcome of both the intrinsic and the instrumental width. This should be taken into account when the line width has to be measured (e.g., to assess damping coefficients).

A slit is sometimes inserted in the collected light beam.[4] The collection solid angle is thus reduced, achieving a significant reduction of both the difference between the average and the nominal $k_{||}$ and the spread of $k_{||}$. The instrumental peak width is thus significantly reduced, at the cost of a

significant reduction of collected intensity, meaning an increase in measurement times.

For scattering by bulk waves the situation is slightly different. Projection of the wave vectors onto the surface is not involved; this implies that because of the perfect rotational symmetry of the collection cone around the nominal collection direction, the exchanged wave vectors are distributed with cylindrical symmetry around the nominal one. The average exchanged wave vector $<k>$ has therefore the same direction as the nominal one. However all the wave vectors in the collection cone, except the nominal one, are not perfectly opposite to the incident wave vector, meaning that the exchanged wave vectors have a modulus slightly smaller than the nominal one (see Equation 10.56). Therefore the finite collection angle causes a broadening of the spectral peak, with a shift in its center of mass.[80]

10.3.3.4 Measurement Accuracy

The overall precision and accuracy can be assessed by summarizing the above observations. First, the scattered intensity is measured by photon counting after narrow band-pass filtering by the Fabry-Perot interferometer (see above). Due to the weakness of Brillouin doublets the count rates can be very small (count rates of tens of counts per seconds are not rare) such that the total count numbers can be rather low. With low count numbers the intrinsically statistical nature of photon counting has evident consequences. For each channel of the spectrum analyzer the photon count n is a statistical variable; since the intensity is stationary it is the outcome of a Poissonian process which has an intrinsic variance of $\sqrt{n}$. The relative variance $\sqrt{n}/n$ is therefore a slowly decreasing function of the count number. This gives the spectra a granular or noisy appearance; the relative amplitude of the noise band in the spectra can only be decreased by increasing the measurement time. Since the decrease is slow, the advantage of a better definition of the spectrum has to be assessed against the increased measurement time. The central frequency ω of a spectral peak is typically found by fitting a predetermined line shape; the uncertainty $\delta\omega$ associated with the fitting procedure

can typically be obtained by the procedure itself. It was mentioned in Section 1 that the most efficient number of spectral channels is of the order of twice the finesse. The uncertainty in the identification of the central frequency of a peak is typically below one channel, meaning that with a finesse of the order of 100 the uncertainty in the frequency measurement due to the photon counting process is of the order of a fraction of a percent. This uncertainty, although immediately evident, may not be the main cause of uncertainty. A comparable uncertainty comes from the calibration of the frequency scale. The most common calibration procedures are the measurement of a reference peak of known frequency and the attribution of the FSR frequency to the position of the ghosts. Both procedures involve the determination of the position of a spectral feature, which is affected by the same type of uncertainty discussed above.

Geometrical imperfections, whose effect is intrinsically deterministic, must also be analyzed in statistical terms because imperfections are, by definition, not known. If θ_i is measured with an uncertainty for which an upper bound $\delta\theta_i$ can be assigned, the value of $k_{||}$ is known to a relative uncertainty, which in backscattering is $\delta k_{||}/k_{||} = \delta\theta_i/\tan\theta_i$, as shown above. The backscattering geometry is generally the configuration that optimizes the accuracy of $k_{||}$. Remembering that $k_{||} = q_i \times (\sin\theta_i - \sin\theta_s)$ (Equation 10.60), where θ_i is positive and θ_s is taken positive in forward scattering and negative in backward scattering, in the latter case $k_{||}$ is the sum of two terms of the same sign (in particular in backscattering $\theta_i = -\theta_s$ and the two contributions have identical weight); in forward scattering $k_{||}$ is significantly smaller, being the sum of two terms of the opposite sign. Since the uncertainties $\delta k_{||}$ are the same, the relative uncertainty $\delta k_{||}/k_{||}$ is much worse in forward scattering. Furthermore, all the configurations other than backscattering require separate incidence and collection optics, introducing additional error causes.

The finite collection angle has the deterministic effect discussed in Section 2. It leads to a spread of the $k_{||}$ values (Equation 10.63), which affects the precision, since it increases the uncertainty in the identification of the central frequency of the spectral peak. More importantly, it affects the accuracy, because the average exchanged wave vector $<k_{||}>_g$ or $<k_{||}>_\sigma$ is shifted from the nominal one $k_{||0}$ (Equation 10.64)). The relative difference can reach 0.5% for an f/2 lens aperture, and is reduced well below 0.1% for an f/5.6 lens aperture. As discussed in Section 2, this shift can be computed and corrected for; it can also be strongly reduced by the adoption of a slit. However, in the case of the slit the simple estimates of Equation 10.63 and Equation 10.64 are no longer fully significant, because the subset of wave vectors considered by these equations is no longer fully representative, and the full computation of $<k_{||}>$ must be considered.

Since $c_{SAW} = \omega/k_{||}$, uncertainties $\delta\omega$ and $\delta k_{||}$ induce velocity uncertainties δc_{SAW} of the measured velocity such that $|\delta c_{SAW}/c_{SAW}| = |\delta\omega/\omega|$ and $|\delta c_{SAW}/c_{SAW}| = |\delta k_{||}/k_{||}|$. The geometrical causes of bias and uncertainty are summarized and quantitatively evaluated in Table 10.1. Geometrical imperfections give relative uncertainties $|\delta v/v|$ proportional to $1/\tan\theta_i$, and are

TABLE 10.1

Summary of the Geometrical Sources of Error in SBS Measurements

Cause	Effect	Primary Uncertainty	Velocity Uncertainty $\delta c/c$ (%)
Error in θ_i: $\delta\theta_i$	$\delta k_{||}/k_{||0} = \delta\theta_i/\tan\theta_i$	$\delta\theta_I = 0.5 \div 3.5$ mrad	0.09 ÷ 0.61 ($\theta_i = 30°$)
			0.02 ÷ 0.13 ($\theta_i = 70°$)
Error in θ_s: $\delta\theta_s$	$\delta k_{||}/k_{||0} = \delta\theta_s/(2\tan\theta_i)$	$\delta\theta_s = 5 \div 10$ mrad	0.43 ÷ 0.86 ($\theta_i = 30°$)
			0.09 ÷ 0.18 ($\theta_i = 70°$)
Collection angle	$<k_{||}> \neq k_{||0}$	Lens aperture = f/2 ÷ f/5.6	0.1 ÷ 0.5

therefore more severe at small θ_i. In Table 10.1 estimates are given at the extremes of the commonly adopted interval $\theta_i = 30° \div 70°$. It can be noted that at large incidence angles and for the lower bounds of the primary uncertainties (meaning accurate alignment and positioning procedures) the uncertainties in the velocity indicated in Table 10.1 are smaller than the intrinsically statistical ones, which have therefore a dominant role. Instead, for small incidence angles and for the upper bounds of the primary uncertainties (meaning not very accurate alignment and positioning procedures) the uncertainties of Table 1 are larger than the statistical ones, and are therefore the limiting factor for measurement accuracy.

10.3.4 Derivation of the Elastic Constants

A single Brillouin spectrum gives the circular frequencies ω of the observable spectral peaks. As discussed in Section 10.3.1.1 the scattering geometry and the laser wavelength fully determine the wave vector $k_{||}$ exchanged with SAWs (see Equation 10.61) for the backscattering case), while the wave vector k exchanged with bulk waves also depends on the refractive index n (see Equation 10.58) for the backscattering case). The velocities of SAWs and of bulk waves are immediately obtained as $\omega/k_{||}$ and ω/k, respectively. Different values of k can be obtained by different scattering geometries, but this is seldom necessary since the bulk wave velocities do not depend on the modulus of k, although they can depend on its direction. Different values of $k_{||}$ are obtained with the same backscattering geometry by simply changing the incidence angle. The dispersion relation $c_{SAW}(k_{||})$ is thus measured, and this is often useful since SAW velocities can depend on $k_{||}$. However, since measurements with an incidence angle close to zero are not practical (elastically reflected light becomes very intense because the scattered direction is too close to the specular reflection, and the effect of geometrical inaccuracies becomes more relevant, see Section 10.3.3.), with the standard configuration the range of $k_{||}$ that can be explored does not exceed a factor of 3. An experimental procedure to overcome this limitation was recently developed.[92]

Scattering by bulk waves has been extensively used to measure the elastic properties and the elasto-optic constants of bulk samples of nonmetallic materials.[45,69,70,93] In the simplest case of isotropic materials the velocities of longitudinal and transverse (primary and secondary) waves are simply given by $\sqrt{C_{11}/\rho}$ and $\sqrt{C_{44}/\rho}$, respectively, and the two moduli are immediately obtained when both the P and S peaks are measured, and when the mass density is known. For crystalline materials the number of independent elastic constants is higher, and measurements with different directions of k, possibly requiring crystals with different cuts, can be needed.

The analysis of scattering by SAWs depends on the nature of the sample. The cases of the semi-infinite homogeneous medium and of a supported film are the most relevant, and are considered here. It must be remembered (see Section 10.3.1.1) that in backscattering the bulk waves are probed at wavelength $\lambda_0/(2n)$ (see Equation 10.58), which is a fraction of a micrometer, and

that SAWs are probed at parallel wavelength $\lambda_0/(2\sin\theta_i)$ (see Equation 10.61), which is larger but still smaller than a micrometer (with the usually adopted green light and with incidence not too close to normal). In supported films having thickness larger than a couple of micrometers, or even less, these wavelengths imply that bulk waves are already fully present and can be detected if the film is transparent enough. They also imply that since the decay depth of the RW is the same as the wavelength, the displacement field of the RW hardly reaches the substrate, meaning that such a wave is almost unaffected by the substrate. In other words, when the film thickness exceeds 1 Im, or little more than that, the presence of the substrate becomes irrelevant, and the data analysis can be performed as for a semi-infinite medium (i.e., a bare substrate).[7,72,94] Accordingly, a precise value of thickness is not needed, while the limitation of the scattering volume, due to the finite film thickness or to the limited transparency of the material, causes a peak broadening, but not a spectral shift. An exception occurs when high order resonances can be measured.[92]

It must also be remembered that the RWs that are detected propagate in the outermost layer, of depth of the order of 1 Im, and their behavior is determined by the properties of the material in this outermost layer. If, in a nominally homogeneous material, a gradient of material properties is present in the outermost layer, the sample is better schematized by one or more films, of different properties, on a substrate.

In the semi-infinite medium case the propagation velocity does not depend on the modulus of $k_{||}$, but can depend on its direction if the material is anisotropic. In the case of a film of thickness h the propagation velocity also depends on the modulus of $k_{||}$, namely through the nondimensional product $k_{||}h$. In both cases the dependence can be computed, as indicated in Section 5. Sets of velocities $c_i^{comp}(C_j)$ can be computed as a function of one or more free parameters C_j (typically, but not necessarily, elastic moduli), the index i typically standing for a set of values of $k_{||}h$ or a set of propagation directions (see below). If, for the same set of values of $k_{||}h$ or of propagation directions, the velocities c_i^{meas} are measured, and the free parameters are determined by a standard least squares minimization procedure. The sum of squares is computed

$$\chi^2(C_j) = \sum_i \left(\frac{c_i^{comp}(C_j) - c_i^{meas}}{\sigma_i} \right)^2$$

where it has been assumed that the variances σ_i of each c_i^{meas} can be individually estimated; according to standard estimation theory the minimum of $\chi^2(C_j)$ identifies the most probable values ($\overline{C}_j$) of the parameters in the (C_j) space, and the isolevel curves of the ratio $\chi^2(C_j)/\chi^2(\overline{C}_j)$ identify the confidence region at any predetermined confidence level.[95,96] As discussed below for some cases, in some instances a well-defined minimum of $\chi^2(C_j)$ is found, allowing a good identification of the parameters,[96–98] while in other

cases a broad minimum is found, in the shape for instance of a valley. In such cases a good identification of the parameters is not possible,[57,99,100] although sometimes some combination of the parameters can be identified with better precision than the individual parameters.[57,97,98] It was also shown that in some cases two significantly different sets of elastic constants fit the measured dispersion relation in a comparable way.[101]

The poor or good identification of the minimum of $\chi^2(C_j)$ depends on the amount of available information. When a single acoustic mode is detected, the values of $\chi^2(C_j)$ can remain low in a relatively wide region in the (C_j) space, meaning that the precision in the measurement of $\chi^2(\overline{C}_j)$ is poor. If additional information is obtained by the measurement of one or more other (surface or bulk) acoustic modes the precision in the measurement of the parameters can be significantly improved.[72,97–99,102–106] In these cases the minimization procedure can be split; if one of the modes allows a good determination of a first parameter, the others can be determined assuming a fixed value of the already identified one.[107] In other cases the relatively wide region in which $\chi^2(C_j)$ is not far from its minimum value has been delimited by imposing some physical acceptability criterion, like imposing an upper limit for the value of the bulk elastic modulus at the value of diamond.[108,109] In some cases a fixed value of Poisson modulus was imposed *a priori*.[6] It can be noted that several published works only give the values of the parameters obtained by the minimization procedure, without presenting an analysis of the precision and reliability of the results.

It must also be noted that this least squares identification procedure is essentially independent of the technique by which the c_i^{meas} are measured, and the analysis of data obtained by, for example, acoustic microscopy (see Chapter 11) proceeds in the same way.[110] Differences are at most quantitative: acoustic microscopy operates at wavelengths that are two orders of magnitude larger than those probed by Brillouin spectroscopy, making its sensitivity to thin films is much smaller.

The two cases of the semi-infinite homogeneous medium and of the supported film are discussed in more detail in the two following sections. It can be mentioned that Brillouin scattering has been exploited also in other cases such as LB films[111] and buried layers in silicon-on-insulator structures.[112] In addition, besides the determination of elastic constants in mesoscopically compact films, other applications have included the analysis of the transition between nonpropagating and propagating excitations in cluster assembled films.[113]

10.3.4.1 Semi-Infinite Medium

In a semi-infinite homogeneous medium (as noted above, a supported film having thickness of little more than 1 Im already behaves as a semi-infinite medium), the translational invariance is broken only by the free surface, and the sample has no intrinsic length scale; consequently, for any acoustic mode, the velocity is independent of the wavelength. Measurements at different

values of $k_{||}$, which in backscattering means measurements at different inci-
dence angles, are useful only because they allow detection of the modes
whose frequency scales as $\sin\theta_i$, allowing the identification of the modes.
Apart from this, measurements at various values of $k_{||}$ only give the same
improvement in precision, coming from repeated measurements, that would
be obtained by repeated measurements at the same $k_{||}$. Beside bulk waves,
a semi-infinite homogeneous medium supports the RW and, as noted in
Section 10.3.1.1., in sufficiently transparent materials in which the elasto-
optic scattering mechanism is dominant, the so-called LGM, a mode travel-
ling parallel to the surface, can also give a spectral peak.[72] In isotropic
materials this mode has the same velocity as the longitudinal bulk wave,
and directly supplies the value of the C_{11} elastic constant, or, if the longitu-
dinal bulk wave is also measured, the values of C_{11} and of the refractive
index n. In isotropic materials the Rayleigh velocity only identifies a combi-
nation of the elastic constants, and approximate expressions are often used
(see Section 10.3.4); exact expressions for specific crystalline symmetries have
also been used.[114] In anisotropic materials the dependence of the Rayleigh
velocity on the propagation direction gives access to individual values of
the constants.[8,10,94] If bulk waves can also be measured, the additional infor-
mation improves the precision and the number of constants that can be
determined, up to the determination of the whole set of elastic constants,[7,72,94]
also in a low-symmetry case.[115] The dependence of the effective elastic con-
stants on the propagation direction and on the position in the film has also
been exploited to explore internal stresses.[79]

10.3.4.2 Supported Film

In a sample formed by a substrate and a supported film the film thickness
h identifies a specific length scale, and the propagation velocity depends on
the ratio of the acoustic length to h. This is typically expressed as a depen-
dence of the acoustic velocity on the nondimensional product $k_{||}h$, and the
behaviour of the semi-infinite medium of the film material is asymptotically
approached for high values of $k_{||}h$. Measurements at different values of $k_{||}$
allow measurement of the dispersion relation $c_{SAW}(k_{||}h)$. As noted at the
beginning of Section 10.3.4, in backscattering the accessible range for $k_{||}$ does
not exceed a factor of 3. In order to explore a wider range of $k_{||}h$, in some
cases sets of films of different thicknesses have been used.[95,102,107,116] The
independence of film properties on thickness is assessed checking that the
parts of the dispersion relation measured on different samples fall on the
same curve. This procedure was adopted also for unsupported films.[117] In
other cases, in which the dependence of film properties on thickness was
precisely the objective of the investigation,[109] this procedure could not be
adopted.

   As discussed in Section 10.3.1.1, in the case of a supported film, various
types of modes can be present, according to the properties of the film and
the substrate and to film thickness. As already discussed in Section 10.3.4,

the quality of the information that can be obtained on the film material depends on the amount of information obtained from the observed acoustic branches. In addition to the RW modified by the presence of the film (modified Rayleigh wave), which is generally present, further information has been gained by the detection of the LGM.[107,108] or of Sezawa or other modes.[10,95,103,105,116] The information that can be obtained from the modified Rayleigh wave was assessed in a model case (isotropic film on silicon substrate) by a sensitivity analysis.[118] It was found that the modified RW velocity is most sensitive to the values of the Young modulus and the shear modulus, meaning that both moduli can be determined with good precision, but least sensitive to the Poisson's ratio v, the bulk modulus B, and the C_{11} elastic constants, meaning that these parameters remain poorly determined. It was also found that the sensitivity to the film thickness and mass density is not high, meaning that for the identification of the elastic moduli an extreme accuracy in the measurement of thickness and density is not crucial. It was finally found, considering the possible detection of a second branch, that the LGM significantly contributes to the determination of v and B, while the first Sezawa mode does not. These results justify the adoption of physical plausibility limits for v and B, by which the Young modulus and shear modulus could be determined for films of thickness down to a couple of nanometers.[100,109]

In a case of a semitransparent layer on a solid, treated by a number of authors,[20–22,24,25] the full calculation requires a knowledge of the complex refractive indices and elasto-optic constants of the layer and substrate (which are not always readily available) and the near-surface dynamics, and takes account of the interference between ripple and elasto-optic scattering.[119] Where elasto-optic scattering plays a minor or subsidiary role, SBS spectra can often be semiquantitatively understood with just a knowledge of the surface dynamic response. In particular, the positions (but not the intensities) of the RW and Sezawa peaks are independent of the scattering mechanism. Interestingly, when elasto-optic scattering predominates, the dip in the Lamb shoulder at the P threshold reverses and becomes a peak very close to the P threshold, called the LGM.[46]

10.4 Case Studies in Surface Brillouin Scattering

Representative results obtained by SBS are reviewed in this section. As was mentioned in the introduction, SBS measures SAW velocities in the frequency range from a few GHz to 30 GHz with a lateral resolution of the order of several microns; the area subjected to the measurement is the focusing spot of the incident laser, which can be as small as ~ 5 µm on the focal plane. Within this area, light interacts with acoustic waves of submicrometric wavelength.

The frequency range and spatial resolution determine the potential for SBS applications in nondestructive evaluation.

The ability to measure SAWs at high frequency has allowed the characterization of the elastic properties of the submicrometric films widely used in modern high-tech industry.[109] The high spatial resolution allows the study of the elastic properties of very small samples. A good example is offered by the new superhard phases synthesized at high pressure and high temperature (high P-T). The samples obtained by this technique are often not homogeneous and consist of several phases having different elastic properties and dimensions ranging from tens to hundreds of microns. The SBS technique is ideally suited for characterizing such specimens.[106]

10.4.1   Selected Results for Isotropic Bulk Solids

As already discussed in Section 10.3.4, in the supported films whose thickness exceeds about 1 Ìm, the behavior of SAWs is completely analogous to the behavior in semi-infinite media. The ability of Brillouin scattering to perform local measurement allows the characterization of very small samples. This is particularly relevant for materials, such as the new superhard materials obtained from fullerenes at high temperatures and pressures, which can be obtained only as extremely small specimens.

The discovery of the fullerene molecule C_{60} has led to extensive experimental studies of amorphous and nanocrystalline carbon phases in both bulk[19] and thin film[120] forms. Heating C_{60} at pressures above 8 GPa results in formation of 3-dimensional polymerized amorphous phases of C_{60}, and has fueled the debate on the existence of ultrahard fullerene-based phases with hardness higher than diamond.[121] Superhard phases can be obtained only in very small sizes, and they are opaque; Brillouin spectroscopy has allowed their elastic characterization. Manghnani et al.[106] reported the successful SBS measurements of the elastic properties of the superhard amorphous carbon synthesized from C_{60} under high pressure (13 to 13.5 GPa) and high temperature (800 to 900°C). The SBS spectra obtained from 2 bulk amorphous carbon (a-C) samples synthesized from C_{60} fullerite powder are shown in Figure 10.7. Surface scattering from the RW, at an incidence angle of 60°, gives the velocity of 6.49 km/secec for sample A (synthesized at 800°C) and 10.06 km/secec for sample B (synthesized at 900°C); these velocities are lower that that of diamond. For sample B scattering from the surface skimming longitudinal wave or longitudinal mode (see Sections 1 and B) was also observed (see Figure 10.5).

The spectra were interpreted following the approach by Camley and Nizzoli,[63] computing the longitudinal power spectra $<|u_1(k_{||},\omega)|^2>$ and the shear surface spectra $<|u_3(k_{||},\omega)|^2>$ for the elastic properties of the sample given in Table 10.1 (see Figure 10.4). As can be seen from Figure 10.4, from which the RW was omitted for clarity, the power spectrum $<|u_3(k_{||},\omega)|^2>$ associated with the ripple scattering mechanism vanishes for $\omega/k_{||} = c_P$ (the

(see Sections 1 and B): Sections have been renumbered. Should this be section 10.3.1.1 & 10.3.2? Please confirm.
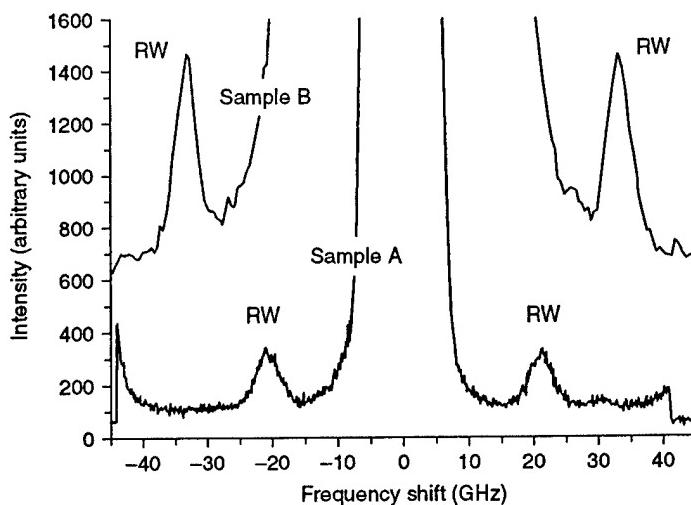
FIGURE 10.7

Experimental SBS spectra at $\theta = 60°$, of superhard amorphous carbon synthesized from C_{60} under high pressure and high temperature. Sample A synthesized at 13 GPa and 800°C, and sample B synthesized at 13 GPa and 900°C. (From Manghnani, M.H. et al., *Phys. Rev. B*, 6412, 121403, 2001. With permission.)

minimum is too deep and too thin to be visible in Figure 10.4), whereas the longitudinal power spectrum $< |u_1(k_{||},\omega)|^2>$ associated with elasto-optical interaction has a well defined maximum at $\omega/k_{||}= c_P$. The significance of this maximum was discussed in Section B.

The determination of the whole set of elastic constants by SBS[106] was made possible by the detection of the longitudinal mode. When only the RW velocity can be measured, the value of the elastic constants cannot be determined precisely, but it is possible to identify ranges for the Young modulus E and the shear modulus μ. Pastorelli et al.[122] used SBS to measure elastic properties of the thick (600 nm) cubic boron nitride (cBN) using some *a priori* information. Elastic properties of the cBN films are of interest for industrial applications because cBN is the second hardest material after diamond, and only recently a method to deposit cBN films was developed.[123] The measurement by SBS[122] was one of the first measurements of the elastic properties of the cBN films. It was done on thick cBN films that could be considered as semi-infinite media. Only the RW was detected in these films. To estimate the Young modulus and shear modulus Pastorelli et al. exploited two additional conditions: (1) Poisson's ratio must lie between 0.0 and 0.5, and (2) the bulk modulus should not be greater than the bulk modulus of diamond (444 GPa). Applying these restrictions to the results of the RW measurements, a fairly narrow interval for elastic constants was obtained: 593 GPa $< E <$ 703 GPa, and 266 GPa $< \mu < 322$ GPa.

AU: Section B: Are you refering to Section 10.3.2? Please confirm.

In transparent media the interaction of the light with SAWs is expected to be weak, possibly too weak for experimental observation. Sussner et al.[124] showed that SAWs can be observed if the transparent material is coated by a thin aluminum layer. It was demonstrated that coating by a 40nm thick aluminum layer made it possible to detect SAWs in quartz, sapphire and polymethylmetacrylate (PMMA).

10.4.2 Selected Results for Anisotropic Bulk Solids

SBS has been successfully used for the detection of SAWs in anisotropic media, and SBS of cubic crystals is a good example showing the potential of the technique. Investigations of the SAW angular dispersion on cubic crystal surfaces revealed that, in addition to the GRW, a PSAW can exist.[36,38] Some properties of the PSAW for the three main planes of cubic crystals [i.e., (001), (110), and (111)] have been summarized by Farnell,[36] and an analysis of the use of SBS for detecting different types of waves propagating on the principal cubic crystal cuts has been reported by Velasco and Garcia-Moliner.[23]

The elastic properties of cubic crystals are determined by the three elastic constants C_{11}, C_{12}, and C_{44}, and the shape of the angular dispersion curve; hence the strategy in SBS measurements is determined largely by the anisotropy coefficient $\eta = 2C_{44}/(C_{11} - C_{12})$. Considering the (001) surface,[36,125] if $\eta < 1$, the variation of the GRW velocity with the propagation direction is small and the GRW is always distinct from the bulk slow transverse wave (STW) mode. In this case, the (001) plane is not very useful for the SBS characterization of the anisotropic elastic properties. For $\eta > 1$, as it is for silicon (Si) and gallium arsenide (GaAs), the angular variation of the velocity of the GRW and of the PSAW that exists in a certain angular range provides an opportunity for determining the elastic constants of a crystal from the angular dependence of the surface wave velocities alone, without the use of lateral wave data.[8,126,127]

Figure 10.8 is a grey scale image representing the calculated Brillouin intensity as a function of velocity $c = \omega/k_{||}$ and of direction φ measured from the [100] direction, for scattering from the (001) plane of gallium arsenide (GaAs). The grey scale intensity in this image is proportional to $\omega^{-1} Im [G_{33}(k_{||}, x_3 = 0, \omega + i0)]$ (see Equation 10.6). The elastic moduli of the GaAs were taken from reference[128] (see Table 10.1). The two bulk wave solutions for symmetry directions, the pure transverse vertical or fast transverse wave (FTW) and the pure transverse horizontal or STW, are displayed in Figure 10.8 as solid and dotted lines, respectively. Both the velocity and the intensity of the GRW velocity show considerable variation with direction. Toward the [110] direction the polarization of the STW tilts over toward the horizontal and becomes more weakly coupled to GRW in G_{33}. As a result, the trace of the GRW shows decreasing intensity, ultimately vanishing as the GRW degenerates with the limiting STW bulk wave in the [110] direction. Also, as the GRW approaches this degenerate condition, its displacement field penetrates ever more deeply
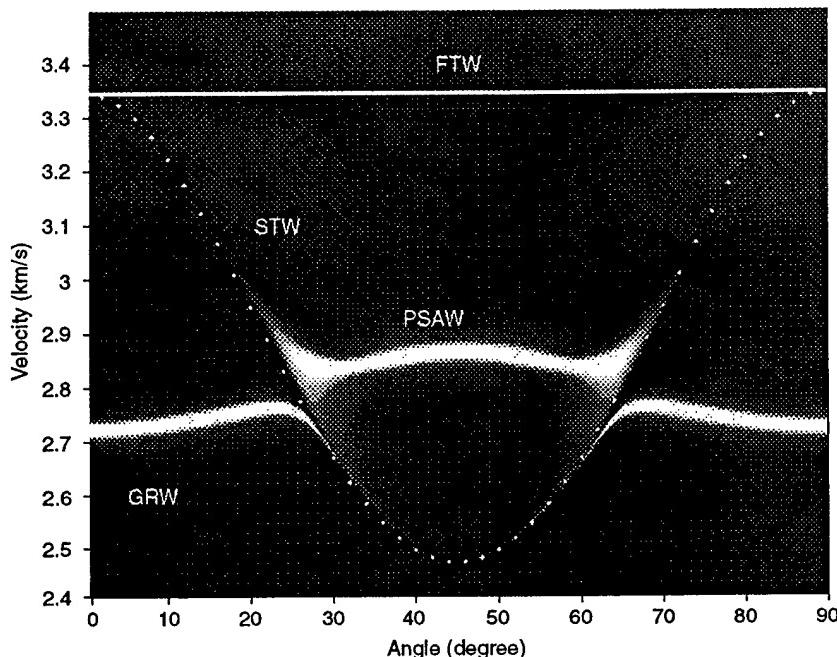
FIGURE 10.8

Green's function $G_{33}(k_{||}, \omega)$ for the [100] direction in the GaAs(001) surface.

into the solid, which further diminishes its contribution to the surface response.

Extending out to about 20° on either side of the [110] direction is a sharp resonance within the bulk wave continuum, which is associated with a PSAW. This mode consists predominantly of two evanescent partial waves, but with the addition of a bulk wave component of small amplitude, which causes radiation of the energy of this wave into the substrate, resulting in attenuation of the wave as it travels along the surface. At the PSAW det $|\mathbf{B}|$ (see Section B) is small but nonzero, except in isolated directions where the PSAW becomes a true supersonic SAW and det $|\mathbf{B}|$ vanishes.[129]

The angular dispersion curves in the (001) plane of cubic crystals have been investigated for nickel (Ni),[127] Si,[8,64] or GaP,[130] and for InSb,[131] and their behavior has been found to be properly predicted by Green's function approach. Figure 10.9 illustrates the good agreement between theoretical simulation and experimental behavior of the SAW dispersion curve in the (001) plane of the GaAs.[132] SBS studies of GaAs[132] demonstrated the coexistence of GSW and PSAW around 20° as predicted by Green's function simulations (see Figure 10.8).

SAW propagation on the (111) plane in various cubic crystals has been extensively investigated by Kuok et al. (Si,[133] InSb,[131] GaAs,[132]). Figure 10.10 shows the measured angular dispersion curves of the 3 surface waves on

AU: Section B: Sections have been renumbered. Should this be Section 10.2.2? Please confirm
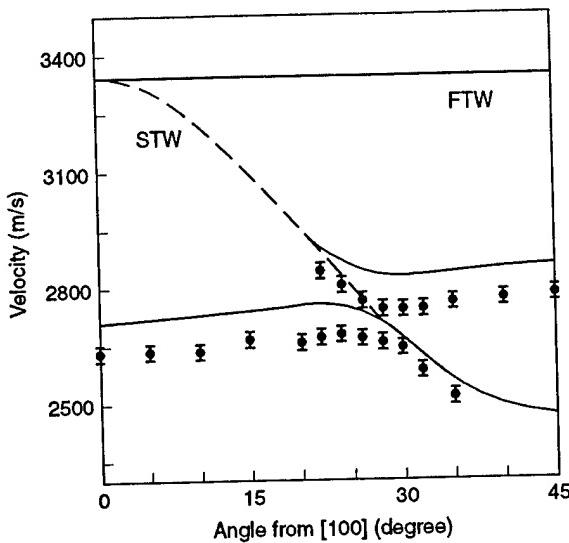
FIGURE 10.9
Angular dependence of the measured GSW and PSW velocities on (001) GaAs. Experimental data for GSW and PSW are denoted by circles and squares, respectively. Solid curves represent the theoretical surface wave velocities, while the FTW and STW bulk wave velocities are shown as dashed curves. (From Kuok, M.H. et al., *J. Appl. Phys.* 89, 7899, 2001. With permission.)
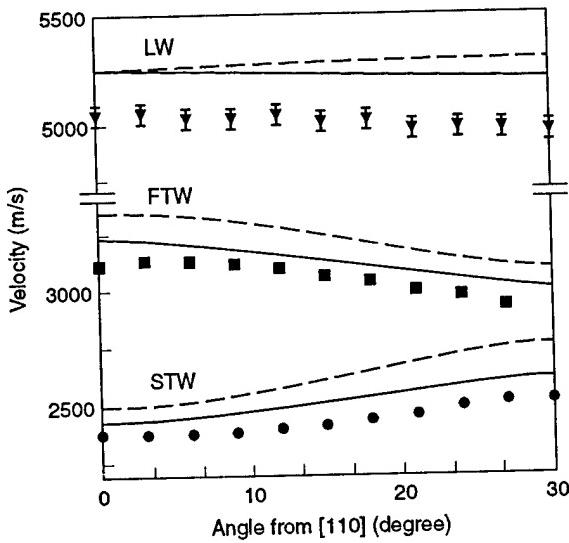
FIGURE 10.10
Angular dependence of the surface acoustic wave velocities on (111) GaAs. The experimental data for GSW, PSW, and HFPSW are represented by circles. (From Kuok, M.H. et al., *J. Appl. Phys.* 89, 7899, 2001. With permission.)

(111) GaAs. It reveals that the PSW can propagate only in limited direction ranges on this surface. The velocities of GSW and LLSW on the (111) plane turn out to be less sensitive to the propagation direction than in the other two basal planes. Scattering from the PSW is strongest at azimuthal angle φ = 0° ([110] direction), but its intensity decreases with increasing azimuthal angle until it is no longer measurable at φ = 30°. These observations are consistent with the theoretical findings of Lim and Farnell: they predicted that as φ approaches 30° the penetration depth of PSW into the bulk increases until it degenerates into a transverse bulk wave at $\varphi = 30°$.[134]

The SBS measurements of SAW dispersion on a (111) face of an fcc film of C_{60} (fullerite) grown on Ni(110) and BS data on longitudinal bulk wave allowed the determination of the three independent elastic constants of fcc C_{60}[94]. Similar work was done on chemical vapor deposited on polycrystalline diamond.[135]

SAWs on (110) faces of cubic GaAS, InSb, Ge and InAs ($\eta > 1$) have been investigated by Aleksandrov et al.[125] and more recently by Kuok et al. (GaAs,[132] InSb[131]). The angular dispersion curve of SAWs on the (110) plane in the cubic crystals represents a fascinating picture. Figure 10.11 represents Green's function simulations for the (110) plane of GaAs. In the (110) plane the FTW and STW curves cross each other at φ = 55° ; beyond this point the PSAW does not exist, and it gradually disappears as the propagation direction tends to [100]. Indeed, experimental SBS measurements (Figure 10.12)
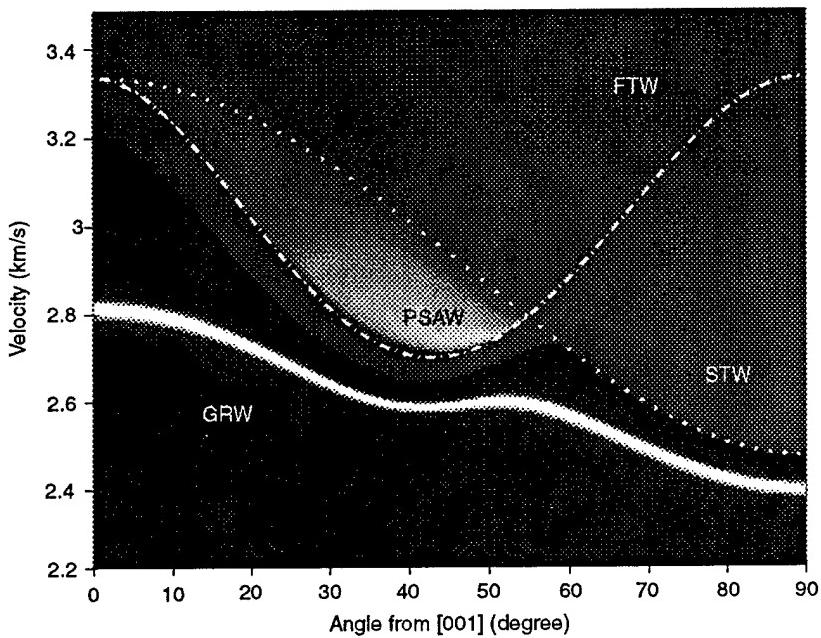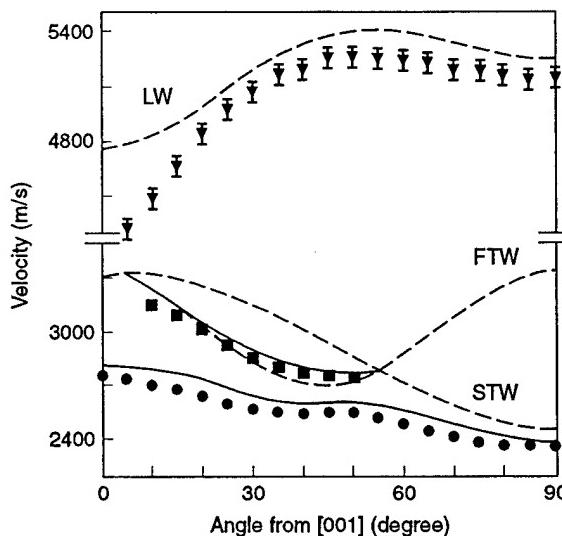

FIGURE 10.11
Green's function $G_{33}(k_{||}, \omega)$ for the [100] direction in the GaAs (001) surface.

FIGURE 10.12

Angular dependence of the surface acoustic wave velocities on (110) GaAs. The experimental data for GSW, PSW, and HFPSW are represented by circles, squares, and inverted triangles, respectively. Solid curves represent theoretical surface wave velocities, while theoretical bulk wave velocities are shown as dashed curves. (From Kuok, M.H. et al., *J. Appl. Phys.* 89, 7899, 2001. With permission.)

show that PSAW propagation on the (110) plane is restricted to the azimuthal angular region $10° < \varphi < 55°$.[132] The GRW was found to propagate in all directions on the surface with an intensity that is quite independent of direction. The LLSW has been detected on the (110) plane of GaAs as well. It is interesting to note that it was found that experimental data values for velocity were about 2%[64,132] lower than the calculated ones. Discussion on this subject can be found elsewhere.[8,64]

The most prominent features in a SBS spectrum are usually the RW and the PSAW peak, but with sufficient data collection times and adequate filtering the Lamb shoulder can be distinguished, and from it the bulk mode threshold velocities can be measured. SAW propagation in a vanadium carbide (VC) cubic crystal, for which $\eta \sim 0.8 < 1$, have been studied by Zhang et al.[57] In this study 2 key features of the spectrum were exploited to determine the elastic constants of $VC_{0.75}$, namely the directional dependence in the (110) surface of the RW velocity, and the sharp dip in the Lamb shoulder lying at about 8500 m/sec, which corresponds to the P-wave threshold. The theoretical spectrum of $VC_{0.75}$ in Figure 10.3 has been calculated using Equation 10.5, and is in good agreement with the measured one [57]. The lateral wave LLSW is most sensitive to the longitudinal elastic constants[136] C_{11} and $C_{12} + 2C_{44}$, while the RW is more sensitive to C_{44} and $(C_{11} - C_{12})/2$. From the observed spectra, the elastic constants of $VC_{0.75}$ were determined to be $C_{11} = 440$ GPa, $C_{12} = 92$ GPa and $C_{44} = 136$ GPa.[57].

Most of the SBS studies of SAW propagation in anisotropic crystals have been performed on cubic crystals. For crystals of lower than cubic symmetry the detection of the GRW alone does not provide sufficient information for studying elastic properties of the crystals.[137] Carlotti et al.[138] were successful in determining five effective elastic constants of a thick (1.3 μm) transparent film (ZnO) of hexagonal symmetry. The constants C_{13}, C_{33}, and C_{44} were obtained from detection of the RW and of the longitudinal bulk mode propagation at different angles from the surface normal. The constant C_{11} was determined from the observation of the LLSW mode, and C_{66} was determined from detection of the shear horizontal mode traveling parallel to the film surface. As a rule, bulk Brillouin scattering is preferable[45] for low symmetry crystals.[132]

10.4.3   Selected Results for Layered Media

One of the major applications for SBS is the study of the elastic properties of thin films. Thin films have a huge number of applications in modern industry. Ohring, in the preface of his monograph on science of thin films, wrote, "Thin-film science and technology plays a crucial role in the high-tech industries that will bear the main burden of future American competitiveness."[139] In addition, elastic properties of the newly developed films, particularly superhard films, need to be determined experimentally because they strongly depend on the synthesis conditions, and cannot be derived from theoretical considerations alone. The thickness of such films ranges commonly from a few tens of nanometers up to the order of a micrometer. The nanoindentation technique widely used for mechanical characterization of thin micron films does not allow measurements of the hardness and elastic moduli of the submicron coating and substrate separately. Conventional methods usually employ SAWs. The surface wave displacements are concentrated within a wavelength from the surface and can probe the samples within a depth inversely proportional to the frequency used. For submicron films, frequencies in the range 5 to 30 GHz are needed, and therefore the SBS technique offers a unique opportunity to cover this range of frequencies.

SBS was used to study SAW in unsupported films (Lamb waves).[117,140] Measurements conducted on 23 nm unsupported Al films[140] illustrated that both the line and positions and relative intensities of the Lamb modes observed in the experimental spectra are well accounted for by theory. SBS of unsupported thin films are rather exceptional researches. The main direction of SBS in thin film characterization is the elastic characterization of thin supported films. For isotropic layered materials, the SAW velocity is dependent on the frequency (i.e., there is frequency dispersion). For anisotropic solids, the SAW velocity also exhibits a variation with the direction of propagation, called angular dispersion. The elastic properties of anisotropic solids can be extracted from measured dispersion curves. SBS usually operates within the frequency range of 10 to 30 GHz. At such frequencies the elastic

properties of thin layers from several nanometers up to a micron or so can be determined. Thicker films generally behave as bulk media. Recent measurements of the SAW dispersion in ultrathin diamond-like carbon films[109] show that mechanical properties of 2-nm thick film can be extracted from SBS data.

The measurement of the SAW dispersion curve by SBS is highly dependent on the type of the layer under investigation. Single layers on substrates are commonly divided into two classes: loading or slow-on-fast layers and stiffening or fast-on-slow layers. The origin of these designations seems to be the paper of Tiersten[141] in which he studies the slope of the dispersion curve for $kh > 0$. A layer is said to stiffen the substrate when its presence, at whatever thickness, and increases the velocity of the surface wave above that of the RW velocity of the substrate[43] and vice versa. Farnell and Adler[43] have established sufficient conditions for the layer to be loading or stiffening: $c_S^- < \sqrt{2}c_S^+$ and $c_S^- > \sqrt{2}c_S^+$ (c_S^- is the shear velocity in the layer, c_S^+ is the shear velocity in the substrate).

10.4.3.1 Slow Film on Fast Substrate

Surface wave propagation in loading layers has been widely studied by SBS for various combinations of film and substrate: Al/Si,[142] gold/glass,[143] Al/NaCl,[101] CaF_2/Si,[144] ZnO/Si and ZnO/Al_2O_3,[14] polystyrene/Si,[146] and ZrB_3/Si.[71] An Al layer on Si was the first layered system where guided acoustic modes, detected by SBS, were satisfactorily explained in terms of ripple scattering at the film surface.[46] As an example, SAW propagation of an amorphous Si (*a*-Si) layer produced by ion bombardment will be considered here. Figure 10.13 depicts $ImG_{33}(k_{||}, \omega)/\omega$ by a grayscale as a function of $c = \omega/k_{||}$ and $k_{||}h$ for an amorphous silicon film on Si(001). In Figure 13, we plot only the modes with displacements confined to the sagittal plane. For the loading case, an infinite number of surface waves propagate:[43] RWs, PSAWs, Sezawa and Lamb modes, and various resonances within the continuum of bulk wave scattering. In Figure 10.13 the RW curve is much more intense than the Sezawa wave (SW) curves, because the RW is concentrated near the film surface to which $G_{33}(k_{||}, \omega)$ pertains. In the RW the displacement field is mainly concentrated near the free surface of the layer and it has a velocity that, with increasing layer thickness, approaches that of the RW of Si. It starts at the value of the RW on the substrate, 4.91 km/sec; for large $k_{||}h$, the Rayleigh SAW velocity tends asymptotically to a constant value of 4.25 km/sec, which is the phase velocity of the Rayleigh wave on the surface of bulk amorphous silicon.

The 2 horizontal lines labeled c_S(a-Si), 4.62 km/sec, and c(Si), 5.84 km/sec, are transverse bulk-wave-phase velocities in the layer and in the substrate, respectively. A lower transverse bulk-wave-phase velocity in the layer as compared with that of the substrate is necessary in order for SWs to exist. The horizontal-dashed line, $c = 5.65$ km/sec, corresponds to the transonic state in the substrate. The curves below the transonic state are the various

Ultrasonic Nondestructive Evaluation
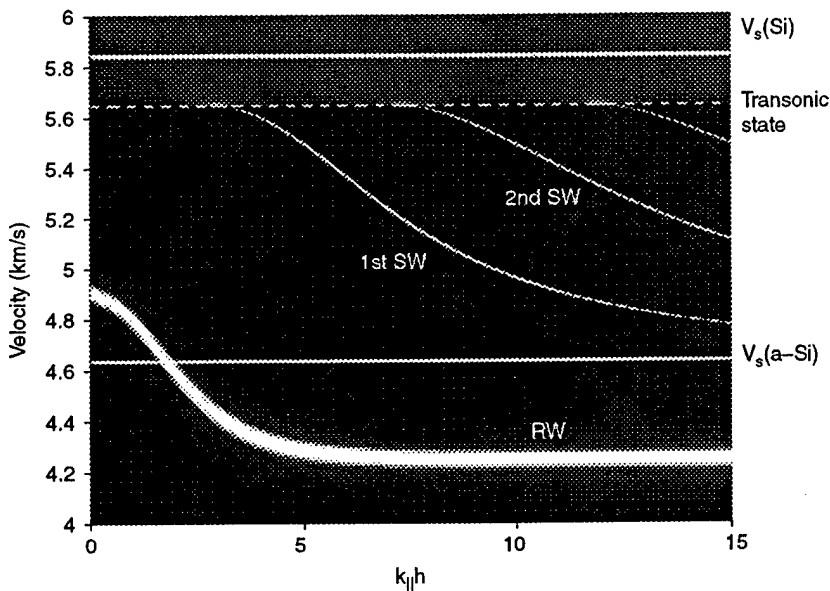
FIGURE 10.13

$ImG_{33}(k_{||}, \omega)/\omega$ for an amorphous silicon film on Si(001) for the [100] direction, a slow on fast system. It shows the dispersion of the Rayleigh and Sezawa waves.

orders of SWs, while curves for the pseudo-SWs lie above the transonic state. The essential difference between the SW and pseudo-SWs is understood in term of k_3 values of the partial waves. For the SW, which lies in subsonic range in Figure 10.13, the partial waves in the substrate all have a complex value of k_3, and the corresponding displacement amplitudes decrease in an exponential fashion into the interior of the substrate. These properties allow the SW to propagate without attenuation along the surface, making it a true surface wave. In the case of a pseudo-SW, which lies in the supersonic range in Figure 10.13, one or more of the partial waves in the substrate has a real value of k_3. This bulk-wave component carries energy away from the surface into the interior of the substrate and causes the wave to decay with distance. We use the term pseudo-SW here because this particular pseudo-SAW is so closely related to the true Sezawa wave. The transition from one mode to the other is also clearly seen by the change in attenuation (Figure 10.13), which decreases suddenly when the wave no longer leaks energy into the substrate.

Figure 10.14 shows the measured and calculated dispersion curves for the Rayleigh SAW and Sezawa-type modes. For the dispersion curves of the Rayleigh and Sezawa-like modes, the solid lines are calculated using best fit elastic constants determined by comparison with SBS measurements in the paper.[26] There are also calculated curves for the higher order Sezawa (Figure 10.14), but these modes were not observed for a-Si layer on Si.[26] For purposes of comparison, the dispersion curves of the Rayleigh-SAW and the
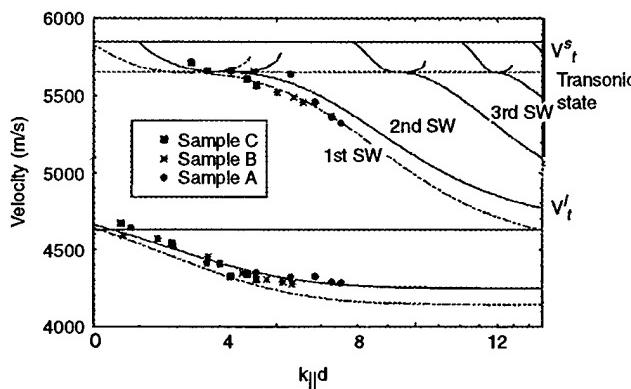
FIGURE 10.14

Dispersion relations for the [100] direction for an amorphous silicon film on Si(001),. The two solid lines marked V_t^s and V_l^s represent the transverse bulk-wave velocity for the crystalline-silicon substrate and the amorphous silicon layer, respectively. The dotted-horizontal line indicates the transonic state. The solid curves represent calculated dispersion curves based on the model of a uniform amorphous layer on the (001) silicon surface and the elastic constants of the layer obtained from the present measurements. Dashed curves represent calculated dispersion curves from the elastic constants given in the Table 10.2. RW: Rayleigh wave. 1st SW, etc., different orders of Sezawa waves. (From Zhang, X. et al., *Phys. Rev. B*, 58, 13677, 1998. With permission.)

first Sezawa-like excitation are also calculated using the literature values of the elastic constants of amorphous silicon. The agreement is within 2%.

The Sezawa and pseudo-Sezawa modes are commonly used in SBS for extracting elastic properties of slow-on-fast layers.[26,103] In the case of Brillouin spectroscopy measurements, very high velocity modes can be detected, so that for slow-on-fast layers numerous generalized Lamb modes can be measured on a single sample.[146]

The SAW dispersion for a-Si on Si mentioned above is representative of the slow-on-fast dispersion, although a small difference exists among these layers. Sklar[56] showed that depending on the layer/substrate combination, the pseudo-Sezawa mode for very thin layers tends to a different value. When $c_p < 2c_s$: for $k_{||}h \to 0$ the pseudo-Sezawa tends to the lateral wave, whose velocity is the longitudinal velocity of the substrate; when $c_p > 2c_s$: the pseudo-Sezawa mode tends to a wave below the lateral longitudinal wave.

SAW wave propagation in the one-layer system, when layer and substrate have very close properties, has been discussed in detail by Lefeuvre.[147]. The combination is situated near the border between stiffening and the loading layers. Such systems concern only a very few cases in practice, since the purpose of coatings is to change the surface properties of the material, generally affecting the elastic properties of the surface. For some combination of materials, a Stoneley wave can propagate.[43] A Stoneley wave is a localized mode that propagates along interface between two solids. It is nonattenuative

because its velocity is lower than the bulk velocities of the two materials. When one of the materials is transparent, laser detection of interfacial waves is rendered possible.[48] Stoneley waves have thereby been measured by Brillouin spectroscopy by Bortolani et al.[148] for Ni on fused silica, by Bell et al.[149] at the interface molybdenum/fused silica, and by Jorna et al.[150] for Ni on ZnO.

10.4.3.2   Fast Film on Slow Substrate

Recent theoretical predictions[151] of the new superhard materials and production of the new superhard films such as cubic boron nitride (cBN), carbon nitride β-C_3N_4, B_4C, and CVD diamond films have excited considerable interest in the mechanical properties of thin hard and superhard films. Their hardness and abrasion resistant qualities, highly valued in technology and industry, are controlled by the their large elastic moduli. Elastic properties of the superhard films need to be determined experimentally because they strongly depend on the synthesis conditions, and they cannot be derived from theoretical considerations alone. The thickness of such films commonly ranges from a few tens of nanometers up to the order of a micrometer. Recent studies have shown that SBS is an ideal technique for characterizing the new hard and superhard films.[95,105,107,152,153]

Despite the extensive literature on SAW propagation in layered solids, detailed study of SAW in stiffening layers (i.e., fast-on-slow systems) has only started recently.[152,154–156] Earlier computations of SAW propagation were usually restricted to true surface modes (surface waves that do not leak energy into bulk), but for stiffening layers the SAW propagation is mostly characterized by PSAWs. Also, the calculation of PSAWs is complicated by the attenuated nature of these modes; two parameters, the velocity and the attenuation of the SAW, should be computed. There have been only a few experimental studies performed on hard coatings because attenuation causes scattering in the results and lowers the quality of the signal.

Recent calculations of the dispersion of SAW above cutoff in stiffening systems[154] have revealed two types of SAW dispersion for fast-on-slow systems. It was shown that the SAW velocity initially grows with increasing $k_{||}h$. At a critical value $k_{||}h_{cut}$ the SAW meets and degenerates with the bulk wave continuum. Beyond this cutoff, while a true SAW no longer exists, there is a PSAW, which radiates energy into the substrate and attenuates with distance as it travels along the surface. The first type of behavior comes about when the elastic properties of the layer and the substrate are not very different, and has the velocity of the pseudo-SAW beyond cutoff increasing up to the RW velocity of the layer. This type of behavior is called the *nonsplitting* type and was first observed experimentally by Pang et al.[152,157] The second type of behavior arises when the elastic properties of the two materials are quite dissimilar and has the PSAW evolving into a strongly attenuated interfacial mode, while a second mode appears at a higher velocity and evolves into the RW at the free surface of the layer. This second type of behavior of the dispersion relation was called the *splitting type*.[154] A more
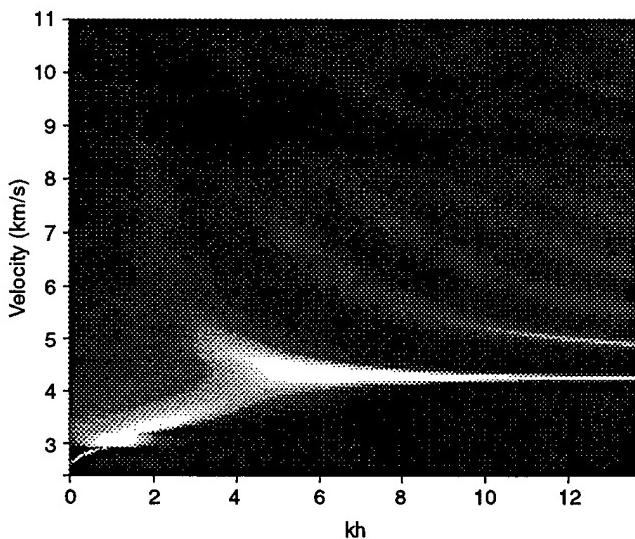
FIGURE 10.15

Two-dimensional gray image of the calculated Brillouin spectra of Si_3N_4/GaAs at free Si_3N_4 surface. (From Zinin, P.V. et al., *Phys. Rev. B*, 60, 2844, 1999. With permission.)

detailed description of the behavior of the SAW dispersion curves for fast-on-slow systems for different combinations of films and substrates can be found elsewhere.[147]

The dispersion of SAWs in Si_3N_4 film on a GaAs substrate is an example of the splitting type of dispersion curve measured by SBS. Si_3N_4 film on a GaAs is a stiffening system since c_S of the Si_3N_4 and GaAs are 4.7 km/sec and 3.3 km/sec, respectively.[105] In experiments, only one branch of the dispersion curve was measured. It corresponded to SAWs propagating in the [100] direction on the (001) GaAs surface. The Si_3N_4 film was assumed to be isotropic.[158] Grayscale images representing the calculated Brillouin intensity as a function of velocity $c = \omega / k_{||}$ and $k_{||}h$, for scattering from the free surface of the film and from the interface between the film and substrate for the [100] direction in the (001) surface of GaAs are presented in Figure 10.15 and Figure 10.16, respectively. The grayscale intensity in these images is proportional to $\omega^{-1}Im[G_{33}(k_{||}, x_3, \omega + i0)]$, with $x_3 = 0$ for the interface and $x_3 = -h$ for the surface of the film. Elastic constants used for the calculation are given in Table 10.2. For $k_{||}h = 0$, the velocity corresponds to the SAW velocity on the GaAs substrate. With increasing $k_{||}h$ the SAW velocity approaches the bulk wave threshold or limiting shear slowness $k_{||}/\omega$, which is reached at $k_{||}h_{cut} \approx 1.5$. Below $k_{||}h_{cut}$ the Brillouin spectrum displays a sharp peak that is associated with the true surface wave and a continuum extending from the bulk wave threshold to higher frequencies, which is known as the Lamb shoulder.

In our calculation of Green's function (Equation 10.41), a small amount of artificial damping [58] is introduced to avoid a true singularity. In the region

Ultrasonic Nondestructive Evaluation

TABLE 10.2

The Elastic Properties Used in the Calculations of the Power Spectra Shown
in Figures 10.4, 10.8, 10.11, 10.13, 10.15, and 10.16

Materials	Density (kg/m³)	C_{11} (GPa)	C_{22} (GPa)	C_{44} (GPa)	Ref.
a-carbon (sample B)	3150	868		376	106
Si	2332	165.7	63.9	79.6	26
a-Si	2230	138		48	26
GaAs	5318	118.1	53.2	59.4	128
Si_3N_4 (polycrystalline)	2500	189		56	158
bcc Co		212	165	53	159
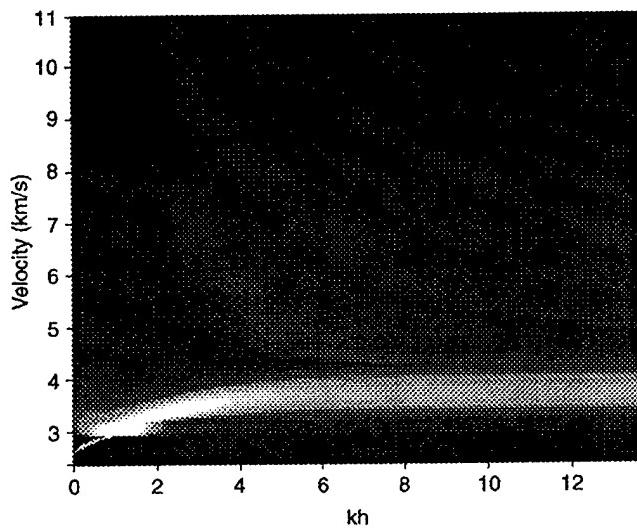
FIGURE 10.16
Two dimensional gray image of the calculated Brillouin spectrum at Si_3N_4/GaAs interface (From
Zinin, P.V. et al., *Phys. Rev. B*, 60, 2844, 1999. With permission.)

below cutoff, the position of the SAW peak is the same for surface and
interface scattering. At $k_{||}h_{cut}$, the SAW degenerates with the bulk continuum,
and beyond cutoff there is no true SAW. In its place there are broadened
resonances that are associated with attenuated PSAWs at the interface or
surface of the film and that leak energy into the substrate. Somewhat above
the cutoff velocity, the Brillouin spectrum for the interface displays a broad
peak that becomes independent of the film thickness beyond $k_{||}h \sim 4$. This
peak is associated with a highly damped interfacial wave. Its broadening is
due to leakage of energy into the substrate as discussed in Lefeuvre et al.[154]
In the same spectral region, the calculated Brillouin spectrum for the surface
of the film displays a broad peak that fades away by $k_{||}h \sim 4$. At this point
another broad peak appears that becomes narrow with increasing $k_{||}h$ as the
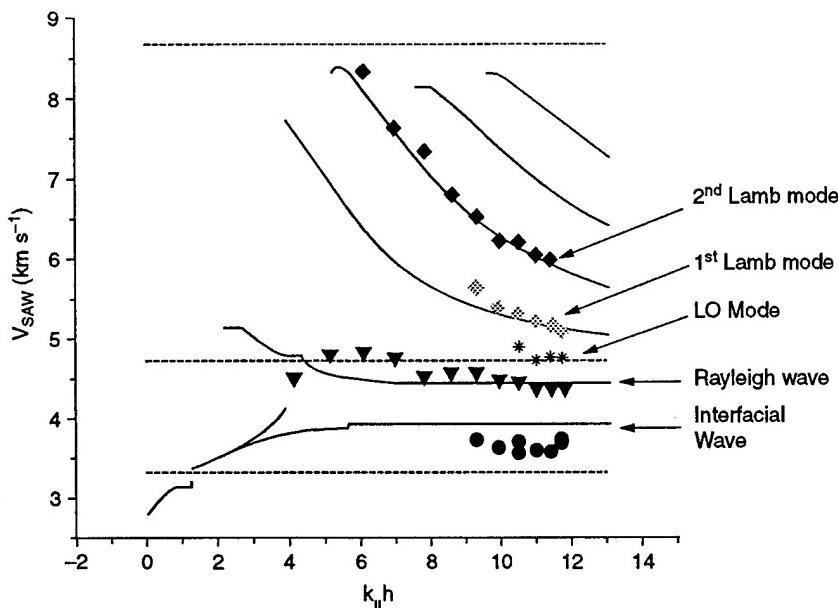
FIGURE 10.17

Dispersion curves calculated using Green's function and experimental results of Si_3N_4/GaAs. Dashed lines are shear cutoff (lower line), longitudinal cutoff (middle line) for GaAs and longitudinal cutoff for Si_3N_4 (upper line) (From Zinin, P.V. et al., *Phys. Rev. B*, 60, 2844, 1999. With permission.)

associated mode tends toward the Rayleigh mode of Si_3N_4. For very large $k_{||}h$ this becomes the true nondispersive Rayleigh SAW.

The dispersion curves in Figure 10.17 represent the traces of the maxima of the calculated Brillouin intensity (Figure 10.16) for the interface (the lowest solid line) and surface (Figure 10.15; the upper solid lines) and of the measured Brillouin intensity. The experimental data are found to be in excellent agreement with the theoretical predictions, except for the interfacial mode and the fact of the disappearance of the first Lamb mode in the measured spectrum at small $k_{||}h$. The former discrepancy suggests that the interface is more complicated than assumed in our model.

Among all hard or stiff films, diamond-like coatings (DLCs) appear to have widest range of applications. It was found recently that SBS measurements of thin DLC films allow to detect the LGM.[107,108] Detection of the LGM allows both C_{11} and C_{44} of such films to be obtained from SBS measurements.

10.4.3.3 Anisotropic Supported Films

The elastic properties of anisotropic layered solids can be investigated either by measuring the frequency or the angular dispersion curves by SBS. Experimental data[159] for a body-centered-cubic cobalt (Co) film on the (110) plane
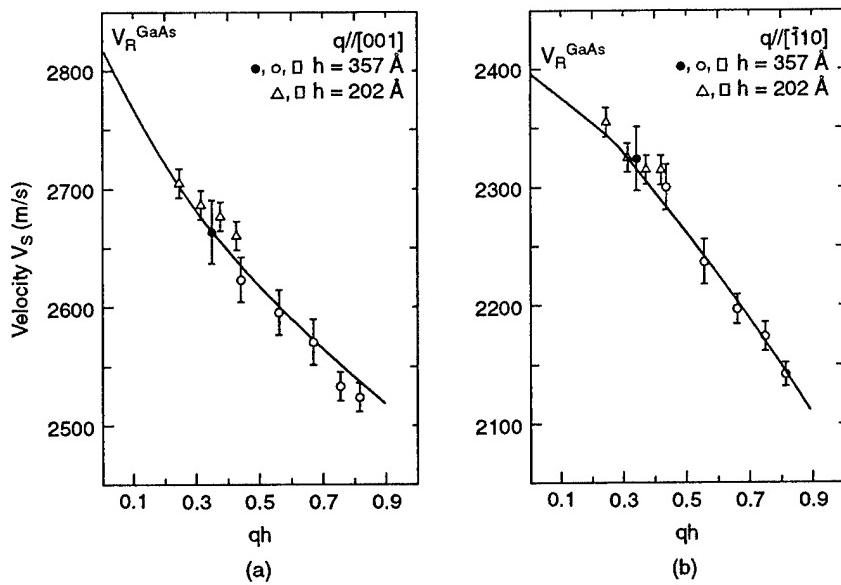
FIGURE 10.18

The measured (solid and triangles) and calculated (solid line) dispersion curves for the Rayleigh mode for 35.7- and 20.0-nm-thick bcc cobalt films of (110) GaAs. The two panels refers to propagation direction along [001] and [$\bar{1}$10]. Data represented by open circles and triangles were taken with 515-nm radiation, while solid circle was taken at 647 nm. (From Subramanian, S. et al., *Phys. Rev. B*, 49, 17319, 1994. With permission.)

of GaAs are presented in Figure 10.18. A strong RW peak is observed in the SBS spectrum along the [001] and [$\bar{1}$10] directions in the (110) oriented film. To determine the elastic moduli of the cubic Co films (C_{11}, C_{12} and C_{44}), Subramanian et al.[159] proposed simultaneously fitting the frequency RW dispersions in these directions. Figure 18 shows the frequency dispersion curves for Co films along the [001] and [$\bar{1}$10] directions in (110) oriented Co film on (110) GaAs. The study again demonstrated that values of the elastic moduli of thin films generally are different from the corresponding values in the bulk. Measurements of the frequency dispersion curve of the RW yield up to a 65% reduction in the values of C_{11} and C_{44} for the Co film.

Nizzoli at al.[111] reported SBS experiments on LB films, for which the anisotropy of the elastic properties could be regarded as having hexagonal symmetry, with the c axis, in the plane of the films. LB layers were grown on molybdenum and represent slow on fast systems. The stiffness matrix of anisotropic solids of hexagonal symmetry contains five independent elastic moduli (C_{11}, C_{12}, C_{13}, C_{33} and C_{44}), and it is a nontrivial matter to determine all five constants[160] from conventional SBS measurements. In the article[111] the x_3-axis was chosen to be parallel to the molecular c-axis of the films and was in the plane of the film. The x_1-axis was chosen to be normal to the molecular c-axis of the films and was in the plane of the film. In such a coordinate

system, C_{33} (C_{11}) is the longitudinal elastic modulus for phonons propagating parallel to the film and parallel (perpendicular) to the molecular axis. Observation of the LGM along the x_1-axis gave the value of the C_{11} modulus. SBS measurements along x_1 for different films thicknesses provided the dispersion curves for the RWs and SWs. A best fit to the data points of the RW and SW gave values of the C_{12} elastic modulus. The elastic modulus C_{33} was determined from the position of the LGM peak observed in the x_3-direction. To obtain the last two moduli, C_{44} and C_{13}, Nizzoli et al.[111] fitted the RW and bulk peaks in the SBS spectrum measured in the x_3-direction.

SAW propagation in hexagonal hBN films on a silicon substrate was studied by Wittkowski et al.[116] It was claimed that four independent elastic constants had been determined from the frequency dispersion of the Rayleigh and Sezawa modes. The elastic moduli obtained by Wittkowski et al. were used to describe SAW propagation in a two layer system: a stiff layer of cBN on a soft layer of hBN deposited on Si(111).[156] The GRW below shear cutoff and the PSAW above cutoff were detected by SBS. It was found that incorporating the hBN interlayer into a model of the SBS response and precise thickness measurement of the cBN layer and hBN interlayer fully describes the behavior of the SAW dispersion in deposited cBN layered systems. The most prominent example of application of SBS in studying elastic properties of multilayered systems is elastic characterization of superlattices, structures that consist of altering layers of different media with different thicknesses.[3] The ability to design a layered structure from films of different symmetry has resulted in a wide variety of superlattices with different elastic properties.[161-163] SBS has proved to be a powerful nondestructive tool for the elastic characterization of superlattices, but this is a subject beyond the scope of this chapter. For detailed discussion of the subject see Lomonosov et al.[3] and Comins.[16]

10.5 Concluding Remarks

Brillouin scattering, the scattering of an optical wave by an acoustical wave, provides a method to measure acoustical velocities at submicrometric wavelengths, corresponding to frequencies ranging from a few gigahertz to above 20 GHz for SAWs and up to above 100 GHz for bulk waves. Measurements are contactless, requiring only optical access to the sample, and local, allowing measurements on millimetric and submillimetric specimens. These characteristics qualify Brillouin scattering as a nondestructive ultrasonic testing technique. SBS has been extensively exploited to probe the acoustical properties and derive the elastic properties of bulk materials and thin films. SBS has a particular potential for the characterization of both submicrometric and nanometric films. The principles of the method have been reviewed, and the technical implementation has been discussed. An overview has

finally been given of various recent applications of SBS to the characterization of various types of materials and of films.

The range of application of SBS has been growing in recent years as the dimensions of structures used in industry has moved down to the nanoscale region, for which SBS measurements of SAWs can be done most effectively. It must be noted that this is an active field of research; the performances of SBS for the elastic characterization of films are being pushed further, and nontraditional applications are being explored. Indeed, SBS has been used to study the melting transition of tin nanocrystals embedded in a silica film,[9] as well as probe residual stress through the acoustoelastic effect.[164] Thin films deposited on a substrate are usually in a state of stress that can reach several gigapascal, as in the case of epitaxial films such as Ge on Si, and surface wave velocity measurements constitute a valuable method for characterizing such a stress state. Other growing applications exploit the contact-less nature of the technique to extend SBS measurements to high temperature[152] and high pressure[104] regions. Measurements of the velocities of the RWs and SWs in thick gold film at 4.8 GPa demonstrated the potential of the SBS techniques in high-pressure physics of the elastic properties of opaque materials.

Acknowledgment

References

1. Zinin, P.V., Quantitative acoustic microscopy of solids, in *Handbook of Elastic Properties of Solids, Liquids, and Gases. Volume I: Dynamic Methods for Measuring the Elastic Properties of Solids*, Levy, M., Bass, H., Stern, R., and Keppens, V., Eds., Academic Press, New York, 2001, pp. 187–226.
2. Lomonosov, A., Mayer, A.P., and Hess, P., Laser controlled surface acoustic waves, in *Handbook of Elastic Properties of Solids, Liquids, and Gases. Volume I: Dynamic Methods for Measuring the Elastic Properties of Solids*, Levy, M., Bass, H., Stern, R., and Keppens, V., Eds., Academic Press, New York, 2001, pp. 137–186.
3. Nizzoli, F. and Sandercok, J.R., Surface Brillouin scattering from phonons, in *Dynamical Properties of Solids*, Horton, G.K. and Maradudin, A.A., Eds., Elsevier, New York, 1990, pp. 285–335.

4. Mutti, P., Bottani, C.E., Ghislotti, G., Beghi, M., Briggs, G.A.D., and Sandercock, J.R., Surface Brillouin scattering: extending surface wave measurements to 20 GHz, in *Advanced in Acoustic Microscopy*, Briggs, A., Ed., Plenum Press, New York, 1995, pp. 249–300.

5. Sathish, S., Mendik, M., Kulik, A., Gremaud, G., and Wachter, P., Polish induced surface damage in nickel — scanning acoustic microscopy and Brillouin scatterings study, *Appl. Phys. Lett.*, 59, 167–168, 1991.

6. Jiang, X., Wang, M., Schmidt, K., Dunlop, E., Haupt, J., and Gissler, W., Elastic constants and hardness of ion beam sputtered TiNx films measured by Brillouin scattering and depth-sensing indentation, *J. Appl. Phys.*, 69, 3053–3057, 1991.

7. Jiang, X., Harzer, J.V., Hillebrands, B., Wild, C., and Koidl, P., Brillouin light scattering on chemical vapor deposited polycrystalline diamond: evaluation of the elastic moduli, *Appl. Phys. Lett.*, 59, 1055–1057, 1991.

8. Stoddart, P.R., Comins, J.D., and Every, A.G., Brillouin-scattering measurements of surface-acoustic-wave velocities in silicon at high-temperatures, *Phys. Rev. B*, 51, 17574–17578, 1995.

9. Bottani, C.E., Li Bassi, A., and Kofman, R., Melting in metallic Sn nanoparticles studied by surface Brillouin scattering and synchrotron-x-ray diffraction, *Phys. Rev. B*, 59, R15601, 1999.

10. Zhang, X., Comins, J.D., Every, A.G., and Derry, T.E., Use of surface Brillouin scattering to examine a structural phase transition in carbon-ion-bombarded silicon during high-temperature annealing, *Phys. Rev. B*, 65, 012106, 2002.

11. Bassett, W.A., Dynamic measurements of elastic moduli of samples at high pressure and temperature, in *Handbook of Elastic Properties of Solids, Liquids, and Gases. Volume I: Dynamic Methods for Measuring the Elastic Properties of Solids*, Levy, M., Bass, H., Stern, R., and Keppens, V., Eds., Academic Press, New York, 2001, pp. 469–487.

12. Sandercock, J.R., Trends in Brillouin-scattering: studies of opaque materials, supported films, and central modes, in *Light Scattering in Solids. III. Recent Results*, Cardona, M. and Guntherodt, G., Eds., Springer -Verlag, Berlin, 1982, pp. 173–206.

13. Landau, L.D. and Lifshitz, E.M., *Mechanics*, 2nd ed., Pergamon Press, Oxford, New York, 1969.

14. Nye, J.F., *Physical Properties of Crystals*, Clarendon Press, Oxford, 1985.

15. Every, A.G., The elastic properties of solids: static and dynamic principles, in *Handbook of Elastic Properties of Solids, Liquids, and Gases. Volume I: Dynamic Methods for Measuring the Elastic Properties of Solids*, Levy, M., Bass, H., Stern, R., and Keppens, V., Eds., Academic Press, New York, 2001, pp. 3–36.

16. Comins, J.D., Surface Brillouin scattering, in *Handbook of Elastic Properties of Solids, Liquids, and Gases. Volume I: Dynamical Methods for Measuring the Elastic Properties of Solids*, Levy, M., Bass, H., Stern, R., and Keppens, V., Eds., Academic Press, New York, 2001, pp. 349–378.

17. Loudon, R., Theory of surface-ripple Brillouin scattering by solids, *Phys. Rev. Lett.*, 40, 581–583, 1978.

18. Loudon, R., Theory of lineshapes for normal-incidence Brillouin scattering by acoustic phonons, *J. Phys. C: Solid State Phys.*, 11, 403–417, 1978.

19. Subbaswamy, K.R. and Maradudin, A.A., Photoelastic and surface-corrugation contribution to Brillouin scattering from an opaque crystal, *Phys. Rev. B*, 18, 4181–4199, 1978.

20. Loudon, R. and Sandercock, J.R., Analysis of the light-scattering cross section for surface ripples on solids, *J. Phys. C: Solid State Phys.,* 13, 2609–2622, 1980.

21. Marvin, A.M., Bortolani, V., and Nizzoli, F., Surface Brillouin scattering from acoustic phonons. I. General theory, *J. Phys. C: Solid State Phys.,* 13, 299–317, 1980.

22. Marvin, A.M., Bortolani, V., Nizzoli, F., and Santoro, G., Surface Brillouin scattering from acoustic phonons. II. Application to semiconductors, *J. Phys. C: Solid State Phys.,* 13, 1607–1616, 1980.

23. Velasco, V.R. and Garcia-Moliner, F., Theory of surface waves in anisotropic cubic crystals, *J. Phys. C: Solid St. Phys.,* 13, 2237–2256, 1980.

24. Rowell, N.L. and Stegeman, G.I., Theory of Brillouin scattering from opaque media, *Phys. Rev. B,* 18, 2598–2615, 1978.

25. Mills, D.L. and Subbaswamy, K.R., Surface and size effects on the light scattering spectra of solids, in *Progress in Optics,* Wolf, E., Ed., North Holland, Amsterdam, 1981, p. 45.

26. Zhang, X., Comins, J.D., Every, A.G., Stoddart, P.R., Pang, W., and Derry, T.E., Surface Brillouin scattering study of the surface excitations in amorphous silicon layers produced by ion bombardment, *Phys. Rev. B,* 58, 13677–13685, 1998.

27. Dil, J.G., Brillouin scattering in condensed matter, *Rep. Prog. Phys.,* 45, 285–334, 1982.

28. Fedorov, F.I., *Theory of Elastic Waves in Crystals,* Plenum Press, New York, 1968.

29. Musgrave, M.J.P., *Crystal Acoustics: Introduction to the Study of Elastic Waves and Vibrations in Crystals,* Holden-Day, San Francisco, CA, 1970.

30. Achenbach, J.D., *Wave Propagation in Elastic Solids,* North-Holland, Amsterdam, 1973.

31. Dieulesaint, E. and Royer, D., *Elastic Waves in Solids: Applications to Signal Processing,* John Wiley, Chichester, 1980.

32. Auld, B.A., *Acoustic Fields and Waves in Solids,* Robert E. Krieger Publishing Company, Malabar, FL, 1990.

33. Nayfeh, A.H., *Wave Propagation in Layered Anisotropic Media: With Applications to Composites,* Elsevier, Amsterdam, New York, 1995.

34. Rose, J.L., *Ultrasonic Waves in Solid Media,* Cambridge University Press, London, 1999.

35. Wolfe, J.P., *Imaging Phonons: Acoustic Wave Propagation in Solids,* Cambridge University Press, London, 1998.

36. Farnell, G.W., Properties of elastic surface waves, in *Physical Acoustics,* Mason, W.P. and Thurston, R.N., Eds., Academic Press, New York, 1970, pp. 109–166.

37. Hickernell, F.S., Surface acoustic wave technology: macrosuccess through microseisms, in *Physical Acoustics,* Thurston, R.N., Pierce, A.D., and Papadakis, E., Eds., Academic Press, New York, 1999, pp. 136–208.

38. Every, A.G., Pseudosurface wave structures in phonon imaging, *Phys. Rev. B,* 33, 2719–2732, 1986.

39. Stoneley, R., Elastic waves at the surface of separation of two solids, *Proc. Roy. Soc.,* 106, 416–428, 1924.

40. Scholte, J.G., The range and existence of Rayleigh and Stoneley waves, *Mon. Not. Roy. Astron. Soc.,* (Geophys. Suppl.) 5, 120–126, 1947.

41. Pilant, W.L., Complex roots of the Stoneley-wave equation, *Bull. Seismol. Soc. Am.,* 62, 285–299, 1972.

42. Hillebrands, B., Lee, S., Stegeman, G.I., Cheng, H., Potts, J.E., and Nizzoli, F., A new class of guided longitudinal acoustic phonons in ZnSe films on GaAs found by surface Brillouin-scattering, *Surf. Sci.,* 211, 387–393, 1989.

43. Farnell, G.W. and Adler, E.L., Elastic wave propagation in thin layers, in *Physical Acoustics*, Mason, W.P. and Thurston, R.N., Eds., Academic Press, New York, 1972, pp. 35–127.

44. Viktorov, I.A., *Rayleigh and Lamb Waves: Physical Theory and Applications*, Plenum Press, New York, 1967.

45. Grimsditch, M., Brillouin scattering, in *Handbook of Elastic Properties of Solids, Liquids, and Gases. Volume I: Dynamical Methods for Measuring the Elastic Properties of Solids*, Levy, M., Bass, H., Stern, R., and Keppens, V., Eds., Academic Press, New York, 2001.

46. Bortolani, V., Nizzoli, F., and Santoro, G., Surface density of acoustic phonons in GaAs, *Phys. Rev. Lett.*, 41, 39–42, 1978.

47. Albuquerque, E.L., Loudon, R., and Tilley, D.R., Theory of normal incidence Brillouin scattering by acoustic phonons in a supported thin film, *J. Phys. C: Solid State Phys.*, 12, 5297–5310, 1979.

48. Albuquerque, E.L., Theory of Brillouin scattering by Stoneley waves, *J. Physics C: Solid St. Phys.*, 13, 2623–2639, 1980.

49. Albuquerque, E.L., Oliveros, M.C., and Tilley, D.R., Theory of Brillouin-scattering from an isotropic elastic film, *J. Phys. C. Solid State Phys.*, 17, 1451–1463, 1984.

50. Bortolani, V., Marvin, A.M., Nizzoli, F., and Santoro, G., Theory of Brillouin scattering from surface acoustic phonons in supported films, *J. Phys. C. Solid State Phys.*, 16, 1757–1776, 1983.

51. Byloos, C., Giovannini, L., and Nizzoli, F., Theory of the elasto optic coupling for surface Brillouin scattering in a supported bilayer, *Phys. Rev. B*, 51, 9867–9874, 1995.

52. Every, A.G., Unpublished, 1996.

53. Cottam, M.G. and Maradudin, A.A., Surface linear response functions, in *Surface Excitations*, Agranovich, V.M. and Loudon, R., Eds., Elsevier Science, London, 1984, pp. 5–193.

54. Byron, F.W. and Fuller, R.W., *Mathematics of Classical and Quantum Physics*, Dover Publications, New York, 1992, p. 248.

55. Nayfeh, A.H., The general problem of elastic wave propagation in multilayered anisotropic media, *J. Acoust. Soc. Am.*, 89, 1521–1531, 1991.

56. Sklar, Z., *Quantitative Acoustic Microscopy of Coated Materials*, University of Oxford, 1993.

57. Zhang, X., Comins, J.D., Every, A.G., and Stoddart, P.R., Surface Brillouin scattering studies on vanadium carbide, *Int. J. Refrac. Metals Hard Mater.*, 16, 303–308, 1998.

58. Every, A.G., Kim, K.Y., and Maznev, A.A., The elastodynamic response of semi-infinite anisotropic solid to sudden elastic surface loading, *J. Acoust. Soc. Amer.*, 102, 1–10, 1997.

59. Malischewsky, P., Surface Waves and Discontinuities, Elsevier, Amsterdam, 1987.

60. Malischewsky, P.G., Comment to "A new formula for the velocity of Rayleigh waves" by D. Nkemzi, [*Wave Motion*, 26, 199–205, 1997], *Wave Motion*, 31, 93–96, 2000.

61. Royer, D., A study of the secular equation for Rayleigh waves using the root locus method, *Ultrasonics*, 39, 223–225, 2001.

62. Nkemzi, D., A new formula for the velocity of Rayleigh waves, *Wave Motion*, 26, 199–205, 1997.

AU: Ref 52 (Every AG): Add more information (i.e., title of unpublished work).

63. Camley, R.E. and Nizzoli, F., Longitudinal resonance in surface acoustic phonons, *J. Phys. C. Solid Stat. Phys.*, 18, 4795–4804, 1985.

64. Sandercock, J.R., Light scattering from surface acoustic phonons in metals and semiconductors, *Solid State Commun.*, 26, 547–551, 1978.

65. Glass, N.E. and Maradudin, A.A., Leaky surface-elastic waves of both flat and strongly corrugated surfaces for isotropic, nondissipative media, *J. Appl. Phys.*, 54, 796–805, 1983.

66. Mozhaev, V.G., Bosia, F., and Weihnacht, M., Types of leaky SAW degeneracy in crystals, in Proc. *of 1998 IEEE Ultrasonics Symp.*, Levy, M., Schneider, S.C., and McAvoy, B.R., Eds., Institute of Electrical and Electronics Engineers, New York, 1998, pp. 143–148.

67. Rahman, N. and Barber, J.R., Exact expressions for the roots of the secular equation for Rayleigh waves, *ASME J. Appl. Mech.*, 62, 250–252, 1995.

68. Krüger, J.K., Brillouin spectroscopy and its application to polymers, in *Optical Techniques to Characterize Polymer Systems*, Bassler Elsevier, Amsterdam, 1989.

69. Zouboulis, E.S., Grimsditch, M., Ramdas, A.K., and Rodriguez, S., Temperature dependence of the elastic moduli of diamond: a Brillouin-scattering study, *Phys. Rev. B*, 57, 2889–2896, 1998.

70. Vogelgesang, R., Ramdas, A.K., Rodriguez, S., Grimsditch, M., and Anthony, T.R., Brillouin and Raman scattering in natural and isotopically controlled diamond, *Phys. Rev. B*, 54, 3989–3999, 1996.

71. Chirita, M., Xia, H., Sooryakumar, R., Tolle, J.B., Torres, V.M., Wilkens, B.J., Smith, D.J., Kouvetakis, J., and Tsong, I.S.T., Elastic properties of nanocrystalline zirconium–silicon–boron thin films, *J. Appl. Phys.*, 89, 4349–4353, 2001.

72. Djemia, P., Dugautier, C., Chauveau, T., Dogheche, E., De Barros, M.I., and Vandenbulcke, L., Mechanical properties of diamond films: A comparative study of polycrystalline and smooth fine-grained diamonds by Brillouin light scattering, *J. Appl. Phys.*, 90, 3771–3779, 2001.

73. Fukui, M., Toda, O., So, V.C.Y., and Stegemann, G.I., Surface plasmon enhanced Brillouin scattering from metal films, *Solid State Commun.*, 36, 995–1000, 1980.

74. Fukui, M., Toda, O., So, V.C.Y., and Stegemann, G.I., Enhanced Brillouin scattering involving surface plasmon polaritons, *J. Phys. C*, 14, 5591–5607, 1981.

75. Moretti, A.L., Robertson, W.M., Fisher, B., and Bray, R., Surface enhanced Brillouin scattering on silver films, *Phys. Rev. B*, 31, 3361–3368, 1985.

76. Robertson, W.M., Moretti, A.L., and Bray, R., Surface plasmon enhanced Brillouin scattering on silver films — double-resonance effect, *Phys. Rev. B*, 35, 8919–8928, 1987.

77. Rowell, N.L. and Stegeman, G.I., Brillouin scattering in thin film optical waveguides. II. Scattering theory, *Can. J. Phys.*, 60, 1804–1820, 1982.

78. Krüger, J.K., Embs, J., Brierley, J., and Jimenez, R., A new Brillouin scattering technique for the investigation of acoustic and opto-acoustic properties: application to polymers, *J. Phys. D: Appl. Phys.*, 31, 1913–1917, 1998.

79. Krüger, J.K., Embs, J., Lukas, S., Hartmann, U., Brierley, J., Beck, C.M., Jimenez, R., Alnot, P., and Durand, O., Spatial and angle distribution of internal stresses in nano- and microstructured chemical vapor deposited diamond as revealed by Brillouin spectroscopy, *J. Appl. Phys.*, 87, 74–77, 2000.

80. Vaughan, J.M., *The Fabry-Perot Interferometer*, Adam Hilger, Bristol, U.K., 1989.

81. Sandercock, J.R., Brillouin scattering study of SbSI using a double-passed, stabilised scanning interferometer, *Opt. Commun.*, 2, 73–76, 1970.

82. Dil, J.G. and Brody, E.M., Brillouin scattering from isotropic metals, *Phys. Rev. B*, 14, 5218–5227, 1976.

83. Dil, J.G. and van Hijningen, N.C.J., Brillouin scattering near a rigid interface, *Phys. Rev. B*, 22, 5924–5935, 1980.

84. Dil, J.G., van Hijningen, N.C.J., van Dorst, F., and Aarts, R.M., Tandem multipass Fabry-Perot interferometer for Brillouin scattering, *Appl. Opt.*, 20, 1374–1381, 1981.

85. Lindsay, S.M., Anderson, M.W., and Sandercock, J.R., Construction and alignment of a high performance multipass vernier tandem Fabry–Perot interferometer, *Rev. Sci. Instrum.*, 52, 1478–1486, 1981.

86. Hillebrands, B., Progress in multipass tandem Fabry–Perot interferometry: I. A fully automated, easy to use, self-aligning spectrometer with increased stability and flexibility, *Rev. Sci. Instrum.*, 70, 1589–1598, 1999.

87. Vacher, R. and Pelous, J., Behavior of thermal phonons in amorphous media from 4 to 300 K, *Phys. Rev. B*, 14, 823–828, 1976.

88. Tanaka, H. and Sonehara, T., Superheterodyne light beating spectroscopy for Rayleigh–Brillouin scattering using frequency-tunable lasers, *Rev. Sci. Instr.*, 73, 1998–2010, 2002.

89. Tanaka, H. and Sonehara, T., New method of superheterodyne light beating spectroscopy for Brillouin scattering using frequency-tunable lasers, *Phys. Rev. Lett.*, 74, 1609–1612, 1995.

90. Stoddart, P.R., Crowhurst, J.C., Every, A.G., and Comins, J.D., Measurement precision in surface Brillouin scattering, *J. Opt. Soc. Am. B*, 15, 2481–2489, 1998.

91. Agarwal, G.S., Interaction of electromagnetic waves at rough dielectric surfaces, *Phys. Rev. B*, 15, 2371–2383, 1977.

92. Zhang, X., Sooryakumar, R., Every, A.G., and Manghnani, M.H., Observation of organ-pipe acoustic excitations in supported thin films, *Phys. Rev. B*, 64, 081402(R), 2001.

93. Vacher, R. and Boyer, L., Brillouin scattering: A tool for the measurement of elastic and photoelastic constants, *Phys. Rev. B*, 6, 639–673, 1972.

94. Fioretto, D., Carlotti, G., Socino, G., Modesti, S., Cepek, C., Giovannini, L., Donzelli, O., and Nizzoli, F., Brillouin-scattering determination of the elastic constants of epitaxial fcc C_{60} film, *Phys. Rev. B*, 52, R8707–R8710, 1995.

95. Lefeuvre, O., Pang, W., Zinin, P., Comins, J.D., Every, A.G., Briggs, G.A.D., Zeller, B.D., and E.T.G., Determination of the elastic properties of a barrier film on aluminium by Brillouin spectroscopy, *Thin Solid Films*, 350, 53–58, 1999.

96. Beghi, M.G., Bottani, C.E., and Pastorelli, R., High accuracy measurement of elastic constants of thin films by surface Brillouin scattering, in *Mechanical Properties of Structural Films*, Muhlstein, C. and Brown, S.B., American Society for Testing and Materials, Conshohoken, PA, 2001, pp. 109–126.

97. Comins, J.D., Every, A.G., Stoddart, P.R., Zhang, X., Crowhurst, J.C., and Hearne, G.R., Surface Brillouin scattering of opaque solids and thin supported films, *Ultrasonics*, 38, 450–458, 2000.

98. Zhang, X., Stoddart, P.R., Comins, J.D., and Every, A.G., High-temperature elastic properties of a nickel-based superalloy studied by surface Brillouin scattering, *J. Phys. Condens. Matter.*, 13, 2281–2294, 2001.

99. Makarov, S., Chilla, E., and Frolich, H.J., Determination of elastic constants of thin films from phase velocity dispersion of different surface acoustic wave modes, *J. Appl. Phys.*, 78, 5028–5034, 1995.

100. Beghi, M.G., Ferrari, A.C., Bottani, C.E., Libassi, A., Tanner, B.K., Teo, K.B.K., and Robertson, J., Elastic constants and structural properties of nanometre-thick diamond-like carbon films, *Diamond Relat. Mater.*, 11, 1062–1067, 2002.

101. Nizzoli, F., Bhadra, R., Delima, O.F., Brodsky, M.B., and Grimsditch, M., Problems with the determination of elastic constants from higher order surface waves: results for Al on NaCl, *Phys. Rev. B*, 37, 1007–1010, 1988.

102. Lee, S., Hillebrands, B., Stegeman, G.I., Cheng, H., Potts, J.E., and Nizzoli, F., Elastic properties of epitaxial ZnSe(001) films on GaAs measured by Brillouin spectroscopy, *J. Appl. Phys.*, 63, 1914–1916, 1988.

103. Beghi, M.G., Bottani, C.E., Ossi, P.M., Lafford, T.A., and Tanner, K., Combined surface Brillouin scattering and x-ray reflectivity characterization of thin metallic films, *J. Appl. Phys.*, 81, 672–678, 1997.

104. Crowhurst, J.C., Hearne, G.R., Comins, J.D., Every, A.G., and Stoddart, P.R., Surface Brillouin scattering at high pressure: Application to a thin supported gold film, *Phys. Rev. B*, 60, R14990–R14993, 1999.

105. Zinin, P., Manghnani, M.H., Tkachev, S., Askarpour, V., Lefeuvre, O., and Every, A., Brillouin spectroscopy of surface in thin film Si3N4 on GaAs, *Phys. Rev. B*, 60, 2844–2850, 1999.

106. Manghnani, M.H., Tkachev, S., Zinin, P.V., Zhang, X., Brazhkin, V.V., Lyapin, A.G., and Trojan, I.A., Elastic properties of superhard amorphous carbon pressure synthesized from C_{60} by surface Brillouin scattering, *Phys. Rev. B*, 6412 (12), 121403, 2001.

107. Chirita, M., Sooryakumar, R., Xia, H., Monteiro, O.R., and Brown, I.G., Observation of guided longitudinal acoustic modes in hard supported layers, *Phys. Rev. B*, 60 (8), 5153–5156, 1999.

108. Ferrari, A.C., Robertson, J., Beghi, M.G., Bottani, C.E., Ferulano, R., and Pastorelli, R., Elastic constants of tetrahedral amorphous carbon films by surface Brillouin scattering, *Appl. Phys. Lett.*, 75, 1893–1895, 1999.

109. Beghi, M.G., Ferrari, A.C., Teo, K.B.K., Robertson, J., Bottani, C.E., Libassi, A., and Tanner, B.K., Bonding and mechanical properties of ultrathin diamond-like carbon films, *Appl. Phys. Lett.*, 81, 3804–3806, 2002.

110. Kim, J.O., Achenbach, J.D., Mirkarimi, P.B., Shinn, M., and Barnett, S.A., Elastic constants of single-crystal transition-metal nitride films measured by line-focus acoustic microscopy, *J. Appl. Phys.*, 72, 1805–1811, 1992.

111. Nizzoli, F., Hillebrands, B., Lee, S., Stegeman, G.I., Duda, G., Wegner, G., and Knoll, W., Determination of the whole set of elastic-constants of a polymeric Langmuir-Blodgett film by Brillouin spectroscopy, *Phys. Rev. B*, 40, 3323–3328, 1989.

112. Ghislotti, G. and Bottani, C.E., Brillouin scattering from shear horizontal surface phonons in silicon-on-insulator structures: theory and experiment, *Phys. Rev. B*, 50, 12131–12137, 1994.

113. Casari, C.S., LiBassi, A., Bottani, C.E., Barborini, E., Piseri, P., Podesta, A., and Milani, P., Acoustic phonon propagation and elastic properties of cluster-assembled carbon films investigated by Brillouin light scattering, *Phys. Rev.*, 64, 085417, 2001.

114. Lee, S.A. and Lindsay, S.M., Surface Brillouin scattering from graphite, *Phys. State Solid, B*, 157, K 83–K 86, 1990.

115. Boekholt, M., Harzer, J.V., Hillebrands, B., and Guntherodt, G., Determination of the sound velocities and the complete set of elastic-constants for $Bi_2Sr_2CaCu_2O_8$+delta single-crystals using Brillouin light scattering, *Physica C*, 179, 101–106, 1991.

116. Wittkowski, T., Jorzick, J., Jung, K., and Hillebrands, B., Elastic properties of thin h-BN films investigated by Brillouin light scattering, *Thin Solid Films*, 353, 137–143, 1999.

117. Grimsditch, M., Bhadra, R., and Schuller, I.K., Lamb waves in unsupported thin films: a Brillouin scattering study, *Phys. Rev. Lett.*, 58, 1216–1219, 1987.

118. Pastorelli, R., Tarantola, S., Beghi, M.G., Bottani, C.E., and Saltelli, A., Design of surface Brillouin scattering experiments by sensitivity analysis, *Surf. Sci.*, 468, 37–50, 2000.

119. Bortolani, V., Nizzoli, F., Santoro, G., and Sandercock, J.R., Strong interference effects in surface Brillouin scattering from a supported transparent film, *Phys. Rev. B*, 25, 3442–3445, 1982.

120. Murugavel, P., Narayana, C., Govindaraj, A., Sood, A.K., and Rao, C.N.R., Brillouin scattering from C70 and C60 films: a comparative study of elastic properties, *Chem. Phys. Lett.*, 331, 149–153, 2000.

121. Blank, V.D., Buga, S.G., Serebryanaya, N.R., Dubitsky, G.A., Mavrin, B.N., Popov, M.Y., Bagramov, R.H., Prokhorov, V.M., Sulyanov, S.N., Kulniskiy, B.A., and Tatyanin, Y.V., Structures and physical properties of superhard and ultra-hard 3D polymerized fullerites created from solid C_{60} by high pressure high temperature treatment, *Carbon*, 36, 665–670, 1998.

122. Pastorelli, R., Ossi, P.M., Bottani, C.E., Checchetto, R., and Miotello, A., Elastic constants of cubic boron nitride films, *Appl. Phys. Lett.*, 77, 2168–2170, 2000.

123. Mirkarimi, P.B., McCarty, K.F., and Medlin, D.L., Review of advances in cubic boron nitride film synthesis, *Mater. Sci. Eng.*, R21, 47–100, 1997.

124. Sussner, H., Pelous, J., Schmidt, M., and Vacher, R., Brillouin scattering from surface waves on Al-coated transparent media, *Solid State Commun.*, 36, 123–125, 1980.

125. Aleksandrov, V.V., Gladkevitch, A., Mozhaev, V.G., Giovannini, L., and Nizzoli, F., Brillouin scattering study of the pseudosurface acoustic mode on the (110) face of cubic-crystals having elastic anisotropy ratio above unity, *J. Appl. Phys.*, 76, 2176–2180, 1994.

126. Mendik, M., Sathish, S., Kulik, A., Gremaud, G., and Wachter, P., Surface acoustic wave studies on single crystal nickel using Brillouin scattering and scanning acoustic microscope, *J. Appl. Phys.*, 71, 2830–2834, 1992.

127. Mendik, M. and Sathish, S., Response to comment on Surface acoustic wave studies on single crystal nickel using Brillouin scattering and scanning acoustic microscope [*J. Appl. Phys.*, 75, 5459, 1994], *J. Appl. Phys.*, 75 (10 Pt1), 5461–5462, 1994.

128. Briggs, A., *Acoustic Microscopy*, Clarendon Press, Oxford, 1992.

129. Maznev, A.A. and Every, A.G., Secluded supersonic surface waves in germanium, *Phys. Lett. A*, 197, 423–427, 1995.

130. Zuk, J., Kiefte, H., and Clouter, M.J., Brillouin scattering study of surface acoustic waves in crystalline GaP, *J. Appl. Phys.*, 72, 3504–3508, 1992.

131. Kuok, M.H., Ng, S.C., and Zhang, V.L., A Brillouin study of the angular dispersion of generalized surface and pseudosurface acoustic waves on the (001) surface of InSb, *Appl. Phys. Lett.*, 77, 1296, 2000.

132. Kuok, M.H., Ng, S.C., and Zhang, V.L., Angular dispersion of surface acoustic waves on (001), (110), and (111) GaAs, *J. Appl. Phys.*, 89, 7899–7902, 2001.

133. Kuok, M.H., Ng, S.C., and Liu, T., Brillouin scattering from pseudo surface acoustic waves in (111) silicon, *Solid State Commun.*, 110, 185, 1999.

134. Lim, T.C. and Farnell, G.W., Character of pseudo surface waves on anisotropic crystals, *J. Acoust. Soc. Am.*, 45, 845–851, 1969.

135. Jiang, X., Zhou, J.W., Reichelt, K., and Gruenberg, P., The study of mechanical properties of a-C:H films by Brillouin scattering and ultralow load indentation, *J. Appl. Phys.*, 66, 4729–4735, 1990.
136. Every, A.G. and Sachse, W., Sensitivity of inversion algorithms for recovering elastic constants of anisotropic solids from longitudinal wavespeed data, *Ultrasonics*, 30, 43–48, 1992.
137. Yoshihara, A., Fujimura, T., Oka, Y., Fujisaki, H., and Shirotani, I., Surface Brillouin scattering in black phosphorus, *Phys. Rev. B*, 34, 7467–7470, 1986.
138. Carlotti, G., Fioretto, D., Socino, G., and Verona, E., Brillouin-scattering determination of the whole set of elastic constants of a single transparent film of hexagonal symmetry, *J. Phys.: Condens. Mater.*, 7, 9147–9153, 1995.
139. Ohring, M., *The Materials Science of Thin Films*, Academic Press, Inc., Boston, 1992.
140. Bhadra, R., Grimsditch, M., Schuller, I. K., and Nizzoli, F., Brillouin scattering from unsupported Al films, *Phys. Rev. B*, 39, 12456–12459, 1989.
141. Tiersten, H.F., Elastic surface waves guided by thin films, *J. Appl. Phys.*, 40, 770–789, 1969.
142. Bortolani, V., Nizzoli, F., Santoro, G., Marvin, A.M., and Sandercock, J. R., Brillouin scattering from surface phonons in Al-coated semiconductors, *Phys. Rev. Lett.*, 43, 224–227, 1978.
143. Hillebrands, B., Baumgart, P., Mock, R., Guntherodt, G., and Bechthold, P.S., Dispersion of localized elastic modes in thin supported gold layers measured by Brillouin-scattering, *J. Appl. Phys.*, 58, 3166–3168, 1985.
144. Karanikas, J.M., Sooryakumar, R., and Phillips, J.M., Dispersion of elastic waves in supported CaF$_2$ Films, *J. Appl. Phys.*, 65, 3407–3410, 1989.
145. Carlotti, G., Socino, G., and Verona, E., Investigation of elastic properties of ZnO films by Brillouin scattering, *J. Appl. Phys.*, 65, 1370–1372, 1989.
146. Sun, L., Dutcher, J.R., Giovannini, L., Nizzoli, F., Stevens, J.R., and Ord, J.L., Elastic and elasto-optic properties of thin-films of poly(styrene) spin-coated onto Si(001), *J. Appl. Phys.*, 75, 7482–7488, 1994.
147. Lefeuvre, O., Characterisation of stiffening layers by acoustic microscopy and Brillouin spectroscopy, D. Phil. thesis, University of Oxford, 1998.
148. Bortolani, V., Nizzoli, F., and Santoro, G., Brillouin scattering at interfaces and long wave-length acoustic phonons, *J. De Physique*, 45, 45–53, 1984.
149. Bell, J.A., Zanoni, R., Seaton, C.T., Stegeman, G.I., Makous, J., and Falco, C.M., Elastic constants of, and Stonely waves in, molybdenum films measured by Brillouin scattering, *Appl. Phys. Lett.*, 52, 610–612, 1988.
150. Jorna, R., Visser, D., Bortolani, V., and Nizzoli, F., Elastic and vibrational properties of nickel films measured by surface Brillouin scattering, *J. Appl. Phys.*, 65, 718–725, 1989.
151. Liu, A.Y. and Cohen, M.L., Prediction of new low compressibility solids, *Science*, 245, 841–842, 1989.
152. Pang, W., Stoddart, P.R., Comins, J.D., Every, A.G., Pietersen, D., and Marais, P.J., Elastic properties of TiN hard films at room and high temperatures using Brillouin scattering, *Int. J. Refrac. Metals Hard Mater.*, 15, 179–185, 1997.
153. Lefeuvre, O., Zinin, P., and Briggs, G.A.D., Leaky surface waves propagating on a fast on slow system and the implications for material characterization, *Ultrasonics*, 36, 229–232, 1998.
154. Lefeuvre, O., Zinin, P., Briggs, G.A.D., and Every, A., Surface wave dispersion beyond cutoff for a fast layer on a slow substrate, *Appl. Phys. Lett.*, 72, 856–857, 1998.

155. Wittkowski, T., Cortina, P., Jorzick, J., Jung, K., and Hillebrands, B., Brillouin light scattering from surface phonons in hexagonal and cubic boron nitride films, *Diamond Relat. Mater.*, 9, 1957–1964, 2000.

156. Zinin, P., Manghnani, M.H., Zhang, X., Feldermann, H., Ronning, C., and Hofsass, H., Surface Brillouin scattering of cBN films, *J. Appl. Phys.*, 91, 4196–4204, 2002.

157. Pang, W., Every, A.G., Comins, J.D., Stoddart, P.R., and Zhang, X., Brillouin scattering from acoustic excitations in TiN films on high speed steel—A stiffening system, *J. Appl. Phys.*, 86, 311–317, 1999.

158. Hickernell, T.S., Fliegel, F.M., and Hickernell, F.S., The elastic properties of thin-film siliconnitride, in *Proc. IEEE 1990 Ultrasonics Symp.*, McAvoy, B.R., Ed., Institute of Electrical and Electronics Engineers, New York, 1990, pp. 445–449.

159. Subramanian, S., Sooryakumar, R., Prinz, G.A., Jonker, B.T., and Idzerda, Y.U., Elastic constants of body-centered cubic cobalt films, *Phys. Rev. B*, 49, 17319–17324, 1994.

160. Lefeuvre, O., Kolosov, O.V., Every, A.G., Briggs, G.A.D., and Tsukahara, Y., Elastic measurements of layered nanocomposite materials by Brillouin spectroscopy, *Ultrasonics*, 38, 459–465, 2000.

161. Grimsditch, M., Effective elastic constants of superlattices, *Phys. Rev. B*, 31, 6818–6819, 1985.

162. Grimsditch, M. and Nizzoli, F., Effective elastic constants of superlattices of any symmetry, *Phys. Rev. B*, 33, 5891–5892, 1986.

163. Bell, J.A., Bennett, W.R., Zanoni, R., Stegeman, G.I., Falco, C.M., and Nizzoli, F., Elastic constants of Mo/Ta superlattices measured by Brillouin scattering, *Phys. Rev. B*, 35, 4127–4130, 1987.

164. Osetrov, A.V., Frohlich, H.J., Koch, R., and Chilla, E., Acoustoelastic effect in anisotropic layered structures, *Phys. Rev. B*, 62, 13963, 2000.

11

Theory and Applications of Acoustic Microscopy

Pavel V. Zinin and Wieland Weise

All things should be done as simple as possible, but not simpler.

Albert Einstein

CONTENTS

11.1 Introduction

Modern technologies require materials that withstand extreme conditions with high reliability. One of the key parameters that have a strong impact on the life expectancy of a material is its microstructure. The acoustic microscope was developed as a tool for studying the internal microstructure of nontransparent solids. In acoustic microscopy, a sample is imaged by ultrasound waves, and the contrast in reflection furnishes a map of the spatial distribution of the mechanical properties. Several books and handbook articles[1-4] give detailed historical outlines. Briefly, the development of the first high-frequency scanning acoustic microscope was motivated by the idea of using an acoustic field to study the spatial variations of the elastic material properties with nearly optical resolution. The first experiments date back to the 1940s when high-frequency acoustic images were obtained by the Leningrad scientist Sokolov.[5] He observed an acoustical image using the tube named after him, in which the acoustic picture was converted into a television display. The first scanning acoustic microscope was created by Lemons and Quate at Stanford University in 1973.[6] It was mechanically driven and operated in the transmission mode. Since then, gradual mechanical and electronic circuit improvements have been made and image recording has been automated. In general, acoustic microscopes now work in the reflection mode,[7] which will be described in the next section.

Many applications are described in the 1992 book *Acoustic Microscopy*.[2] Considerable progress in the acoustic microscopy of solid structures has been made since then. Developments in the theory of the image formation of subsurface defects[8] and three-dimensional objects[9,10] allow size and location of objects inside solids to be determined. Combining the time-of-flight technique with acoustic microscopy provides a powerful tool for investigating adhesion problems[11] as well as the microstructure of small superhard samples.[12] Acoustic microscopy can be used to visualize stress inside solid materials[13]. With the development of the ultrasonic force microscope[14] and the atomic force acoustic microscope,[15] the capability of the conventional acoustic microscope has been expanded to nanometer resolution. Recent developments in quantitative acoustic microscopy are described in the series *Advances in Acoustic Microscopy*.[16,17]

The main objective of this chapter is twofold. First, we will describe the main principles and the theory of image formation and interpretation in acoustic microscopy. Second we will to demonstrate the capabilities of acoustic microscopy as a nondestructive tool for studying the microstructure of modern materials.

11.2 Basic Principles of the SAM

The scanning acoustic microscope (SAM) can be characterized by a combination of operating principles distinguishing it from other microscope types.

These principles are image generation by scanning, far-field wave imaging, and the use of acoustic waves.

Image generation by scanning is basically different from the functionality of a conventional optical microscope, which is the oldest microscope type. The conventional microscope can be considered a parallel processing system[18] in which we can see all points of the object at the same time. In contrast to this, the SAM is a sequential imaging system in which a piezo-electric transducer emits a focused ultrasound beam that propagates through a coupling liquid, usually water, to the sample. The beam is scattered by the sample, and the scattered ultrasound wave is detected piezoelectrically. The output signal is just one single voltage. As the sample is scanned, the voltage is recorded in each scanning position of the focus and a grayscale image is generated. While medical ultrasound devices scan by electronic beam-steering, acoustic microscopes mechanically move either the microscope head or the sample.

The use of a focused beam leads to the second operating principle. As the focus is formed by converging propagating waves, the size of the focal spot (or focal area) is limited by diffraction. Also, as the detector is positioned remote from the sample, no near-field effects of the waves can be deployed. This distinguishes the SAM from near-field microscopes, including scanning atomic force acoustic microscopes. Two different techniques are commonly used to achieve convergence of the ultrasound wave in the SAM. The simplest way to generate a focused beam is to employ a piezoelectric transducer, which is already shaped like a spherical cap. Another technique is used in high resolution microscopes, where the ultrasound wave is focused by means of an acoustic lens made from a buffer rod (Figure 11.1). A flat transducer is connected to one end face of the buffer rod. A spherical cavity is ground
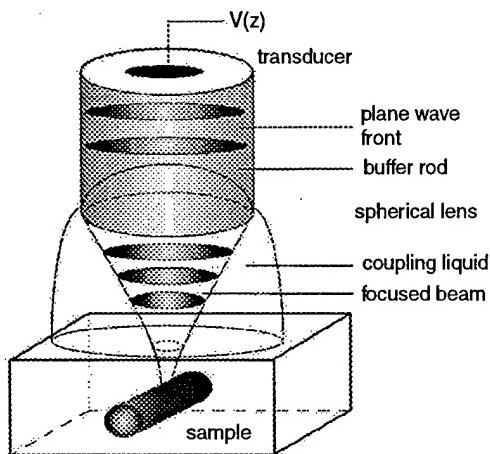

FIGURE 11.1
Schematic diagram of the reflection acoustic microscope.

into the other face, which is coated with a quarter-wavelength matching layer to increase transmission. The ultrasound radiated from the lens is coupled by a fluid (usually water) to the surface of a solid sample. The spherical lens, (i.e., the lens with a spherical cavity) focuses sound onto a spot whose size is comparable with the sound wavelength in the fluid (Figure 11.1). For nondestructive testing purposes, cylindrical lenses, which have a line focus are often applied. Their performance is better than that of spherical lenses for the examination of surface waves propagating in aniso-tropic media.[19]

The acoustical microscopes for nondestructive testing usually operate in reflection mode. In the reflection microscope, the same lens and transducer as for emission are used to gather the waves reflected back from the sample (Figure 11.1). The reflection microscope therefore is always a confocal device. The term confocal indicates that both the detection and the emission are focused and that the two focal points coincide.[18] The confocal setup sup-presses contrast from sample areas outside the focal point and thus yields higher resolution. In the transmission microscope, the forward scattered waves are detected by a second unit, and confocal operation is possible by adjustment of the detector.

The reflection acoustic microscope operates in the pulse-echo mode[20]; the same transducer emits the acoustic wave and receives the signal scattered from the sample. In most SAMs, the transducer is excited with a narrowband tone-burst. Time-limited excitation is used so that the first reflection from the sample can be gated out.[21] However, the theoretical framework for inter-preting images is simpler when a single frequency is considered. More details regarding the electrical circuit and the type of signal used in the acoustic microscope can be found elsewhere.[2,20]

Imaging with ultrasound is the third operating principle. The operating frequencies of SAMs are between 100 MHz and 2 GHz; the high frequency provides the opportunity to obtain accurate measurement results for crack and void distributions with a resolution of up to 1 μm at a depth of 10 μm. The use of higher frequencies is restricted by the presence of wave attenu-ation in the coupling liquid, which is proportional to the frequency squared. The maximum possible working distance between the microscope and a sample therefore is about 60 μm at 2 GHz. The electroacoustic transducer always emits and detects the sound coherently. This is the reason why acoustical images can exhibit granular artifact structures, the so-called speckle. Speckle in ultrasound imaging (and all coherent imaging systems) is caused by the interference of waves from randomly distributed scatterers, which are too small to be resolved by the imaging system. The speckle degrades both the spatial and the contrast resolution in acoustical images, but in the SAM it fortunately does not often occur.

In optics a similar type of microscope exists — the scanning optical micro-scope (SOM). Though in this microscope light waves are used for imaging while acoustic waves are used in the SAM, the theory of image formation is very similar for the two types of microscopes.[22] Because of that similarity,
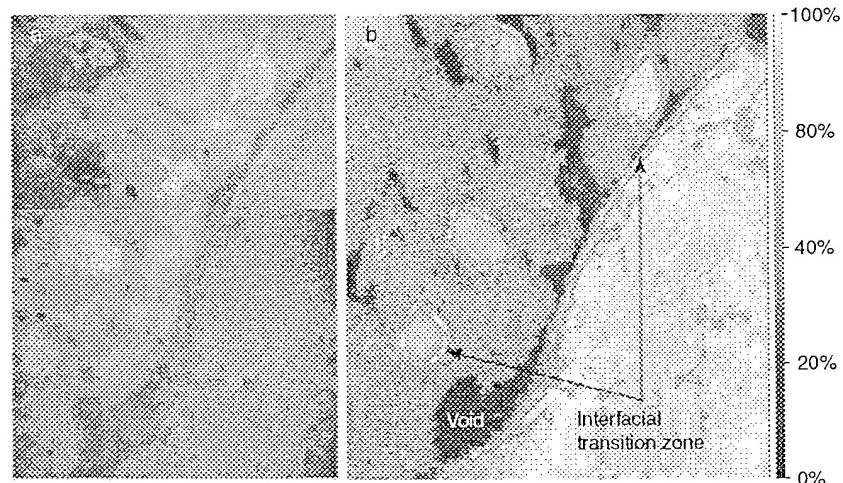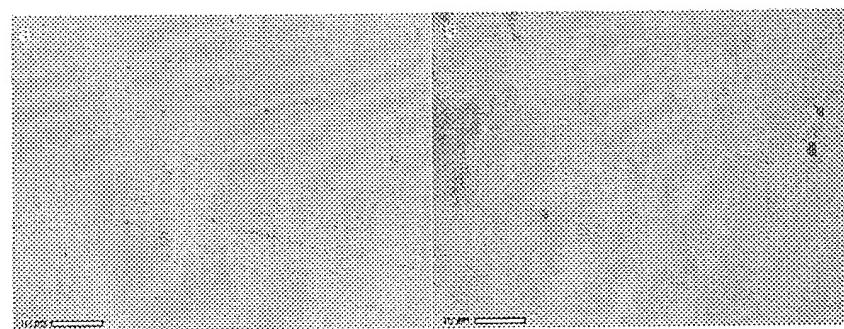
FIGURE 11.2

(a) Optical image of a concrete sample made with limestone aggregate grains. Magnification 50*1.25; (b) Acoustical image of the same sample. The acoustic image was made at ultrasound frequency 400 MHz, defocus value $Z = 0$. The image size is 1000*1000 μm.

most characteristic parameters developed for optical confocal microscopy, such as point spread function, optical transfer function,[23] and pupil function,[24] can also be used in scanning acoustic microscopy. We will describe all these functions in the next section. The type of microscope that is applied for a particular task depends on the difference in underlying contrast mechanisms that reveal different physical properties. Optical images reflect the variation of optical properties such as the refractive index of the sample surface; the contrast in acoustic images is determined by the variation of the acoustical impedance.[25] Figure 11.2 shows optical and acoustical images of a concrete sample loaded with ettringite. Two features can be distinguished in the acoustical image. First, there is a rim around the aggregates that is not visible in the optical micrograph; second, large voids can be seen in the acoustical image. The rim was identified as the interfacial transition zone filled with ettringite.[26] Identification of the interfacial transition zone is of importance for the concrete industry, as it is considered an important factor of concrete deterioration.

For some materals the SAM provides information invisible even in the scanning electron microscope. Figure 11.3 shows acoustic and scanning electron microscope images of a granitic aggregate in a cement matrix. The various mineral compositions were identified by energy dispersive (X-ray) spectroscopy analysis.[27] The acoustic image in Figure 11.3 demonstrates various types of aggregate grain boundaries within the matrix.[28] The quartz grains, and to some extent also the plagioclase grains, have sharp and well defined boundaries. The acoustical images are much sharper than the scanning electron

Ultrasonic Nondestructive Evaluation
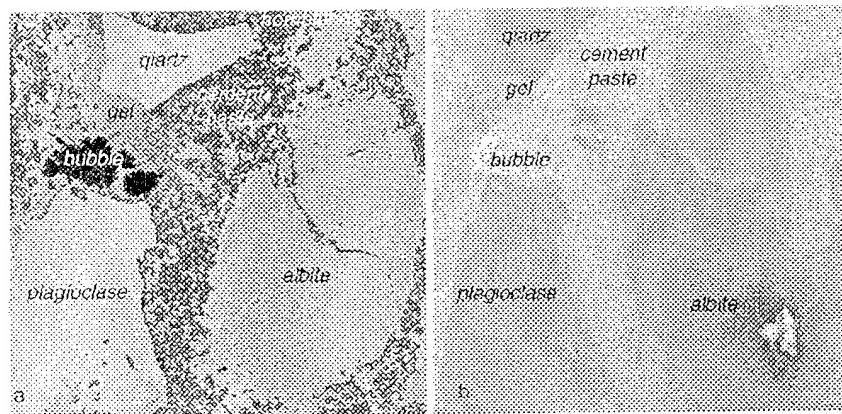
FIGURE 11.3
(a) Acoustic and (b) the scanning electron microscope images of a concrete sample made with granitic aggregate grains and Portland cement paste. The acoustic image was made at 400 MHz, $Z = 0$. The image size is $1000*1000$ μm. (From Prasad, M. et al., *J. Mater. Sci.*, 35, 3607, 2000. With permission.)

FIGURE 11.4
SAM image made by OXSAM of a standard epoxy layer on aluminum at 300 MHz: (a) $Z = 0$; (b) $Z = -20$ μm.

microscope image. This is important for analysis, as the smooth boundaries of quartz and plagioclase grains imply chemical inertness of the aggregates.

Images made by the SAM are called C-scans. They are obtained when the acoustic microscope mechanically scans a sample in a plane parallel to the sample surface. Figure 11.4 represents C-scan images of an epoxy layer on aluminum at different defocus positions (Z). Images obtained at different defocus positions allow the depth of voids to be located and their size to be estimated. Voids can be considered as strong scatterers and the brightness of the small void image is maximal when the focal point of the microscope is in coincidence with the void. The image of the side of an epoxy layer reveals

many small surface defects as can be seen from Figure 11.4(a). The image in Figure 11.4(b) is focused on the epoxy/aluminum interface; bright spots can therefore be attributed to voids or small bubbles close to the interface.

The first transmission SAM, created by Lemons and Quate, was a confocal microscope, as the focal point of the transmitting lens was in coincidence with that of the receiving lens. It is interesting to note that the transmission microscope is mostly used in nonconfocal mode, in a two-lens acoustic microscope.[4] Two-lens microscopy permits a variety of different techniques. In the ultrasonic flux imaging technique[29,30], two point focus lenses are focused on the opposite faces of a crystal. Such a lens configuration makes visible a fascinating picture of bulk sound waves propagating in an anisotropic solid—a very effective method of determining elastic constants of crystals.[31] Tsukahara et al.[32] used a spherical lens as the transmitter and a planar transducer as the detector to measure the reflection coefficients of anisotropic solids.

Time-resolved acoustic microscopy adds an additional degree of freedom to visualize the internal microstructure of solids, namely time-of-flight. For layered materials, the reflected signal represents a train of pulses. The signal detected is displayed vs. the time of occurrence (A-scan). The first pulse is attributed to the reflection from the liquid/sample interface. The second pulse appears as a result of reflection from the first internal interface. The time delay of the pulses and their amplitudes provides information about the elastic properties and attenuation of sound in the layer. The combination of the time-of-flight method with mechanical scanning along a line is called B-scan. The B-scan produces a sectional view through the sample. Time-resolved acoustic microscopy helps to investigate adhesion problems,[11] and is a very powerful tool for characterizing subsurface cracks.[33] Figure 11.5 shows C- and B-scans of blister located at the interface between epoxy coating and aluminum at
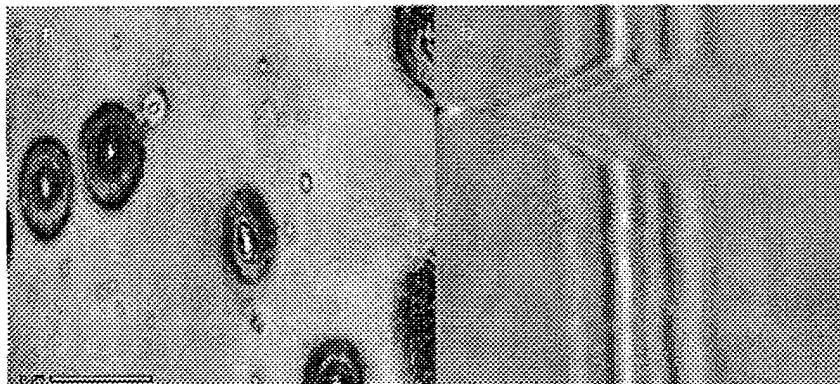

FIGURE 11.5

SAM image made by OXSAM of a 1-μm epoxy layer on 10-μm oxide anodized alumina on aluminum at 300 MHz: (a) $Z = -15$ μm; (b) time-resolved image made at $Z = -15$ μm, field of view is 50 nsec*300 μm.

Ultrasonic Nondestructive Evaluation

300 MHz of a 1-μm epoxy layer on a 101-μm oxalic acid anodized oxide layer on aluminum. The blisters were developed in the sample during 11 days in hot water (60°C). Images were made by OXSAM, the microscope built in Oxford.[34] The time-resolved image (Figure 11.5[b]) makes the shape of the blister visible and also provides information about delaminations.

## 11.3 Theory of Image Formation in the SAM

One of the main features of acoustic microscopy is the possibility to visualize structures below the object surface, as no material is totally acoustically opaque. In acoustic microscopy we therefore have to do with three-dimensional image formation; reflected acoustic waves come not only from a single plane, but also from the layers located above and below the focal plane. As a result, SAM images are often difficult to interpret directly, and a theoretical formulation is required to understand their basic features. A theory is also necessary to obtain quantitative information about subsurface features such as location and size of voids and elastic properties of subsurface micro-objects.

To obtain the analytical solution of the output signal of the microscope we assume that the duration of the radio frequency signal of the microscope is long enough to justify continuous-wave analysis for the scattering problem. For example,[35] the field of the radiator may be described as a continuous wave solution if the pulse train contains several oscillations of the carrier frequency and the pulse length is large in comparison to the sample area relevant to contrast formation.

The direct way to derive the output signal of the acoustic microscope consists of five steps:

1. Simulation of the propagation inside a sapphire rod of the acoustical wave generated by a piezoelectric transducer situated at one end

2. Diffraction of the sound wave by a spherical cavity serving as the focusing lens at the other end and propagation of the focused wave through an immersion liquid to the sample

3. Analysis of the sound backscattered by the object

4. Diffraction of the backscattered waves by the spherical cavity

5. Propagation of the acoustic wave through the rod and generation of the electrical signal by the transducer

Each of these steps requires tedious simulations. Fortunately, application of the electromechanical reciprocity principle as formulated by Auld[36] and of the Fourier transform approach (spectrum approach) provides an elegant way to formulate the theory of image formation in scanning acoustic microscopy in an analytical form.[9,10,37,38] With the aid of the reciprocity principle,
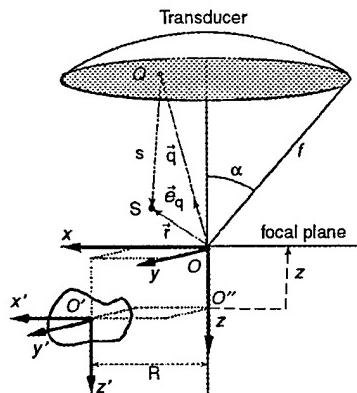
FIGURE 11.6

Model of the reflection acoustic microscope used for calculation: spherical transducer with focal length f, three-dimensional object defocused by Z, and shifted aside by R.

the detection properties of the microscope can be attributed to the emission properties.[37] With the spectrum approach the propagation of waves from one plane to another parallel one can be described simply by including a propagation factor. In the following paragraphs we will formulate the theory of the image formation in reflection and transmission microscopes using the Fourier spectrum approach.[9,10]

The model of the reflection acoustic microscope as it is used for calculation is presented in Figure 11.6. A time harmonic acoustic field at an arbitrary position in the immersion liquid can be represented by its scalar potential $\Phi(x,y,z)$ (see Chapter 1). The time factor $\exp(-it)$ is suppressed as follows, ω being angular frequency. As Φ must satisfy the Helmholtz equation, every solution can be decomposed into plane waves $\exp(ik_x x + ik_y y + ik_z z)$ with wave vector $k = (k_x, k_y, k_z)$, $|k| = \omega/c$, and c being the velocity of sound in the coupling liquid. If $k_x^2 + k_y^2 \leq k^2$, then $k_z = \pm\sqrt{k^2 - k_x^2 - k_y^2}$. Such waves are denoted as homogeneous waves. The positive or negative sign is for waves propagating in the positive or negative z-direction, respectively. If $k_x^2 + k_y^2 > k_z$, then $k_z = \pm i\sqrt{k_x^2 + k_y^2 - k^2}$ will be imaginary.[39] This means that the wave exponentially decays in the positive or negative z-direction, respectively. Such waves are denoted as evanescent waves. They are important to describe a field in the vicinity of irregular structures (near-field imaging). We assume that the whole acoustic wave with a potential Φ is propagating and evanescing either in the positive or in the negative z-direction, and the sign of k_z is therefore unambiguous. The two-dimensional angular spectrum $U(k_x, k_y, z)$ of $\Phi(x, y, z)$ at fixed coordinate $z = Z$ is then defined by the double Fourier integral[39]

$$U(k_x, k_y, Z) = \int_{-\infty}^{\infty} \int_{-\infty}^{\infty} \Phi(x, y, Z) \exp[-i(k_x x + k_y y)] dx\, dy \qquad (11.1)$$

Conversely, the potential can then be written as the inverse Fourier transform of the angular spectrum.

$$\Phi(x, y, Z) = \frac{1}{(2\pi)^2} \int\limits_{-\infty}^{\infty} \int\limits_{-\infty}^{\infty} U(k_x, k_y, Z) \exp[i(k_x x + k_y y)] dk_x dk_y \qquad \textbf{(11.2)}$$

The inverse Fourier transform (Equation 11.2) represents the acoustic field in the plane Z as a superposition of plane waves $\exp(ik_x x + ik_y y)$. A detailed description of the Fourier transform and its properties can be found elsewhere.[40] Atalar[37] applied Auld's reciprocity principle to derive the output voltage V of the detector of the reflection SAM in terms of angular spectra on an arbitrary plane z

$$V = \int\limits_{-\infty}^{\infty} \int\limits_{-\infty}^{\infty} U_i(-k_x, -k_x) U_s(k_x, k_x) k_z dk_x dk_y \qquad \textbf{(11.3)}$$

where $U_i(k_x, k_y)$ is the angular spectrum of the field the microscope detector emits into the coupling liquid, $U_s(k_x, k_y)$ is the angular spectrum of the field resulting from scattering of the field incident on the object. It is the spectrum of the field the microscope detects. In Equation 11.3 a proportionality constant is omitted. The position of the plane z at which the spectra are evaluated is the same for both but z can be chosen arbitrarily. In the following, we will take the spectra in the focal plane where they might occur only virtually if the focus lies inside the object. We can interpret the signal generation as follows: A scattered field plane wave component with a particular wave vector (k_x, k_y, k_z) is weighted with the emission strength of the emitted plane wave with wave vector $(-k_x, -k_y, -k_z)$. So the weighting factor belongs to the emitted plane wave traveling exactly in the direction opposite to the detected plane wave. The weighting factor represents the detection properties of the transducer which are equal to the emission properties. This is a consequence of the electromechanical reciprocity principle for transducers. Finally, the detection is integrated coherently.

The expression in Equation 11.3 is also valid for the transmission microscope.[37] Then U_i is the spectrum the detecting transducer would emit if it were driven as the source. Note that for both microscope types U_i describes properties of the detector. A comprehensive derivation of Equation 11.3 can be found elsewhere.[41] Representation of the output signal in the form of Equation 11.3 provides a relatively simple way to omit steps (4) and (5) in the description. The problem of image formation therefore reduces to the simulation of the incident beam and to its scattering by an object.

The microscope is most easily modeled as a focusing transducer with the shape of a spherical cap radiating directly into the coupling liquid (Figure 11.6). We describe the strength of the emitted wave field along the transducer surface by the pupil function $P(\theta, \varphi)$, with θ and φ denoting the meridianal

and azimuthal angles of the vector from a point on the transducer surface to the focal point (see Figure 11.6). The origin of the coordinate system is placed in the focus of the transducer. The positive z-direction is chosen away from the emitter. Due to reciprocity, the pupil function also describes the sensitivity of this transducer and might contain a phase factor to account for aberration.[1,22,24] The pupil function here does not have a unit. It may be regarded as proportional to the oscillation velocity.

Spherical transducers can be produced, for example, from piezoelectric plastic foils.[42] However, the spherical transducer can also serve as a model for the usual system consisting of a planar transducer, a buffer rod guiding the acoustic wave, and a spherical concave lens forming a converging wave. The two simply must emit the same angular spectrum. For numerical simulations several pupil functions are often used. The most elementary pupil function, which is discontinuous at the edge of the aperture with opening semiangle α, has the form

$$P(\theta) = \begin{cases} 1, \theta \leq \alpha \\ 0, \theta > \alpha \end{cases} \qquad (11.4)$$

Here every part of the transducer moves equally towards the coupling liquid. More realistic modelling for a plane transducer insonifying only a circular fraction of the lens is provided by a pupil function that is continuously differentiable at the edge:[43]

$$P(\theta) = \begin{cases} \dfrac{1}{2}\left[1 + \cos\left(\pi\dfrac{\cos\theta - 1}{\cos\alpha - 1}\right)\right], & \theta \leq \alpha \\ 0, & \theta > \alpha \end{cases} \qquad (11.5)$$

It has been shown that the pupil function of the microscope can be derived from images of a rigid spherical particle when the focal point is scanned along the sphere's half radius.[24] The two-dimensional pupil function (absolute value) of an acoustic microscope is presented in Figure 11.7. It is nonzero only inside the circle $\sqrt{(k_x')^2 + (k_y')^2} \leq k\sin\alpha$. The broad fringes exhibit the sound field generated by the piston transducer, while the small rings are artifacts from imperfect scanning.

Our first task is to find the angular spectrum of the field emitted by a focusing transducer with given pupil function. We will calculate the (displacement) potential distribution in the focal plane, from which the angular spectrum is easily derived. By application of the Huygens-Fresnel principle[44,p. 436], the field Φ at a point r whose distance from the focal point is small compared to the focal length f of the transducer is given by

$$\Phi_i(\vec{r}) = -\frac{1}{2\pi}\int\limits_0^{2\pi}\int\limits_0^{\pi/2} u_0 P(\theta, \varphi)\frac{\exp(iks)}{s}f^2 \sin\theta d\theta d\varphi \qquad (11.6)$$
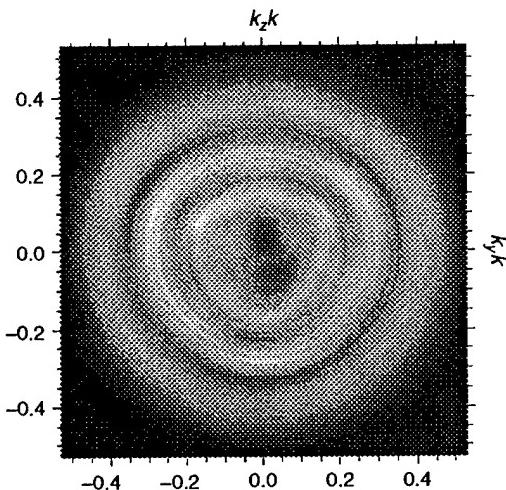
FIGURE 11.7
Experimental image of the pupil function of the ELSAM 400 MHz lens. Image was obtained by imaging a steel sphere ($ka = 334$), focusing at half radius of the sphere. (From Weise, W. et al., *J. Acoust. Soc. Am.*, 104, 181, 1998. With permission.)

where s denotes the distance between point Q on the transducer surface and point S, $s = |r - q|$ (see Figure 11.6). The product $u_0 P(\theta, \varphi)$ is the displacement of the transducer surface. The integration can be performed over the whole upper hemisphere, as the aperture is restricted by $P(\theta, \varphi)$. In the vicinity of the focal point, $r \ll f, s$, and we have in good approximation

$$(s - f) \approx e_q r \tag{11.7}$$

where e_q is the unit vector directed along vector q. Introducing Equation 11.7 into the exponential function in (11.6) and replacing s by f in the denominator of the integrand of Equation 11.6 we obtain the following:

$$\Phi_i(\bar{r}) = -\frac{u_0 \exp(ikf)}{2\pi} \int_0^{2\pi} \int_0^{\pi/2} \exp(ike_q(\theta, \varphi)r) P(\theta, \varphi) f \sin\theta \, d\theta \, d\varphi \tag{11.8}$$

In the limit $f \to \infty$ (Debye approximation[45, p. 24]), this equation is valid throughout the whole space.[44, p. 436] It expresses the field in the focal region as a superposition of plane waves whose propagation vectors fall inside a geometrical cone formed by drawing straight lines from the edge of the aperture through the focal point, which, in contrast to the usual Debye integral,[45] are weighted with $P(\theta, \varphi)$. The vector $ke_q(\theta, \varphi)$ has now assumed the meaning of the wave vector k, and we may say that each point on $P(\theta, \varphi)$ is responsible

for the emission (and, by reciprocity, for the detection) of the plane wave component emitted along the line from the point on $P(\theta,\varphi)$ through the focal point.

To find the angular spectrum of the emitted field in the focal plane, we set the third coordinate of r equal to zero and substitute Cartesian coordinates for the angular integration variables. For the vector components of k hold:

$$k_x = k \sin\theta \cos\varphi$$

$$k_y = k \sin\theta \sin\varphi \tag{11.9}$$

$$k_z = \cos\varphi = \sqrt{k^2 - k_x^2 - k_y^2}$$

The Jacobi determinant corresponding to Equation 11.9 yields

$$\sin\theta \, d\theta \, d\varphi = \frac{1}{k^2 \cos\theta} dk_x dk_y = \frac{1}{kk_z} dk_x dk_y \tag{11.10}$$

Denoting the Cartesian coordinates of r by x, y, z, Equation 11.8 can be rewritten

$$\Phi_i(x,y,z=0) = \frac{1}{(2\pi)^2} \int_{-\infty}^{\infty} \int_{-\infty}^{\infty} P(k_x,k_y) \exp[i(k_x x + k_y y)] \frac{dk_x dk_y}{kk_z} \tag{11.11}$$

Up to a constant $P(k_x, k_y)$ is defined as:

$$P(k_x, k_y) = \begin{cases} P(\theta,\varphi), & k_x^2 + k_y^2 \leq k^2 \\ 0, & elsewhere \end{cases} \tag{11.12}$$

with the relation between θ, φ, and k_x, k_y as given by Equation 11.9. From the definition of $P(k_x, k_y)$ we could set the integration limits in Equation 11.11 to infinity. In Equation 11.11 Φ_i obviously is the two-dimensional inverse Fourier transform of the function $P(k_x, k_y)/(k\,k_z)$. Comparison with Equation (11.2) shows that this is the angular spectrum of the transducer field in the focal plane provided that $\Phi_i(x, y, 0)$ has the same Fourier transform as the transducer field in the focal plane. However, Equation 11.11 might not describe the field in the focal plane far away from the focal point. But if both fields are focused, the squared field amplitude $|\Phi_i|^2$, integrated over the focal plane but excluding the region around the focal point, will for both give approximately zero (almost all the radiated energy passes through the focal region). Hence, from Parseval's theorem, the contribution of the field in these outer regions to the Fourier transformation may be neglected,
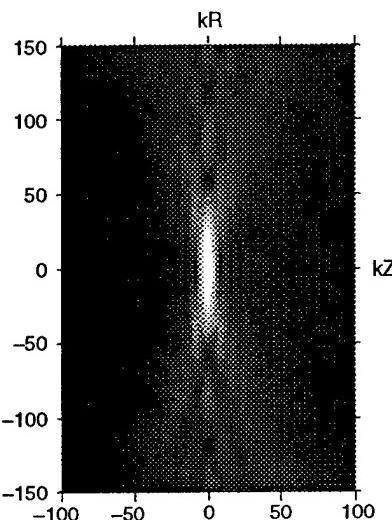
FIGURE 11.8
Calculated acoustic field near the focus of an elementary acoustic microscope lens with
semiaperture angle $\alpha = 20°$. (From Weise, W., PhD thesis, University of Bremen, 1997. With
permission.)

and the two fields can be described by the same angular spectrum through-
out the focal plane. We can therefore write:

$$U_i(k_x, k_y) = \frac{P(k_x, k_y)}{kk_z} \qquad (11.13)$$

It should be noted that function $P(k_x, k_y)$ is defined in a spatial coordinate
system rather than in the frequency (k) space, and it cannot be interpreted
as an angular spectrum. Equation 11.13 is a result of the application of the
Debye approximation. "In the Debye approximation, there is not an abrupt
cut-off not of the incident field, as in Kirchhoff approximation, but of the
angular spectrum of the incident field."[45, p. 24] Figure 11.8 shows the ampli-
tude of the acoustical field distribution near the focus of the spherical lens
with the pupil function (Equation 11.4).[41] It is called point spread function
(PSF) because it illustrates "what should be a point focus by geometrical optics
is spread out by diffraction."[2] For the simple pupil function (Equation 11.4)
the lateral distribution (field in the focal plane) is given by a *jinc* function

$$\Phi(r_t) = \frac{J_1(kr_t \sin\alpha)}{kr_t \sin\alpha} \qquad (11.14)$$

where $r_t = \sqrt{x^2 + y^2}$ and J_1 is the cylindrical Bessel function. The axial field distribution (acoustical field along the z-axes: $x = 0, y = 0$) is described by a *sinc* function:

$$\Phi(z) = \frac{\sin[kz(1 - \cos\alpha)]}{kz(1 - \cos\alpha)}$$

(11.15)

Equation 11.14 and Equation 11.15 provide the lateral and the axial resolutions of the SAM. The jinc function has a maximum at $r_t = 0$, the first zero of $\Phi(r_t)$ is given by the Airy radius[39, p. 78]

$$r_{Airy} = \frac{0.61\lambda}{\sin\alpha}$$

(11.16)

where λ is the wavelength of the sound wave in the immersion liquid. The Rayleigh criterion states "that the images of two points may be considered resolved if the principal diffraction maximum of one falls exactly on the first diffraction minimum of the other."[46] Equation 11.16 gives the distance between the maximum and the first minimum of the acoustic field in the focal plane; it is called Rayleigh distance[47] and determines the axial resolution of the SAM. A detailed discussion of the different resolution criteria can be found in the book by Kino.[47]

The axial resolution (resolution along the z-axes) can be defined in the same way. The distance between the maximum and the first minimum along the z-axes is

$$z_{axial} = \frac{0.5\lambda}{(1 - \cos\alpha)}$$

(11.17)

Equation 11.17 determines the axial resolution of the SAM. Figure 11.9 illustrates the behavior of the resolution of SAM operating at 1 GHz (Equation 11.16 and Equation 11.17) as a function of the aperture angle. The lateral resolution depends weakly on the aperture angle (Figure 11.9). It is 1.1-μm for a lens with a semiaperture angle of 60° at 1 GHz. In contrast to this, the axial resolution can be improved by a factor of 6 by increasing the semiaperture angle from 20 to 60°. For a microscope with a small angle lens, the focal length (the length of the main maximum of the field in the axial direction) is much longer (see Figure 11.8) than the focal width (the width of the main peak in the radial direction). Due to the high attenuation of sound in water, the highest frequency used in commercial microscopes is 2 GHz. In order to minimize the attenuation, Hamidioglu and Quate[48] used boiling water as the immersion liquid. They achieved a resolution of 0.2 μm at 4.4 GHz. Foster and Rugar[49] were able to obtain a resolution of 20 nm in low-velocity superfluid liquid helium at a temperature of 0.2 K.
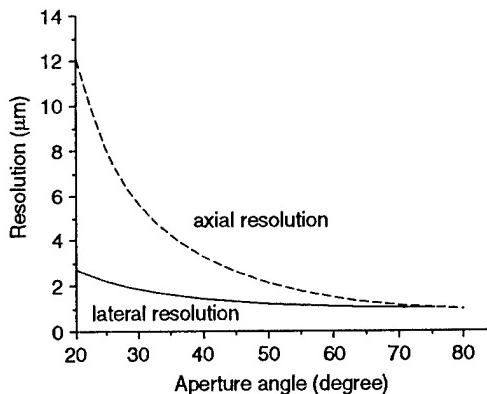
FIGURE 11.9

Calculated lateral (Equation 11.16) and axial (Equation 11.17) resolutions of a SAM operating at 1 GHz as a function of the aperture angle α. Water was chosen as immersion liquid for simulations.

Now we know the spectrum incident on the object and we want to calculate the scattered spectrum. Consider imaging of a three-dimensional object as depicted in Figure 11.6. In the case of a reflection microscope, the same transducer serves as emitter and as detector, while for the transmission microscope the detector is situated confocally across from the emitter. We will use three coordinate systems, (x, y, z) with origin in the focal point and (x', y', z') in point O' linked to the particle. The z- and z'-axis are directed away from the emitter (Figure 11.7). The coordinates of the system O' are (X, Y, Z) from the focal point. We introduce also an intermediate coordinate system with its origin in point O'' with vector (x, y, z').

Following Somekh et al.[38] we determine the density of the back scattered spectrum or the scattering function $g_s(k_x, k_y, k'_x, k'_y)$ in the system O' linked to the particle as the spectrum of the reflected field in response to the incident spectral component with wave number coordinates (k'_x, k'_y). The spectrum U'_i of the incident field as well as the spectrum U'_s of the reflected field are also given in the spatial coordinate system that originates at O'. Since the magnitude of k is fixed, the wave vector is completely specified by the vector $k_t = (k_x, k_y)$; k_x, k_y denote the wave vector components of the scattered field, and k'_x, k'_y denote the wave vector components of the incident field. To calculate the spectrum of the scattered field we must integrate over all incident spectral components

$$U'_s(k_x, k_y) = \frac{1}{(2\pi)^2} \int_{-\infty}^{\infty} \int U'_i(k'_x, k'_y) g_s(k_x, k_y, k'_x, k'_y) dk'_x\, dk'_y \qquad (11.18)$$

Now we have to determine the reflected spectrum with the help of the incident spectrum in system O, and then express the reflected spectrum in

system O'. Let us first express the spectrum U_i incident in the focal plane system O in system O'' (see Figure 11.6). The spectrum U_i'' incident on the object plane at position Z is calculated by including a propagation factor $\exp(ik_z Z)$

$$U_i'(k_x', k_y') = U_i(k_x', k_y') \exp(ik_z' Z) \qquad \textbf{(11.19)}$$

For the incident spectrum $k_z' = \sqrt{k^2 - (k_x')^2 - (k_y')^2}$. Here we introduce the notation for the incident and scattered spectra in system O'' as $U_i''(k_x', k_y')$ and $U_s''(k_x, k_y)$, respectively. It should be noted that as the incident wave propagates in the positive direction, the phase shift is positive if Z is positive. The spectrum in system O'' and O' can be linked with the help of the shift theorem.[39, p. 277] Since $x = x' + X, y = y' + Y$, the spectrum of the shifted object is

$$U_i'(k_x', k_y') = U_i''(k_x', k_y') \exp[i(k_x' X + k_y' Y)] \qquad \textbf{(11.20)}$$

Introducing first (11.20) and then (11.19) into (11.18), we obtain for $U_s'(k_x, k_y)$

$$U_s'(k_x, k_y) = \frac{1}{(2\pi)^2} \int_{-\infty}^{\infty} \int_{-\infty}^{\infty} U_i(k_x', k_y') g_s(k_x, k_y, k_x', k_y') \exp[i(k_x' X + k_y' Y + k_z' Z)] dk_x' dk_y'$$

$$\textbf{(11.21)}$$

To return to system O, the spectrum $U_s'(k_x, k_y)$ is first shifted to the O'' system by multiplying by $\exp[-i(k_x X + k_y Y)]$

$$U_s''(k_x, k_y) = U_s'(k_x, k_y) \exp[-i(k_x X + k_y Y)] \qquad \textbf{(11.22)}$$

Since the integration in Equation 11.3 is made on the focal plane we must return to the focal plane by multiplying Equation 11.22 by $\exp(-ik_z Z)$:

$$U_s(k_x, k_y) = U_s''(k_x, k_y) \exp[-i(k_z Z)] \qquad \textbf{(11.23)}$$

For the reflection SAM, we have $k_z = -\sqrt{k^2 - (k_x)^2 - (k_y)^2}$, since the backscattered wave propagates opposite to the z-direction. Combining Equation 11.3, Equation 11.13, and Equation 11.21 to Equation 11.23, we obtain the output signal of the reflection SAM as

$$V(X, Y, Z) = \int_{-\infty}^{\infty} \int \int_{-\infty}^{\infty} \int P(-k_x', -k_y') P(k_x', k_y') g_s(k_x, k_y, k_x', k_y')$$

$$\exp[i(k_x' - k_x)X + (k_y' - k_y)Y + (k_z' - k_z)Z] \frac{dk_x' dk_y' dk_x dk_y}{kk_z'} \qquad \textbf{(11.24)}$$

On an additional assumption, Equation 11.24 is valid for the transmission acoustic microscope as well. The main difference from the reflection microscope is that $k_z = +\sqrt{k^2 - (k_x)^2 - (k_y)^2}$. Additionally, in the transmission microscope, transmitting and receiving lenses may have different pupil functions. Then the first pupil function in Equation (11.24) belongs to the detector and the second to the emitter.

An analytical expression for the integral in Equation 11.24 can be derived only in a few cases of simply shaped objects: solid half-space,[50] spherical particle,[51] subsurface spherical cavity,[8] disk,[10] cylindrical inclusion,[52] and surface-breaking crack.[38,53] We will consider most of these cases in this chapter. When an analytical solution cannot be derived, several mathematical methods can be used to understand the basic features of image formation for complex objects. One of these is the method of stationary point.[45] Despite its complex rigorous formulation,[45] it is very often implicitly used in image interpretation. One prominent example is the derivation of the formula for the period of the $V(Z)$ oscillations related to the generation of the Rayleigh surface wave.[54] Parmon and Bertoni[54] postulated that the periodical character of the so-called $V(Z)$ curve is determined by interference of two rays: the central ray and the ray that excites the Rayleigh wave on the surface of the solid half-space (see Figure 11.10[a]). In this model only rays hitting the surface of the hemispherical transducer perpendicularly should be taken into account. These rays appear to come from the focus when they intersect the transducer[55] and have a stationary point in the integral in Equation 11.24. The use of the method of a stationary point for interpreting acoustical images is closely related to the fact that we used the Debye approximation for deriving Equation 11.24. According to Stamnes,[45] the Debye approximation "is a geometrical-optics approximation in the sense that only the contribution of the interior stationary points is accounted for the asymptotic evaluation of the angular spectrum; the end point contribution is neglected."

11.3.1   Two-Dimensional Objects

11.3.1.1 Signal from a Half-Space

Knowing the general expression for the output signal of the SAM, we can derive the expression of the images of simply shaped objects. We start with the simplest case, the SAM signal from a homogeneous half-space. In this case, we can present the spectrum of the reflected field as a simple multiplication of the incident field and the reflection coefficient.[56]

$$U_s(k_x, k_y) = \Re(k_x, k_y) U_i(k_x, k_y) \tag{11.25}$$

From Equation 11.3 and Equation 11.18 we obtain

$$g_s(k_x, k_y, k'_x, k'_y) = (2\pi)^2 \delta(k_x - k'_x)\delta(k_y - k'_y)\Re(k'_x, k'_y), \tag{11.26}$$
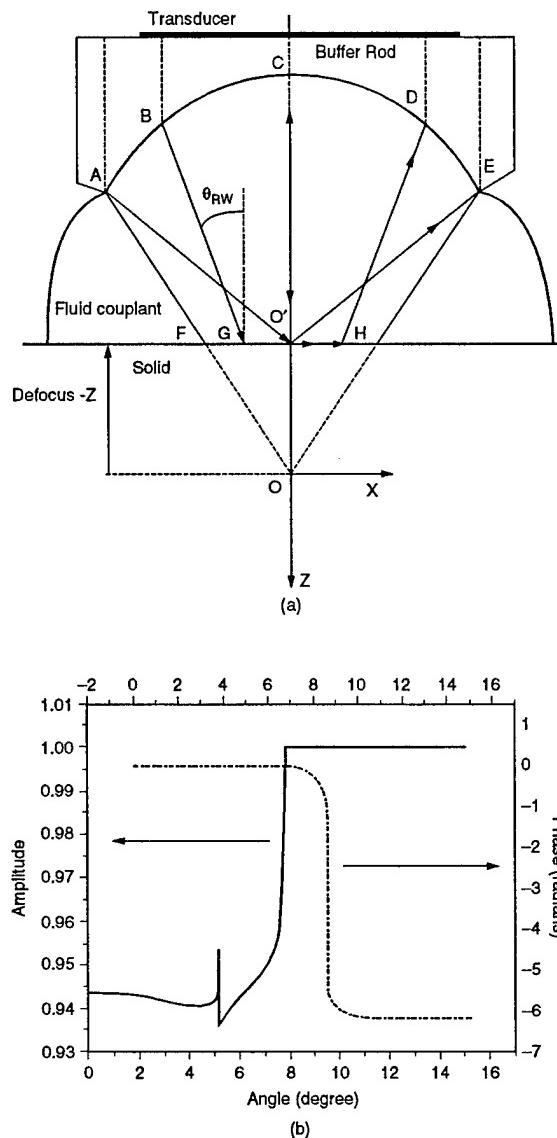
FIGURE 11.10

(a) Ray model interpretation for the paths of different wave components in the case of negative defocus (Z < 0). CO′ is the trajectory of a specular or geometrical wave. BGHD is the trajectory of a leaky (pseudo) Rayleigh wave. In the ray model the leaky Rayleigh wave is excited by ray BG, striking the surface at the angle $\theta_{SAW} = v_w/v_{SAW}$. AO˘E is the trajectory of the edge wave. Rays AF, BG, HD, and EK are assumed to be normal to the hemispherical surface and appear to come from the focus when they intersect the transducer and liquid/solid interface. (b) Magnitude (solid line) and phase (dotted line) of the reflection coefficient from a water/ superhard amorphous carbon interface.

where δ is the Dirac delta function. Substituting Equation 11.26 into Equation 11.24, we finally have as the output signal for the reflection microscope

$$V(Z) = \int\int_{-\infty}^{\infty} P(-k_x, -k_y)P(k_x, k_y)\mathfrak{R}(k_x, k_y)\exp(i2k_zZ)\frac{dk_x dk_y}{kk_z} \qquad (11.27)$$

The fact that the signs in the arguments for the two pupil functions are different is important to investigating the inclined surfaces.[57] Taking into account that in the Debye approach the maximum angle of integration is restricted by the semiaperture angle α of the pupil to $\sqrt{(k'_x)^2 + (k'_y)^2} \leq k\sin\alpha$,[58] and introducing spherical coordinates in k space, we can replace Equation 11.27 by

$$V(Z) = \int_0^{2\pi} d\varphi_k \int_0^{\alpha} P(\theta_k, \varphi_k)P(\theta_k, \varphi_k + \pi)\mathfrak{R}(\theta_k, \varphi_k)\exp(i2k\cos\theta_k Z)\sin\theta_k d\theta_k$$

$$(11.28)$$

Assuming isotropy of the pupil function and integrating over φ_k we obtain an expression for the signal variation with the distance from the sample

$$V(Z) = \frac{V_o}{(1-\cos\alpha)}\int_0^{\alpha} P^2(\theta)\mathfrak{R}(\theta)\exp(i2kZ\cos\theta)\sin\theta d\theta \qquad (11.29)$$

where V_0 is the signal of the acoustic microscope from a perfectly reflecting surface located in the focal plane[59]. The normalizing coefficient $V_0/(1-\cos\alpha)$ is important for simulating the signal from a subsurface defect described below. For a perfectly reflecting object ($\mathfrak{R}(\theta) = 1$) and a lens with elementary pupil function, the $V(Z)$ curve is a *sinc* function:

$$V(Z) = \frac{\sin[kZ(1-\cos\alpha)]}{kZ(1-\cos\alpha)} \qquad (11.30)$$

The physical interpretation of the $V(Z)$ curve can be obtained by introducing the substitution[60,61] $t_\theta = 2/\lambda \cos\theta$ into the integral in Equation 11.29:

$$V(Z) = \int_{2/\lambda\cos\alpha}^{2/\lambda} P^2(t_\theta)\mathfrak{R}(t_\theta)\exp(i2\pi t_\theta k_z Z)dt_\theta \qquad (11.31)$$

The normalizing constant in Equation 11.31 is omitted. Since the pupil function is unequal to zero only within $0 < \theta \leq \alpha$, or when $(2/\lambda)\cos\alpha \leq t\theta \leq 2/\lambda$,

Theory and Applications of Acoustic Microscopy   673

the limits of the integral in Equation 11.31 can be extended from $-\infty$ to ∞

$$V(Z) = \int_{-\infty}^{\infty} P^2(t_\theta)\Re(t_\theta)\exp(i2\pi t_\theta k_z Z)dt_\theta \qquad (11.32)$$

Therefore, the $V(Z)$ curve is the Fourier transform of the product of the pupil function squared and the reflection coefficient. Equation 11.31 was used to reconstruct the complete reflection function of the solid sample and to study the surface acoustic wave propagation in multilayered solids.[43,60,62,63] An analytical expression of the reflection coefficient for a solid half-space is given in Appendix A. Figure 11.10[b] illustrates the behavior of amplitude and phase of the reflection coefficient for superhard amorphous diamond obtained at high-pressure (13.5 GPa) and high temperature (900 ± 100°C) (see parameters in Table 11.1). The amplitude shows a small dip associated with the longitudinal critical angle, $\sin\theta_P^c = c/c_p$. The phase of the reflection coefficient has a small kink for the same angle. Obviously, above this angle, only shear waves penetrate into the substrate. Above the shear critical angle ($\sin\theta_S^c = c/c_s$), the magnitude of the reflection coefficient equals 1. At the Rayleigh angle, which is bigger than the shear angle, a phase change of 2π occurs, which is characteristic of Rayleigh surface wave propagation.[2]

The theory of the $V(Z)$ curve is important for understanding contrast formation in the SAM.[2] However, it is beyond the scope of this chapter, and we discuss this theory only briefly. To analyze the image formation in the reflection acoustic microscope, Atalar et al.[64] monitored the amplitude of the transducer voltage V as a function of lens-to-sample spacing Z, or the $V(Z)$ curve. A famous feature of the $V(Z)$ curve is the oscillation behavior[65] (see Figure 11.11). The periodicity of dips appearing in the $V(Z)$ curves reported by Weglein and Wilson[65] soon was linked to surface wave propagation.[54,65,66] Invention of the line focus acoustic microscope with a cylindrical lens by Kushibiki et al.[67] made it possible to measure the anisotropy of surface acoustic waves on a crystal surface.[19] Considerable progress in contrast formation or $V(Z)$ curve theory has been made since then. Now the theory of the $V(Z)$ curve has been developed for multilayered solids,[68,69] plates,[70] for anisotropic materials,[71,72] and for different types of surface acoustic waves[73,74] and curved surfaces.[75,76] Detailed description of the $V(Z)$ curve formation and recent developments in application of the $V(Z)$ curve measurement for material characterization in quantitative acoustic microscopy can be found in references.[2,4,19]

11.3.1.2   Image Formation of Two-Dimensional Objects

Images of many solid samples in the SAM exhibit a strong Rayleigh wave contrast.[2] We will return to this point in the next paragraph and consider now image formation of two-dimensional objects when Rayleigh waves are not excited. Such an approach can be used for a SAM having a lens with a small semiaperture angle (J must be smaller than the Rayleigh angle), which

TABLE 11.1

Velocities, Critical Angles, Wavelength for the Rayleigh wave (Equal to the Penetration Depth of the Rayleigh Wave at 1 GHz) and Depth of the Longitudinal and Shear Waves Penetration for Different Isotropic Materials

Material	Density (kg/m³)	c_P (km/sec)	θ_P^c (°)	c_S (km/sec)	θ_S^c (°)	c_{RW} (km/sec) λ_{RW} at 1 GHz (μm)	$Z_{P\text{-}30}$ (μm)	$Z_{S\text{-}30}$ (μm)	Ref.
Plexiglass	1100	2.70	33.7	1.10		1.04	16.7	40.9	
Gold	19281	3.24	27.6	1.2		1.13	13.8	37.5	2
Amorphous carbon film	2800	4.4	19.9	3.7	40.0	2.7	10.2	12.2	
Quartz (fused)	2200	5.97	14.6	3.2	27.9	3.0	7.5	14.1	2
Aluminum	2700	6.2	13.5	3.0	29.6	2.8	7.0	15	2
TiN	5300	9.4	9.2	5.7	15.2	5.2	4.8	7.9	154
Si_3N_4	3185	10.6	8.1	6.2	14.0	5.7	4.2	7.3	2
SiC	3210	12.1	7.1	7.5	11.5	6.8	3.7	6	2
cBN	3500	15.8	5.4	10.4	8.3	9.3	2.8	4.3	155
Amorphous carbon obtained from C^{60}	3150	16.6	5.2	10.2	8.5	9.8	2.7	4.4	87
Diamond	3515	18.1	4.7	12.3	6.9	10.9	2.5	3.7	156
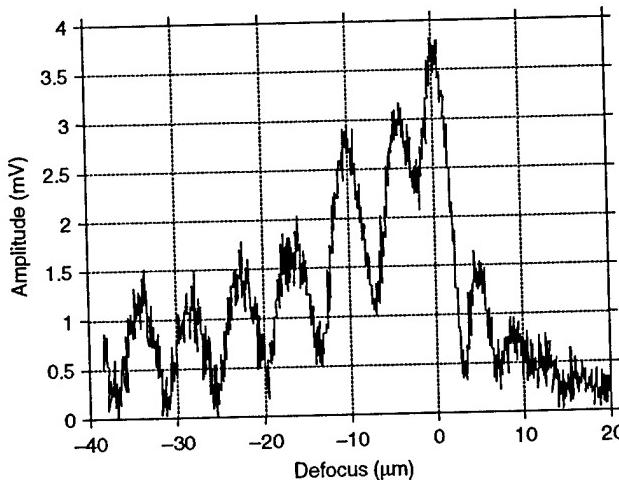
FIGURE 11.11
$V(Z)$ curve of 0.2-μm oxide film on aluminum measured at 980 MHz. Measurements were made at Oxford LFM and modified for high frequency. (From Sklar, Z., *Quantitative acoustic microscopy of coated materials*, 1993; Sklar, Z. et al., *Advances in Acoustic Microscopy*, Plenum Press, New York, 1995, pp. 209–247. With permission.)

is widely used in nondestructive evaluation (NDE) for imaging subsurface structures.[77] In this approximation it is also assumed that at each point in the sample, the surface reflection is independent of the angle of the incident spectral component: $\Re(\theta) = $ const.

Without excitation of surface acoustic waves, the problem can be simplified. The reflection properties can be defined by the reflectance function $R_o(x, y)$ of the object.[39, p52] The acoustic field Φ_s reflected from the sample is proportional to the product of the incident field and the reflectance function in the spatial domain

$$\Phi_s(x,y) = \Phi_i(x,y)R_o(x,y) \tag{11.33}$$

If we introduce the Fourier transform of the reflection function $R_o(x, y)$,

$$\Re_o(k_x,k_y) = \int\int_{-\infty}^{\infty} R_o(x',y')\exp[-i(k_x x' + k_x y')]dx'dy' \tag{11.34}$$

With the help of the convolution theorem of Fourier analysis, the Equation 11.33 can be rewritten as

$$U'_s(k_x,k_y) = \frac{1}{(2\pi)^2}\int\int_{-\infty}^{\infty} U'_i(k'_x,k'_y)\Re_o(k_x - k'_x, k_y - k'_y) dk'_x dk'_y \tag{11.35}$$

Comparing Equation 11.18 and Equation 11.35 we see that the density of the scattered spectrum is

$$g_s(k_x, k_y, k_x', k_y') = \Re_o(k_x - k_x', k_y - k_y') \tag{11.36}$$

The dependence of the scattering function g_s only of the variable differences enables us to present the output signal as an inverse Fourier integral of the object spectrum and the optical transfer function (OTF). We introduce Equation 11.36 into Equation 11.24 and substitute k_x' for $k_x - k_x'$ and k_y' for $k_y - k_y'$ and keep k_x, k_y. After changing the order of integration, we obtain

$$V(X, Y, Z) = \int\int_{-\infty}^{\infty} \Re_o(k_x', k_y') H_R(k_x', k_y', Z) \exp[-i(k_x' X + k_y' Y)] dk_x' dk_y' \tag{11.37}$$

with the OTF for reflection SAM

$$H_R(k_x', k_y', Z) = \int\int_{-\infty}^{\infty} dk_x dk_y P(k_x - k_x', k_y - k_y') P(-k_x, -k_y)$$

$$\frac{\exp\left[i\sqrt{k^2 - (k_x - k_x')^2 - (k_y-)^2} Z\right]\left[i\sqrt{k^2 - k_x^2 - k_y^2} Z\right]}{\sqrt{k^2 - (k_x - k_x')^2 - (k_y - k_y')^2}} \tag{11.38}$$

In Equation 11.38 we have taken into account that $k_z = -\sqrt{k^2 - k_x^2 - k_y^2}$. The OTF describes the spectral properties of the imaging system. It determines how the different angular spectrum components of the object contribute to the image contrast.

The calculation of the OTF can be performed analytically only for the elementary pupil function in Equation 11.4.[10,78] The determination of the OTF for a real microscope system is a complex problem.[79] For a SAM it has been investigated elsewhere.[77,80] A direct method for measuring the OTF of a focused system ($Z = 0$) was presented by Atalar,[81] who has shown that the image scanned along the surface of a spherical particle exhibits the transfer function of the microscope. This method has been extended to measure the defocused OTF using three-dimensional images of steel spheres.[82] Figure 11.12(a) is an X-Z-scan of the top of a steel sphere. The value of the image amplitude is stored and the spherical scan extracted from the data. The method is valid for determination of the complex transfer function if phase measurement results are available. The moduli of the transfer function at different focal positions derived from Figure 11.12(a) are depicted in Figure 11.12(b).
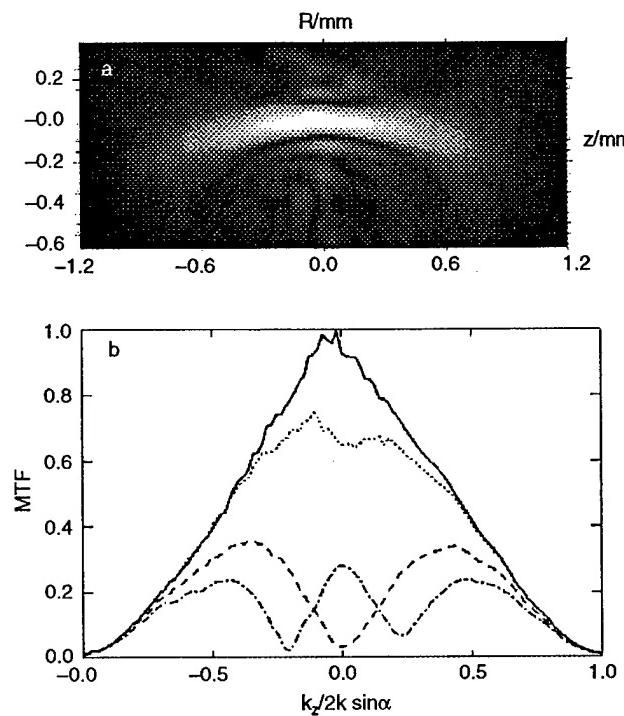
FIGURE 11.12

(a) X-Z scans of a steel ball of 2.5-mm radius taken at a frequency of 91 MHz. Semiaperture angle of the lens is equal to 27°. (b) Defocused OTF obtained in the LFM by scanning along an arc at different normalized defocusing positions $w = kZ\sin_2\alpha$. Solid line for $w = 0$, dotted for $w = 3$, dashed for $w = 6$, dash-dotted for $w = 8$. (From Zinin, P. et al., *Optik*, 107, 45, 1997. With permission.)

The basic features of two-dimensional objects imaging can be illustrated by using a perfectly reflecting disk. The circular disk is widely used as a model of penny shaped subsurface cracks. To calculate the images of a disk at different focal plane positions we will use the OTF in the paraxial approximation $(k_x, k_y \ll k)$ for the SOM.[10,83] In the simplified Kirchhoff approximation, a perfectly reflecting disk is defined by the reflectance function of the object.[39, p. 52] $r_d(x,y) = 1$ for (x, y) inside the disk, and $r_d(x,y) = 0$, otherwise. The perfectly reflecting disk of radius a, has the angular spectrum[39, p. 64]

$$\Re_d(k_x, k_y) = 2\pi a \frac{J_o(k_t a)}{k_t} \qquad (11.39)$$

Here we have defined the cylindrical transverse radial spatial frequency as $k_t = \sqrt{k_x^2 + k_y^2}$. The images of a rigid reflecting disk-shaped plane calculated
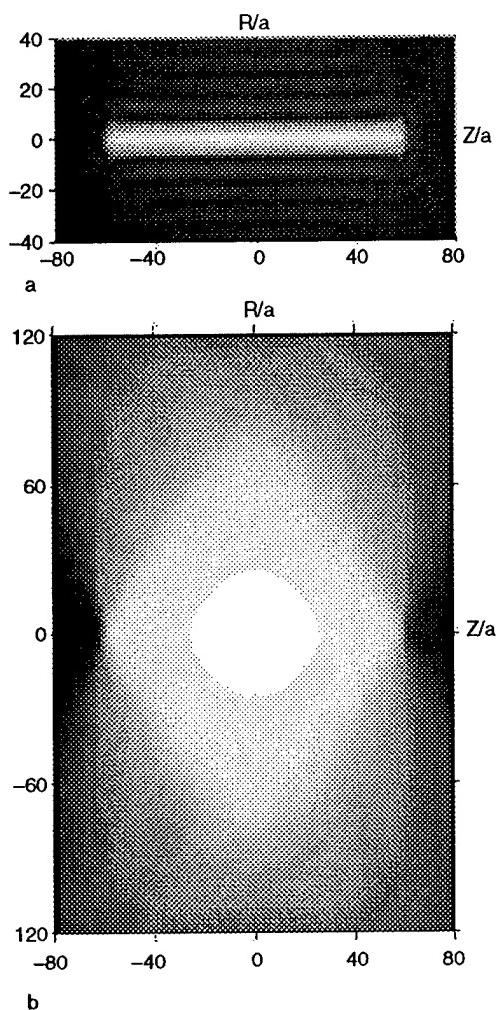
FIGURE 11.13

X-Z medial section of a rigid disk ($ka = 60$) calculated for a reflection SAM (top) and of a circular hole in a rigid screen ($ka = 60$) for a transmission SAM (bottom). Semiaperture angle of the transducer is equal to 60°. Axes scaled in units of the disk's radius. (From Zinin, P. et al., *Wave Motion*, 25, 213, 1997. With permission.)

with the help of Equation 11.39 in reflection and transmission SAMs are presented in Figure 11.13. In the reflection SAM, the three-dimensional area in which the image contrast mainly occurs can be regarded as a thin bright layer (Figure 11.13[a]). In the lateral direction, the dimension of the image is approximately equal to the dimension of the object. The thickness of this layer is proportional to the width of the main maximum of the $V(Z)$ curve/

$(1 - \cos \alpha)$ (Equation 11.27). For the transmission microscope, we consider a circular hole in a perfectly reflecting screen. In contrast to the image in the reflection SAM, the image in Figure 11.13(b) is elongated, the elongation depending on the semiaperture angle. In the focus, the lateral size of the image coincides with that of the sample.

11.3.1.3 Image Formation of Surface Breaking Cracks

In this section we will take a closer look at the reflection coefficient in case Rayleigh surface waves are excited by the wave incident from the coupling liquid. The results will then be applied to investigate the effect of surface breaking cracks.

Along the surface of a solid sample, Rayleigh surface waves can propagate. If the surface is loaded with a liquid, these waves are denoted as leaky Rayleigh waves, as they can radiate into the liquid. Reciprocally, they can also be excited by waves arriving on the surface from the liquid. As Rayleigh waves exhibit a strong motion component orthogonal to the surface, they strongly interact with fluid waves.

The effect of Rayleigh waves on the SAM output signal may be included in the reflection coefficient $\Re$ in Equation 11.25 of an infinite half-space. In the simplest form, $\Re$ may be approximated by the sum of the reflection coefficient $\Re_o$ without the Rayleigh wave and a second term with singularities in the complex plane that contains the effect of the Rayleigh wave[38]

$$\Re(k_x, k_y) \approx \Re_o(k_x, k_y) + \frac{4i\alpha_R k_R}{k_x^2 + k_y^2 - k_p^2} \tag{11.40}$$

Here $k_p = k_R + i\alpha_R$ is the complex wave number of the Rayleigh wave. The imaginary part $i\alpha_R$ describes the exponential decay of the wave due to energy loss by irradiation into the coupling liquid. Real and imaginary parts must be equal in sign to describe a decaying wave; for convenience, we choose both to be positive. For Equation 11.40 to be valid it is assumed that the damping α_R is much smaller than k_R. The second term in Equation 11.40 describes the excitation and re-radiation into the coupling liquid of the leaky Rayleigh wave. It has a considerable influence on the reflection coefficient only if $\sqrt{k_x^2 + k_y^2} = k_R$. This is the condition for excitation and radiation of the surface wave. The angle θ_R the fluid wave then forms with the surface normal is given by $k \sin \theta_R = k_R$ in accordance with Snell's law.

If a lens with a semiaperture angle wider than the Rayleigh angle is used in the SAM, the $V(Z)$ curve is strongly influenced by Rayleigh waves. On the detector the radiated Rayleigh wave signal and the specularly reflected wave signal will interfere. This interference changes when the distance between microscope and surface changes. But this will only hold if the defocus Z is negative. For positive defocus, the excited Rayleigh wave is not detected by the microscope, and the second term in Equation 11.40 does not

give a signal. As the speed of the Rayleigh wave depends on the material properties, the signal recorded at changing distance, the $V(Z)$ curve, will exhibit a characteristic signature of the material for negative defocus, as can be observed from Figure 11.11. In general this $V(Z)$ curve is evaluated to investigate the properties of the sample. Instead of point focus lenses line focus lenses are often used for material investigation because the relative contribution of the Rayleigh wave and the specularly reflected wave to the microscope signal are more similar in this case. Material parameters may then be derived more precisely. The spectrum of line focus lenses can be assumed as independent of k_y.

In the following we will formulate the effect of Rayleigh waves on reflection in terms of a Green function. For simplicity, we will restrict to the case of the line focus lens. The one-dimensional relation between the reflected field distribution along the surface of a solid half-space and its angular spectrum is similar to that given by Equation 11.2

$$\Phi_s(x) = \frac{1}{2\pi} \int_{-\infty}^{\infty} U_s(k_x) \exp(ik_x x) dk_x \qquad (11.41)$$

The part of the reflected wave field $\Phi_s(x)$ that is due to the Rayleigh wave is obtained by inroducing Equation 11.25 into Equation 11.41, introducing the 2nd term from Equation 11.40 and writing $U_i(k_x)$ as the Fourier transform of $\Phi_i(x)$

$$\Phi_s(x) = \frac{1}{2\pi} \int_{-\infty}^{\infty} \int_{-\infty}^{\infty} \frac{4i\alpha_R k_R}{k_x^2 - k_p^2} \Phi_i(x') \exp[ik_x(x-x')] dx' dk_x \qquad (11.42)$$

After changing the order of integration, the integral over k_x is evaluated with the aid of the calculus of residues. For $x - x' > 0$ the path of integration is complemented through the upper half of the complex k_x plane enclosing the pole at k_p (remember we chose the real part of k_p greater than 0). For $x - x' < 0$ the path is complemented through the lower half and the pole at $-k_p$ is enclosed. Equation 11.42 yields:

$$\Phi_s(x) = 2\alpha_R \left\{ \int_{-\infty}^{x} \Phi_i(x') \exp[ik_p(x-x')] dx' + \int_{x}^{\infty} \Phi_i(x') \exp[ik_p(x'-x)] dx' \right\} \qquad (11.43)$$

This may be rewritten with the aid of the Green function $G(x, x')$:

$$\Phi_s(x) = \int_{-\infty}^{\infty} G(x, x') \Phi_i(x') dx' \qquad (11.44)$$

where $G(x, x')$ is defined by

$$G(x,x') = -2\alpha_R \exp(ik_p \, |x - x'|) \tag{11.45}$$

The Green function can be easily interpreted: It describes the field reflected from the sample surface at position x due to excitation at position x'. Equation 11.45 shows that the connection from x' to x is arranged by the decaying Rayleigh wave with wave vector k_p.

Interesting effects on the image obtained with the SAM will occur when there are surface discontinuities such as cracks or an abrupt change in the material properties and if a lens with a high semiaperture angle is used. Even if the width of a crack is much smaller than the resolution limit, it will immediately be recognized by fringes surrounding.[84,85] The reason for this is that Rayleigh waves generated on the surface will be reflected at the discontinuity. The reflected Rayleigh wave is then detected by the microscope.[86] Its phase will change when scanning parallel to the surface toward the discontinuity or away from it, leading to a change of the interference with the rest of the signal. This interference leads to fringes parallel to the crack, as can be observed in Figure 11.14. The Figure shows a SAM image of superhard amorphous carbon obtained at high-pressure (13 GPa) and high-temperature (800 ± 100°C) (for details see Manghnani et al.[87]). The defocus is $z = -20$ μm at 400 MHz. Strong fringes can be seen around the cracks and close to the sample edges. In the following paragraphs, we will quantitatively investigate the effect of a crack according to a derivation by Somekh et al.[38]
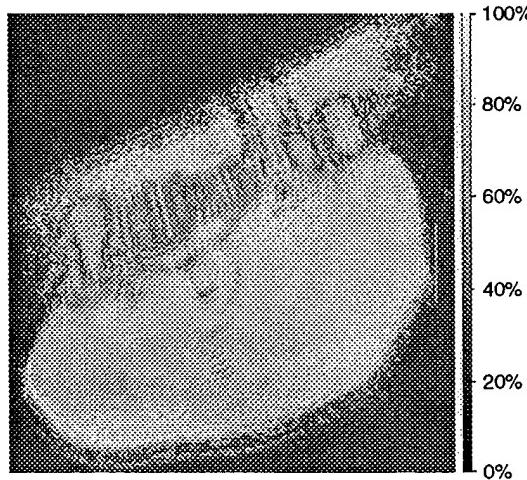

FIGURE 11.14
Acoustic image of amorphous carbon (the elastic properties are given in Table 11.1) at 400 MHz and at a defocus $z = -20$ μm.

The reflection in the vicinity of the crack will show a structural difference as compared to Equation 11.40. Let us assume that the crack runs in the y-direction. Then an incident plane wave with a wave vector component k_x will not simply be reflected with $k_x' = k_x$, but will include an additional part from the Rayleigh wave reflected at the discontinuity with the wave vector component $k_x' = -k_x$. We therefore will have to describe the reflected wave in terms of the scattering function $g_s(k_x, k_y, k_x', k_y')$ from Equation 11.18 instead of a reflection coefficient from Equation 11.40. It is now assumed that the reflection coefficient without the Rayleigh wave $\Re_o$ will not be influenced by the crack. This requires that the width of the crack be small in comparison to the wavelength in the coupling liquid and that its presence not change the surface elasticity or compliance so that no edge diffraction occurs. Moreover, we assume that no other surface waves are of importance. We will consider only the case that the field is constant in the y-direction, as for a SAM with a line focus lens oriented parallel to the crack. A treatment of the case of a point focus lens can be found in Rebinsky and Harris.[53] We will intuitively make use of the Green function (Equation 11.45) to construct the reflected field. We will assume that on the two sides of the crack the same material is found (for different materials see Somekh et al.[38]).

If a Rayleigh wave reaches the crack, it will in part be reflected with an in-plane reflection coefficient R and in part be transmitted with an in-plane transmission coefficient T. The values of R and T depend on the depth of the crack in comparison to the penetration depth of the Rayleigh wave. As some energy may be transformed into waves other than a Rayleigh surface wave, $R^2 + T^2$ may be less than 1. Without restriction of generality, we assume that the surface is located at $z = 0$ and the crack at position $x = 0$.

Let us first consider the field scattered into the coupling liquid from the surface left of the crack, hence $x < 0$. The Rayleigh waves arriving at position x will have different histories. Part of the Rayleigh wave is not affected by the crack. These waves have been excited either at positions x' with $x' < x$ traveling to the right, or at positions x' with $x < x' < 0$ traveling to the left. The contributions of these two parts are

$$-2\alpha_R\left[\int_{-\infty}^{x} \Phi_i(x')\exp[ik_p(x-x')]dx' + \int_{x}^{0} \Phi_i(x')\exp[-ik_p(x-x')]dx'\right] \qquad (11.46)$$

Another part has been excited at $x' < 0$; traveled to the right toward the crack; and after reflection at the crack, traveled to the left. Finally, one part has been excited at $x' > 0$, traveled to the left, and has been transmitted through the crack. The contributions of the latter two parts are

$$-2\alpha_R\exp[-ik_p(x-0)]\left[R\int_{-}^{0} \Phi_i(x')\exp[ik_p(0-x')]dx' + T\int_{0}^{-} \Phi_i(x')\exp[-ik_p(0-x')]dx'\right]$$

$$(11.47)$$

Note that in Equation 11.47 the Rayleigh wave is excited only before interaction with the crack. This restricts the integration over x'. The construction of the contributions arriving at a point x situated to the right of the crack is derived accordingly.

We now will assume that the whole expression for $\Phi_s(x)$, as given by the sum of the Equation 11.46 and Equation 11.47, is written with aid of a Green function in the form of Equation 11.45. We therefore may assume that the finite limits of the integrals are accounted for by multiplying the integrands with step functions. The different form of G for $x < 0$ and $x > 0$ may also be accounted for by step functions. To calculate the scattering function $g_s(k_x, k'_x)$ we Fourier transform the whole expression and express $\Phi_i(x')$ as inverse Fourier transform of $U_i(k'_x)$ according to Equation 11.2 and Equation 11.1:

$$U_s(k_x) = \int\limits_{-\infty}^{\infty} \int\limits_{-\infty}^{\infty} G(x,x') \left\{ \frac{1}{2\pi} \int\limits_{-\infty}^{\infty} U_i(k'_x) \exp(ik'_x x') dk'_x \right\} \exp(-ik_x x) dx' dx \qquad \textbf{(11.48)}$$

Changing the order of integration we find by comparison to Equation 11.18 that

$$g_s(k_x, k'_x) = \int\limits_{-\infty}^{\infty} \int\limits_{-\infty}^{\infty} G(x, x') \exp(ik'_x x') \exp(-ik_x x) dx' dx \qquad \textbf{(11.49)}$$

For the evaluation of the integration over x' with an infinite boundary on one side, it may be utilized that the damping α_R leads to a decay of the integrand toward this boundary. The remaining integration over x can be carried out using a property of the delta function

$$\int\limits_{-\infty}^{\infty} \exp\left[i(k'_x - k_x)x\right] dx = 2\pi\delta(k'_x - k_x) \qquad \textbf{(11.50)}$$

Including the term $\Re_o \delta(k'_x - k_x)$ that describes the specularly reflected field, we finally obtain

$$g(k_x, k'_x) = \delta(k'_x - k_x)\left[\Re_0 + \frac{4i\alpha_R k_R}{k_x^2 - k_p^2} \right]$$

$$- \frac{\alpha_R(1-T)}{\pi}\left[\frac{1}{(k'_x - k_p)(k_x - k_p)} + \frac{1}{(k'_x - k_p)(k_x - k_p)} \right]$$

$$- \frac{\alpha_R R}{\pi}\left[\frac{1}{(k'_x - k_p)(k_x - k_p)} + \frac{1}{(k'_x - k_p)(k_x - k_p)} \right] \qquad \textbf{(11.51)}$$

The term in the first square brackets describes the reflection at the half-space without crack. It is the only part that remains for $T = 1$ and $R = 0$. The Rayleigh term there is a Lorentz function that is the Fourier transform of an exponential wave decaying to both sides of $x = 0$. The delta function makes the effect of this term translation invariant in the position space. The other terms are due to transmission or reflection of the surface wave. Their forms are due to the wave cutoff at the position of the crack. In both variables the terms are Fourier transforms of exponential waves which are set to 0 on either side of $x = 0$ and decay to the other side. The terms containing $(1 - T)$ reduce beyond the crack the amplitude of the waves that are due to the Lorentz function. For positive defocus besides the specular reflection, only the terms containing R have considerable influence on the microscope signal.

The fringe spacing around a surface breaking crack or a material boundary can be used to determine the Rayleigh velocity. It simply is half the wavelength of the Rayleigh wave. For the sample shown in Figure 11.14, this yields a Rayleigh wave velocity of (8.0 ± 2.1) km/sec, whereas Brillouin scattering measurements[87] of the Rayleigh wave velocity of the same sample yields (6.7 ± 0.3) km/sec. We note that though the error of the measured Rayleigh wave velocity by the SAM is greater than that determined by Brillouin scattering, the SAM measurements provide a reasonable estimate of the surface acoustic wave velocity of the superhard sample.

11.3.2   Image Formation of Three-Dimensional Objects

In confocal optical microscopy the theories of three-dimensional image formation are usually based on the Born approximation and so are valid only for weakly scattering objects.[88] In the case of biological materials, the Born approximation to the scattering problem can be used both in acoustics and in optics. Because acoustic microscopy is widely applied to hard materials involving strong scattering, it is necessary to extend the theories available today to include these objects. In this section, we will present a theory of image formation for strongly scattering spheres in the reflection SAM following a method proposed by Weise et al.[9] The imaging of spheres forms the basis for understanding the contrast of many objects, extending from bubbles or spherical inclusions in solids to curved surfaces in general. Moreover, beads are used as well-defined phantom objects for testing imaging systems.[89] From the theoretical point of view, spheres are the only three-dimensional particles for which an analytical solution of the scattering problem is available. Due to its sectioning ability, the confocal microscope is frequently used for surface profiling. It can be done by searching the axial contrast maximum.[90] However, spherical particles are an example that contrast maxima may also occur when the surface is considerably defocused (when the focus is in the center of the curvature).

In general the part of the scattering function describing the behavior of homogeneous (non-evanescent) waves, which is important for confocal

Theory and Applications of Acoustic Microscopy   685

imaging, can also be obtained directly from the far-field distribution of the scattered wave. The asymptotic behavior of the field distribution Φ_s scattered from a bounded obstacle for an incident plane wave with wave vector k' can be written as[91]

$$\Phi_s\left(\frac{k}{k}r\right) = f\left(\frac{k}{k'}\frac{k'}{k'}\right)\frac{\exp(ikr)}{r}, \quad \text{as} \quad kr \to \infty \qquad (11.52)$$

where r is the distance from the origin and $f\left(\frac{k}{k'}\frac{k'}{k'}\right)$ is the far-field scattering amplitude. The relation of the homogeneous wave part of the scattering function g to the far-field scattering amplitude $f\left(\frac{k}{k'}\frac{k'}{k'}\right)$ can be obtained using the angular spectrum representation of the far-field distribution[92, p.114]

$$g_s(k_x,k_y,k_x',k_y') = \frac{i}{2\pi k_z}f\left(\frac{k}{k'}\frac{k'}{k'}\right) \quad \text{for} \quad k_x^2 + k_y^2 < k^2. \qquad (11.53)$$

Combining Equation 11.24 and Equation 11.53 and omitting the normalizing constant, we obtain

$$V(X,Y,Z) = \int\int_{-\infty}^{\infty}\int\int_{-\infty}^{\infty} P(-k_x,-k_x)P_s(k_x',k_x')f\left(\frac{k}{k'}\frac{k'}{k'}\right)$$

$$\exp[i(k_x'-k_x)X + (k_y'-k_y)Y + (k_z'-k_z)Z]\frac{dk_x'dk_y'dk_xdk_y}{kk_z'kk_z} \qquad (11.54)$$

The same expression has been obtained in Zinin et al.,[10] but tedious calculation is required. The far-field angular distribution for scattering by a spherical particle can be found analytically[91]

$$f\left(\frac{k}{k'}\frac{k'}{k'}\right) = \frac{1}{k}\sum_{n=0}^{\infty}(2n+1)A_nP_n(\cos\gamma_k) \qquad (11.55)$$

where the A_n describe the scattering amplitudes which depend on particle size and material properties, and P_n are ordinary Legendre polynomials. γ_k is the angle between k and k'. In the scalar theory the A_{nm} are independent of m. [93]

In order to separate incident wave and reflected wave coordinates in Equation 11.55, we use the addition theorem for spherical harmonics[94] $Y_{n,m}$

$$P_n(\cos\gamma_k) = \frac{4\pi}{(2n+1)}\sum_{n=-m}^{m}Y_{n,m}^*\left(\frac{k'}{k'}\right)Y_{n,m}\left(\frac{k}{k}\right) \qquad (11.56)$$

In order to evaluate integral in Equation 11.54 we introduce spherical coordinates (Equation 11.9) and assume that P is independent of φ_k. After combining Equation 11.54 to Equation 11.56; writing $Y_{n,m}$ with the aid of the associated Legendre polynomials[94] $P_n^m(\cos\theta), Y_{n,m}(\theta_k, \varphi_k) = \sqrt{\frac{(2n+1)(n-m)!}{4\pi(n+m)!}}\, P_n^m(\cos\theta_k)\exp(im\varphi_k)$; and using the integral definition of the cylindrical Bessel functions J_m,

$$J_m(kR\sin\theta_k) = \frac{(\pm i)^m}{2\pi}\int_0^{2\pi}\exp\left[\pm i\left(kR\sin\theta_k\cos\theta_k + m\varphi_k\right)\right]d\varphi_k \qquad (11.57)$$

we finally obtain the output signal of the reflection SAM

$$V(R,Z) = \frac{V_o}{(1-\cos\alpha)}\sum_{n=0}^{\infty}\sum_{m=0}^{n}(-1)^n(2-\delta_{om})A_n I_{nm}^2(R,Z) \qquad (11.58)$$

$$I_{nm}(R,Z) = (-1)^m\int_0^{\alpha}P(\theta)\exp(ikZ\cos\theta)J_m(kR\sin\theta)\overline{P}_n^m(\cos\theta)\sin\theta\,d\theta \qquad (11.59)$$

where $\overline{P}_n^m(\cos\theta) = P_n^m(\cos\theta)N_{nm}$ and $N_{nm} = \sqrt{(2n+1)(n-m)!/[2(n+m)!]}$ are the normalizing coefficients and δ_{om} is the Kroneker delta symbol. To derive Equation 11.59, we also used properties of the Legendre polynomials: $P_n^m(-\cos\theta) = (-1)^{n+m}P_n^m(\cos\theta)$. For the transmission SAM the expression for the output signal has the form

$$V(R,Z) = \frac{V_o}{(1-\cos\alpha)}\sum_{n=0}^{\infty}\sum_{m=0}^{n}(-1)^n(2-\delta_{om})A_n I_{nm}(R,Z)I_{nm}^*(R,Z) \qquad (11.60)$$

where the superscript * denotes the complex conjugate. The model given by Equation 11.59 to Equation 11.60 describes contrast formation in the reflection SAM for spherical particles. C-scan images of spherical particles are formed by scanning in the xy-plane at a fixed Z position. If $Z = 0$, the focal plane passes through the center of the sphere. If $Z = a$, the focal plane touches the front surface of the sphere. Because of axial symmetry, the image of a sphere can be characterized by a curve that depends only on the distance R between the center of sphere and the axis of the lens ($V(R)$ curve). In such a case only the X-Z medial section (X-Z-scan) of the three-dimensional images may be considered.

Experimental and simulated X-Z-scans of a steel sphere are presented in Figure 11.15(a) and Figure 11.15(b). To calculate the X-Z-scan of a spherical particle in the reflection and the transmission SAM, we use the elementary pupil function and expand the integral I_{nm} in a series.[93] The images of a steel particle are strongly dependent on the semiaperture angle, so the same
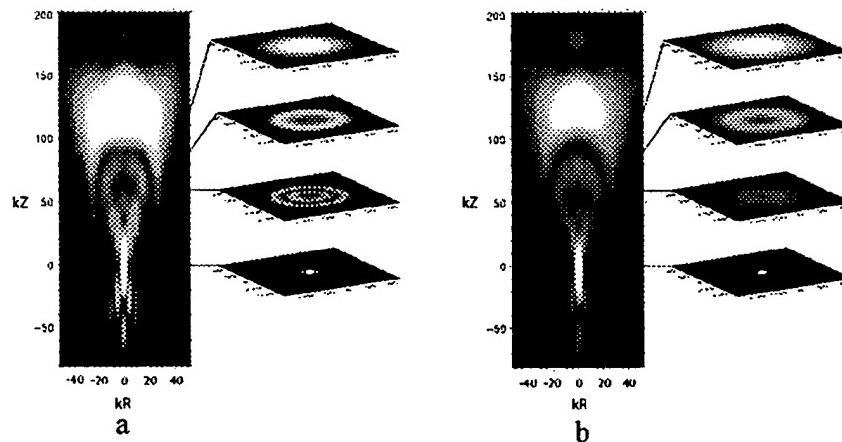
FIGURE 11.15
(a) X-Z scan through a steel sphere for a reflection microscope (OXSAM) at 105 MHz. The radius of the sphere was 560 µm. The semiaperture angle of the microscope lens was 26.5°. Z = 0 corresponds to focusing to the center of the sphere. (b) X-Z scan through a steel sphere for reflection microscope calculated with the same parameter as in (a) (From Zinin, P. et al., *Optik*, 107, 45, 1997. With permission.)

spherical particle has quite different X-Z-scans. Two regions of high image contrast occur. The maximum amplitude of the output signal is encountered when the focal point scans the top surface (top image) or the region close to the particle center. It has been shown that the image contrast obtained when scanning laterally or axially in the vicinity of the center of sphere reproduces the field emitted by the transducer contracted twice and is independent of the properties of the sphere.[93,95] A contraction by a factor of two of the center images in the lateral direction had been predicted by Atalar[37] and has been experimentally proven.[96] The image appears when the shape of the wave front emitted by the transducer and the shape of the particle coincide. For an object whose shape is far from spherical, there is no such image.[95]

In an X-Z-scan, the contrast of the top images looks like a thin layer. With increasing surface inclination, the thickness of this layer increases while its contrast decreases. The bigger the semiaperture angle of the lens, the thinner the layer. With increasing α, the images are even more similar to the object. The main features of contrast formation close to the surface can be well described quantitatively by the approximation proposed by Weise et al.[57] In that paper the signal obtained with a SAM from an uneven surface is approximated by the signal from a plane. This plane is tangential to the object surface at the point closest to the focal point of the transducer. It was shown that the image taken with the focus scanned at a fixed offset from the sphere's surface in the z-direction has the same form as the defocused OTF (see Figure 11.12). The normalized amplitude of the signal in a SAM for scanning along the surface of a rigid sphere is presented in Figure 11.12(b).
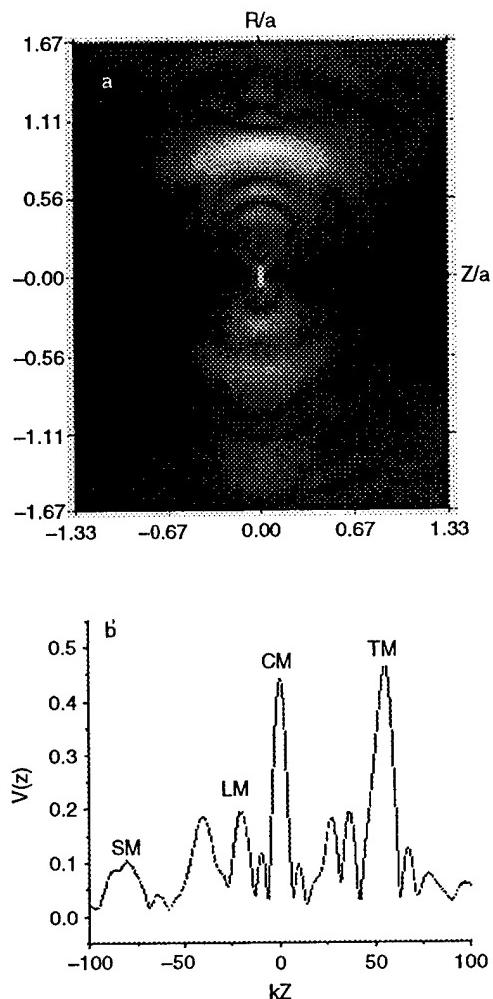
FIGURE 11.16

(a) X-Z medial section of a plexiglass sphere, $ka = 60$ calculated for reflection SAM. Axes scaled in units of the sphere's radius. (b) $V(Z)$ curve for a plexiglass sphere $(kR = 0)$. TM = top maximum, CM = center maximum, LM = longitudinal maximum, SM = shear maximum. The semiaperture angle is equal to $60°$. (From Zinin, P. et al., *Wave Motion*, 25, 213, 1997. With permission.)

The contrast is inversely dependent on the inclination of the surface under focus. The maximum follows the surface profile. An elegant analytical form of the top image of a sphere in the SOM was obtained recently.[97]

Let us now consider the effects of acoustical parameters of particles on the image contrast. In the case of particles that can be penetrated by sound, we can see the bottom of the particle — dark side of the moon (see Figure 11.16,

calculated for a Plexiglas sphere with parameters from Table 11.1). With increasing differences in the acoustical properties between particles and immersion liquids ($c > c_p$, c_p is the longitudinal velocity inside the particle) the dark side image moves toward the particle center. In the case of a solid particle, we can distinguish two bottom images as two kinds of waves that are focused inside the solid particles: the longitudinal and the transverse wave.[76] The radius of these images can be estimated from the position of the corresponding peaks on the $V(Z)$ curves (see Figure 11.16[b]). In Figure 11.16 there are 4 maxima on the $V(Z)$ curves for a liquid particle. The first maximum appears when the front surface of a sphere ($Z = a$, top maximum [TM]), and the second one appears when the center ($Z = 0$, center maximum [CM]) coincides with the focal point. The distance between these two maxima is equal to the sphere radius. The third maximum of the $V(Z)$ curves is due to focusing of the longitudinal waves onto the back of the sphere.[76] The top and bottom images have the form of an arc. The radius of the top arc is equal to that of the sphere, while the radius of the bottom arc is equal to the distance between CM and LM. For materials in which the shear waves can propagate we expect an image due to focusing of transverse waves by the bottom of the particle. The position of the maxima can be estimated by the following formula:[76]

$$Z_{P,S} = \frac{a}{2c_{P,S}/c - 1} \tag{11.61}$$

where $Z_{P,S}$ and $c_{P,S}$ are the positions of the maxima on the $V(Z)$ curve and sound velocities for longitudinal and shear wave, respectively. For a highly reflecting sphere such as steel or aluminum, the dark side images merge with the central image[76] (see Figure 11.15). The appearance of the region between CM and TM is influenced by the generation of Rayleigh waves.

For large spherical particles ($ka \gg 1$), the maximum radius of the top image appears to be reduced to about $ka \sin \alpha$. Hence the maximum area of contrast depends on the aperture of the microscope. This phenomenon was investigated theoretically[59] and experimentally[96] and was called the spherical particle size reduction effect. It arises because the reflection SAM cannot image surfaces inclined by an angle bigger than the semiaperture angle.[57] Therefore, from SAM images it is often not possible to attribute the vanishing of contrast to the edge of the object.

Now it is not difficult to predict the appearance of a three-dimensional image of an arbitrary uneven surface. The image must have the form of a thin layer whose shape follows the surface of the object. The thickness and brightness of this layer will be dependent on the surface inclination.

The images of spheres in transmission microscopes are quite different from those we have observed in the reflection SAM. In the transmission case, the width of the central dark spot or dark ring for $Z = 0$ is close to the real radius value of the sphere (see Figure 11.17). The dimension of the image in the

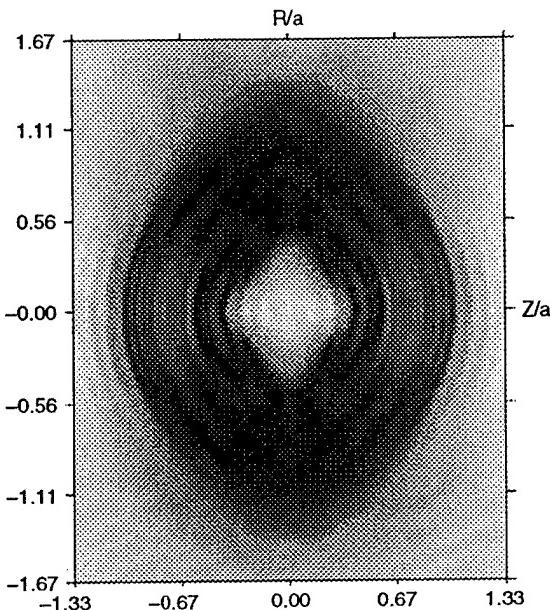**FIGURE 11.17**
X-Z medial section of a plexiglass sphere calculated for transmission SAM. The parameters of the sphere are the same as in Figure 11.16. The semiaperture angle of the transducer is equal to 60°. Axes scaled in units of the sphere's radius. (From Zinin, P. et al., *Wave Motion*, 25, 213, 1997. With permission.)

axial direction equals $a/\sin\alpha$, and elongation can be simply described by

$$a_{elong} = \frac{a(1-\sin\alpha)}{\sin\alpha} \qquad (11.62)$$

Interesting pictures are obtained when solid particles are investigated (see Figure 11.17). They exhibit a fringe pattern structure that is characteristic for the individual particle. It can be attributed to multiple reflection inside the particle, rainbow formation, and surface wave excitation.

11.3.3 Subsurface Imaging

Consider now imaging of a subsurface defect. The schematic diagram is given in Figure 11.18. The center of the spherical cavity is placed at point O' with coordinates $(X, Y, Z + D)$. Here $(Z + D)$ is the distance from the center of curvature of the transducer along the transducer axis. The distance between the liquid/solid interface and the center of the cavity O' is D, and the distance from the center of curvature of the transducer and the solid
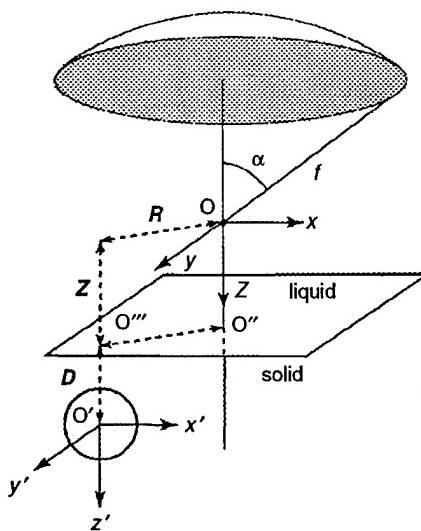
FIGURE 11.18

Problem geometry for subsurface imaging. 1 = spherical focusing transducer, 2 = liquid/solid interface, 3 = spherical cavity.

liquid interface is Z. The horizontal distance from the transducer axis is $\sqrt{X^2 + Y^2} = R$ and the radius of the cavity a.

To obtain an analytical solution for the output signal of the microscope for this system, it is necessary to make several assumptions. We will consider the waves scattered by the cavity only once and disregard the multiplied scattered waves. It is also assumed that the wave reflected at the liquid/solid interface is not disturbed by the cavity, so the signal due to reflection from the liquid/solid interface can be represented in the standard form of the $V(Z)$ curve for a half-space. This assumption is valid when the cavity is located below the Rayleigh wave penetration depth; it is also valid when the waves scattered from the cavity are weak compared to those reflected at the liquid/solid interface, so that their contribution to Rayleigh wave generation can be neglected. The latter holds for a cavity smaller than the wavelength of the Rayleigh wave. On these assumptions we will proceed with the theory.

It is convenient to write the output signal as a superposition of contributions of different wave types. First, the transducer receives a signal that is due to the wave reflected at the liquid/solid interface. This signal has the form of the $V(Z)$ curve of the solid in the absence of the cavity,[66] and we will denote it as V_R (R for reflection). The first signal from the cavity received by the transducer is the wave transmitted as a longitudinal wave into the solid and scattered by the cavity as a longitudinal wave. We will denote this wave as the PP wave and the output signal from this wave will be denoted as V_{PP}. Thereafter two waves reach the transducer simultaneously. A wave is transmitted into the solid as transverse wave and scattered by the cavity as

longitudinal wave (PS wave) and its reverse (SP wave). The output signal corresponding to these two waves is $(V_{SP} + V_{PS})$. The slowest wave received by the transducer is the SS wave. It is transmitted into the solid as a transverse wave and scattered by the cavity as a transverse wave. The voltage corresponding to this signal is V_{SS}. The total output signal V generated by the scattered waves is equal to

$$V(R,Z) = V_R(Z) + V_{PP}(R,Z) + (V_{SP}(R,Z) + V_{PS}(R,Z)) + V_{SS}(R,Z) \quad \textbf{(11.63)}$$

A detailed derivation of each term of Equation (11.63) requires solving of the spherical particle diffraction problem of shear and longitudinal wave propagation in solids and would exceed the scope of this chapter. For a spherical cavity, the subject was discussed in detail by Lobkis et al.[8] Here we present only the final expression as developed there.[8] Omitting a constant, the terms in Equation 11.63 may be written as

$$V_{PP}(R,Z) = \frac{\rho_s c_P}{\rho\,c} \sum_{n=0}^{\infty} \sum_{m=0}^{n} (-1)^n (2 - \delta_{0m}) A_n^{PP} \, L_{nm}^2(R,Z) \quad \textbf{(11.64)}$$

$$V_{SP}(R,Z) + V_{PS}(R,Z) = \frac{\rho_s}{\rho\,c} \sum_{n=0}^{\infty} \sum_{m=0}^{n} (-1)^n (2 - \delta_{0m}) \left(c_P A_n^{PS} + c_S A_n^{SP} \right) L_{nm}(R,Z) T_{nm}^{SV}(R,Z)$$

$$\textbf{(11.65)}$$

$$V_{SS}(R,Z) = \frac{\rho_s c_S}{\rho\,c} \sum_{n=0}^{\infty} \sum_{m=0}^{n} (-1)^n (2 - \delta_{0m}) \left[A_n^{SS} \left(T_{nm}^{SV}(R,Z) \right)^2 - A_n^{SH} \left(T_{nm}^{SH}(R,Z) \right)^2 \right]$$

$$\textbf{(11.66)}$$

with the definitions

$$L_{nm}(R,Z) = (-1)^m \int_0^\alpha P(\theta) T_P(\theta) \exp[i(kZ\cos\theta + k_P D\cos\theta_P)] J_m(kR\sin\theta) \overline{P}_n^m(\cos\theta_P)\sin\theta d\theta$$

$$\textbf{(11.67)}$$

$$T_{nm}^{SV}(R,Z) = (-1)^m \int_0^\alpha P(\theta) T_S(\theta) \exp[i(kZ\cos\theta + k_S D\cos\theta_S)] J_m(kR\sin\theta) \frac{\partial \overline{P}_n^m(\cos\theta_S)}{\partial\theta_S} \sin\theta d\theta$$

$$\textbf{(11.68)}$$

$$T_{nm}^{SH}(R,Z) = (-1)^m \int_0^\alpha P(\theta) T_S(\theta) \exp[i(kZ\cos\theta + k_S D\cos\theta_S)] J_m(kR\sin\theta) \frac{m\overline{P}_n^m(\cos\theta_S)}{\sin\theta_S} \sin\theta d\theta$$

$$\textbf{(11.69)}$$

724   *Ultrasonic Nondestructive Evaluation*

141. Lawrence, C.W., Briggs, G.A.D., and Scruby, C.B., Acoustic microscopy of ceramic-fiber composites.3. Metal-matrix composites, *J. Mater. Sci.*, 28, 3653–3660, 1993.

142. Lawrence, C.W., Briggs, G.A.D., and Scruby, C.B., Acoustic microscopy of ceramic-fiber composites.2. Glass ceramic- matrix composites, *J. Mater. Sci.*, 28, 3645–3652, 1993.

143. Lawrence, C.W., Briggs, G.A.D., Scruby, C.B., and Davies, J.R.R., Acoustic microscopy of ceramic-fiber composites. 1. Glass-matrix composites, *J. Mater. Sci.*, 28, 3635–3644, 1993.

144. Zhai, T., Knauss, D., Briggs, G.A.D., and Martin, J.W., Mixed-mode crack mouth reflection in time-resolved acoustic microscopy of short fatigue cracks in single-crystal aluminum, *J. Phys. D*, 27, 719–725, 1994.

145. Yen, C.E. and Tittmann, B.R., Fiber-matrix interface study of carbon-carbon composites using ultrasonics and acoustic microscopy, *Composit. Eng.*, 5, 649, 1995.

146. Rats, D., von Stebut, J., and Augereau, F., High frequency scanning acoustic microscopy: a novel non-destructive surface analytical tool for assessment of coating-specific elastic moduli and tomographic study of subsurface defects, *Thin Solid Films*, 355–356, 347–352, 1999.

147. Connor, Z.M., Fine, M.E., Achenbach, J.D., and Seniw, M.E., Using scanning acoustic microscopy to study subsurface defects and crack propagation in materials, *JOM-e* 50, http://www.tms.org/pubs/journals/JOM/9811/Connor/Connor-9811.html, 1998.

148. Arnold, W., Fassbender, S.U., and Weides, G., Measurement of elastic properties related to the R-Curve-behavior of ceramics, (in press), 2002.

149. Drescher-Krasicka, E. and Willis, J.R., Mapping stress with ultrasound, *Nature*, 384, 52–55, 1996.

150. Landa, M. and Plesek, J., Contrast enhancement of ultrasonic imaging of internal stresses in materials, *Ultrasonics*, 40, 531–535, 2002.

151. Grill, W., Hillmann, K., Kim, T.J., Lenkeit, O., Ndop, J., and Schubert, M., Scanning acoustic microscopy with vector contrast, *Physica B*, 263, 553–558, 1999.

152. Schubert, M., Lenkeit, O., and Grill, W., Volume imaging by three dimensional scanning acoustic microscopy with phase contrast, *Instrum. Sci. Tech.*, 27, 227, 1999.

153. Ihara, I., Jen, C.-K., and Ramos França, D., Ultrasonic imaging, particle detection, and V(z) measurements in molten zinc using focused clad buffer rods, *Rev. Sci. Instrum.*, 71, 3579–3586, 2000.

154. Lefeuvre, O., Characterisation of Stiffening Layers by Acoustic Microscopy and Brillouin Spectroscopy, D. Phil. thesis, University of Oxford, 1998.

155. Manghnani, M.H., Elastic properties of cBN as a function of temperature and pressure: a comparison with diamond, in *5th NIRIM Int. Symp. Adv. Mater. (ISAM' 98)*, National Institute for Research in Inorganic Materials, Chicherster, 1998, pp. 73–78.

156. Field, J.E., *The Properties of Natural and Synthetic Diamond*, Academic Press, London, 1992.

157. Dragonette, L.R. and Uberall, H., RST analysis pf monostatic and bistatic acoustic echoes from an elastic sphere, *J. Acoust. Soc.Am.*, 73, 1–12, 1983.

123. Zinin, P., Manghnani, M.H., Newtson, C., and Livingston, R. A., Acoustic microscopy of steel reinforcing bar in concrete, *J. Nondestrucive. Evaluation,* 31, 153–161, 2002.

124. Weglein, R.D., Integrated-circuit inspection via Acoustic microscopy, *IEEE Trans. Sonics Ultrasonics,* 30, 40–42, 1983.

125. Attal, J., Acoustic microscopy: imaging microelectronic circuits with liquid metals, in *Scanned Image Microscopy,* Ash, E.A., Ed., Academic Press., London, 1980, pp. 97–118.

126. Pfannschmidt, G., Characterization of electronic components in acoustic microscopy, in *Advances in Acoustic Microscopy,* Briggs, A. and Arnold, W., Eds., Plenum Press, New York, 1996, pp. 1–38.

127. Crean, G.M., Flannery, C.M., and Mathuna, S.C., Acoustic microscopy analysis of microelectronic interconnection and packing technologies, in *Advanced in Acoustic Microscopy,* Briggs, A., Ed., Plenum Press, New York, 1995, pp. 1–48.

128. Ousten, Y., Mejdi, S., Fenech, A., Deletage, J.Y., Bechou, L., Perichaud, M.G., and Danto, Y., The use of impedance spectroscopy, SEM and SAM imaging for early detection of failure in SMT assemblies, *Microelectron. Reliab.,* 38, 1539–1545, 1998.

129. Moore, T.M., C-Mode acoustic microscopy applied to integrated-circuit package inspection, *Solid-State Electronics,* 35, 411–421, 1992.

130. Barton, J., Compagno, T., and Barrett, J., Scanning acoustic mycroscopy studies of microelectronic packging, in *Acoustical Imaging,* Halliwell, M. and Wells, P.N.T., Kluwer Academic, New York, 2000.

131. Benstetter, G., Ruprecht, M.W., and Hunt, D.B., A review of ULSI failure analysis techniques for DRAMs 1. Defect localization and verification, *Microelectron. Reliab.,* 42, 307–316, 2002.

132. Jipson, V.B., Acoustic microscopy of interior planes, *Appl. Phys. Lett.,* 35, 385–387, 1979.

133. Levin, V.M., Blank, V.D., Prokhorov, V.M., Soife, J.M., and Kobelev, N.P., Elastic properties of solid C_{60}: measurements and relationship with nanostructure, *J. Phys. Chem. Sol.,* (in press), 2000.

134. Wickramasinghe, H.K., Mechanically scanned B-scan system for acoustic microscopy of solids, *Appl. Phys. Lett.,* 39, 305–307, 1981.

135. Bray, R.C., Quate, C.F., Calhoun, J., and Koch, R., Film adhesion studies with the acoustic microscope, *Thin Solid Films,* 74, 295–302, 1980.

136. Addison, R.C., Somekh, M., and Briggs, G.A.D., Techniques for the characterization of film adhesion, *IEEE 1986 Ultrason. Symp. Proc.,* New York, 1986, pp. 775–782.

137. Parthasarathi, S., Tittmann, B.R., and Ianno, R J., Quantitative acoustic microscopy for characterization of the interface strength of diamond-like carbon thin films, *Thin Solid Films,* 300, 42–50, 1997.

138. Wang, L., The contrast mechanism of bond defects with the scanning acoustic microscopy, *J. Acoust. Soc. Am.,* 104, 2750, 1998.

139. Guo, Z., Achenbach, J.D., Madan, A., Martin, K., and Graham, M.E., Modeling and acoustic microscopy measurements for evaluation of the adhesion between a film and a substrate, *Thin Solid Films,* 394, 188–200, 2001.

140. Kendig, M., Abdelgawad, M., and Addison, R., Cathodic disbonding in microelectronics observed by insitu scanning acoustic microscopy, *Corrosion,* 48, 368–372, 1992.

AU: Ref. 133 (Levin et al. 2000): in press: Update?

106. Zhang, J., Baboux, J.C., and Guy, P., PVDF large aperture spherical transducer in the transient mode, in *Proc. IEEE 1994 Ultrasonic Symp.*, McAvoy, B.R., Levy, M., and Scheider, S.C., Eds., IEEE Press, New York, 1994, pp. 517–520.

107. Xiang, D., Hsu, N.N., and Blessing, G.V., The design, construction and application of a large-aperture lens- less line-focus PVDF transducer, *Ultrasonics*, 34, 641–647, 1996.

108. Li, W. and Achenbach, J.D., Determination of elastic constants by time-resolved line-focus acoustic microscopy, *IEEE Trans. Ultrasonic Ferroelectric Frequency Control*, 44, 681–687, 1997.

109. Papoulis, A., *The Fourier Integral and Its Applications*, McGraw-Hill, New York, 1962.

110. Zhang, J., Guy, P., Baboux, J.C., and Jayet, Y., Theoretical and experimental responses for a large-aperture broadband spherical transducer probing a liquid-solid boundary, *J. Appl. Phys.*, 86, 2825–2835, 1999.

111. Hollis, R.L.H.R., Defect detection for microelectronics by acoustic microscopy, in *Scanned Image Microscopy.*, Ash, E.A., Ed., Academic Press, 1980, pp. 155–164.

112. Khuriyakub, B.T., Reinholdtsen, P., and Jun, K.S., Subsurface Defect Detection Using Acoustic Microscopy, in *IEEEE 1984 Ultrasonics Symp. Proc.*, Vols. 1&2, Piscataway, NJ, 1984, pp. 580–583.

113. Ishikawa, I., Kanda, H., and Katakura, K., An acoustic microscope for subsurface defect characterization, *IEEE Trans. Sonics Ultrasonics*, 32, 325–331, 1985.

114. Atalar, A., Penetration depth of the scanning acoustic microscope, *IEEE Trans. Sonics Ultrasonics*, 32, 164–167, 1985.

115. Miyasaka, C., Tittmann, B.R., and Ohno, M., Practical shear wave lens design for improved resolution with acoustic microscope, *Res. Nondestructive Evaluation*, 11, 97–116, 1999.

116. Levin, V.M., Maev, R.G., Maslov, K.I., Senjushkina, T.A., Grigorieva, I.G., and Baranchikova, I., Study of structure and properties of highly anisotropic materials by acoustomicroscopic methods, in *Acoustical Imaging*, Ermert, H. and Harjes, H.P. Plenum Press, New York., 1992, pp. 651–656.

117. O'Neill, B.E. and Maev, R.G., Integral approximation method for calculating ultrasonic beam propagation in anisotropic materials, *Phys. Rev. B*, 58, 5479–5485, 1998.

118. Miyasaka, C., Tittmann, B.R., and Ohno, M., Practical shear wave lens design fro improved resolution with acoustic microscope, *Res. Nondestructive Evaluation*, 11, 97–116, 1999.

119. Bechou, L., Angrisiani, L., Ousten, Y., Dallet, D., Levi, H., Daponte, P., and Danto, Y., Localization of defects in die-attach assembly by continuous wavelet transform using scanning acoustic microscopy, *Microelectron. Reliab.*, 39, 1095–1101, 1999.

120. Angrisani, L., Bechou, L., Dallet, D., Daponte, P., and Ousten, Y., Detection and location of defects in electronic devices by means of scanning ultrasonic microscopy and the wavelet transform, *Measurement*, 31, 77–91, 2002.

121. Maslov, K.I., Kundu, T., and Lobkis, O.I., Acoustic microscopy for spherical inclusion characterization, *J. Acoust. Soc. Am.*, 100, 80–85, 1996.

122. Berezina, S., Blank, V., Levin, V., and Prokhorov, V., Observation of ultrasound velocity gradient in fullerene ceramics by acoustic microscopy, *Ultrasonics*, 38, 327–330, 2000.

AU: Ref 111: Please add all article authors (Last name & first initials).

86. Yamanaka, K. and Enomoto, Y., Observation of surface cracks with scanning acoustic microscope, *J. Appl. Phys.*, 53, 846–850, 1982.
87. Manghnani, M.H., Tkachev, S., Zinin, P.V., Zhang, X., Brazhkin, V.V., Lyapin, A.G., and Trojan, I.A., Elastic properties of superhard amorphous carbon pressure- synthesized from C_{60} by surface Brillouin scattering, *Phys. Rev. B*, 6412, 121403, 2001.
88. Steibl, N, Three-dimensional imaging by a microscope, *J. Opt. Soc. Amer. A.*, A2, 121–127, 1985.
89. McNally, J.G., Preza, C., Conchello, J., and Thomas, L.J., Artifacts in computational optical-sectioning microscopy, *J. Opt. Soc. Amer. A.*, 11, 1056–1067, 1994.
90. Hamilton, D.K. and Wilson, T., Surface profile measurement using the confocal microscope, *J. Appl. Phys.*, 53, 5320–5322, 1982.
91. Landau, L.D. and Lifshits, E.M., *Quantum mechanics: non-relativistic theory,* 2d, rev. and enl. ed. Pergamon Press; [sole distributors in the U.S.A.] Addison-Wesley Pub. Co., Reading, MA, Oxford, New York,, 1965.
92. Mandel, L. and Wolf, E., *Optical Coherence and Quantum Optics*, Cambridge University Press, Cambridge, 1995.
93. Zinin, P., Weise, W., Lobkis, O., Kolosov, O., and Boseck, S., Fourier optics analysis of spherical particles image formation in reflection acoustic microscopy, *Optik*, 98, 45–60, 1994.
94. Jackson, J.D., *Classical Electrodynamics*, John Wiley, New York, 1995.
95. Kolosov, O.Y.Y.L.O.Z.P., Evaluation of a Point-spread-function of focusing systems using spherical reflector, in *Ultrasonic International'93*, Butterworth-Heinemann, London, 1993, pp. 547–550.
96. Kolosov, O.V., Lobkis, O.I., Maslov, K.I., and Zinin, P.V., The effect of the focal plane position on the images of spherical objects in the reflection acoustic microscope, *Acoust.Lett.*, 16, 84–88, 1992.
97. Aguilar, J.F., Lera, M., and Sheppard, C.J.R., Imaging of spheres and surface profiling by confocal microscopy, *Appl. Opt.*, 39, 4621–4628, 2000.
98. Truell, R., Elbaum, C., and Chick, B.B., *Ultrasonic Methods in Solid State Physics*, Academic Press, New York, 1969.
99. Einspruch, N.G., Witterbolt, E.J., and Truel, R., Scattering of a plane transverse wave by a spherical obsticale in an isotropic elastic solid, *J. Acoust. Soc. Amer.*, 31, 806, 1960.
100. Ying, C.F. and Truel, R., Scattering of a plane longitudinal wave by a spherical obstacle in an isotropic elastic solid, *J. Acoust. Soc. Amer.*, 27, 1086, 1956.
101. Lobkis, O.I., Maslov, K.I., Kundu, T., and Zinin, P.V., Spherical inclusion characterization by the acoustical microscope - axisymmetrical case, *J. Acoust. Soc. Amer.*, 99, 33–45, 1996.
102. Yamanaka, K., Surface acoustic wave measurement using an impulse converging beam, *J. Appl. Phys.*, 54, 4323–4329, 1983.
103. Daft, C.M.W., Briggs, G.A.D., and Obrien, W.D., Frequency-Dependence of Tissue Attenuation Measured By Acoustic Microscopy, *J. Acoust. Soc. Amer.*, 85, 2194–2201, 1989.
104. Weaver, J.M.R., Daft, C.M.W., and Briggs, G.A.D., A quantitative acoustic microscope with multiple detection modes, *IEEE Trans. Ultrasonic Ferroelectric Frequency Control*, 36, 554–560, 1989.
105. Sinton, A.M., Briggs, G.A.D., and Tsukahara, Y., Time-resolved acoustic microscopy of polymer-coatings, in *Acoustical Imaging*, Kushibiki, J., Ed., Plenum Press, New York, 1989, pp. 87–95.

AU: Ref 95: Kolosov, O.Y.Y.L.O.Z.P.: Is author's name correct as written?

66. Atalar, A., An angular-spectrum approach to contrast in reflection acoustic microscopy, *J. Appl. Phys.*, 49, 5130–5139, 1978.

67. Kushibiki, J., Ohkubo, A., and Chubachi, N., Anisotropy detection in sapphire by acoustic microscope using line-focus beam, *Electron. Lett.*, 17, 534–536, 1981.

68. Kundu, T., Mal, A.K., and Weglein, R.D., Calculation of the acoustic material signature of a layered solid, *J. Acoust. Soc. Amer.*, 77, 353–361, 1985.

69. Kundu, T., A complete acoustic microscopic analysis of multilayered specimens, *J. Appl. Mech.*, 59, 54–60, 1992.

70. Kundu, T. and Mal, A.K., Acoustic material signature of a layered plate, *Int. J. Eng. Sci.*, 24, 1819–1829, 1986.

71. Somekh, M.G., Briggs, G.A.D., and Ilett, C., The effect of elastic anisotropy on contrast in the scanning acoustic microscope, *Phil. Mag. A*, 49, 179–204, 1984.

72. Every, A.G. and Deschamps, M., Principal surface wave velocities in the point focus acoustic materials signature V(z) of an anisotropic solid, in *Review of Progress in Quantitative Nondestructive Evaluation*, Thompson, D.O. and Chimenti, D.E., Eds., American Institute of Physics, College Park, MD, 2003, pp. 51–58.

73. Kushibiki, J., Ishikawa, T., and Chubachi, N., Cut-off characteristic of leaky Sezawa and pseudo-Sezawa wave modes for thin-film characterization, *Appl. Phys. Lett.*, 57, 1967–1969, 1990.

74. Chan, K.H. and Bertoni, H.L., Ray representation of longitudinal lateral waves in acoustic microscopy, *IEEE Trans. Ultrasonic Ferroelectric Frequency Control*, 38, 27–34, 1991.

75. Weglein, R.D., Acoustic microscopy of curved surfaces, *Appl. Phys. Lett.*, 38, 516–518, 1981.

76. Maslov, K.I., Zinin, P.V., Lobkis, O.I., and Kundu, T., V(z) curve formation of solid spherical microparticles in scanning acoustic microscopy, *J. Microsc.*, 178 (Pt2), 125–133, 1995.

77. Reinholdtsen, P.A. and Khuri-Yakub, B.T., Image processing for a scanning acoustic microscope that measures amplitude and phase, *IEEE Trans. Ultrasonic Ferroelectric Frequency Control* 38, 141–147, 1991.

78. Baker, L., Optical transfer function: foundation and theory. selected papers, in *SPI Milestone Series*, SPIE Optical Engineering Press., Bellingham, 1992.

79. Baker, L., Optical transfer function: measurement. selected papers, in *SPI Milestone Series*, SPIE Optical Engineering Press., Bellingham, 1992.

80. Lee, U.W. and Bond, L.J., Characterising of ultrasonic imaging system using transfer function, *Ultrasonics*, 141, 48–56, 1993.

81. Atalar, A., Modulation transfer function for the acoustic microscope, *Electron. Lett.*, 15, 321–323, 1979.

82. Zinin, P., Weise, W., Zhai, T., Briggs, G.A.D., and Boseck, S., Determination of the defocused transfer function of a confocal reflection microscope by imaging of a sphere, *Optik*, 107, 45–48, 1997.

83. Sheppard, C.J.R., Hamilton, D.K., and Cox, I.J., Optical microscopy with extended depth of field, *Proc. Royal Soc. London A.*, A387, 171–186, 1983.

84. Yamanaka, K. and Enomoto, Y., Fringe pattern around surface crack observed with scanning acoustic microscope, *Electron. Lett.*, 17, 638–640, 1981.

85. Ilett, C., Somekh, M.G., and Briggs, G.A.D., Acoustic microscopy of elastic discontinuities, *Proc. Royal Soc. London A.*, 393, 171–183, 1984.

45. Stamnes, J.J., *Waves in Focal Regions,* Adam Hilger, Bristol, 1986.
46. Emiliani, C., *Dictionary of the Physical Sciences,* Oxford University Press, Oxford, 1987.
47. Kino, G.S., *Acoustic Waves: Devices, Imaging and Analog Signal Processing,* Prentice-Hall, Englewood Cliffs, NJ, 1987.
48. Hadimioglu, B. and Quate, C.F., Water acoustic microscopy at suboptical wavelengths, *Appl. Phys. Lett.,* 43, 1006–1007, 1983.
49. Foster, J.S. and Rugar, D., High-resolution acoustic microscopy in superfluid-helium, *Appl. Phys. Lett.,* 42, 869–871, 1983.
50. Sheppard, C.J.R. and Wilson, T., Effects of high angles of convergence on V(Z) in the scanning acoustic microscope, *Appl. Phys. Lett.,* 38, 858–859, 1981.
51. Lobkis, O.I. and Zinin, P.V., Imaging of spherical object in acoustic microscope, in *Mathematical Modelling and Application of Diffraction Phenomena, Proc. All-Union Scientific Seminar. Moscow.* Moscow, 1990, pp. 59–60.
52. Howe, M.S., On the image of a cylindrical Inclusion in the scanning acoustic microscope, *Proc. Royal Soc. London A.,* 435, 393–403, 1991.
53. Rebinsky, D.A. and Harris, J.G., The acoustic signature for a surface-breaking crack produced by a point focus microscope, *Proc. Royal Soc. London A.,* 438, 47–65, 1992.
54. Parmon, W. and Bertoni, H.L., Ray interpretation of the material signature in the acoustic microscope, *Electron.Lett.,* 15, 684–686, 1979.
55. Bertoni, H.L. and Somekh, M.G., Ray-optical analysis of spherical focusing transducers for acoustic microscopy, in *IEEE 1985 Ultrasonics Symp. Proc.,* McAvoy, B.R., Ed., IEEE Press, New York, 1985, pp. 715–719.
56. Brekhovskikh, L.M., *Waves in Layered Media,* 2nd ed., Academic Press, New York, 1980.
57. Weise, W., Zinin, P., and Boseck, S., Modeling of inclined and curved surfaces in the reflection scanning acoustic microscope, *J. Microsc.,* 176, 245–253, 1994.
58. Levin, V.M., Lobkis, O.I., and Maev, R.G., Investigation of the spatial structure of acoustic field by a spherical focusing transducer, *Sov. Phys. Acous.,* 36, 391–395, 1990.
59. Zinin, P., Maslov, K., Lobkis, O., and Kolosov, O., The effect of spherical-particle size reduction in imaging of species by the reflection acoustic microscope, in *Ultrasonics Int. 93: Conf. Proc.,* Butterworth-Heinemann, 80 Montvale Avenue, Stoneham Ma 02180 Butterworth-Heinemann, Linacre House, Jordan Hill, Oxford Ox2 8dp United Kingdom, 1993, pp. 65–68.
60. Hildebrand, J.A., Liang, K., and Bennett, S.D., Fourier-transform approach to materials characterization with the acoustic microscope, *J. Appl. Phys.,* 54, 7016–7019, 1983.
61. Sheppard, C.J.R., Confocal interference microscopy, in *Confocal Microscopy,* Wilson, T., Ed., Academic Press, London, 1990, pp. 389–411.
62. Liang, K.K., Kino, G.S., and Khuri-Yakub, B.T., Material characterization by the inversion of V(z), *IEEE Trans. Sonics Ultrasonics,* 32, 213–224, 1985b.
63. Duquesne, J.Y., Inversion of complex V(Z) at high-frequencies for acoustic microscopy, *Rev. Sci. Instr.,* 67, 2656–2657, 1996.
64. Atalar, A., Quate, C.F., and Wickramasinghe, H.K., Phase imaging in reflection with the acoustic microscope, *Appl. Phys. Lett.,* 31, 791–793, 1977.
65. Weglein, R.D. and Wilson, R.G., Characteristic material signatures by acoustic microscopy, *Electron. Lett.,* 14, 352–354, 1978.

25. Hirsekorn, S., Pangraz, S., Weides, G., and Arnold, W., Measurement of elastic impedance with high-spatial-resolution using acoustic microscopy, *Appl. Phys. Lett.*, 67, 745–747, 1995.

26. Livingston, R.A., Manghnani, M.H., Wang, Y., and Zinin, P., Detection of cracks and interfacial transition zone in concrete by acoustic microscopy, in *Second US-Japan Symposium on Advances in NDT. Proceeding of the International Symposium*, Katoh, M. and Djordjevic, B.B., Eds., The Japanese Society for Non-Destructive Inspection, Tokyo, 1999, pp. 136–141.

27. Brundle, C.R., Evans, C.A., and Wilson, S., *Encyclopedia of Materials Characterization*, Butterworth-Heinemann, Boston, 1992.

28. Prasad, M., Manghnani, M.H., Wang, Y., Zinin, P., and Livingston, R.A., Acoustic microscopy of portland cement mortar aggregate/paste interfaces, *J. Mater. Sci.*, 35, 3607–3613, 2000.

29. Hauser, M.R., Weaver, R.L., and Wolfe, J.P., Internal diffraction of ultrasound in crystals: Phonon focusing at long wavelength, *Phys. Rev. Lett.*, 17, 2604–2607, 1992.

30. Weaver, R.L., Hauser, M.R., and Wolfe, J.P., Acoustic flux imaging in anisotropic media, *Zeitschrift Fur Physik B*, 90, 27–46, 1993.

31. Grill, W., Hillmann, K., Wurtz, K.U., and Wesner, J., Scanning ultrasonic microscopy with phase contrast, in *Advances in Acoustic Microscopy*, Briggs, A. and Arnold, W., Eds., Plenum Press, New York, 1996, pp. 167–218.

32. Tsukahara, Y., Nakaso, N., Ohira, K., and Yanaka, M., Interaction of acoustic waves with solid surfaces, in *Advances in Acoustic Microscopy*, Briggs, A. and Arnold, W., Eds., Plenum Press, New York, 1996, pp. 103–165.

33. Knaus, D., Zhai, T., Briggs, G.A.D., and Martin, J.M., Measuring short cracks by time-resolved acoustic microscopy, in *Advances in Acoustic Microscopy*, Briggs, A., Ed., Plenum Press, New York, 1995, pp. 49–77.

34. Daft, C.M.W. and Briggs, G.A.D., Wideband acoustic microscopy of tissue, *IEEE Trans. Ultrason. Ferroelect. Freq. Contr.*, 36, 258–263, 1989.

35. Krautkramer, J. and Krautkrämer, H., *Ultrasonic Testing of Materials*, 4th fully rev. ed. Springer-Verlag, Berlin, New York, 1990.

36. Auld, B.A., General electromechanical reciprocity relations applied to the calculation of elastic wave scattering coefficients, *Wave Motion*, 1, 3–10, 1979.

37. Atalar, A., A backscattering formula for acoustic transducers, *J. Appl. Phys.*, 51, 3093–3098, 1980.

38. Somekh, M.G., Bertoni, H.L., Briggs, G.A.D., and Burton, N.J., A two-dimensional imaging theory of surface discontinuities with the scanning acoustic microscope, *Proc. Royal Soc. London A.*, 401, 29–51, 1985.

39. Goodman, J.W., *Introduction to Fourier Optics*, 2nd ed., McGraw-Hill, New York, 1996.

40. Bracewell, R.N., *The Fourier transform and its applications*. McGraw-Hill, New York, 1987.

41. Weise, E., *Konfokale Rastermikroskopie zur Abbildung kugelförmiger Objekte*, PhD thesis, University of Bremen, Germany, 1997.

42. Liang, K.K., Kino, G.S., and Khuri-Yakub, B.T., Material characterization by the inversion of V(z), *IEEE Trans. Sonics Ultrasonics*, 32, 213–224, 1985a.

43. Sasaki, Y., Endo, T., Yamagishi, T., and Sakai, M., Thickness measurement of a thin-film layer on an anisotropic substrate by phase-sensitive acoustic microscope, *IEEE Trans. Ultrasonic Ferroelectric Freqency Control*, 39, 638–642, 1992.

44. Born, M. and Wolf, E., *Principles of Optics: Electromagnetic Theory of Propagation, Interference and Diffraction of Light*, Pergamon Press, Oxford, 1980.

4. Zinin, P.V., Quantitative acoustic microscopy of solids, in *Handbook of Elastic Properties of Solids, Liquids, and Gases. Volume I: Dynamic Methods for Measuring the Elastic Properties of Solids*, Levy, M., Bass, H., Stern, R., and Keppens, V., Eds., Academic Press, New York, 2001, pp. 187–226.

5. Sokolov, S., The ultrasonic microscope, *Doklady Akademia Nauk SSSR* (in Russian), 64, 333–336, 1949.

6. Lemons, R.A. and Quate, C.F., Acoustic microscope-scanning version, *Appl. Phys. Lett.*, 24, 163–165, 1974.

7. Quate, C.F., Atalar, A., and Wickramasinghe, H.K., Acoustic microscope with mechanical scanning: a review, *Proc. IEEE*, 67, 1092–1113, 1979.

8. Lobkis, O.I., Kundu, T., and Zinin, P.V., A theoretical analysis of acoustic microscopy of spherical cavities, *Wave Motion*, 21, 183–201, 1995.

9. Weise, W., Zinin, P., Wilson, T., Briggs, A., and Boseck, S., Imaging of spheres with the confocal scanning optical microscope, *Opt. Lett.*, 21, 1800–1802, 1996.

10. Zinin, P., Weise, W., Lobkis, O., and Boseck, S., The theory of three-dimensional imaging of strong scatterers in scanning acoustic microscopy, *Wave Motion*, 25, 213–236, 1997.

11. Crossen, J.D., Sykes, J.M., Zhai, T., and Briggs, G.A.D., Study of the coating/substrate interface by scanning acoustic microscopy: Cathodic disbonding of epoxy-polyamide lacquer from mild steel, *Faraday Discussions*, 107, 417–424, 1997.

12. Levin, V.M., Blank, V.D., Prokhorov, V.M., Soifer, J.M., and Kobelev, N.P., Elastic properties of solid C_{60}: measurements and relationship with nanostructure, *J. Phys. Chem. Sol.*, 61, 1017–1024, 2000.

13. Drescherkrasicka, E. and Willis, J.R., Mapping stress with ultrasound, *Nature*, 384, 52–55, 1996.

14. Kolosov, O. and Yamanaka, K., Nonlinear detection of ultrasonic vibrations in an atomic-force microscope, *Jap. J. Appl. Phys. Part 2*, 32, L1095–L1098, 1993.

15. Rabe, U. and Arnold, W., Atomic-force microscopy at MHz frequencies, *Annalen Der Physik*, 3, 589–598, 1994.

16. Briggs, A., *Advances in Acoustic Microscopy*, Plenum Press, New York, 1995, pp. 153–208.

17. Briggs, A. and Arnold, W., *Advances in Acoustic Microscopy*, Plenum Press, New York, 1996.

18. Wilson, T. and Sheppard, C., *Theory and Practice of Scanning Confocal Microscopy*, Academic Press, London, 1984.

19. Kushibiki, J. and Chubachi, N., Material characterization by line-focus-beam acoustic microscope, *IEEE Trans. Son. Ultrasonics*, 32, 189–212, 1985.

20. Atalar, A. and Hoppe, M., High-performance acoustic microscope, *Rev. Sci. Instr.*, 57, 2568–2576, 1986.

21. Reinholdtsen, P. A. and Khuri-Yakub, B.T., Amplitude and phase acoustic microscope using digital heterodyning, *Rev. Sci. Instr.*, 61, 1236–1242, 1990.

22. Forgber, E., Heygster, G., and Boseck, S., Modeling the imaging properties of SAM, *Optik*, 87, 170–178, 1991.

23. Heygster, G., Block, H., Gadomski, A., and Boseck, S., Modeling of the optical transfer-function (OTF) of the scanning acoustic microscope (SAM) and its relation to the other scanning microscopes, *Optik*, 85, 89–98, 1990.

24. Weise, W., Zinin, P., Briggs, A., Wilson, T., and Boseck, S., Examination of the two-dimensional pupil function in coherent scanning microscopes using spherical particles, *J. Acoust. Soc. Am.*, 104, 181–191, 1998.

Appendix C

The explicit form of the coefficients A_n^{ij} is

$$A_n^{SH} = -\frac{j_n(x_S) - x_S j_n'(x_S)}{h_n(x_S) - x_S h_n'(x_S)},$$

$$A_n^{PP} = -\frac{\Delta_n^{PP}}{\Delta_n}, \quad A_n^{PS} = -\frac{\Delta_n^{PS}}{\Delta_n}, \quad A_n^{SP} = -\frac{\Delta_n^{SP}}{\Delta_n}, \quad A_n^{SS} = -\frac{\Delta_n^{SS}}{\Delta_n}$$

(11.C.1)

where

$$\Delta_n = n(n+1)[h_n(x_P) - x_P h_n'(x_P)][h_n(x_S) - x_S h_n'(x_S)]$$
$$- [(\beta_n - 1)h_n(x_P) + 2x_P h_n'(x_P)][\beta_n h_n(x_S) + x_S h_n'(x_S)],$$

$$\Delta_n^{PP} = n(n+1)[j_n(x_P) - x_P j_n'(x_P)][h_n(x_S) - x_S h_n'(x_S)]$$
$$- [(\beta_n - 1)j_n(x_P) + 2x_P j_n'(x_P)][\beta_n h_n(x_S) + x_S h_n'(x_S)],$$

$$\Delta_n^{SS} = n(n+1)[h_n(x_P) - x_P h_n'(x_P)][j_n(x_S) - x_S j_n'(x_S)]$$
$$- [(\beta_n - 1)h_n(x_P) + 2x_P h_n'(x_P)][\beta_n j_n(x_S) + x_S j_n'(x_S)],$$

$$\Delta_n^{PS} = -\frac{i}{x_S}(1 + \beta_n), \quad \Delta_n^{SP} = -\frac{i}{x_P}(1 + \beta_n),$$

and

$$x_P = k_P a, \quad x_S = k_S a, \quad \beta_n = 1 + \frac{x_S^2}{2} - n(n+1).$$

References

1. Lemons, R. A. and Quate, C.F., Acoustic microscopy, in *Physical Acoustics*, Mason, W.P. and Thurston, R.N., Eds., Academic Press., London, 1979, pp. 1–92.
2. Briggs, A., *Acoustic Microscopy*, Clarendon Press, Oxford, 1992.
3. Gilmore, R.S., Industrial ultrasonic imaging/microscopy, in *Physical Acoustics*, Thurston, R.N., Pierce, A.D., and Papadakis, E., Eds., Academic Press, New York, 1999, pp. 275–346.

Theory and Applications of Acoustic Microscopy 715

Appendix B

For spherical elastic particles, the coefficients A_n are given by[157]

$$A_n = \frac{A_1^*(d_{22}d_{33} - d_{32}d_{23}) - A_2^*(d_{12}d_{33} - d_{32}d_{13})}{d_{11}(d_{22}d_{33} - d_{32}d_{23}) - d_{21}(d_{12}d_{33} - d_{32}d_{13})},$$

$$d_{11} = \frac{\rho}{\rho_i}(k_s a)^2 h_n(ka),$$

$$d_{12} = \left[2n(n+1) - (k_s a)\right]^2 j_n(k_p a) - 4(k_p a)^2 j_n'(k_p a),$$

$$d_{13} = 2n(n+1)\left[(k_s a) j_n'(k_s a) - j_n(k_s a)\right],$$

$$d_{21} = -(ka) h_n'(ka),$$

$$d_{22} = \left(k_p a\right) j_n'(k_p a),$$

$$d_{23} = n(n+1) j_n(k_s a),$$

$$d_{31} = 0,$$

$$d_{32} = 2[j_n(k_s a) - (k_p a) j_n'(k_p a)],$$

$$d_{33} = 2(k_s a) j_n'(k_s a) + [(k_s a)^2 - 2n(n+1) + 2] j_n(k_s a),$$

$$A_1^* = \frac{\rho}{\rho_s}(k_s a)^2 j_n(ka),$$

$$A_2^* = (ka) j_n'(ka)$$

(11.B.1)

here j_n are the spherical Bessel functions and $h^{(1)}$ the spherical Hankel functions of the first kind, $k_p = \frac{\omega}{c_p}$, $k_s = \frac{\omega}{c_s}$; c_p and c_s are longitudinal and shear velocities of the spherical particle. The stroke denotes the derivation.

714   *Ultrasonic Nondestructive Evaluation*

here $\tilde{Z}$ are the acoustic impedances defined by

$$\tilde{Z}_P = \frac{\rho_S c_p}{\cos\theta_P}, \ \tilde{Z}_S = \frac{\rho_S c_s}{\cos\theta_S}, \ \tilde{Z} = \frac{\rho\,c}{\cos\theta}, \ \tilde{Z}_{tot} = \tilde{Z}_P \cos^2(2\theta_S) + \tilde{Z}_S \cos^2(2\theta_S)$$

$$(11.A.2)$$

and ρ_s, c_p, and c_s are density, longitudinal wave velocity, and shear wave velocity of the sample; ρ and c are density and longitudinal wave velocity of water. The angles θ_P and θ_S are determined from Snell's law

$$\sin\theta_P = \frac{c_p}{c}\sin\theta, \quad \sin\theta_S = \frac{c_s}{c}\sin\theta \qquad (11.A.3)$$

The transmission coefficients for longitudinal (T_P) and shear waves (T_S) are given by[2]

$$T_P(\theta) = \frac{2\tilde{Z}_P\cos(2\theta_S)}{\tilde{Z}_{tot} + \tilde{Z}}, \ \ T_S(\theta) = \frac{-2\tilde{Z}_S\cos(2\theta_S)}{\tilde{Z}_{tot} + \tilde{Z}} \qquad (11.A.4)$$

For an incident energy flux E, the energy flux propagating away from the surface is[2]

$$E_T = \left|\Re(\theta)\right|^2 E \qquad (11.A.5)$$

while the transmitted longitudinal is

$$E_P = \frac{\rho\tan\theta}{\rho_s\tan\theta_p}\left|T_P(\theta)\right|^2 E \qquad (11.A.6)$$

and the transmitted shear is

$$E_S = \frac{\rho\tan\theta}{\rho_s\tan\theta_S}\left|T_S(\theta)\right|^2 E \qquad (11.A.7)$$

Conventionally, SAM images show variations of the amplitude of the acoustical signal. Reinholdtsen and Khuri-Yakub[21,77] measured amplitude and phase of the SAM signal at low frequency (3 to 10 MHz) to improve subsurface images. By modifying the two-dimensional point spread function, the transverse resolution was improved by about 20%, and the obscuring effect of surface roughness from images of subsurface features was eliminated.[77] Grill et al.[151] extended this technique to high frequency (1.2 GHz). This technique permits reconstruction of the surface relief of the sample with submicron resolution.[152]

The highest resolution in acoustic microscopy was achieved at low temperature.[49] However, high-temperature applications of the SAM appeared to be more attractive from the industrial point of view. Recently, an important step has been made in the direction of imaging subsurface structures in melts. Ihara et al.[153] developed a sound imaging technique to see a small steel object immerged in molten zinc at 600°C.

Exercise

Construct the contributions to the scattered field of the Rayleigh waves excited by the wavefield $\Phi_i(x')$ at a point x situated to the right of a crack at $x = 0$.
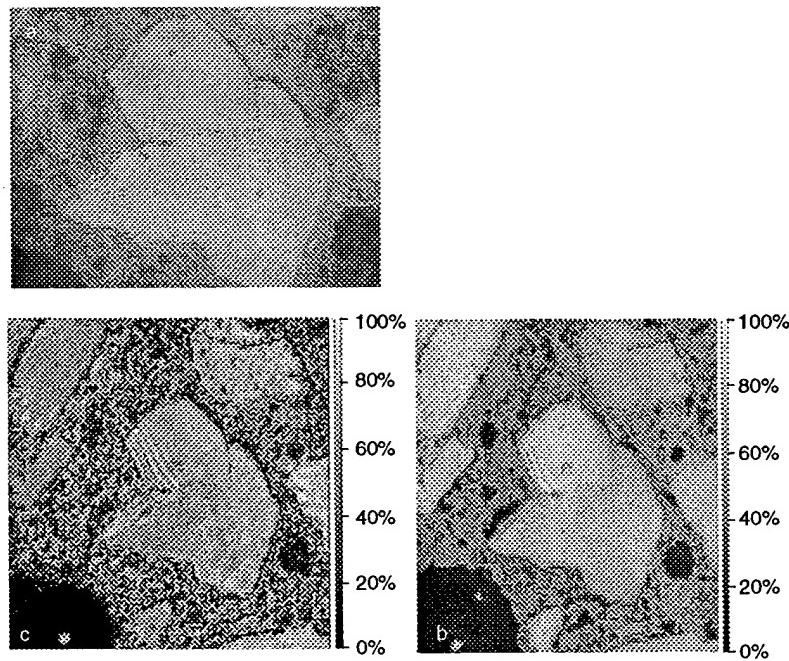
Acknowledgment

Appendix A

For solid liquid interface, the reflection coefficient can be expressed using acoustical impedances[2,115]

$$\Re(\theta) = \frac{\tilde{Z}_{tot} - \tilde{Z}}{\tilde{Z}_{tot} + \tilde{Z}} \qquad (11.A.1)$$
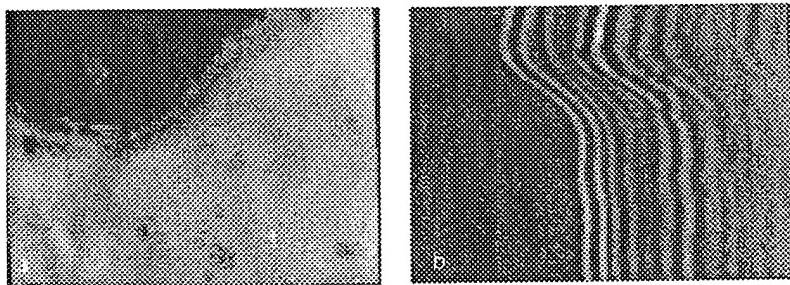
FIGURE 11.31

Concrete sample made with granitic aggregate grains and with plainement paste. (a) Reflected light microscopy; acoustic microscopy at 400 MHz. (b) $Z = -10$ μm, (c) $Z = -100$ μm (From Zinin, P., *Nondestructive Testing Evaluation Int.*, 33, 283, 2000. With permission.)

They must be either very thin surface breaking or subsurface cracks originating not deeper than the length of the Rayleigh wave.

SAM can be used not only for detection but also for crack characterization. Knauss *et al.* measured the depth of the short surface-breaking cracks by time-resolved microscopy.[33] Hidden from optical microscope, scratch-induced cracks have been observed in Al-Cu-Fe alloy coatings.[146] SAM can detect hidden fatigue cracks in riveted lap-joint samples (two aluminum alloys panels).[147] Arnold et al.[148] investigated the formation of microcracks in a frontal processing area around a crack. Lawrence et al.[142] demonstrated detection of cracks at the boundary between matrix and fiber in fiber composites.

11.4.5 Other SAM applications

A very interesting application for acoustic microscopy was found by Dresher-Krasiska. She demonstrated that time-resolved acoustic microscopy allows stress distribution to be visualized inside compressed aluminum.[149] Recently, Landa et al.[150] developed an approach that provides a quantitative description of the phenomena.

FIGURE 11.30

Acoustical images of the degraded joint of the same area as in Figure 11.29. Sample was in 90°C water for 49 days: (a) defocus distance = 23 μm; (b) time of flight SAM image shows cross section of the blister.

is likely due to corrosion of the aluminum rather than to disbonding at the interface.

11.4.4 Imaging Cracks

Cracking is a common cause for the degradation of materials used in industry, therefore early non-destructive detection of cracks is of importance. Scanning acoustic microscopy has proved to be of great value for the detection of cracks in a variety of materials such as ceramics,[2,141-143] metals,[144] and fiber composites.[145] Different types of cracks can be visualized by SAM, including surface-breaking cracks[33,86] and tensile cracks in hard coatings.[146]

For some materials SAM is the only method to detect cracks. For example, the ability to locate cracks at the aggregate/paste interface and subsurface cracks in aggregates in concrete is unique to SAM, since the cracks do not appear in optical images. In contrast, the scanning electron microscope can visualize only surface-breaking cracks. In addition, it may introduce cracks in the concrete as a result of sample preparation. Cracks that often appear during electron microscopy studies are due to the vacuum used for electron microscopy.

Acoustic microscopy shows its definite advantage over other techniques in identifying cracks within rocks and solids by the presence of the Rayleigh fringe contrast.[84] The theory of the fringe formation close to cracks is described in Section 11.3.1.3. Figure 11.31 shows a defocused acoustical image of granitic grains in Portland cement paste. The two acoustic images (Figure 11.31[b] and Figure 11.31[c]) were taken at 400 MHz. The Rayleigh wave fringes appear in the slightly defocused acoustical image ($Z = -10$ μm), indicating the existence of some cracks. At higher defocus ($Z = -100$ μm), two cracks are visible in the SAM image with excellent contrast. The reflected light optical micrograph (Figure 11.31[a]) does not show any cracks. It is difficult to estimate the depth of the cracks from the acoustical image in Figure 11.31 since the cracks are not visible in optical or in acoustical images focused on to the surface.

leads to concentric fringes that reveal the heights and profiles of individual blisters.

Acoustic microscopy provides an opportunity not only to detect delaminations, but also to investigate the structure and shape of the disbonding. We demonstrate this capability by describing SAM studies on adhesive bonding as is widely used in the aircraft industry. In order to increase adhesion between aluminum and epoxy, a special surface pretreatment used on aluminum adherents in aerospace applications produces a honeycomb-like oxide structure on the adherent surface. The adhesive penetrates some distance into the honeycomb cells to form a microcomposite. The overall thickness of this interlayer between the bulk adhesive and the bulk adherent in a typical aluminum-epoxy joint is of the order of 1 μm only. Degradation of the boundary between the interlayer and epoxy can be observed only under severe degradation conditions.

Figure 11.29 shows the degradation of a sample comprising an anodized layer 1-μm thick and covered by 15 μm with epoxy after immersion in a 90°C water bath for 22 days. Blisters about 100 μm in diameter were found at the interface (see Figure 11.29[a] and Figure 11.29[b]). The SAM images illustrate that degradation occur at discrete sites, rather than being uniformly distributed over the surface. After 49 days in 90°C water, a small blister, seen in the white square in Figure 11.29(b), becomes visible at a defocus $z = 23$ μm (Figure 11.30[a]). In the time scan (Figure 11.30[b]) the vertical axis corresponds to the direction of the line scan 600 μm in length. The horizontal axis corresponds to the time individual reflections take to return to the transducer, with the frame width corresponding to 100 ns.

A pulse reflected at the epoxy water interface shows a light-dark-light contrast, whereas the signal reflected at the epoxy/blister interface has the reverse dark-light-dark contrast due to a phase shift. The phase shift occurs when the pulse is reflected at the interface between a fast medium and a soft substrate. Since the reflection at the substrate is not visible, the blister
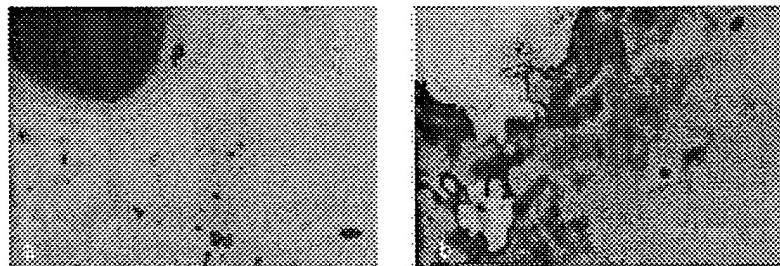

FIGURE 11.29

Acoustical images of a degraded joint between 15-μm epoxy layer and 1-μm oxide layer on pure aluminum. Sample was in 90°C water for 22 days. (a) Defocus distance = 0 μm; superficial blister can be seen in the top-left corner. (b) Defocus distance = 65 μm; the start of degradation can be seen (bright spot in the left bottom corner).

strength; however, interface stiffness parameters measured by the SAM may indicate the bond quality between film and substrate.

Characterization of the bonding by measuring bond compliances is one of the real future challenges to acoustic microscopy. Modern microscopes can distinguish two states of bonding: a perfect bond and full delaminations or disbonding. It has recently been proven that the acoustic microscope distinguishes regions of interfacial degradation at the earliest stages while optical microscopy remains insensitive.[136,140] An illustrative example of the use of SAM for studying disbonding is the research conducted at the University of Oxford.[11] Crossen et al. applied acoustic microscopy to monitor the propagation of the cathodic disbonding of an epoxy-polyamide coating on steel exposed to an NaCl solution. A linear scribe was made to initiate degradation. The disbonding (light area on both sides of the scratch in Figure 11.28[a] through Figure 11.28[d]) stops after about 50 min, with subsequent development of microblistering. Figure 11.28 shows the propagation of blisters beyond the disbonded region. Individual blisters grow with time and new blisters form at ever increasing distances from the cut as time progresses. The separation between the substrate and the coating on blisters eventually
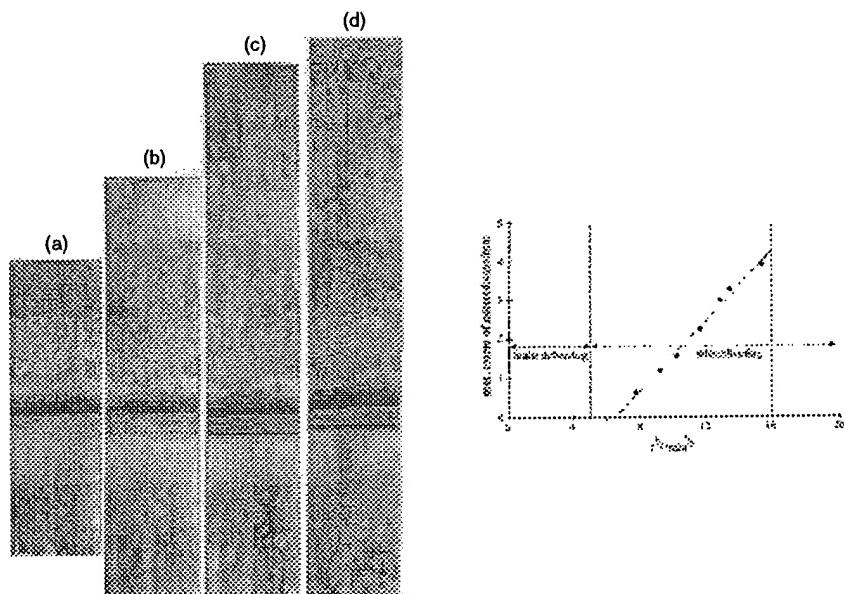
FIGURE 11.28
(a–d) SAM images (at 300 MHz) showing the developing of blisters beside a scribe in an epoxy-polyamide coating on mild steel. The exposure time to a 0.05-m NaCl solution increases to 4 hours. (d) The width of the bars is 100 μm. (e) The extent of the blister zone vs $(time)^{1/2}$ during exposure; the points correspond to the time when images (a–d) were taken. (From Crossen, J.D. et al., *Faraday Discuss.*, 107, 417, 1997. With permission of the Royal Society of Chemistry.)
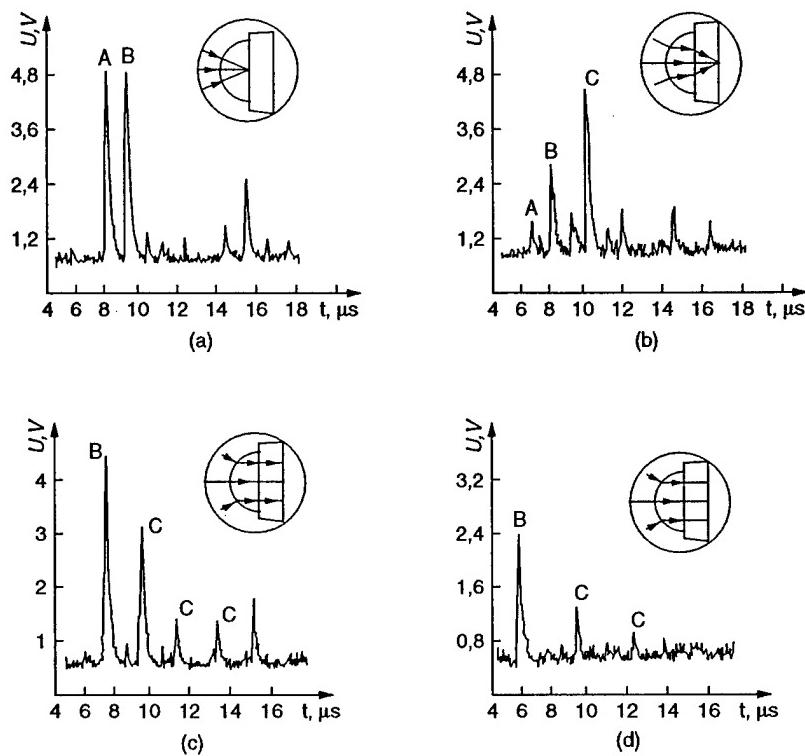
FIGURE 11.27

Pulse trains for a thick (5.68 mm) glass plate with spherical steel transformer ($r = 3.36$ mm) obtained at the frequency 13.5 MHz for focusing the beam on the (a) front and (b) back faces of the plate. In (c) and (d) the transformer body forms a narrow quasi-collinear beam of the longitudinal and shear wave, correspondingly.

for inspection of layered solids with bond defects. Wang used a Fourier spectrum approach to model a confined bond defect between layer and substrate. The bond defect was characterized by shear ($s(x)$) and normal ($n(x)$) bond compliances. The total disbonding corresponds to $s = n = \infty$, and perfect bonding corresponds to $s = n = 0$. An analytical expression for the Green function of the bond defect can be obtained only when n and s are small (the Born approximation). It has a complicated form, and we will not present it in this chapter. To simulate responses of the acoustic microscope in the case of strong disbonding, numerical calculation is required. Results of the numerical simulations showed that the acoustic microscopy response was sensitive to the normal bond compliance in all defocus ranges. However, the shear bond compliance has an influence on the response only at large defocus.[138] Parthasarathi et al.[137] and Guo et al.[139] modeled the bond defect as an infinitely thin layer with normal and tangential stiffness parameters. They concluded that the SAM cannot directly measure the interface

Theory and Applications of Acoustic Microscopy   707
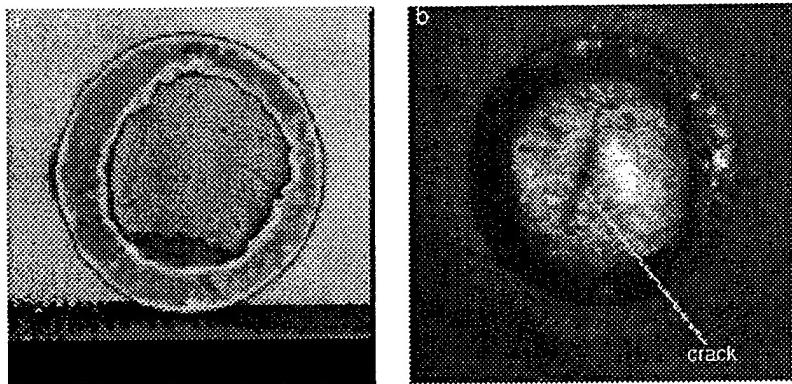
FIGURE 11.26

C-scan images of a hard amorphous carbon sample: (a) surface image, (b) interior image
obtained by the impulse reflected from the back side of the sample. The field of view is 7*7
mm^2 (From Berezina, S. et al., *Ultrasonics*, 38, 327, 2000. With permission.)

be investigated only by low-frequency acoustic microscopes,[122] in which the
defocusing distance is not limited by the attenuation of sound in the immer-
sion liquid as in the case of a microscope operating at 1 GHz.

To conduct quantitative SAM measurements of the elastic properties of
fast/hard materials, Wickramasinghe[134] suggested using a solid hemisphere
(transformer) as an additional refraction surface to decrease the beam aber-
ration inside the solid objects (Figure 11.27). A steel transformer was suc-
cessfully used by Berezina[122] to detect a signal from the back side of fullerene
ceramics. The steel hemisphere provided good acoustic impedance matching
between mercury and the hard sample. Because of the transformer, the
energy of the whole aperture (aperture angle θ = 23°) beam is transmitted
into the sample. Using a transformer, it is also possible to focus the beam
onto the significant depth and to create the quasi-collinear beam by moving
the transformer surface toward the lens. Figure 11.27(a) and Figure 11.27(b)
represent the pulse trains obtained at the frequency 13.5MHz when the beam
is focused onto the front or back surface of the 5.68-mm glass plate. Figure
11.27c and d represent the acoustic responses of the plate to the collinear
beams of longitudinal and shear waves. The transformer was then effectively
applied for measuring the longitudinal sound velocity in the new hard
phases of carbon.[122]

11.4.3 Evaluation of Adhesion by SAM

The detection of bond defects in layered structures is another area of non-
destructive testing where acoustic microscopy has been successfully used
for many years.[135,136] Recently, Parthasarathi et al.,[137] Wang,[138] and Gao et al.[139]
discussed the theoretical aspects of the application of scanning acoustic
microscopy for evaluating the adhesion between a film and a substrate and

surface and defocused to $Z = -6$ and -8 μm, respectively. All images reveal surface and subsurface defects in the coatings. A comparison of the brightness of the defects in the two images shows that the defects in the circles in Figure 11.25(b) are subsurface defects while those in the rectangles are surface defects.

A close look at the two images also shows that subsurface defects that were not visible in the in-focus image (Figure 11.25[a]) appeared in the defocused images (Figure 11.25[c] through Figure 11.25[d]), such as that marked in Figure 11.25(c). The interpretation of the images is more complicated than for softer materials. The brightness of the contrast in Figure 11.25 also suggests that defects are in focus when $Z = -6$ μm. Equation 11.86 gives 2.04 μm for Z_p. The penetration depth of the Rayleigh wave is 2.1 μm at 1.3 GHz. Therefore the Rayleigh wave does not interact with defects, and the images in Figure 11.25 are formed by longitudinal or shear waves. The wavelength of the longitudinal wave (3.8 μm) is greater than the film thickness (2.9 μm). In such a case, images can be called near-field images. For near-field images, the ray theory does not provide the location of the defects, and the rigorous solution in Equation 11.63 through Equation 11.69 should be used. The characterization of the subsurface defects located in the near-field of the liquid/solid interface has not been extensively investigated in acoustic microscopy and will be a challenging future problem.

11.4.1.3 Subsurface Imaging in Stiff/Hard Solids

Imaging defects and the subsurface microstructure in stiff/hard materials are a complicated task. The behavior of the transmission coefficients (Figure 11.22[b]) provides a clear picture of the problems arising when the SAM is used to imagine the subsurface microstructure of stiff/hard materials (see also Jipson[132]). The transmission coefficient in Figure 11.22(b) was simulated for a superhard amorphous carbon synthesized at high pressure and high temperature. The elastic parameters of the sample are given in Table 11.1. Superhard materials synthesized from C_{60} at high pressure and high temperature can be obtained only in small amounts (several millimeters in length). The strong mismatch between the coupling liquid and the sample (as regards both velocities and impedances) significantly reduces the energy of the transmitted beam (see Figure 11.22[b]). To reduce the mismatch, mercury can be used as a coupling liquid.[133] Figure 11.26 is a C-scan of hard amorphous carbon ($c_p \sim 11$ km/sec) synthesized at the pressure of 11 GPa and the temperature of 1450 K. The image was taken by SAM operating at 30 MHz, and the thickness of the sample was 2 mm. Use of mercury as an immersion liquid makes it possible to obtain an image of the back side of the sample. The impedance of mercury matches better with the impedance of the sample, and the energy transmitted into the sample increases (see Figure 11.22[b]). The back side image (Figure 11.26) revealed the crack and the gradient of the velocity (variation of the grey-scale) in the hard amorphous carbon. It should be noted that very fast or superhard materials can

Theory and Applications of Acoustic Microscopy 705

objects in Section 11.3. It has been shown that the radius of the image of a spherical object is always smaller than the actual radius of the sphere and can be estimated as *ka sinα*.

As can be seen from the examples, SAM is a powerful tool for subsurface imaging of the defects inside soft opaque materials. As a result, acoustic microscopy is widely applied in the non-destructive inspection of electronic and optoelectronic structures,[124–128] integrated circuit packages,[129] electronic packaging,[130] and defect localization in the computer memory DRAM.[131]

11.4.1.2 Subsurface Imaging in Moderately Hard Solids

One of the expanding applications of the SAM is the inspection of the thin hard film as is widely used in current industrial developments. It is now recognized that new diamond-like carbon (DLC) coatings have an extraordinary potential to extend the life of machine components. The thicknesses of the DLC films used in industry are usually about several microns. The SAM operating at high frequency likely is an ideal device for studying film microstructures. Figure 11.25(a) through Figure 11.25(d) shows the 1.3-GHz acoustical images of a flat steel sample coated with a Cr-DLC film obtained with the Leitz ELSAM acoustic microscope. The thickness of the film was 2.9 μm. The elastic properties measured by Brillouin scattering are given in Table 11.1. In the figures the acoustic microscope is focused onto the top

AU:
ELSAM...:
Please spell
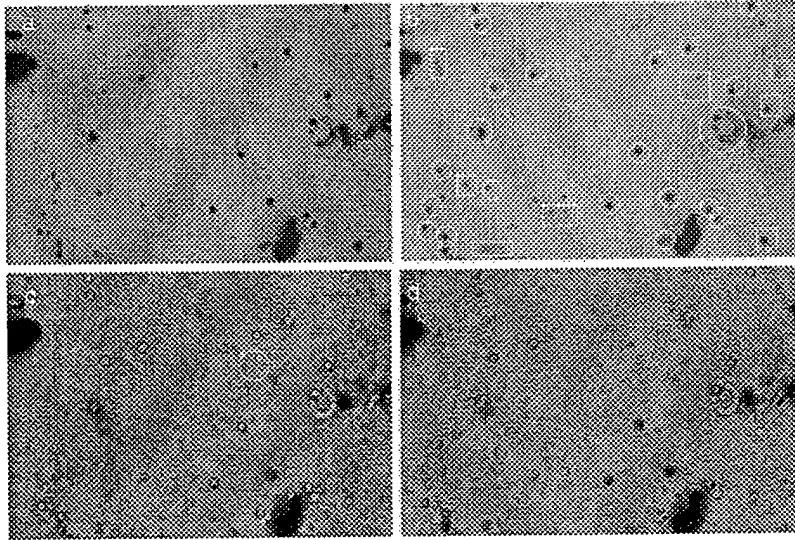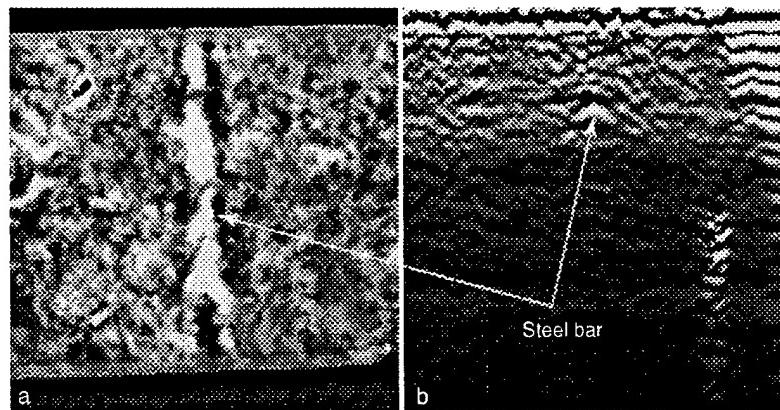out acronym
on 1st ref.

FIGURE 11.25

Acoustical image of the surface of the coated sample (Cr DCL) at 1.3 GHz. The field of view is 200*130 μm: (a–b) image was taken at focus. Defects inside the circles are subsurface defects, inside the squares are (c) surface defects image that were taken at defocus Z = –6 μm; (d) image was taken at defocus Z = –8 μm.

Ultrasonic Nondestructive Evaluation

FIGURE 11.24
Acoustical image of the surface of a concrete sample at 50 MHz. (a) Subsurface image of a steel
bar in concrete. The field of view is 36*36 mm. (b) Time-resolved image of the same sample, B-
scan normal to the steel bar.

Corrosion of reinforcing steel in concrete is one of the leading causes of
infrastructure deterioration. Recently, it has been found that the time-
resolved SAM is able to determine the mechanical properties of a thin layer
of concrete of several millimeters around a steel bar and to perform subsur-
face imaging of the steel/concrete interface.

Figure 11.24(a) shows acoustical images of the reinforced concrete sample
taken from the top surface at 50 MHz by the low-frequency acoustic micro-
scope KSI 50 (Krämer Scientific Instruments). The image of the rebar located
below the surface at a depth of 2 mm shows a good contrast[123] (see Figure
11.1). Attempts to get images of the rebar located deeper than 2 mm were
not successful with the given frequency of the microscope. The image con-
tains dark areas near the rebar, which can be attributed to high-porosity areas
in which sound attenuation is very high.[123] The bright areas in the images
(Figure 11.24[a] and Figure 11.24[b]) represent voids (filled with air) and
aggregates. The images of the rebar are fairly sharp and demonstrate that
the acoustic microscope operating at 50 MHz is capable of evaluating the
properties of the rebar/concrete interface. B-scans of the sample are pre-
sented in Figure 11.24(b). In these images, the horizontal axis corresponds
to the direction of the line scan. The vertical axis corresponds to the time
measured for individual reflections to return to the transducer. The first
reflection pulse is seen as a series of white-black-white lines due to reflection
at the water/concrete interface. The pulse reflected at the concrete/rebar
interface is represented as a signal with the same polarity (white-black-white
lines), though the first positive peak (white) is not as pronounced as the
second one. The sickle shape in the middle of the images is a signal reflected
at the concrete/steel interface. The shape of the image in Figure 11.24 is in
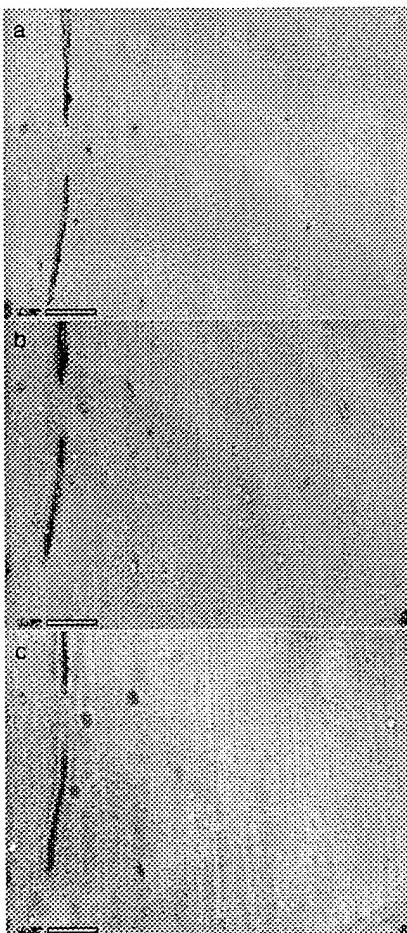quantitative agreement with the theoretical prediction made for spherical

Theory and Applications of Acoustic Microscopy 703

FIGURE 11.23
Acoustical images of the defects in epoxy layer on aluminum at 300 MHz made by OXSAM:
(a) $Z = 0$, (b) $Z = -26$ μm, (c) $Z = -43$ μm.

epoxy-aluminum interface occurs when the defocus is 26 μm. A comparison of images of the epoxy surface (Figure 11.23[a]) and of the epoxy-aluminum interface (Figure 11.23[b]) shows that most of the defects (voids) are located near the interface. The contrast of the defects gets brighter as the SAM focus moves closer to the interface and more defects become visible. Further defocusing (Figure 11.23[c]) degrades the contrast of the defects at the epoxy-aluminum interface, showing several defects in the aluminum.

Steel bars in concrete provide another example of imaging subsurface structures in soft materials. This example attracts our attention because Portland cement concrete is one of the manmade materials most commonly used.

Defocusing greater than 30 μm can damage the lens, as its focal length f usually does not exceed 80 μm. Analyzing the data in Table 11.1, we can conclude that for materials stiffer than silicon nitride in Table 11.1 the contrast of the subsurface images at 1 GHz is mainly determined by the Rayleigh wave. For these materials, the Rayleigh wave penetrates deeper than the location of the focal points of longitudinal and shear waves. A rigorous analysis of the image formation of micron-size defects in hard or superhard materials by high-frequency SAM has not yet been made.

Several techniques have recently been developed to improve the imaging of the subsurface defects, and we will mention several of them that seem to be the most promising. Miyasaka et al.[118] designed two kinds of lenses using the shear wave for subsurface imaging. One is a high-aperture acoustic lens operating at low-frequency (30 MHz), and the other is a center-sealed high-frequency (400 MHz or 1 GHz) acoustic lens. The latter has the central area of its aperture sealed to prevent longitudinal waves from traveling into the sample so that the acoustic image is essentially composed of shear wave components. The high-aperture acoustic lens has an aperture with a large aperture angle for exciting shear waves in the object. Miyasaka et al.[118] claim that the use of shear wave acoustic microscopy allows an increase in resolution for subsurface imaging of approximately 50%. Interesting results can be achieved with modern signal processing algorithms. Bechou et al.[119] applied advanced digital signal processing based on continuous wavelet transform time-resolved SAM images. Application of the technique to a non-destructive analysis of a dye-attached assembly showed the good abilities of the algorithm to detect and localize weak defects such as cracks in the dye.[120] Maslov et al.[121] monitored the phase of the signal reflected by the subsurface inclusion. It was shown that detection of the phase of the acoustical signal can be used to determine the nature of defects and to distinguish voids from solid inclusions in light casting alloys.

In the following we will consider the SAM application for imaging subsurface defects inside solids for three different types of materials as are used in modern industry: soft materials (epoxy, concrete), superhard materials (amorphous carbon synthesized from C_{60} at high pressure and temperature[122]), and intermediate case amorphous carbon films on steel (see Table 11.1).

11.4.1.1 Subsurface Imaging in Moderately Soft Solids

As has been noted above, the imaging of subsurface defects inside of soft solids is an easy task. Figure 11.23 illustrates the imaging of defects located at the interface between aluminum and a 15-μm epoxy layer. Epoxy and polymer coatings are widely used by modern industry for protection purposes and as an adhesive. The surface image of the epoxy layer (Figure 11.23[a]) shows several defects as dark and bright spots. The velocity of the longitudinal wave in the epoxy imaged by SAM was 2.6 km/sec (Table 11.1). According to Equation 11.86, focusing of the acoustic beam onto the
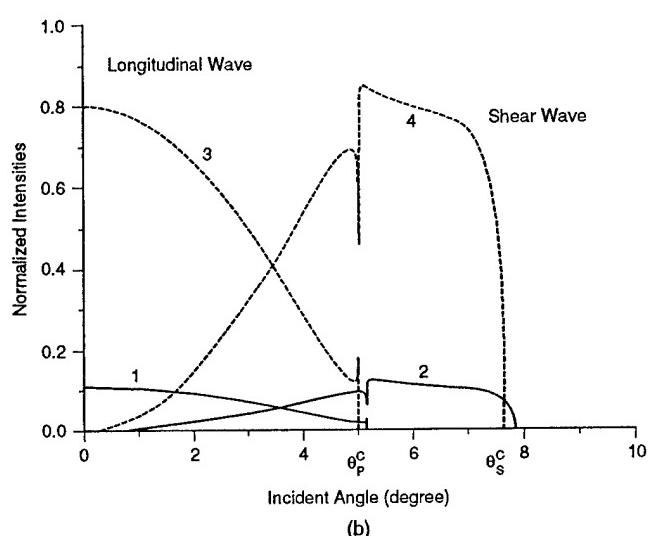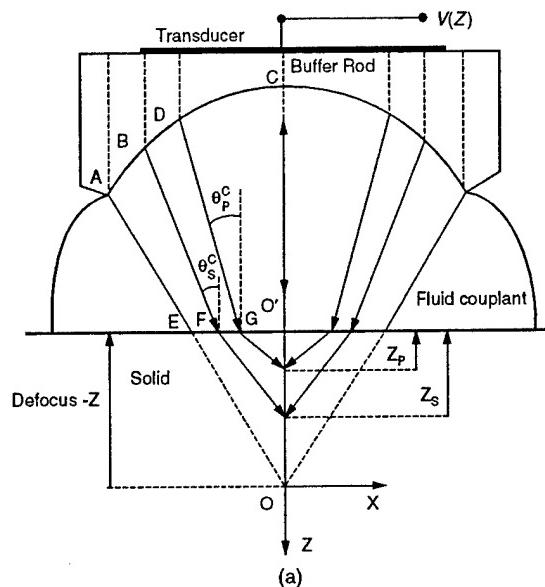
FIGURE 11.22

(a) Ray picture of shear and longitudinal waves focusing inside a solid sample in the case of negative defocus (Z < 0). Rays AF, BG, HD, and EK are normal to the transducer surface. (b) The calculated relative intensity distribution of the longitudinal and shear waves for wave propagation from water (mercury) into superhard amorphous carbon (see Figure 11.10[b] and Table 11.1 for elastic constants) as a function of incident angle: (1) longitudinal wave, and (2) shear wave crossing water-carbon interface; (3) longitudinal wave, and (4) shear wave crossing mercury-carbon interface.

materials is determined by a Rayleigh surface acoustic wave. In stiff materials, the longitudinal and the shear waves cannot be focused deep enough because of the high-impedance mismatch between immersion liquid and sample, but the Rayleigh waves can be excited efficiently.[20] For stiff and heavy materials the penetration depth is therefore limited by the wavelength of the Rayleigh wave on the sample surface. On the other hand, "for low-impedance (light and soft) materials both longitudinal and shear waves can penetrate into the object with a reasonable focusing performance."[114] We illustrate these statements by considering the sound focusing below the solid surface at high frequency (1 GHz). Figure 11.22(a) shows the ray model of waves propagating in a solid.

As discussed in Section 11.3, in the geometrical optics approach we should only take into account rays that appear to come from the focus when intersecting the transducer. A set of curves of the power distribution of the longitudinal and the shear waves traveling in the solid for amorphous carbon is shown in Figure 11.22(b). Here, the y-axis shows the normalized intensities for longitudinal and shear waves represented as E_P/E and E_S/E, and the x-axis represents the angle θ of the incident wave from liquid to solid. Expressions E_P/E and E_S/E are given in Appendix A. Simulations of the refraction of a focused beam into a stiff solid (see Figure 11.22) show that only a small part of the energy emitted from the lens penetrates into the solid. Only waves coming from the coupling liquid inside the cone with a vertical semiangle $\theta < \theta_P^c$ can be transmitted into the solid as longitudinal waves. The longitudinal critical angle θ_P^c can be derived from Snell's law. For solids with high longitudinal velocities, the critical angles can be very small (see Table 11.1). This is similar for the shear waves (Figure 11.22[b]). For the numerical simulations presented in Figure 11.22(b), we used data for superhard amorphous carbon obtained from C_{60} at high pressure and high temperature[87] (see Table 11.1). For this sample the critical angles for longitudinal and shear waves are 5 and 8°, respectively.

Using a geometrical optics approach, it is easy to derive an expression for the locations of the focal points for longitudinal (Z_P) and shear waves (Z_S) inside a solid (see Figure 11.22[a]) if the (virtual) defocusing distance of the microscope is Z

$$Z_{P,S} = Z \frac{c}{c_{P,S}} \tag{11.86}$$

A realistic picture of elastic wave focusing inside the isotropic[115] and the anisotropic[116,117] solids can be simulated numerically using a Fourier spectrum approach. Table 11.1 presents calculations of the Rayleigh wave penetration depth and the depth of the focal positions of the longitudinal (Z_p) and shear (Z_S) wave at 1 GHz derived from Equation 11.86 for several hard materials. The defocusing distance (Z) was chosen as 30 μm for numerical simulations, as this is the maximal displacement of the lens operating at 1 GHz.
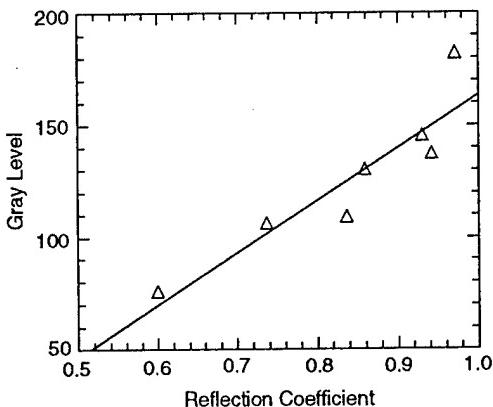
FIGURE 11.21
Grey-scale values of maximal specular reflection amplitude of $V(Z)$ curves as a function of the reflection coefficient for perpendicular sound incidence. The values are calculated from material densities and sound velocities of epoxy, Mg, Al, Si, Cu, Ni, and W (in order of increasing reflection coefficient). The zero grey scale value does not correspond to zero reflection. (From Hirsekorn, S. *et al., Appl. Phys. Lett.* 67, 745, 1995. With permission.)

coefficient $\Re(\theta)$, which has a simple form for a liquid/solid interface.[56] Its analytical expression is given in Appendix A. The reflection coefficient contains all relevant information about wave propagation in the sample.

The analysis of Equation 11.85 by Hirsekorn et al.[25] demonstrated that the magnitude of the grey levels in an image obtained with an acoustic microscope can be used as a measure of the acoustic impedance of a sample with the spatial resolution of the instrument[25] (see Figure 11.21).

Numerical calculations show that the reflection coefficient is nearly constant and equal to its value for the zero incidence angle within more than 90% of the region from $\theta = 0$ to the longitudinal wave critical angle (see Figure 11.10[b]). Hirsekorn et al.[25] suggested the following procedure for the calibration curve: A set of polished samples of different materials covering a wide range of acoustic impedances is imaged with the SAM. The maximal amplitude of the specular reflection for each sample is recorded, stored, and plotted against the reflection coefficient for perpendicular incidence. This plot yields a straight line (Figure 11.21). The impedance of an unknown material can then be evaluated by interpolation from the maximal amplitude of the specular reflection.

11.4.1 Imaging of Subsurface Defects

The most common application of the acoustic microscope is likely the detection of subsurface defects.[111,112,113] Atalar distinguished between two methods of subsurface imaging.[114] The contrast of subsurface defects in heavy or stiff

form

$$s(t,Z) = \int_0^\alpha \frac{\sin\left[\Omega\left(t - \frac{2Z}{c}\cos\theta\right)\right]}{\Omega\left(t - \frac{2Z}{c}\cos\theta\right)}\sin\theta\, d\theta \qquad (11.83)$$

The integral in Equation 11.83 can be presented with the aid of the integral sine Si

$$s(t,Z) = Si\left[\Omega\left(\frac{z}{c} - t\right)\right] - Si\left[\Omega\left(\frac{z}{c}\cos\alpha - t\right)\right] \qquad (11.84)$$

The solution in Equation 11.84 consists of two parts: one due to reflection of the central ray from the rigid surface and the second due to the rays radiated from the edge of the transducer (edge wave), marked in Figure 11.10 as AO'E. The contribution of the edge wave to the signal is smaller than that of the specularly reflected ray and the Rayleigh wave.[110] Detection of the edge wave has been demonstrated by Zhang et al.[110]

11.4 Applications of SAM in Nondestructive Evaluation

The use of acoustic microscopy is widespread and it is difficult to describe all areas in one chapter. We will only discuss the area of NDE where information often can be provided only by the SAM. In acoustic microscopy, the variation of the mechanical properties with depth can be studied by scanning the sample in various focal depth. The lens position in which the acoustic wave is focused onto the sample surface is termed as being in focus. When the focal point of the acoustic waves is at the position below the sample surface, the condition is termed defocused. Consider first the contrast of the acoustic microscope when the surface of the object is in focus ($Z = 0$). As can be seen from Equation 11.29, the signal from the surface for a microscope with the elementary pupil function in Equation 11.4 has the form

$$V(Z = 0) = \frac{V_o}{(1 - \cos\alpha)}\int_0^\alpha \Re(\theta)\sin\theta\, d\theta \qquad (11.85)$$

The expression for the $V(Z)$ curve gives a clue to understanding the nature of the contrast in SAM images. It is obviously defined by the reflection

A normalizing coefficient has been omitted. The internal integral in Equation (11.77) is the Laplace transform of the function $S_o(\omega)\, \Re\,(\theta, \omega)$ where time is replaced by the expression

$$t - \frac{2Z}{c}\cos\theta \qquad\qquad (11.78)$$

where c is the velocity of sound in the liquid. The integral presentation in Equation 11.77 is of interest for analytical manipulations. We will consider some boundary cases. It can be seen from Equation 11.77 that if the reflection coefficient is real, the signal from the solid half-space $s(t)$ has the form

$$s(t,Z) = \int_0^\alpha P^2(\theta)\Re(\theta,\omega)\sin\theta\, d\theta\, \mathrm{Re}\left\{\int_0^\infty S_o(\omega)\exp\left[i\omega\left(t-\frac{2Z}{c}\cos\theta\right)\right]d\omega\right\}$$

$$(11.79)$$

Equation 11.79 can be rewritten as

$$s(t,Z) = \int_0^\alpha P^2(\theta)\Re(\theta,\omega)s_o\left(t-\frac{2Z}{c}\cos\theta\right)\sin\theta\, d\theta \qquad (11.80)$$

and repeats the shape of the initial signal $s_o(t)$ when the lens is focused on the surface of the solid $(Z = 0)$.

$$s(t,Z=0) = s_o(t)\int_0^\alpha P^2(\theta)\Re(\theta,\omega)\sin\theta\, d\theta \qquad (11.81)$$

To show the influence of the lens properties on the signal shape, consider a rectangular impulse $(S_o(\omega) = 1$, when $(-\Omega \le \omega \le \Omega)$, and 0, when $|\omega| > \Omega$. Then $s_o(T) = (\sin\Omega T)/(\Omega T)$ and

$$s(t,Z) = \int_0^\alpha P^2(\theta)\Re(\theta,\omega)\frac{\sin\left[\Omega\left((t-\frac{2Z}{c}\cos\theta)\right)\right]}{\Omega\left(t-\frac{2Z}{c}\cos\theta\right)}\sin\theta\, d\theta \qquad (11.82)$$

Let the pupil function be constant over the aperture angle (Equation 11.4) and let the half-space be rigid $(\Re(\theta) = 1)$. Then Equation 11.82 has a simple

transform to the spectrum $S(\omega, Z)$

$$s(t, Z) = \int_{-\infty}^{\infty} S_o(\omega)V(\omega, Z)\exp(i\omega t)d\omega \qquad (11.74)$$

where the factor of $1/(2\pi)$ has been omitted. Taking into account the properties of the Fourier transform, the output signal $s(t, Z)$ can be presented in an alternative form:

$$s(t, Z) = \int_{-\infty}^{\infty} s_o(\xi - t)v(\xi, Z)d\xi, \qquad (11.75)$$

where $v(\xi, Z)$ is the inverse Fourier transform of the frequency response function $V(\omega, Z)$. The expression (11.74) has been used in numerous papers.[103–105] The integral in Equation 11.75 has, however, some advantages for numerical simulations.

To calculate the integral in Equation 11.74 numerically, the spectra $S_o(\omega)$ and $V(\omega, Z)$ must be determined for both, positive and negative frequencies. Since the signals $s(t, Z)$ and $s_o(t)$ are real functions of time, functions $S_o(\omega)$ and $S(\omega, Z)$ must be Hermitian.[40,p. 16] Their real parts are even functions of frequency, and their imaginary parts are odd functions of frequency. This property can be succinctly written as $S_o(\omega) = S_o^*(-\omega)$ and $S(\omega, Z) = S^*(-\omega, Z)$, where the superscript $*$ denotes the complex conjugate. To extend $V(\omega, Z)$ to the negative frequency range, we first have to extend the reflection coefficient into the negative frequency range. We recall that the reflection coefficient has been derived for an incident plane wave of monochromatic time dependence $\exp(-i\omega t)$. The phase of the reflection coefficient is just a phase shift for the plane wave due to reflection. Therefore,

$$\Re(-\omega, \theta) = |\Re(\omega, \theta)|\exp[-i\arg|\Re(-\omega, \theta)|] \qquad (11.76)$$

where $\Re(\omega, \theta)$, and $V(\omega, Z)$ necessarily are Hermitian functions as well. Equation 11.76 denotes the argument of a complex function. Using the properties of Hermitian functions[109] and Equation 11.76, we can rewrite Equation 11.74 for the SAM

$$s(t, Z) = \int_0^\alpha P^2(\theta)\sin\theta d\theta \, \text{Re}\left\{\int_0^\infty S_o(\omega)\Re(\theta, \omega)\exp\left[i\omega\left(t - \frac{2Z}{c}\cos\theta\right)\right]d\omega\right\}$$

$$(11.77)$$

where Re denotes the real part and $\Re(\omega, \theta)$ denotes the reflection coefficient.

Theory and Applications of Acoustic Microscopy   695
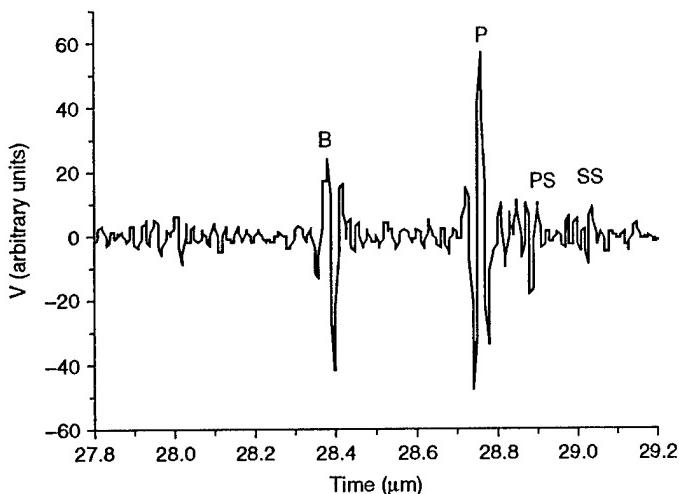
FIGURE 11.20

Time-resolved signal recorded from a hard amorphous carbon sample by a time-resolved SAM (developed at Institute of Biochemical Physics $\vdots$ $\cdots$ Levin V.M. et al., *J. Phys. Chem. Sol.*, 2001 (in press)]). The signals B and L are the result of reflection of the longitudinal wave from the front and back faces of the sample. Signals of the transverse wave arise due to conversion of longitudinal wave on the back face (mixed PS-signal) and due to conversion at the front sample face (SS-signal). (Figure courtesy of S. Berezina.)

the lens is aberration-free and that the pupil function is independent of frequency. The relationship between $s_o(t)$ and $s(t, Z)$ and their Fourier spectra $S_o(\omega)$, $S(\omega, Z)$ are

$$S_o(\omega) = \int_{-\infty}^{\infty} s_o(t)\exp(-i\omega t)dt \qquad \textbf{(11.71)}$$

$$S(\omega, Z) = \int_{-\infty}^{\infty} s(t, Z)\exp(-i\omega t)dt \qquad \textbf{(11.72)}$$

Because of the linearity of the system, the spectrum of the output signal of the SAM $S(\omega, Z)$ is a product of the spectrum of the input pulse $S_o(\omega)$ and the frequency response of the system $V(Z, \omega)$

$$S(\omega, Z) = S_o(\omega)V(\omega, Z) \qquad \textbf{(11.73)}$$

The shape of a typical pulse $s_o(t)$ and its Fourier spectrum can be found elsewhere.[4] To get the time dependence of the output signal of the microscope $s(t, Z)$ in response to the excitation pulse, we apply the inverse Fourier
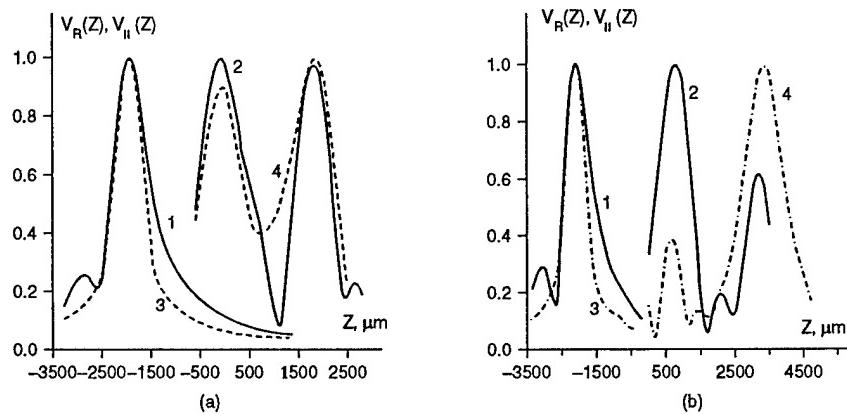
FIGURE 11.19

(a) The $V(0, Z)$ curve for a steel ball in epoxy (a = 0.99 mm, d = 1.95 mm, frequency = 25 MHz, $\alpha = 22°$); 1 = experimental $V(Z)$ curve, 2 = experimental $V_{PP}(Z)$ curve, 3 = theoretical $V(Z)$ curve with pupil function (Equation 11.5), 4 = theoretical $V_{PP}(Z)$ curve. (b) The $V(0, Z)$ curve for hemispherical cavity in glass (a = 1.22 mm, d = 1.95 mm, frequency = 25 MHz, $\alpha = 22°$). 1 = experimental $V(Z)$ curve, 2 = experimental $V_{SS}(Z)$ curve, 3 = theoretical $V(Z)$ curve with pupil function (Equation 11.5), 4. = theoretical $V_{SS}(Z)$ curve. (From Lobkis, O.I. et al., *J. Acoust. Soc. Am.*, 99, 33, 1996. With permission.)

occur because of the small lens aperture. The second and the third peaks are top maximum and center maximum of the cavity. The origin of the peaks is very similar to that of the peaks of a spherical particle as described in Section 11.3.2. The $V(Z)$ curve measured and simulated for shear waves $V_{TT}(R = 0, Z)$ contains three peaks as well. The positions of the TM and CM are different from those for $V_{PP}(R = 0, Z)$.

11.3.4 Theory of Time-Resolved Acoustic Microscopy

The time-of-flight acoustic microscopy technique provides an alternative method to visualize the internal microstructure of solid materials. It has been applied by Yamanaka[102] to measure the surface acoustic wave velocity. An essential contribution to the application of a time-resolving method for layered materials was made by a group from Oxford University.[33,34,103–105] The typical time-resolved signal from a solid sample is presented in Figure 11.20. Separation in time reflection for the different types of waves (P, PS, SS) from the structures located below the sample surface provides additional information about these structures and also allows their location to be determined (e.g., Figure 11.5).

The theory of time-resolved measurement can be found elsewhere.[104,106–108] Here we will obtain a simple solution using a Fourier spectrum approach. Let the defocus Z be fixed and a short acoustic pulse $s_o(t)$ be emitted by the lens toward the sample, and $s(t, Z)$ be the output signal. We suppose that

where $A_n^{PP}, A_n^{SP}, A_n^{PS}, A_n^{SS},$ and A_n^{SH} are the scattering coefficients[8,98-100] for a spherical cavity inside a solid medium (see Appendix B); ρ_s is the density of the solid; c_P and c_S are the velocities of longitudinal and shear waves, respectively, in the solid; and $k_P = \omega/c_P$ and $k_S = \omega/c_S$ are the corresponding wave numbers. The angles θ, θ_P, θ_S follow Snell's law, $k \sin\theta = k_P \sin\theta_P = k_S \sin\theta_S$ (see Appendix A). T_P and T_S are the transmission coefficients for longitudinal and shear waves at the liquid/solid interface. Analytical expressions for the coefficients can be found in Appendix A.

Although Equation 11.64 through Equation 11.69 look cumbersome, they can, however, easily be interpreted using the Fourier spectrum approach. To understand the structure of Equation 11.67 through Equation 11.69, consider the spectrum of a wave incident on the cavity. Using Equation 11.19 and Equation 11.20, we can write it in the coordinate system originating in the center of the cavity

$$U_i(k_x, k_y) = \frac{P(k_x, k_y)}{k_z} T_{P,S}(k_x, k_y) \exp[i(k_x X + k_y Y + k_z Z + k_{P,Sz} D)] \quad (11.70)$$

The first term in Equation 11.70 is the spectrum of the wave incident on the focal plane, and the phase shift $\exp[i(k_x X + k_y Y + k_z Z)]$ moves the origin of the coordinate system to point O''', which is located above the center of object O' on the liquid/solid interface. To calculate the spectrum inside the solid, we multiply the incident spectrum in the liquid by the coefficient $T_{P,S}(k_x, k_y)$, which is the transmission coefficient from a plane wave in the liquid to a longitudinal or transversal wave in the solid.[56,section 7] Finally, to get a spectrum originating in O' we multiply the spectrum at the liquid/solid interface by the propagation factor $\exp[ik_{P,Sz} D]$, with $k_{P,S} = \frac{\omega}{c_{P,S}}$ being the wave vector of the longitudinal wave in the solid. The wave is subject to refraction at the liquid/solid interface and Snell's law yields $k_{P,Sx} = k_x$, $k_{P,Sy} = k_y$, $k_{P,Sz} = \sqrt{k_{P,s}^2 - k_{P,Sx}^2 - k_{P,Sy}^2}$, with k_x, k_y as the components of the wave vector of the incident plane wave in the immersion liquid. Introducing spherical coordinates, we find that the angle θ is used for all operations in the immersion liquid: irradiation, represented by $P(\theta)$, and shifting the coordinate system from O to the system O''' in Figure 11.18, which is included in $\exp[ikZ \cos\theta] J_m(kR \sin\theta)$. The angles $\theta_{P,S}$ are used for operations within the solid such as shifting of the coordinate system from O''' to the system O' as included in $\exp[ik_{P,S} D \cos\theta_{P,S}]$ and scattering, represented by $P_{mn}(\cos\theta_{P,S})$.

Solving the inverse problem of determining size and location of a subsurface cavity from Equation 11.63 is a complex task. Lobkis et al.[101] used the method of stationary phase to derive an analytical expression for the $V(Z)$ curve of a spherical cavity in a solid. Figure 11.19 shows theoretical and experimental $V(R = 0, Z)$ curves for different solids. The $V_{PP}(R = 0, Z)$ curve (measuring only of longitudinal waves was achieved by separation of the reflected tone burst in time) exhibits three distinct peaks. The first is the ordinary $V(Z)$ curve from the liquid solid interface, where no Rayleigh waves

Acoustic Microscopy and Surface Brillouin Scattering of Amorphous Carbon Pressure-Synthesized from C_{60}

Pavel V. Zinin[1], Murli. H. Manghnani[1], Sergey Tkachev[1], Xinya Zhang[1]
Alexander G. Lyapin[2], Vadim V. Brazhkin[2], Ivan A. Trojan[2]
[1] School of Ocean and Earth Science and Technology, University of Hawaii
Honolulu, HI 96822, USA
[2] Institute for High Pressure Physics, Russian Academy of Sciences
Troitsk, Moscow District 142092, Russia

ABSTRACT

Here, we report successful measurements by surface Brillouin scattering (SBS) and scanning acoustic microscopy (SAM) of the elastic properties of small specimens of amorphous carbon obtained from C_{60} under high pressure and temperature. The superhard phases of amorphous carbon were synthesized from C_{60} at pressure 13 - 13.5 GPa and temperature 800-900 °C. Two types of acoustic waves have been detected by SBS in superhard samples: surface Rayleigh wave and bulk longitudinal wave. The longitudinal velocity (v_L) in the hardest sample is slightly lower than longitudinal wave velocity in diamond in [110] direction. Simultaneous measurements of the Rayleigh and longitudinal wave velocities make it possible to determine shear and bulk elastic moduli of the specimens. Obtained elastic properties for amorphous carbon synthesized under pressure 13.5 GPa and temperature 900°C are close to those for diamond, indicating that bonds among amorphous carbon network are diamond bonding dominated.

INTRODUCTION

Recent interest in new superhard materials triggered by the discovery of the fullerene molecule C_{60} has led to a series of extensive experimental studies of amorphous and nanocrystalline carbon phases and their properties in both bulk [1] and deposited as a thin film [2-4] states. Heating at relatively low pressures ($P<8$ GPa) has revealed one-dimensional (1-D)- and two-dimensional (2-D)-polymerization [5] of C_{60} and subsequent collapse of the fullerene structure into graphite-like disordered carbon [6]. Heating the fullerite up to 1000-1300 K under the pressure 3 to 8 GPa leads to a formation of disordered phases with carbon atoms predominantly in sp^2 states. Heating C_{60} at $P>8$ GPa results in formation of three-dimensional (3-D) polymerized amorphous phases of C_{60}, with large number of sp^3 atomic sites [7] and nanocrystalline composites (nanoceramics) of diamond and graphite [8], fueling the most recent debates on the existence of ultrahard fullerene-based phases with hardness higher than diamond [9]. The structure of all these phases contain large amount of 4-fold sp^3 atomic states. The existence of ultrahard fullerene phase with hardness higher than diamond was recently discussed [7, 9]. Such phases can be obtained only in extremely small size.

Here, we report successful measurements by surface Brillouin scattering and scanning acoustic microscopy of the elastic properties of two small bulk specimens of amorphous carbon synthesized from C_{60} under high pressure and temperature. The results of these measurements are of importance in understanding the problem of phase transition of C_{60} under high pressure and temperature and particularly the issue of existing ultra and superhard phases.

It has been shown that under high pressure and temperature C_{60} crystals transform through a series of intermediate polymeric, amorphous and nanocrystalline carbon phases. Heating at relatively low

pressures (P < 8 GPa) results in 1-D and 2-D polymerization of C_{60} [5, 10] and subsequent collapse of the fullerene structure into graphite-like disordered carbon [6, 10]. The 3-D polymerized phases of C_{60} [7], amorphous phases with a large amount of sp^3 atomic sites [11], and nanocrystalline diamond and graphite [7] are formed upon heating at these pressures. The formation of covalent bonds makes the new phases very stable. Hirai et al. [12] reported amorphous diamond prepared from C_{60} by shock compression. Based on the indirect scratching observations [13] and measurements made by time-resolved acoustic microscopy [14], Blank et al. [9] postulated that superhard and ultrahard phases could be synthesized from C_{60}. However, their experimental results have not been independently confirmed. Further, there might exist some discrepancy in their measured values of elastic constants [7] as fullerite materials obtained under high pressure are not homogeneous and consist of several phases with different elastic properties. The dimensions of the different phases vary from tens to hundreds of microns. Thus, Brillouin spectroscopy and acoustic microscopy, which provide high lateral (1 - 30 μ) and axial (1 - 100 μ) resolution in elastic properties measurements, are valuable tools for characterizing such specimens.

The first experimental SBS study of the fullerene product resulting from laser irradiation of a C_{60} single crystal [15] revealed that high laser intensities must be used to detect Brillouin scattering. Sound velocities measured in that experiment (280-700 m/s) are substantially lower than the value reported in literature for solid C_{60}. The shift of the Brillouin doublets observed by Manfredini et al. [15] was in the energy range typical for slow polymer or carbon gels. Polymerized phases obtained under high T-P are much stiffer. One would therefore expect normal laser intensity to produce SBS spectra from hard fullerene materials. To our knowledge Brillouin scattering studies of bulk hard phases synthesized from C_{60} have not been conducted yet.

EXPERIMENTAL DETAILS

Specimens

Two bulk amorphous carbon (a-C) samples, employed in this study, were synthesized from C_{60} fullerite powder at 13 to 13.5 GPa, 800±100°C (sample A) and 900±100°C (sample B) at the Institute for High Pressure Physics, Moscow. Fullerite powder was produced at the Russian Scientific Center "Kurchatov Institute".

Brillouin light scattering

Brillouin light scattering is generally referred to as inelastic scattering of an incident optical wave field by thermally excited elastic waves in a sample [16]. The phonons moving in thermal equilibrium with very small amplitudes can be viewed as a moving diffraction grating by an incident light wave. Mechanism of the light scattering by moving diffraction gating can be explained by the two concepts of Bragg's reflection and Doppler shift. Brillouin light scattering can be viewed as a Bragg's reflection of the incident wave by the diffraction grating created by thermal phonons [17].

For the backscattering geometry, the surface acoustic modes which cause the diffraction of the incident light have wave vector q given by

$$q = \frac{4\pi \sin \theta}{\lambda},$$

λ is the wavelength of the incident laser light, and q is the projection on the surface of the scattering wave vector. The moving corrugating surface scatters the incident light with a Doppler shift, giving scattered photons with shifted frequencies. The frequency shift δf in the light scattering is related to the surface wave velocity v_{SAW} by equation

$$v_{saw} = \frac{\lambda}{2\sin\theta}\delta f$$

At room temperature and above, the Brillouin scattering efficiency or intensity for scattering from the surface of an opaque materials by dynamic rippling of the surface can be represented as [17]

$$I(\omega) = A\frac{T}{\omega}\operatorname{Im} g_{33}(q,\omega)$$

where ω is the angular frequency shift of the light; T is the absolute temperature; factor A depends on the medium (density and permittivity), scattering geometry, polarization and incident photon frequency; $g_{33}(q,\omega)$, Fourier coefficient of the elastodynamic Green's function. A comprehensive description of how $g_{33}(q,\omega)$ is calculated for a multilayered anisotropic medium is given in [17].

Elasto-optic interaction or scattering of light by bulk sound waves result from fluctuations in the dielectric constant caused by the phonons moving in thermal equilibrium. The interaction arises from changes in the refractive index produced by the strain generated by sound waves; the change in refractive index is related to the strain through the elastooptic constants p^{mn}, which determine the degree of interaction between the light and the material [16]. In backscattering, sound velocity (V) can be expressed as a function of the frequency shift and refraction index n by the following formula

$$V = \frac{\lambda\delta f}{2n}$$

Brillouin light scattering technique is ideally suited for studying the elasticity of bulk materials and, especially, thin films [18, 19]. It has proven to be a very effective technique for investigating the near-surface elastic properties of opaque bulk materials.

Acoustic Microscopy

Acoustic microscopy is a relatively new technique that has been developed for non-destructive characterization of the mechanical microstructure of solid materials with a resolution of 1 μm [20]. A schematic diagram of an acoustic microscope working in the reflection mode is presented in Fig. 1. In conventional acoustic microscopy, a monochromatic sound wave is focused onto a specimen by means of an acoustic lens. The same lens is used to record the signal reflected back from the sample. A liquid couplant, usually water, is placed between the lens and the sample. The spherical lens, i.e. the lens with a spherical cavity, focuses sound onto a spot of size comparable to the sound wavelength in the fluid. The fringes, appearing in the acoustic images around cracks and other discontinuities, are Rayleigh wave fringes; they are seen on defocused images as a result of the interference be-

tween waves reflected normal to the specimen surface and waves associated with surface Rayleigh waves [20].
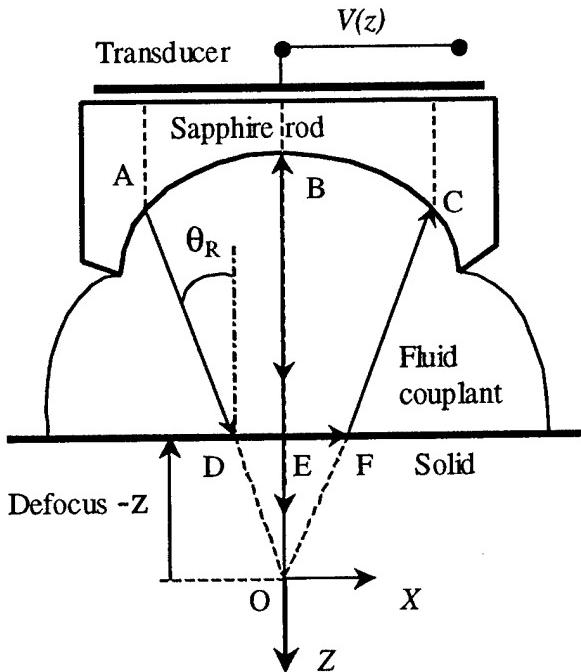

Figure 1. Schematic geometry of the defocused acoustic lens. BE is the trajectory of specular wave, and ADFC is the trajectory of leaky Rayleigh surface acoustic wave (SAW). In the ray model the leaky Rayleigh wave is excited by ray AD, striking the surface at the angle $\theta_R = V_W/V_R$. Here V_W is the velocity of the longitudinal wave in coupling liquid and V_R is the velocity of Rayleigh wave.

RESULTS AND DISCUSSION

Surface scattering from the Rayleigh waves (incident angle = 60°) gives the velocity of 6.5 km/s for the top face of the sample A and 10.1 km/s for the top face of sample B. The top face is a surface where pressure has been applied. The velocity of surface wave along sample surface B is 8% lower than that for [100] diamond. Bulk scattering from the bulk longitudinal wave (LW) can be observed for sample B. Refractive index for the sample is not known. Assuming it to be close to that for C_{60} (n=2.52) [15], the longitudinal velocity in sample B is then equal to 17.5 km/s. The longitudinal velocity (v_L) in the sample B (17.5 km/s) is higher than that in cBN (15.8 km/s) or in ta-C films (15.5 km/s) and is slightly lower than longitudinal wave velocity (18.6 km/s) in diamond in [110] direction.

An acoustic image of sample A made by acoustic microscope (Leitz ELSAM) is shown in Fig. 2. The image was taken from the side surface of sample A. The fringe width in the cross section of the fibers can be used to determine the Raleigh velocity. The fringe distance is simply half a wavelength of the Rayleigh wave. This gives the Rayleigh wave velocity of 8.0 ± 2.1 km/s. We note that, though

the error in the measured Rayleigh wave velocity by SAM is higher than that determined by SBS, the SAM measurements have revealed strong anisotropy in the elastic properties of sample A.
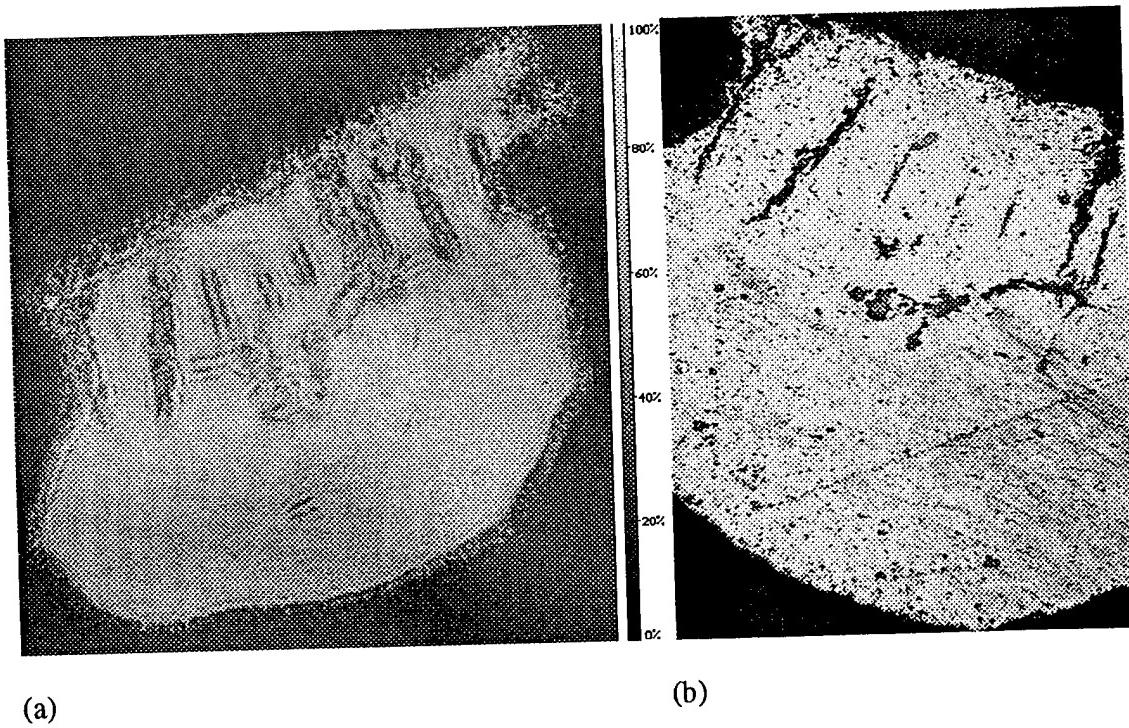

(a)   (b)

Figure 2. (a) Acoustic image of sample A at 400 MHz, and at a defocus z = -20 μm, field of view 700 μm x 700 μm. (b) Optical image of the same sample field of view 700 μm x 700 μm.

CONCLUSIONS

1. Elastic properties of the superhard phases of amorphous carbon synthesized from C_{60} at pressure 13 - 13.5 GPa and temperature $900 \pm 100^\circ C$ have been obtained by surface Brillouin spectroscopy.
2. The longitudinal velocity in the sample B is higher than that in cBN or in ta-C films and is slightly lower than longitudinal wave velocity in diamond in [110] direction.
3. Measured elastic properties for amorphous carbon obtained under pressure 13 - 13.5 GPa and temperature $900 \pm 100^\circ C$ are close to those for diamond.
4. The SBS and SAM techniques have potential value in characterizing extremely small size specimens such as hard amorphous carbon phases.

ACKNOWLEDGEMENTS

REFERENCES

1. B. Sundqvist, *Advances in Physics* **48**, 1 (1999).
2. R. Pastorelli, A.C. Ferrari, M.G. Beghi, *et al.*, *Diamond Relat. Mater.* **9**, 825 (2000).
3. A.C. Ferrari, J. Robertson, M.G. Beghi, *et al.*, *Appl. Phys. Lett.* **75**, 1893 (1999).
4. C.E. Bottani, A.C. Ferrari, A.L. Bassi, *et al.*, *Europhys. Lett*, **42**, 431 (1998).
5. M. Nunez-Regueiro, L. Marques, J.-L. Hodeau, *et al.*, *Phys. Rev. Lett.* **74**, 278 (1995).
6. J.L. Hodeau, J.M. Tonnerre, B. Bouchetfabre, *et al.*, *Phys. Rev. B* **50**, 10311 (1994).
7. V.V. Brazhkin, A.G. Lyapin, S.V. Popova, *et al.*, *J. Appl. Phys.* **84**, 219 (1998).
8. V.V. Brazhkin, A.G. Lyapin, R.N. Voloshin, *et al.*, *JETP Letters* **69**, 869 (1999).
9. V.D. Blank, S.G. Buga, G.A. Dubitsky, *et al.*, *Carbon* **36**, 319 (1998).
10. L. Marques, J.L. Hodeau, M. Nunez-Regueiro, *et al.*, *Phys. Rev. B* **54**, 12633 (1996).
11. H. Hirai and K. Kondo, *Phys. Rev. B* **51**, 15555 (1995).
12. H. Hirai, Y. Tabira, K. Kondo, *et al.*, *Phys. Rev. B* **52**, 6162 (1995).
13. V.D. Blank, S.G. Buga, N.R. Serebryanaya, *et al.*, *Phys. Lett. A* **205**, 208 (1995).
14. V.D. Blank, V.M. Levin, and N.R. Serebryanaya, *JETP* **87**, 741 (1998).
15. M. Manfredini, C.E. Bottani, and P. Milani, *Chem. Phys. Lett.* **226**, 600 (1994).
16. W. Hayes and R. Loudon, *Scattering of Light by Crystals*. 1978, New York: Wiley. x.
17. J.D. Comins, Surface Brillouin Scattering, in *Handbook of Elastic Properties of Solids, Liquids, and Gases. Volume I: Dynamic Methods for Measuring the Elastic Properties of Solids*, edited by M. Levy, *et al.*, (Academic Press, New York, 2001) pp. 349.
18. R. Pastorelli, P.M. Ossi, C.E. Bottani, *et al.*, *Appl. Phys. Lett.* **77**, 2168 (2000).
19. M. Chirita, R. Sooryakumar, H. Xia, *et al.*, *Phys. Rev. B* **60**, 5153 (1999).
20. P.V. Zinin, Quantitative Acoustic Microscopy of Solids, in *Handbook of Elastic Properties of Solids, Liquids, and Gases. Volume I: Dynamic Methods for Measuring the Elastic Properties of Solids*, edited by M. Levy, *et al.*, (Academic Press, New York, 2001) pp. 187.

Elastic properties of cBN films
by surface Brillouin scattering

P. Zinin*[a], M. H. Manghnani[a], X. Zhang[a], H. Feldermann[b], C. Ronning[b], H. Hofsäss[b]

[a]School of Ocean and Earth Science and Technology, University of Hawaii Honolulu, HI, USA;
[b]Institute of Physics, University of Göttingen, Göttingen, Germany

ABSTRACT

Surface Brillouin scattering (SBS) has been used to determine the elastic properties of thin hard submicron films cBN deposited on silicon. In case of cBN films, only the Rayleigh mode can be clearly identified in the Brillouin spectra. The elastic properties of the films have been determined by fitting experimental data to theoretical dispersion curves. A Green's function method was used to predict Brillouin scattering spectra of the acoustic excitation at the free surface. Our results demonstrate that the effect of thin hBN interlayer located between cBN film and Si substrate on the velocity of surface acoustic wave (SAW) does not exceed 2% for thin (16 nm film) and is negligible for cBN films thicker than 100 nm. The elastic properties of the cBN films are not softer than those of bulk cBN.

1. INTRODUCTION

Recently there has been a surge of research effort related to advanced superhard materials, e.g., cBN, C_3N_4, B_4C, CVD diamond and their films [1]. Their hardness and abrasive qualities, highly valued in technology and industry are controlled by the large elastic moduli [2]. Moreover, these materials exhibit unusual combination of physical and chemical properties. One of the biggest applications of new materials is to develop new superior coatings. The system keeps its bulk properties while the film ensures protection against the environment and achieves properties unattainable in the substrate alone. Elastic properties of superhard films need to be determined experimentally because they depend strongly on the synthesis conditions, and they cannot be derived from theoretical considerations alone. The thickness of such films ranges commonly from a few tens of nanometers up to an order of a micrometer. The nanoindentation technique widely used for mechanical characterization of thin micron films does not allow measurements of the hardness and elastic moduli of the submicron coating and substrate separately. The surface Brillouin scattering (SBS) technique offers the unique opportunity to study elastic properties of submicron films.

The cubic phase of boron nitride (cBN) is second in hardness only to diamond . BN films with a high (>85%) percentage of the cubic phase can now be deposited by a variety of techniques [3-5]. SBS studies conducted of the by Pastorelli et al. [6] and Wittkowski [7] on thick (>700 nm) cBN films revealed sufficient (25%) reduction in SAW velocity. The elastic constants obtained in [6, 7] have been derived from experiments made on films that were thicker than the wavelength of the Rayleigh wave (RW) in cBN layer. Such measurements can provide only an estimate value of the shear velocity in the cBN films. For the films thinner than the wavelength of the Rayleigh wave in cBN layer, longitudinal and shear velocities inside the film can be determined by measuring the dispersion curve of SAWs propagating inside the layer. The purpose of this paper is to characterize elastic properties of the thin cBN films.

2. cBN FILMS

We have investigated two cBN samples of thickness 16 and 60 nm. The cBN films were deposited on Si(100) substrates at a temperature of 350°C and 600 eV ion energy. The deposition parameters were chosen so as to facilitate the growth of the film with highest cBN content. Details of the deposition process can be found elsewhere [3]. The deposited films exhibit a layered structure consisting of a disordered Si-B-N interface, followed by 10-15 nm of textured hBN, then by cBN (see Fig. 1).
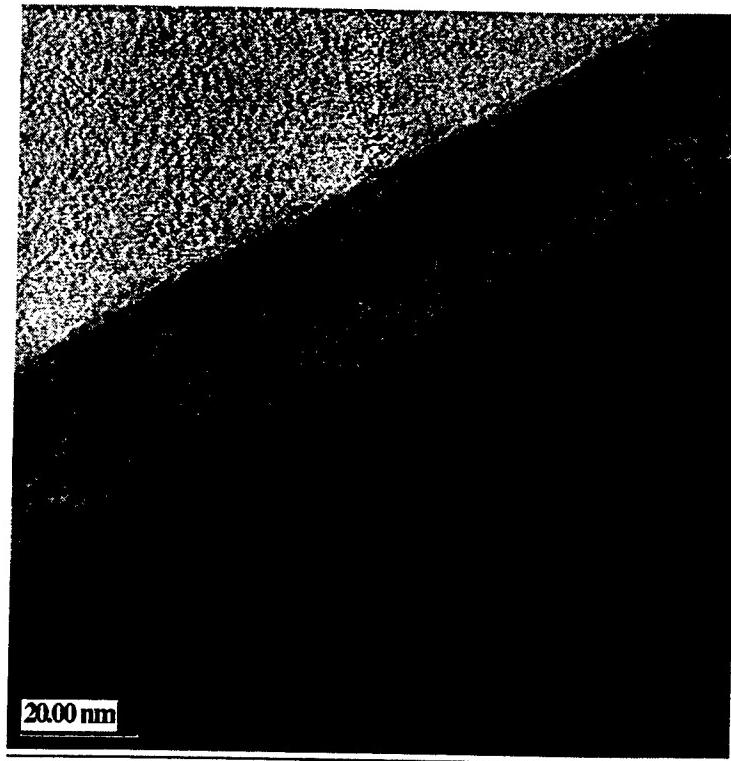
*zinin@soest.hawaii.edu

Figure 1. TEM-picture of sample with 16 nm cBN layer.

The thickness of the hBN layer was 15 nm for 16 nm cBN film, and 10 nm for 60 nm cBN film.

3. EXPERIMENTAL TECHNIQUE

A detailed description of the Brillouin scattering experimental set-up has been published elsewhere [8, 9]. In brief, light from an argon ion laser (λ=514.5 nm and beam power of 60mW) was focused onto the film with a *f/5.6* lens (*f*=50mm). The scattered light was collected with the same lens in the backscattering geometry and analyzed using a high contrast and high resolution Brillouin spectrometer, which incorporated a tandem six-pass Fabry-Perot interferometer [10]. The light was detected by a single photon counting module and its output was stored in a multichannel scaler card for further analysis. Each spectrum was accumulated for 1-2 hours. The frequencies corresponding to each of the peaks were determined by a curve-fitting routine. For the 180° backscattering geometry, the surface acoustic modes, which cause the diffraction of the incident light, have wave vector (Fig. 1) given by

$$k_{\parallel} = \frac{4\pi \sin \theta}{\lambda}, \quad (1)$$

where λ is the wavelength of the incident laser light and $k_{\parallel}$ is the projection on the surface of the scattering wave vector, θ is the scattering angle. The Doppler frequency shift f in the light scattering is related to the surface wave velocity v_{SAW} by

$$v_{saw} = \frac{\lambda}{2 \sin \theta} f . \quad (2)$$

3. THEORY

At room temperature and above, the Brillouin scattering efficiency or intensity for scattering from the surface of opaque materials by dynamic rippling of the surface can be represented as [11-13]:

$$I(\omega) \propto \frac{A}{\omega} \mathrm{Im}\left[g_{33}\left(\vec{k}_\parallel, x_3 = -h_+, \omega\right)\right] \quad (3)$$

where A is a constant and depends on the density and dielectric constants of the medium, scattering geometry, and incident photon frequency and polarization, . The g_{33} is the Fourier coefficient of the elastodynamic Green's function

$$g_{33}\left(\vec{k}_\parallel, x_3 = -h_2, \omega\right) = \int\limits_{-\infty}^{\infty}\int\limits_{-\infty}^{\infty} d^2\vec{x}_\parallel G_{33}\left(\vec{x}_\parallel, \omega\right)\exp\left(-i\vec{k}_\parallel\vec{x}_\parallel\right). \quad (4)$$

pertaining to force and response normal to the surface. Now we briefly describe derivation of the wavevector elastodynamic Green's function g_{33} for two anisotropic layer supported by anisotropic half space, following [12]. We consider a general anisotropic elastic continuum of density ρ and elastic modulus tensor C_{ijkl} occupying the halfspace $x_3 > 0$ and two layers; hBN layer and cBN layer (see Fig. 2). The hBN interlayer occupies the region $-h_- < x_3 < 0$ (Fig. 1), and the cBN layer occupies the region $-h_+ < x_3 < -h_-$. We denote elastic tensor for upper layer as C^+_{ijkl}, and density as ρ^+, and for interlayer as C^-_{ijkl}, and density as ρ^-. A detailed description of how g_{33} is calculated for a one layer anisotropic medium is given in [13, 14].
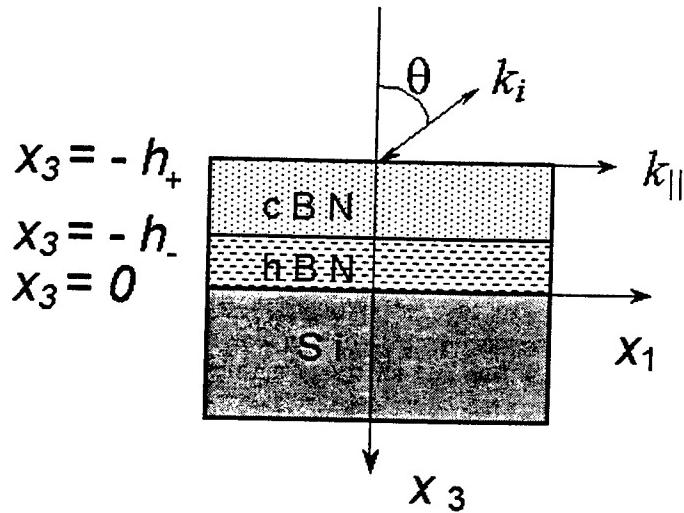

Figure 2. Geometry of the SBS measurements.

Fortran code written for Green's function computations by Prof. A. Every was applied y for two-layer anisotropic system.

4. RESULTS AND DISCUSSION

While SBS has been used in the past for measuring the properties of thin films, its application specifically to hard stiffening films has been very limited. Theoretical consideration of the SAW behavior for hard films [15] shows that the SAW velocity initially grow with increasing kh, where k is the wave number of SAW and h is the thickness of the film. At a critical value kh_{cut} the SAW meets shear wave and degenerates with the bulk wave continuum (cut-off point). Beyond this cut-off, there is a pseudo surface acoustic wave, which radiates energy into the substrate and as a result attenuates with distance as it travels along the surface.

Beyond cut–off, two kinds of behaviour can be distinguished. The first type of behavior comes about when the elastic properties of the layer and the substrate are not very different. The velocity of the pseudo surface wave beyond cut-off increases up to the Rayleigh wave velocity of the layer, while the attenuation of this wave tends asymptotically to zero. This type of behavior has been called the *non-splitting* type. The second type of behavior arises when the elastic properties of two materials are quite dissimilar, and the PSAW evolves into a strongly attenuated interfacial mode, while a second mode appears at a higher velocity and evolves into the Rayleigh wave at the free surface of the layer. This second type of behavior of the dispersion relation has been called the *splitting* type.

The non-splitting type of behaviour has been observed experimentally in an alumina film on aluminium by acoustic microscopy [16], in doped Cr coatings deposited on high speed steel [17], in a titanium film on steel by SBS [18], in diamond-like-films (DCL) [19]. Splitting type of behavior has been observed recently for Si_3N_4 films on GaAs [9]. Green's function simulations demonstrate that the effect of the thin hexagonal boron nitride (hBN) interlayer located between cBN film and Si substrate on the velocity of the surface acoustic wave (SAW) does not exceed 2% for a thin (16 nm) film and is negligible for cBN films thicker than 100 nm. The Fig. 3 shows the variation of the Brillouin spectra with θ and are calculated by the Green's function method mentioned above. The brightness in the grey scale is a measure of the scattering intensity, which is related to the displacement amplitude of these modes at the surface or at the interface. Thus, the intensity is indicative of the mode displacement patterns in the layer. The elastic constants of the cBN film were taken from ultrasonic study of bulk poly-crystalline cBN [20]. Brillouin spectra calculated for 300 nm cBN film on Si (001) with scattering taking place at the surface is shown in Fig. 3. For $\theta = 0$, the velocity corresponds to the SAW velocity on the Si substrate.

With increasing θ the SAW velocity approaches the bulk wave threshold V_T (transverse-wave threshold), which is reached at $\theta \approx 15°$. Below V_T the Brillouin spectrum displays a sharp peak, which is associated with the true surface. At V_T, the SAW degenerates with the bulk continuum, and beyond cut-off there is no true SAW. Somewhat above V_{FT}, the Brillouin spectrum displays a broad peak that gradually disappears. V_{FT} is the fast transverse velocity in the substrate. This peak is associated with leaky or pseudo SAW (PSAW) [15]. As θ or kh increase, the PSAM is transferred into leaky interface wave [9, 15]. In the same spectral region, another broad peak appears, which with increasing θ becomes narrower, as the associated mode tends towards the Rayleigh mode of cBN. For very large θ this becomes the true nondispersive Rayleigh wave (RW). Behavior of the SAW dispersion curve of cBN film on Si substrate can be attributed to the splitting type of behavior. It is obvious from Fig. 3 that 300nm cBN films are difficult for SBS measurement since the range of angle used in SBS (20-70°) contains only highly attenuated PSAW. Dispersion curves of the films thicker than 400 nm, measured by SBS, should contain only Rayleigh SAW in cBN films. True SAW brunch running below shear cut-off can be measured by SBS only in films thinner than 200 nm.

Results of measurements for the 60 nm thick film and for the 16 nm film are depicted by stars in Figs. 4 and 5 as a function of angle. Theoretical Brillouin spectra have been calculated on the basis of the ripple mechanism for scattering at the surface eq. (3). The dispersion curves in Figs. 6 and 7 represent the traces of the maxima of the calculated Brillouin intensity for the surface of the measured Brillouin intensity. The assumed elastic properties of the hBN layer were based on the reported SBS determined values [21].

Basic features of the SBS spectra of Si have been described elsewhere [13]. The Brillouin spectrum displays a sharp peak (Fig. 3) which is associated with the Rayleigh SAW and in addition a continuum extending from the transverse-wave threshold V_T (5.648 km/s) to higher frequencies, which is known as the Lamb shoulder [13]. There are also two minima at the Lamb shoulder. One is at the fast transverse (FT) threshold V_{FT} (5.844 km/s), and another near the longitudinal threshold (8.344 km/s).
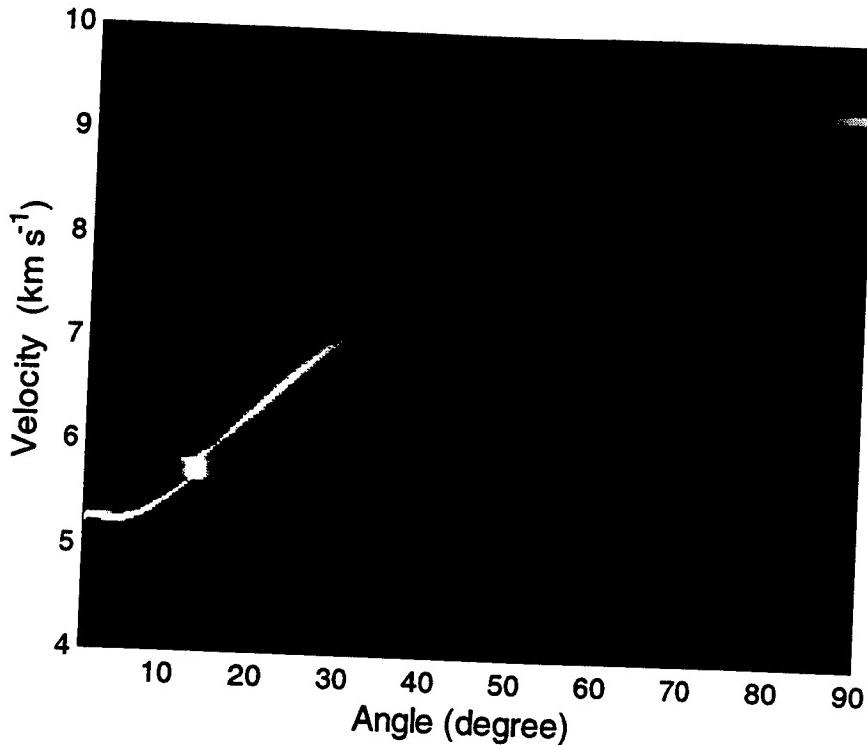
Figure 3. Two-dimensional image of the Brillouin spectra of cBN film (300 nm) on Si (001) calculated for direction [100], using experimentally obtained elastic moduli for cBN [20].

Theoretical dispersion curve and experimental points measured for 60 nm CBN layer sample are shown in Fig. 4. For the case of thick cBN film (60 nm cBN) only lower part of the experimental point can be attributed to true SAW. The upper points belong to PSAW. Theoretical dispersion curve based on the elastic constants obtained in [20] is a good agreement with experimental data. To find the best fit of the experimental data, both C_{11} and C_{44} are varied assuming that the density of cBN film is 3.5 g/cm3. The error sum of squares over all number of experiments n_{exp} [22]

$$ESS = \sum_{i=1}^{n \, exp} \left(v_{calc}^i - v_{meas}^i \right)^2 \qquad (4)$$

is minimized with respect to the variation of the elastic constants of the layered solid. In eq. (4) v_{meas}^i are measured values of the SAW velocity and v_{calc}^i are the corresponding theoretical values.

Deriving elastic constants from experimental data for 16 nm cBN film is more difficult task since velocity of the surface acoustic wave is practically independent of the angle (see Fig. 5). In case of 16 nm cBN film, the SAW branch can be attributed to the true surface waves for all angles of incidence, and their velocities are below shear cut-off (see also Fig. 3). Results of the best fitting procedure are presented in Table 1.

One can concluded that the cBN films deposited by ion deposition method are not softer than the polycrystalline bulk cBN. This conclusion is in contradiction with the results obtained in articles [6, 7] and can be attributed to the different deposition methods.

Figure 4. Theoretical SAW dispersion curve for cBN film (16 nm cBN /15 nm hBN) on Si (001) calculated for [100] direction, and compared with experimental data (stars). V_T is the transverse-wave threshold; and V_{FT} is the fast transverse threshold.
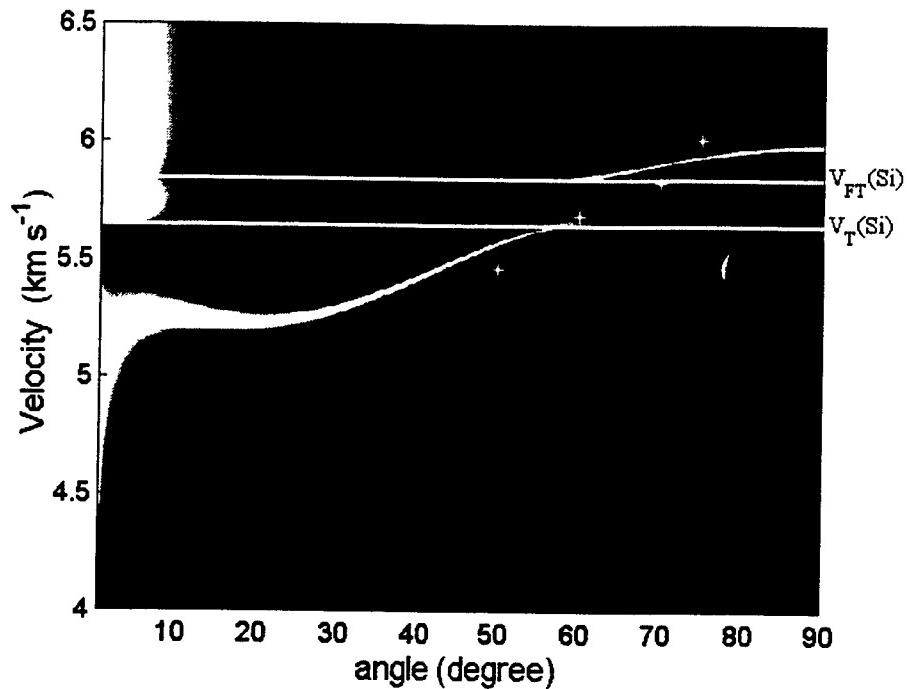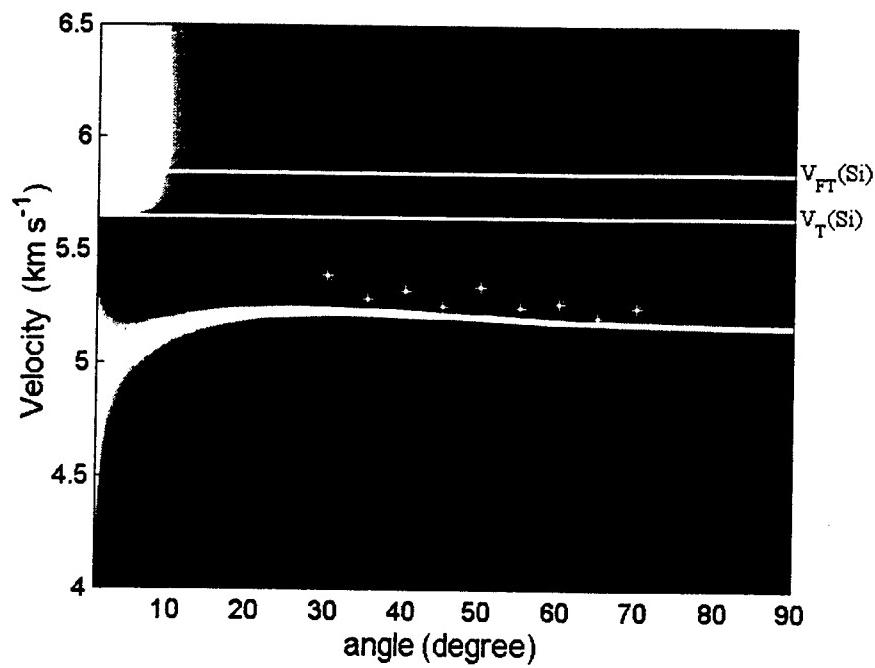

Figure 5. Theoretical SAW dispersion curve for cBN film (16 nm cBN /15 nm hBN) on Si (001) calculated for [100] direction, and compared with experimental data (stars).

Table 1. Velocities and moduli of cBN, hBN and Si.

Materials	Density (kg/m^3)	C$_{11}$ (GPa)	C$_{12}$	C$_{44}$
60 nm cBN/10nm hBN	3500	875		344
16 nm cBN/15nm hBN	3500	875		434
cBN polycrystalline [20]].	3500	875.73		377.69
Si cubic	2339	165.7	63.9	79.6

5. CONCLUSIONS

1. A dispersion curve of SAWs on cBN film on Si (100) has been obtained by surface Brillouin spectroscopy (SBS).
2. Incorporating the hBN interlayer into model of the SBS response and precise thickness measurement of the cBN layer and hBN interlayer fully describes the behavior of the SAW dispersion in deposited cBN layered systems.
3. The elastic properties of the cBN films are not softer than those of bulk cBN.
4. The SBS technique is of potential value in interpreting the elasticity of hBN/cBN layered films.

ACKNOWLEDGMENTS

REFERECES

1. V.K. Sarin, ed. *Science of Hard Materials.* Elsevier, Lausanne, 1996.
2. J.E. Field, *The Properties of Diamond.* Academic Press, London,1979.
3. H. Hofsass, H. Feldermann, M. Sebastian, and C. Ronning, "Thresholds for the phase formation of cubic boron nitride thin films," *Phys. Rev. B.* **55**, pp. 13230-13233, 1997.
4. P.B. Mirkarimi, K.F. McCarty, and D.L. Medlin, "Review of advances in cubic boron nitride film synthesis," *Materials Sciences and Engineering.* **R21**, pp. 47-100, 1997.
5. P.B. Mirkarimi, D.L. Medlin, and J.C. Barbour, "The synthesis, characterization, and mechanical properties of thick, ultrahard cubic boron nitride films deposited by ion-assisted sputtering," *J. Appl. Phys.* **82**, pp. 1617-1625, 1997.
6. R. Pastorelli, P.M. Ossi, C.E. Bottani, R. Checchetto, and A. Miotello, "Elastic constants of cubic boron nitride films." *Appl. Phys. Lett.* **77**, pp. 2168-2170, 2000.
7. T. Wittkowski, P. Cortina, J. Jorzick, K. Jung, and B. Hillebrands, "Brillouin light scattering from surface phonons in hexagonal and cubic boron nitride films," *Diamond Relat. Mater.* **9**, pp. 1957-1964, 2000.
8. V. Askarpour, M.H. Manghnani, S. Fassbender, and A. Yoneda, "Elasticity of Single-Crystal Mgal2o4 Spinel Up to 1273-K By Brillouin Spectroscopy," *Phys. Chem. Minerals.* **19**, pp. 511-519, 1993.
9. P. Zinin, M.H. Manghnani, S. Tkachev, V. Askarpour, O. Lefeuvre, and A. Every, "Brillouin spectroscopy of surface in thin film Si$_3$N$_4$ on GaAs," *Phys. Rev. B.* **60**, pp. 2844-2850, 1999.
10. J.R. Sandercock, "Trends in Brillouin-Scattering - Studies of Opaque Materials, Supported Films, and Central Modes," in *Light Scattering in Solids III. Recent Results.*, M. Cardona and G. Guntherodt, (eds), Springer - Verlag, Berlin, pp. 173-206, 1982.

11. R. Loudon, "Theory of surface-ripple Brillouin scattering by solids," *Phys. Rev. Lett.* **40**, pp. 581-583, 1978.

12. A.G. Every, W. Pang, J.D. Comins, and P.R. Stoddart, "Brillouin scattering study of guided modes in TiN films on high speed steel," *Ultrason.* **36**, pp. 223-227, 1998.

13. X. Zhang, J.D. Comins, A.G. Every, P.R. Stoddart, W. Pang, and T.E. Derry, "Surface Brillouin scattering study of the surface excitations in amorphous silicon layers produced by ion bombardment," *Phys. Rev. B.* **58**, pp. 13677-13685, 1998.

14. J.D. Comins, "Surface Brillouin Scattering," in *Handbook of Elastic Properties of Solids, Liquids, and Gases. Volume I: Dynamic Methods for Measuring the Elastic Properties of Solids*, M. Levy, H. Bass, R. Stern, and V. Keppens, (eds), Academic Press, New York, pp. 349-378, 2000.

15. O. Lefeuvre, P. Zinin, G.A.D. Briggs, and A. Every, "Surface wave dispersion beyond cut-off for a fast layer on a slow substrate," *Appl. Phys. Lett.* **72**, pp. 856-857, 1998.

16. P. Zinin, O. Lefeuvre, G.A.D. Briggs, B.D. Zeller, P. Cawley, A.J. Kinloch, and G.E. Thompson, "Anomalous behaviour of leaky surface waves for stiffening layer near cut-off," *J. Appl. Phys.* **82**, pp. 1031-1035, 1997.

17. P. Zinin, O. Lefeuvre, A. Briggs, B.D. Zeller, P. Cawley, A. Kinloch, X. Zhou, and G. Thompson, "Determination of density and elastic constants of a thin phosphoric acid-anodized oxide film by acoustic microscopy," *The Journal of the Acoustical Society of America.* **106**, pp. 2560-2567, 1999.

18. W. Pang, A.G. Every, J.D. Comins, P.R. Stoddart, and X. Zhang, "Brillouin scattering from acoustic excitations in TiN films on high speed steel—A stiffening system," *J. Appl. Phys.* **86**, pp. 311-317, 1999.

19. M. Chirita, R. Sooryakumar, H. Xia, O.R. Monteiro, and I.G. Brown, "Observation of guided longitudinal acoustic modes in hard supported layers," *Phys. Rev. B.* **60**, pp. 5153-5156, 1999.

20. M.H. Manghnani, "Elastic properties of cBN as a function of temperature and pressure: a comparison with diamond," in *5th NIRIM Int. Symp. Advanc. Mater.*, National Institute For Research in Inorganic Materials, Chicherster, pp. 73-78, 1998.

21. T. Wittkowski, J. Joizick, K. Jung, and B. Hillebrands, "Elastic properties of thin h-BN films investigated by Brillouin light scattering," *Thin Solid Films.* **353**, pp. 137-143, 1999.

22. P.V. Zinin, "Quantitative Acoustic Microscopy of Solids," in *Handbook of Elastic Properties of Solids, Liquids, and Gases. Volume I: Dynamic Methods for Measuring the Elastic Properties of Solids*, M. Levy, H. Bass, R. Stern, and V. Keppens, (eds), Academic Press, New York, pp. 187-226, 2001.

POSSIBLE ARTEFACTS IN MEASUREMENT OF HARDNESS AND ELASTIC MODULUS ON SUPERHARD COATINGS AND THE VERIFICATION OF THE CORRECTNESS OF THE DATA

S. Veprek[*], S. Mukherjee[a], P. Karvankova, H.-D. Männling, J. L. He, J. Xu, J. Prochazka
Institute for Chemistry of Inorganic Materials, Technical University Munich, Lichtenbergstr. 4, D-85747 Garching b. Munich, Germany, A. S. Argon Department of Mechanical Engineering, Massachusetts Institute of Technology, Cambridge, Massachusetts 02139, USA, A. S. Li, Q. F. Fang Institute of Solid State Physics, Chinese Academy of Sciences, Hefei 230031, China, S. Z. Li Qingdao University of Chemical Technology, Qingdao 266042, China, M. H. Manghnani, S, Tkachev, P. Zinin School of Ocean and Earth Science and Technology, University of Hawaii, Honolulu, Hawaii 96822, USA
[a] On leave from Bhabha Atomic Research Center, Mumbai, India

ABSTRACT

Measurements of the hardness and Young's modulus of superhard coatings ($H_V \geq 40$ GPa) by means of automated load-depth-sensing indentation technique can be subject to a number of errors that are discussed and exemplified here. Only load-independent values of hardness for loads larger than 30-50 mN can be considered reliable when the technique of Doerner and Nix (linear extrapolation of the unloading curve) is used to determine the corrected indentation depth. The results are compared with values of Vickers hardness calculated from the contact area of the remaining plastic deformation which was measured by means of calibrated scanning electron microscope. The values of Young's modulus obtained from the indentation are close to the zero-pressure shear modulus of the coatings as measured by means of Vibrating Reed and surface Brillouin scattering techniques.

INTRODUCTION

Plastic indentation hardness is defined as the pressure under the indenter that causes the material to flow [1,2]. Thus, for materials which show little or no strain hardening the hardness $H = L/A_C$ must be independent of the applied load L (A_C is the contact area between the indenter and the material). In the modern automated load-depth-sensing instruments the hardness (or more precisely the corrected indentation depth h_{corr}) and Young's modulus are evaluated from the slope of the unloading curve using either a linear extrapolation of the unloading curve [3] or a power law fit [4]. These and other researchers (e.g. [5,6]) verified that this technique yields values of hardness and Young's modulus in agreement with the results obtained by conventional techniques. Oliver and Pharr emphasized that for very hard materials, which show a large elastic recovery upon unloading, the values obtained by the load-depth-sensing technique may differ from those obtained in the conventional way [7].

This is due to the fact that for ultrahard materials with elastic recovery of $\geq 90\%$ [9,10] the shape of the unloading curve is dominated by the elastic response of the material/diamond indenter pair. This can be also understood when considering the "univesal hardness" $H_U = L_{max}/C \cdot h_{max}^2$ (h_{max} is the maximum indentation depth under the maximum applied load L_{max}, C is a constant converting the indentation depth into the contact area) which converges to a final value of about 22-24 GPa when the plastic hardness approaches that of diamond [11]. Furthermore, the evaluation techniques and the derivation of Sneddon's formula assume a rigid indenter whereas Finite Element Method calculation showed that it undergoes an appreciable elastic deformation upon indentation into superhard materials [12].

These measurements are further complicated for thin superhard coatings on a softer substrate: Because of a finite tip radius of the indenter the indentation depth has to be ≥ 0.2-

0.3 μm [13] but simultaneously it must not exceed 5 % of the thickness of the coatings in order to avoid the effect of the softer substrate [12,14]. Consequently, there is a minimum thickness of ≥ 6-8 μm required for reliable measurements on superhard coatings.

EXPERIMENTAL DETAILS AND RESULTS

For the preparation and characterization of the superhard nanocomposite coatings we refer to our earlier papers (e. g. [9-11,15-19]).The hardness measurements were done by means of the indentometer Fisherscope 100 using a Vickers diamond indenter. This instrument uses linear extrapolation of the unloading curve to determine the stiffness S and corrected indentation depth h_{corr}. The correction for the tip rounding [3] was done prior to each series of measurements and verified by measuring the hardness of Si(111) and Sapphire (001) taking conservative values of the hardness 10.3 GPa and 21-22 GPa for Si [20] and Sapphire [21], respectively. The hardness was also determined for the same indentations from the projected area A_P of the plastic deformation as $H_V = 0.927 \cdot A_P$ [2]. A_P was determined by means of calibrated scanning electron microscope (SEM). A photolithographic mask with an exact spacing of metallic lines was used for the calibration. Figure 1 shows an example of the resulting values. The hardness determined by SEM remains constant to the smallest applied load of 5 mN thus confirming that the pressure under the indenter reached the flow stress of the coatings. In contrast, the hardness value from the indentometer strongly increases with decreasing load. The load-independent values of hardness measured on silicon and Sapphire (Fig. 1b) clearly demonstrates that the tip correction was done correctly.
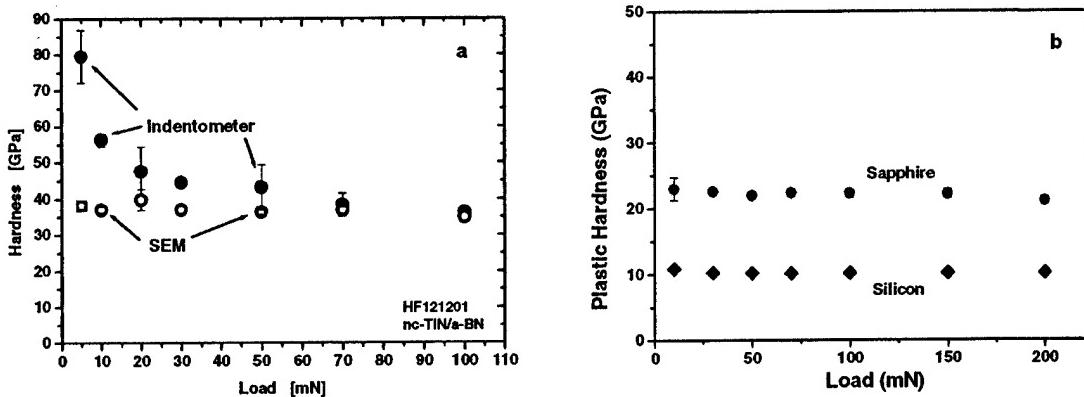

Fig. 1: a: Hardness of a 6 μm thick nc-TiN/a-BN coating on stainless steel substrate determined by means of the load-depth-sensing technique (full symbols) and calibrated SEM (open symbols), respectively and b: Hardness of Si(111) and Sapphire α-Al₂O₃ (001). (See text.)

The very high values of hardness obtained by the carefully calibrated indentometer at low loads are incorrect. The reason for this effect is probably a significant elastic deformation of the indenter as found by FEM calculations [11] but more detailed investigation is needed in order to clarify this question. This "Size Indentation Effect" can also be due to a decreasing probability of the occurrence of a critical flaw within the tested volume, to a finite distance between deformation bands, depth dependent properties of the coatings etc. If the surface roughness is comparable to h_{ind}, smaller values of hardness are found at a low load. Therefore it is necessary to check the measured values by means of calibrated SEM (e.g. [15]).

Fischerscope 100 uses linear extrapolation of the unloading curve to determine the corrected indentation depth h_{corr} as suggested by Doerner and Nix [3] whereas Oliver and Pharr elaborated a power law fit for the determination of the slope of the unloading curve at

the L_{max} from which h_{corr} is calculated [4]. Both techniques yield correct values for the conventional materials but problems arise when applied to superhard ones as illustrated by Fig. 2. The value of hardness obtained from Fischerscope, from the linear extrapolation of 30 % of the unloading curve corrected for the tip rounding and from SEM agree very well whereas that determined from the power law fit is too low. This is in accord with the statement of Oliver and Pharr [7] that for very hard coatings the slope of the upper part of the unloading curve is dominated by the elastic response of the material/indenter pair.
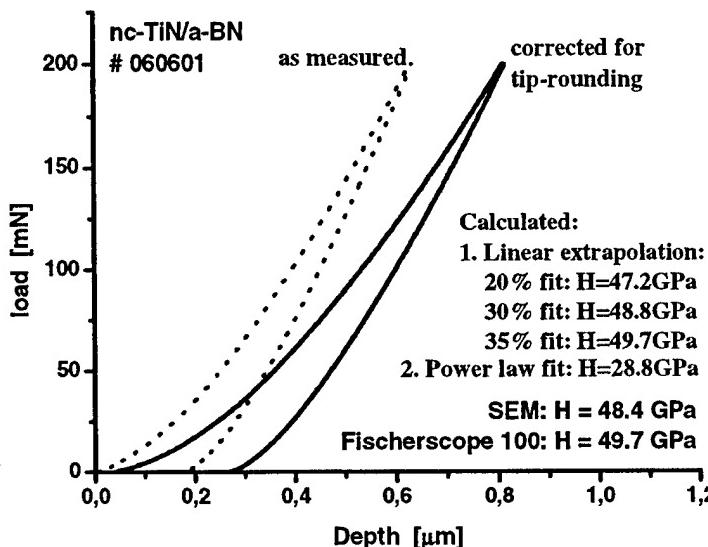

Fig. 2: Comparison of the values of hardness obtained at a high load of 200 mN from Fischerscope 100, by calibrated SEM, by linear extrapolation of the indicated parts of the unloading curve and by the power law fit.

Material	H_V (GPa)	H_U (GPa)
Silicon	10.3	7.3
TiN (P CVD)	21	12
3C-SiC (CVD)	36-38	16
nc-TiN/a-Si_3N_4	48	15.5
nc-TiN/a-Si_3N_4/a-$TiSi_2$	85	17
nc-TiN/a-Si_3N_4/a- & nc-$TiSi_2$	105	18
nc-Diamond	100	17.5
bulk Diamond	105 ± 10 *)	23.4 ± 1

*) average value of 10 measurements

Table I: Correlation between the plastic H_V and universal H_U hardness.

The interpretation of the results from Fig. 2 is further supported by the correlation between the measured "universal hardness" H_U and the plastic one H_V which is illustrated for several materials in Table I. For soft metals, such as Au, Cu, H_U scales approximately as $H_U \approx$ 10·H_V but already for Si the proportionality factor decreases to about 0.63 (see Fig. 7b in [5]). For hard materials, such as TiN and 2C-SiC the proportionality factor decreases to 0.4-0.5, for superhard ones with $H_V \approx$ 40-50 GPa to 0.3-0.4 and for ultrahard coatings, nc- and bulk industrial diamond to about 0.2 (see Table I). Another example illustrating the problem of the correct determination of h_{corr} is the measurement on bulk (ca. 6x6x1 mm^3) industrial diamond. Figure 3 shows one example of more than 20 indentations which we did at maximum applied load between 30 and 150 mN.

Many further artefacts may cause errors in the determination of the hardness of super- and ultrahard coatings. For lack of space we limit ourselves here only ton a brief remark regarding the effect of anelastic response of the steel substrate. Anelasticity is reversible, time

delayed strain response of a material to applied stress [22,23]. In Ref. [14] it has been shown that the anelastic response of a steel substrate can cause a large error particularly when the measurement is done at a low load of ≤ 30 mN.
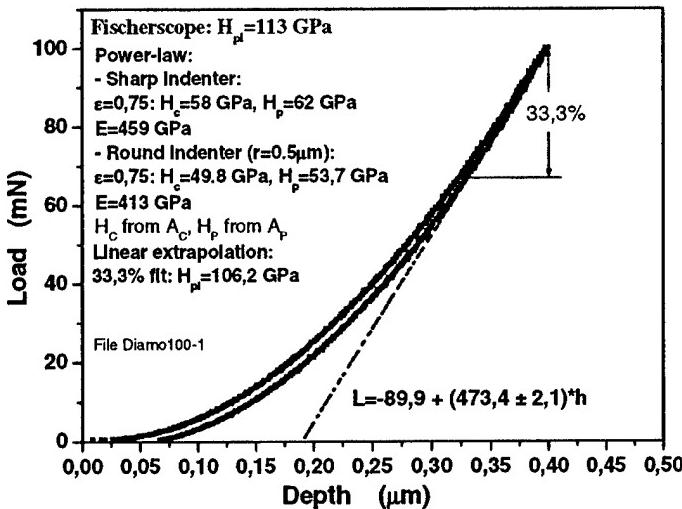

Figure 3: Example of indentation into a bulk industrial diamond with L_{max}= 100 mN. The values of hardness obtained by the linear extrapolation agree reasonably well with that form Fischerscope but the power law fit yields too low values.

The slope of the unloading curve at the maximum load is used to calculate the composite **Young's modulus** of the indenter and material being tested [3-5]. It is based on Sneddon's analysis of the indentation of a rigid flat punch into an elastic half space [24]. This analysis was shown to apply for any axially symmetric indenter [4,25] and also when plastic deformation of the indented material occurs [26]. The researchers also carefully verified that, for conventional materials, this procedure yields the correct values of Young's modulus [3-5]. In the case of superhard coatings when the pressure under the indenter reaches ≥ 40 GPa the pressure dependence of the moduli has to be taken into account [10]. Considering the typical pressure dependence of bulk modulus $B(P) = B(0) + (3-6) \cdot P$ ($B(0)$–zero pressure bulk modulus, $B(P)$–bulk modulus at pressure P) one notices that for suprehard materials where P is of the order of H the pressure enhancement (see the second term on the right hand side of the equation) may amount 100 GPa or more. The problem is however more complicated because of the very non-uniform stress distribution under the indenter and the fact that the elastic response at the unloading curve close to L_{max} comes also from the distant regions of the contact. Furthermore, as already mentioned, the elastic deformation of the diamond cannot be neglected and this is probably at least one of the sources of the errors.

E (Gpa)	B (Gpa)	G (Gpa)	E_{ind} (Gpa)
445 ± 20	295 ± 15	195 ± 15	242 ± 25

Table II: (see text)

Comparative measurements of elastic moduli were done on 4–10 μm thick coatings deposited on steel and 0.1 mm thick 5x50 mm^2 large Mo strips. The coated molybdenum strips were used for the measurement of Young's modulus by means of vibrating reed technique (see Fig. 4 and ref. [27]). The coatings on steel were used for the measurement of elastic moduli by means of Surface Brillouin Scattering (SBS) [28]. Here we briefly summarize the results: A total 7 samples with different hardness were measured and the results compared with the value of elastic modulus obtained from the indentation. The SBS allows us to determine the shear and bulk modulus from which the Poisson's ratio v ≈ 0.25 is calculated. Using this value we can calculate the bulk B and shear G modulus on the basis of the value of Young's modulus measured by the VR technique. All the data available so far show a good agreement and the results are summarized in Table II. E_{ind} is the average value of the elastic

modulus obtained on the coatings by the indentometer. One notices that the values of E_{ind} are between those of bulk, B, and shear, G, moduli determined by the SBS and VR techniques. Considering the fact that the E_{ind} should be pressure enhanced leads to the conclusion that the elastic modulus measured by indentation at superhard coatings is close to shear modulus of these materials. These studies are still in progress and more data are needed, but we consider the values of elastic moduli obtained by VR and SBS as reliable because the resulting bulk modulus agree well with that measured on bulk TiN and three other nc-TiN/a-Si$_3$N$_4$ coatings by means of high pressure XRD [29].
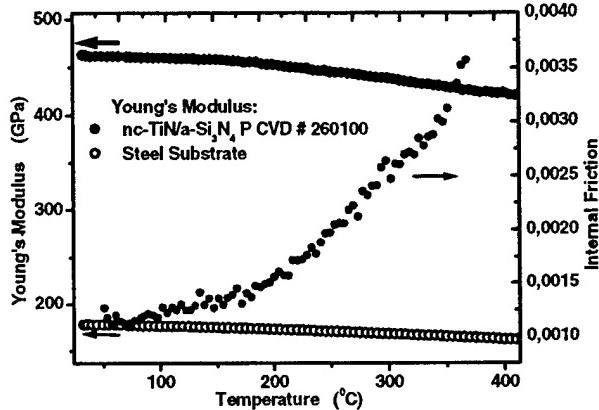

Fig. 4: Temperature dependence of the Young's modulus of the steel substrate and of the coating and the internal friction [27]
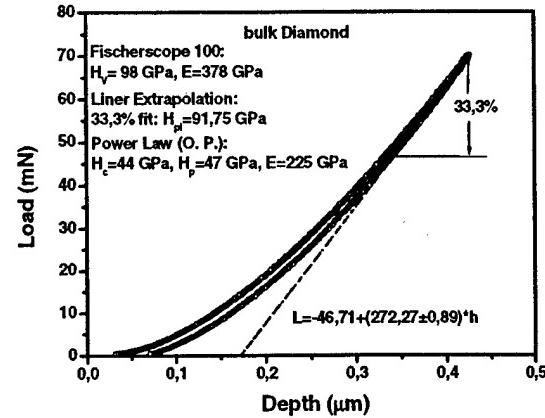
Fig. 5: Example of the evaluation of elastic modulus of bulk diamond by indentation

In order to underline these conclusions we show in Fig. 5 one example of more than 20 indentations into bulk Diamond. One notices that the value of elastic modulus obtained by the linear extrapolation from Fischerscope is again much lower than the standard value of Young's modulus of 1100 ± 50 reported in the literature for bulk diamond and even less than the values of shear $G = 533$ GPa and bulk $B = 442$ moduli [30]. For the discussion of the possible reasons for this discrepancy we refer to the forthcoming full length paper because of the lack of space available here. The elastic deformation of the Diamond indenter is surely one of them, but another one is probably the very complex, non-uniform distribution of the stress under and around the indenter that includes a large fraction of shear.

CONCLUSIONS

Application of the load-depth-sensing indentation technique for the measurement of hardness and elastic modulus of super- and ultrahard coatings and bulk diamond may produce erroneous results. Only load independent values obtained at sufficiently thick coatings and large load of 50-150 mN when using the linear extrapolation of the unloading curve for the determination of the corrected indentation depth can be considered reliable but they should be checked by calibrated SEM. The elastic values of moduli obtained from the unloading curve using the standard procedures are much lower than the value of Young's modulus of the material. For the superhard coatings they seems to be close to the zero-pressure shear modulus.

measurements were carried out at the University of Hawaii under the Army Res. Office Contract No. 19-00-1-069.

REFERENCES

[1] E. Meyer, Zeitschrift des Vereines Deutscher Ingenieure **52**, 645 (1908).

[2] G. Tabor, *The Hardness of Metals* (Clarendon Press, Oxford, 1951).

[3] M. F. Doerner and W. D. Nix, J. Mater. Res. **1**, 601 (1986).

[4] W: C. Oliver an G. M. Pharr, J. Mater. Res. **7**, 1564 (1992).

[5] H.-H. Behnke, Härterei Zechnische Mitteilungen **48**, 2 (1993).

[6] P. Neumaier, Metalloberfläche **2**, 41 (1989).

[7] T.Y. Tsui, W.C. Oliver and G.M. Pharr, MRS Symp. Proc. **436**, 147 (1997).

[8] S. Veprek, M. Haussmann and S. Reiprich, J. Vac. Sci. Technol. **A 15**, 46 (1996).

[9] S. Veprek, J. Vac. Sci. Technol. **A 17**, 2401 (1999).

[10] S. Veprek and A. S. Argon, J. Vac. Sci. Technol. **B 20**, 650 (2002).

[11] A. Niederhofer, Ph D Thesis, Technical University Munich 2001.

[12] Jianli He and Stan Veprek, Surf. Coat. Technol. (2002/3) in press.

[13] S.J. Bull, J. Vac. Sci. Technol. **A19**, 1404 (2001); Thin Solid Films **398-399**, 291 (2001).

[14] S. Veprek at al., invited paper at Int. Conf. Metall. Coatings & Thin Films. San Diego, April 2002, Thin Solid Films, submitted.

[15] S. Veprek, A. Niederhofer, K. Moto, P. Nesladek, H. Männling and T. Bolom, MRS Symp. Proc. **581**, 321 (2000).

[16] A. Niederhofer, P. Nesladek, H.-D. Männling, K. Moto, S. Veprek and M. Jilek, Surf. Coating Technol. **120-121**, 173 (1999).

[17] S. Veprek, A. Niederhofer, K. Moto, T. Bolom, H.-D. Männling, P. Nesladek, G. Dollinger and A. Bergmaier, Surf. Coating Technol. **133**, 152 (2000).

[18] A. Niederhofer, T. Bolom, P. Nesladek, K.Moto, C. Eggs, D. S. Patil and S. Veprek, Surf. Coat. Technol. **146-147**, 183 (2001).

[19] H.-D. Männling, D. S. Patil, K. Moto, M. Jilek and S. Veprek, Surf. Coating Technol. **146-147**, 263 (2001).

[20] P.J. Burnett, in: Properties of Silicon, INSPEC – EMIS Datareviews Ser. No. 4, The Institution of Electrical Engineers, London 1988, p. 27, ff.

[21] G. Berg et al., in: Handbook of Ceramic Materials, Vol. 2, ed. R. Riedel, Wiley-VCH, Weinheim 2000, p. 964 ff (Table I).

[22] C. Zener, Elasticity and Anelasticity of Metals, The University of Chicago Press, 2nd ed., Chicago 1952.

[23] A. S. Nowick and B. S. Berry, Annelastic Relaxation in Crystalline Solids, Academic Press, New York 1972.

[24] I.N. Sneddon, Int. J. Eng. Sci. **3**, 47 (1965).

[25] G.M. Pharr, Mater. Sci. & Eng. **A 253**, 151 (1998).

[26] Che-Min Cheng and Yang-Tse Cheng, Appl. Phys. Lett. **71**, 2623 (1997).

[27] Z.S. Li, Q.F. Fang, S.Z. Li and S. Veprek, Mater. Sci. Eng. A, submitted

[28] M.H. Manghani, S. Tkachev, P. Zinin, P. Karvankova, S. Veprek and C. Glorieoux, Int. Conf. Metal. Coatings & Thin Films, San Diego, April 2003, to be published.

[29] S. Primilan, S. Clark, C. Erdonmenz, P. Alivisatos, D. S. Patil, J. Prochazka, P. Karvankova and S. Veprek, to be published

[30] J. Wilks and E. Wilks, Properties and Applications of Diamond, Butterworth-Heinemann, Oxford 1991.

Evaluation of rubber-PVC blends structure....

Figure 2. Acoustic images of the samples surface of BNR-PVC blends after the exposition under the stretch-strain deformation in ozone: 1 – BNR-18 with 10 PVC p.p.h.r.; 2 – BNR-26 with 20 PVC p.p.h.r.; 3 – BNR-26 with 40 PVC p.p.h.r. Frequency 200 MHz.

These methods require special processing of the samples, which spoils their integrity and changes their mechanical properties. The mechanical properties can be evaluated with standard mechanical tests, most of which are destructive or deforming [Swallow, 1999]. Therefore, there is no conventional method which would allow the evaluation of both microstructure and mechanical properties on the same sample or to repeatedly observe the changes in the process of any experimental exposure. The results obtained in the present study demonstrate that acoustic microscopy gives a new opportunity for the non-destructive investigation of polymer blends. Microstructural characteristics obtained with a scanning acoustic microscope clarify the changes of mechanical strength and chemical resistance, which can also be evaluated using values of sound velocity and acoustic impedance.

4. References

Sawyer L.C., Grubb D.T. (1987) *Polymer Microscopy*, Chapman & Hall, London.

Swallow G.M. (1999) Ultrasonic techniques. *Mechanical properties and testing of Polymers*. Kluwer Acad. Publishers, Dordrecht-London, Ch.57, 260-264.

Lisy F., Hiltner A., Baer E., Katz J.L., Meunier A. (1994) Application of Scanning Acoustic Microscopy to Polymeric Materials. *J.Appl.Polymer Sci.*, **52**, 329-352.

Maev R.G., Maeva E.Y. (1992) Application of Scanning Acoustic Microscopy for polymer studies, *Proc. of 10th European Congress on Electron Microscopy*, Granada, Spain, **1**, 603-604.

Maev R.G., Pyshnyi M.P., Maeva E.Yu., Maslov K.I., Levin V.M. (1996) Acoustic Microscope visualization and Thickness Measurements of Deep Internal Layers in Layered Polymer Systems, *IEEE International Ultrasonic Symposium*, San Antonio, USA, 47-51.

Maev R.G., Popov A.A., Denisov A.F., Denisova L.A., Livanova N.M., Maeva E.Yu., Severin F.M., Bakulin E.Yu. (2002) *Mechanics of composite materials and structures*. (Rus) **8**, 2, 214-22.

Perepechko I.I. (1973) *Acoustical methods in polymer materials investigation* (Rus). Moscow, Chemistry.

ACOUSTIC MICROSCOPY, BRILLOUIN SCATTERING AND LASER-SAW TECHNIQUE FOR DEFECT CHARACTERIZATION IN DLC FILMS

PAVEL V. ZININ[1], DONG FEI[2], DOUGLAS A REBINSKY[2], MURLI H. MANGHNANI[1], SOFIA BEREZINA[3], ROBERT LEMOR[4], CHRIS BLASE[5], ARNAUD CARON[6], DIETER SCHNEIDER[7], KLAUS KRAEMER[8]

[1]*SOEST, University of Hawaii, Honolulu, HI, USA*
[2]*Caterpillar Inc., Peoria, IL, USA*
[3]*University of Zilina, Zilina, Slovakia*
[4]*Fraunhofer-Institut für Biomedizinische Technik, St.Ingbert, Germany*
[5]*J.W. Goethe-Universitat Frankfurt am Main, Frankfurt, Germany*
[6]*Fraunhofer Institute for Non-Destructive Testing, Saarbrücken, Germany*
[7]*Fraunhofer Institute for Material and Beam Technology IWS, Dresden, Germany*
[8]*Kraemer Scientific Instruments, Herborn, Germany*

1. Introduction

DLC films are beginning to find their way into industrial applications to prolong the life of machine components. Preliminary wear tests on nano-structured DLC coated samples demonstrated an appreciable improvement in pitting resistance and usable life. One of the key parameters that have great impact on the wear resistance of a material is its microstructure. The acoustic microscope was developed as a tool for studying internal microstructure of non-transparent solids and now it is widely used for detection of cracks and subsurface defects. Despite the expedient use of this NDE technique, quantitative characterization of the imaged defects is rarely completed because the theory describing image formation caused by subsurface defects is complicated (Lobkis *et al.*, 1995) and it requires knowledge of the material's elastic properties. In this article, we used scanning acoustic microscopy (Leitz ELSAM) to detect and analyze defects in thin chromium-alloyed DLC (Cr-DLC) films. Surface Brillouin scattering (SBS) and detection of the surface acoustic waves (SAWs) by laser (Laser-SAW technique) were applied to measure elastic properties of the films.

2. Acoustic Microscopy

Cr-DLC coating specimen (#624) has been studied using 0.4 GHz and 0.2 GHz transducers with the Leitz ELSAM acoustic microscope. Acoustical images obtained by

Leitz ELSAM acoustic microscope are presented in Figure 1. The defects can be clearly seen in the acoustic images. To locate the depth of the defects, acoustic images were taken at different defocus positions (Zinin and Weise, 2003). The numbers of defects in the acoustical images of the Cr-DLC coating were determined either manually or using the software Image Pro Plus 3.1. The defect density (or the number of defects per area) of different recipes is given in Table 1.

To study micron-size defects in coatings, high frequency images with a smaller field view have also been analyzed. Figures 2(a) and (b) show the 1.3-GHz acoustic images of the Cr-DLC coated specimen at a defocus of 0 μm and -4 μm, respectively. Defects inside circles can be traced from the surface of the coating. Defects inside ellipses are subsurface defects and appear only in the image at $z = -4$ μm. High frequency images of specimen #624 reveal many small defects in the coating (see Table I).
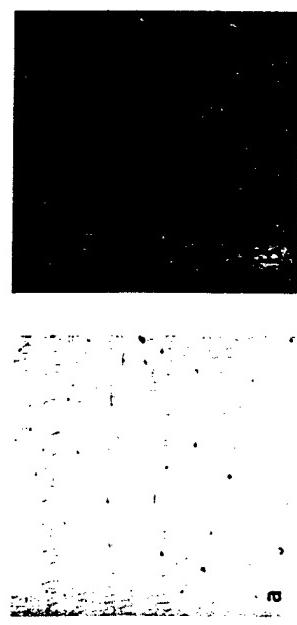
Figure 1. Acoustic images of the surface of the coated specimen (Cr DCL #624) at 0.4 GHz. The the field of view was 1000x1000 μm: (a) image was taken in focus; (b) defocus $z = -10$ μm.
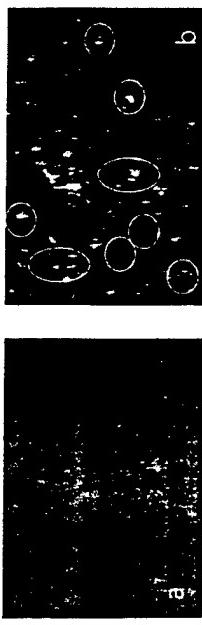
Figure 2. Acoustical images of the surface of the coated specimen (Cr DCL #624) at 1.3 GHz The size of the image in horizontal direction was 100 μm. (a) image was taken at defocus $z = 0$ μm. (b) image was taken at defocus $z = -4$ μm.

Table I. Analysis of micron size defects in specimen #624.

Image Frequency	Field view (μm)	Defect's density (Number/mm^2)	Average diameter (μm)	Maximum diameter (μm)
0.4 GHz	1000x1000	48	4.4 ± 1.1	8.4
1.3 GHz	240x240	486	2.7 ± 3.8	7.4
1.0 GHz	200x130	692	2.9 ± 1.3	6.0

Images of another specimen (#920) deposited with slightly different recipy demonstrate different acoustic contrats at low and high frequency images. Surprizingly, images at low frequency, 200 MHz, can provide a better contrast for small defects than images made at 1 GHz. The obtained acoustical images of Cr-DLC coating specimen (#920) with different defocus are shown in Figures 3 and 4, respectively. The field view was 500 μm $\times$ 500 μm for the 200 MHz images and 312 μm $\times$ 312 μm for the 1 GHz images. The acoustical images at low (200 MHz) and high (1 GHz) frequencies were obtained with different devices and from slightly different areas of the specimen. The subsurface defects (voids) can be more easily identified in the low frequency images (Figure 3) than in high frequency images (Figure 4).

We also note that the numbers of defects in the acoustical images measured at 200 MHz and 1 GHz were in qualitative agreement. However, the number of defects detected at high frequency (348 /mm^2) was higher for all specimens (216 /mm^2).
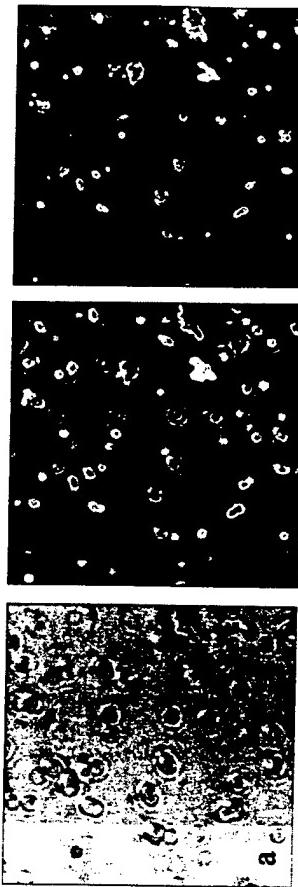
Figure 3. Acoustical images of the Cr-DLC specimen (#920) measured at 200 MHz with different defocuses. The field view of all the images was 500 μm $\times$ 500 μm: (a) $z = 0$; (b) $z = -4$ μm; (c) $z = -6$ μm.

Figure 4. Acoustical images of the five Cr-DLC specimens measured at 1 GHz with different defocuses. The field view of all the images was 312 μm $\times$ 312 μm: (a) $z = 0$; (b) $z = -4$ μm; (c) $z = -6$ μm.

This can be explained using acoustical image formation theory at different frequencies. At high frequency, the wavelength is much smaller than that at low frequency, allowing defects of much smaller size to be imaged. In the 1 GHz images shown in Figure 4, one can see many small defects with size of several microns. At 200 MHz, the sound wavelength in the DLC coating is around 25 μm. Defects with size of several microns could not be imaged at this low frequency and therefore did not appear in the images shown in Figure 3.

3. Atomic Force Microscopy

In order to recognize surface defects we use atomic force microscope (AFM). Figure 5 illustrates the structure of the su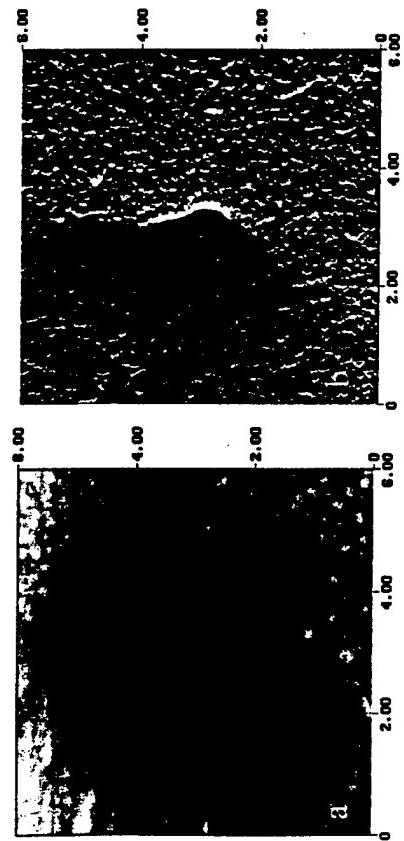rface near a small pit visible as a small dark spot with the optical microscope. The AFM image (Figure 5a) with height contrast provides a value of the pit height. It gives the maximum height of the pit of 230 nm. AMF image with deflection contrast demonstrates the structure of the surface inside the pit. It clearly indicates that the pit does not go down toward the film/substrate interface. Such defects obviously cannot be responsible for the strong contrast of defects seen in Figure 3.

Figure 5. AFM images of the sample #624: (a) height contrast; (b) deflection contrast.

4. Surface Brillouin Scattering

To estimate the depth of the defect location we need to know the elastic properties of the coatings. Surface Brillouin spectroscopy (SBS) is widely used for elastic characterization fo thin films (Beghi et al., 2003). Figure 6 shows the measured Brillouin spectrum in specimen Cr-DLC (#624), from which one can see the peaks resulting from the inelastic interaction between the incident light and the thermally

excited surface acoustic wave in the coating. The frequency positions of these peaks were used to determine V_{SAW}, the SAW velocity of coating, according to

$$V_{SAW} = \frac{\lambda_0}{2\sin\theta}\,\delta f_{SAW},$$ (1)

where λ_0 is the wavelength of the incident laser, θ is the incident angle, δf_{SAW} is the frequency shift of the SAW peak. The Rayleigh wave peak (Figure 6) detected in specimen #624 gives the velocity of the Rayleigh wave of 3.6 km/s.
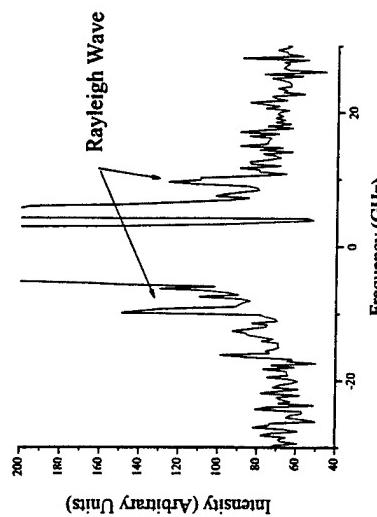
Figure 6. SBS spectrum of the sample #624. The angle of incidence was 60°.

5. Laser SAW Technique

For layered materials, the velocity of SAW is dependent on frequency. Because the shear velocity of the film is faster than that in the substrate, velocity of SAW increases as frequency increases (Lefeuvre et al., 1998). For 2.37 μm film (sample #624), SBS measurements give only one point of the dispersion curve. To derive elastic properties of the film, SAW should be measured at different frequencies. We used Laser SAW technique (Lomonosov et al., 2001) to measure the low frequency part of the SAW dispersion curve. For sample, #624 it is shown in Figure 7.

The elastic moduli of the coatings were evaluated by fitting the surface acoustic wave dispersion curve measured by a Laser-SAW technique. The mass of each wafer was measured before and after the wafer was coated, whose difference gave the mass of the coating. The coating thickness was measured using a ball crater and the area of the coating was calculated based on the dimension of the wafer. The coating density was then determined based on the mass and volume of the coating. From measurements with the four wafers, the coating density was estimated to be about 2.6×10^3 kg/m³, with a

variation of $\pm 0.3 \times 10^3$ kg/m³. The accuracy of the measured density was mainly determined by accuracy of the thickness measurement. Assuming specimen #624 had a density of 2.6×10^3 kg/m³ and using the result of the fitting SAW dispersion curve, the Poisson's ratio and Young's modulus of the coating were estimated to be 0.30 and 57.4 GPa, respectively. It gives the values for velocities of the longitudinal (5.97 km/s), shear (3.2 km/s), and Rayleigh wave (3.1 km/s). The difference of 14% in the values of Rayleigh wave measured by SBS and that obtained from SAW dispersion curve measurements can be attributed to the variation of the elastic properties of the film with depth.
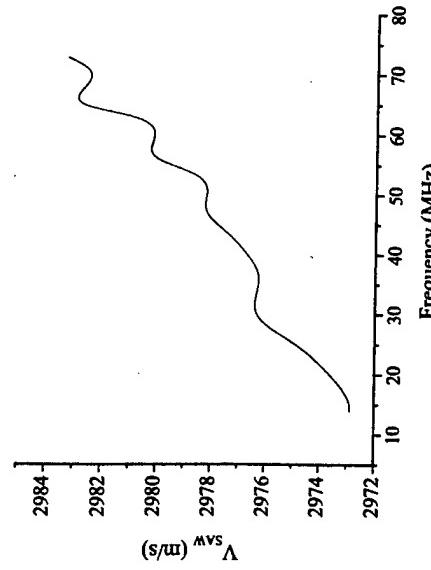

Figure 7. SAW dispersion curve for sample #624.

6. Discussion

In the acoustical images shown in Figure 2b, the small circular features were most likely due to the voids in the coatings. The large non-circular features, if they were not at the sample surface, could be associated with the delamination in the coating. To estimate the depth of these features, a rigorous theory for image formation of subsurface defects should be used (Lobkis *et al.*, 1995). Study on image formation of a spherical defect has shown that the output signal of the acoustic microscope reaches its maximum when the focus of the SAM is in coincidence with the top of the sphere. A simple geometrical optics based model was used here to estimate the location of the focus inside the coating. According to this model,

$$z_i = z \frac{V_{Water}}{V_{Coating}}, \qquad (2)$$

where z is defocus, or the displacement of the lens from the position where the focus is in the surface of the specimen, z_i is the depth of the focus in the coating, V_{Water} and $V_{Coating}$ are the longitudinal sound velocities in water (serving as the coupling medium) and the coating, respectively. The sound velocity in water is 1.48 km/s at room temperature. The surface Brillouin scattering measurement with Cr-DLC #624 showed that the longitudinal wave velocity of the coating was around 5.97 km/s, as has been discussed previously in this report. The ratio of the defocus to the depth of the defect in the coating is therefore about 4:1. By using this ratio and comparing the signal magnitude of a defect in the images from different defocuses, the depth of the defect can be estimated. For example, by comparing the 1 GHz images of specimen #624 shown in Fig. 3, one can see that the signal magnitudes of the small circular defects are maximal (brightest) in the image with a defocus of -4 µm. The defects are therefore approximately 1.0 µm deep.

7. Conclusions

Our main goal was to investigate the distribution of subsurface defects in Cr-DLC coatings deposited on a steel substrate where the thickness of the films varied from 2 to 3 µm. Two frequencies (200 MHz and 1 GHz) were used to detect and image the defects and for size determination. Our study illustrates that a combination of low (200 MHz) and high (1 GHz) frequency images of the subsurface voids provides sufficient information to uniquely determine their distribution and location. Images at 200 MHz revealed a higher sensitivity to the subsurface voids although they did not provide accurate information about the size and location of the defects. Detection and identification of the defects at high frequency (1 GHz), as a rule, were more difficult; however, the high frequency images were useful for determining the size and position of the defects.

8. Acknowledgement

9. References

Beghi, M. G., Every, A. G. and Zinin, P. V. (2003) Brillouin Scattering Measurement of SAW Velocities for Determining Near-Surface Elastic Properties, in T. Kundu, (ed.) *Ultrasonic Nondestructive Evaluation: Engineering and Biological Material Characterization*, CRC Press, Boca Raton pp. (in press).

Lefeuvre, O., Zinin, P. and Briggs, G. A. D. (1998) Leaky surface waves propagating on a fast on slow system and the implications for material characterization, *Ultrasonics* 36(1-5), 229-232.

Lobkis, O. I., Kundu, T. and Zinin, P. V. (1995) A theoretical analysis of acoustic microscopy of spherical cavities, *Wave Motion* 21(2), 183-201.

Lomonosov, A., Mayer, A. P. and Hess, P. (2001) Laser Controlled Surface Acoustic Waves, in M. Levy, H. Bass, R. Stern and V. Keppens, (eds.), *Handbook of Elastic Properties of Solids, Liquids, and Gases, Volume*

228   Acoustic microscopy, Brillouin scattering and laser-SAW technique...

I: Dynamic Methods for Measuring the Elastic Properties of Solids, Academic Press, New York, 1 pp. 137-186.

Zinin, P. V. and Weise, W. (2003) Theory and applications of acoustic microscopy, in T. Kundu, (ed.) Ultrasonic Nondestructive Evaluation: Engineering and Biological Material Characterization, CRC Press, Boca Raton pp. (in press).

APPLICATION OF MICROACOUSTICAL TECHNIQUE TO STUDY ELASTIC PROPERTIES AND MICROSTRUCTURE OF NEW GENI OF BULK METALLIC GLASSES

V.M. LEVIN[1], J.S. PETRONYUK[1], L. WANG[2], J. HU[3], Q.

[1] Lab. of Acoustic Microscopy, Institute of Biochemical Physi Russian Academy of Sciences, 4 Kosygin st., 119991, Moscou
[2] Institute of Physics & Center for Condensed Matter Physics, Academy of Sciences, P.O.Box 603, 100080, Beijing, People's R China;
[3] Lab. of Ultrasonic NDT, Dept. of Electronic Engineering, Univ. of Science & Technology of China, 230026, Hefei, Anhi
[4] Dept. of Electronic Engineering, Graduate School, Chinese Academy of Sciences, 100039, Beijing, China;

Elastic properties of bulk metallic glass (BMG) $Pd_{39}Ni_{10}Cu_{10}P_{21}$ have l basing on sonic velocity data analysis. Different states of the $Pd_{39}Ni_{10}Cu$ (glassy state, super-cooled liquid (SCL) and re-crystallized states) were annealing of the samples at different temperature near the glass transitic crystallization temperature. Microacoustical technique has been applied local values of longitudinal and transverse elastic wave velocities and thei over a specimen body. Finally sonic velocities C_L and C_T, density ρ, bulk Λ elastic moduli were measured for different states of $Pd_{39}Ni_{10}Cu_{10}P_{21}$ BMC shown decreasing values of ρ, C_L and K as temperature. For the re-crys ultrasonic measurements were performed by low-frequency flat transduce high ultrasonic attenuation in this case. Acoustic images (C-scans) evidenc of rough-grain microstructure at this state. It is assumed the rough grant with particles size ~70-80 µm is characteristic for re-crystallized state of BM(

1. Introduction

Multicomponent glass-forming alloys of the Pd-Ni-Cu-P and Zr-Ti-Cu-N are intensively studied due to their extraordinary glass forming ability an elastic properties [1-3]. Investigation of features of bulk metallic glass employed for understanding the nature of the glass transition. Since acous are sensitive to microstructure, ultrasonic methods are widely applied to BMG elastic properties over a wide temperature range. The temperature d elastic wave velocities provides the critical information on the m characteristics of BMG. Standard ultrasonic methods give information elastic and acoustic properties of BMG samples. Application of short-p ultrasound makes it possible to study local physical and structural charac matter. The microacoustical technique provides measuring elastic me